

A Single-Chip Signal Processor in Silicon Photonics Technology

Hong Deng

Doctoral dissertation submitted to obtain the academic degree of
Doctor of Photonics Engineering

Supervisors

Prof. Wim Bogaerts, PhD - Prof. Günther Roelkens, PhD
Department of Information Technology
Faculty of Engineering and Architecture, Ghent University

February 2024



ISBN 978-94-6355-812-9

NUR 959

Wettelijk depot: D/2024/10.500/17

Members of the Examination Board

Chair

Prof. Filip De Turck, PhD, Ghent University

Other members entitled to vote

Prof. Bart Kuyken, PhD, Ghent University

Prof. David Marpaung, PhD, Universiteit Twente, the Netherlands

Antônio Ribeiro Alves Júnior, PhD, formerly Brolis Sensor Technology

Chris Roeloffzen, PhD, LioniX International, the Netherlands

Prof. Guy Torfs, PhD, Ghent University

Supervisors

Prof. Wim Bogaerts, PhD, Ghent University

Prof. Günther Roelkens, PhD, Ghent University

Dankwoord

Five and a half years later, as I write this thesis, I still remember that distant morning when I attended my first team meeting. That was a rainy day, and I was late for the meeting. With this awkwardness, Wim asked me why I had chosen this particular group for my PhD study, and I said, for a mature and reliable process design kit. With no doubt, I got a smile from everyone.

As I reflect on my journey, I feel so lucky that I can be a part of this big group. Maybe the silicon photonic process is not that satisfying, but all the supports I have received here has more than compensated for any imperfections. Thanks, to all those who have kindly assisted me during this incredible journey.

I wish to express my heartfelt gratitude to my promotor, Prof. Wim Bogaerts. Your wealth of knowledge, comprehensive skillset, and limitless help have consistently served as my reliable foundation. Your passion has been a constant source of inspiration, especially before the tapeout deadline :) Also, I am thankful for the freedom you have granted me and for the trust you've placed in me along this way. Without your invaluable support, this thesis work would have never become a reality. I also want to thank my co-promoter, Prof. Günther Roelkens. Thank you for offering kind help and guidance whenever I needed it. The insightful discussions I've had with you have been invaluable to me in my research journey. Thank you for your unwavering support.

I would like to thank all of my PhD jury members: Prof. Filip De Turck, Prof. David Marpaung, Dr. Antonio Ribeiro, Prof. Guy Torfs, Dr. Chris Roeloffzen, and Dr. Bart Kuyken. Thanks for your time.

Thanks to all my teammates in these years. Dr. Umar Khan, thank you for your endless assistance. I know that if I need some help, I can always come to you. Dr. K.P. Nagarjun, we have so much invaluable or valueless discussions. Thanks for sharing so much interesting ideas with me. Xiangfeng, we've shared so many memories. I'm deeply grateful for your friendship. Yuxi, thank you very much for your contribution. Your attitude and hard work truly inspired me. I would also like to express my gratitude to Antonio, Yufei, Mi, Iman, Lukas, Yu, Yichen. Your support and collaboration have been invaluable to me.

It is not so common for one of Wim's student to work in the cleanroom. I am so grateful that I can get so much help from all the cleanroom people. Steven, thanks very much for guiding me about the lithography, lift-off metalization and so many

things. Liesbet, thanks for your help on the FIB cut, which directly rescued the whole thesis work. Jing and Emadreza, thanks for helping me the transfer printing process, and guiding me the characterization of the printed lasers. Dongbo and Yujie, thanks for your help on a lot of small things. Actually it is a little bit hard for me to recognize people in the cleanroom. So sometimes I got assistance, while I really did not know who. Thank you, to whom I don't really know.

I also want to thank Clemens, for the lab managing. Thanks for your help on experiments managing and also your guidance on some rarely used devices. Jasper and Hasan, thank you for the help on the electronic devices and printed circuit boards. Peter Guns, thank you for your great machining work.

I am appreciated that I got quite a lot of help from a number of people from other groups. Prof. Johan Bauwelinck, and Dr. Joris Van Kerrebrouck, thanks very much for guiding me the design of high speed PCBs. Prof. Guy Torfs, Dr. Joris Van Kerrebrouck, Dr. Nishant Singh, and Dr. Olivier Caytan, thank you very much for your selfless supports on the high-speed measurements. Mr. Stijn Duynslager, Dr. Thomas Vervust, Mr. Steven Van Put, thanks for your kind help on processing my samples.

Financial work is always quite annoying. I am grateful that Ilse and Ilse make these things so smooth and easy. Kristien, thank you very much for the technical support, and finding me a good password.

Thanks to all the Chinese colleagues, Yanlu, Yujie, Chupao, Yang, Biwei, Ying, Dongbo, Tingting, Haolan, Xiujun, Ye, Shiqi, Xin, He, Ruifeng, Yichen, Yize, Zhongtao, Chao, Senbiao, Ruqi, Chenming, Yu, Mingxiang, Zhizhi, Bingying, Yu, Yuxi, Xiangfeng, Xiaoning, Yang, Qiang, Zuyang, Chonghuai, Xiaomin, Yuting, Ruijun, Mi, Zheng, Yufei, and Yinghao. Thank you for your companionship, which has transformed Ghent into a true home for me.

Finally, I would like to express my deepest gratitude to my parents. Without your understanding and supports, I cannot make it out. Thanks, for all I have.

Gent, November 2023
Hong Deng

Table of Contents

Dankwoord	i
Nederlandse samenvatting	i
1 Inleiding	i
2 Chip Layout and Packaging	ii
3 Karakterisering	iv
3.1 Micro-transfer-gedrukt laserblok	iv
3.2 Modulatorblok	v
3.3 Filterblok	vi
3.4 Fotodetectorblok	vii
4 Toepassingen	vii
4.1 Instelbaar Microgolf Fotonisch Filter	viii
4.2 Instelbare Opto-elektronische Oscillator (OEO)	viii
4.3 RF Signaal Verdubbeling	viii
5 Conclusie	xii
English summary	i
1 Introduction	i
2 Chip Layout and Packaging	ii
3 Characterization	iv
3.1 Micro-Transfer-Printed Laser Block	iv
3.2 Modulator Block	v
3.3 Filter Block	v
3.4 PD block	vii
4 Applications	vii
4.1 Tunable Microwave Photonic Filter	vii
4.2 Tunable Opto-electronic oscillator	ix
4.3 RF Signal Doubling	ix
5 Conclusion	xi
1 Introduction	1-1
1.1 Silicon Photonics	1-1
1.2 Microwave Photonics	1-10
1.3 Objectives of this thesis	1-16
1.4 Outline of this thesis	1-17

1.5	Publications	1-18
1.5.1	Publications in international journals	1-18
1.5.2	Publications in international conferences	1-18
	References	1-21
2	Silicon Photonic Components	2-1
2.1	Passive Components	2-2
2.1.1	Waveguides	2-2
2.1.2	Couplers	2-5
2.2	Active Components	2-8
2.2.1	Optical phase tuners	2-8
2.2.2	Optical Modulators	2-25
2.2.3	Photodiodes and Monitors	2-28
2.2.4	Heterogeneous-integrated optical amplifiers	2-31
2.3	Workflow: from layout to tests	2-34
2.4	Conclusion	2-43
	References	2-44
3	Silicon Photonic Optical Filters	3-1
3.1	Basic silicon photonic optical filters	3-2
3.1.1	Mach-Zehnder interferometers and tunable optical couplers	3-3
3.1.2	Microring resonators	3-5
3.2	Complex and reconfigurable optical filters	3-8
3.2.1	Optical tunable couplers	3-8
3.2.2	Tunable ring resonators	3-12
3.2.3	Tunable ring-loaded MZI	3-13
3.3	Conclusion	3-20
	References	3-21
4	Microwave Photonics	4-1
4.1	Microwave Photonic Link	4-2
4.1.1	Intensity Modulation	4-2
4.1.2	Phase Modulation	4-3
4.1.3	Imperfect Modulators	4-4
4.1.4	Figures of Merit	4-5
4.2	Microwave Photonic Filter	4-8
4.3	RF signal Generation	4-11
4.3.1	Laser Beating	4-11
4.3.2	Opto-Electronic Oscillator	4-11
4.3.3	Frequency Multiplication	4-13
4.4	Conclusion	4-14
	References	4-15

5	Reconfigurable Modulator	5-1
5.1	Introduction	5-2
5.2	Optical design and principle	5-4
5.3	Simulation and Tested results	5-8
5.4	Conclusion	5-12
	References	5-12
6	Micro-Transfer-Printed SOA and Lasers	6-1
6.1	Micro-Transfer-Printing Process on iSiPP50G	6-2
6.2	SOA Characterization	6-5
6.2.1	Gain	6-5
6.2.2	Cross-Gain and Cross-Phase Modulation	6-8
6.3	Lasers	6-10
6.4	Conclusion	6-13
	References	6-14
7	Single-Chip Fully Integrated Signal Processor	7-1
7.1	Schematic and Principle	7-2
7.1.1	Light generation	7-2
7.1.2	E/O conversion	7-3
7.1.3	Tunable microwave photonic filter	7-4
7.2	Simulation	7-7
7.3	Sample Packaging	7-9
7.3.1	Electrical packaging	7-9
7.3.2	Optical packaging	7-11
7.4	Characterization	7-12
7.4.1	Laser Generation	7-12
7.4.2	Programmable Optical Filtering	7-12
7.4.3	Analog Optical Transmitter. E/O Conversion	7-12
7.4.4	Equalized E/O conversion	7-14
7.4.5	Microwave photonic filtering. E/E conversion	7-15
7.4.6	Opto-Electronic Oscillator. RF Generation.	7-16
7.4.7	Frequency Doubling	7-23
7.4.8	Optical Wavelength Meter / RF Frequency Meter	7-23
7.4.9	Tunable True Time Delay	7-24
7.4.10	Performance Evaluation	7-27
7.5	Discussion	7-30
	References	7-32
8	Conclusion and Future work	8-1
8.1	Conclusion	8-2
8.2	Future work	8-3
8.2.1	More configuration possibilities	8-3
8.2.2	Performance improvement	8-3
8.2.3	Scale-up	8-4

8.2.4 Co-packaging with RF devices 8-4

List of Figures

1	Schematische voorstelling van de voorgestelde signaalprocessor op één chip.	ii
2	Lay-out en gefabriceerd monster van de voorgestelde signaalprocessor op één chip.	iii
3	Een verpakte demonstratie van de signaalprocessor.	iv
4	Karakterisering van het laserblok.	v
5	Schematische voorstelling van het modulatorblok.	v
6	Karakterisering van het modulatorblok.	vi
7	Karakterisering van het filterblok.	vii
8	Instelbaar microwave fotonisch filter.	ix
9	Instelbare opto-elektronische oscillator voor RF-sig-naalgeneratie.	x
10	RF-frequentieverdubbeling met de signaalprocessor.	xi
1	Schematic of the proposed single-chip signal processor.	ii
2	Layout and fabricated sample of the proposed single-chip signal processor.	iii
3	A packaged demonstration of the signal processor.	iii
4	Characterization of the laser block.	iv
5	Schematic of the modulator block	v
6	Characterization of the modulator block.	vi
7	Characterization of the filter block.	vi
8	Tunable microwave photonic filter.	viii
9	Tunable opto-electronic oscillator for RF signal generation.	ix
10	RF frequency doubling with the signal processor.	x
1.1	Silicon photonic integration circuits. Based on Prof. Wim Bo-gaerts's course material.	1-2
1.2	Silicon photonic devices	1-3
1.3	Various methods for hybrid integration	1-4
1.4	silicon photonic transceiver systems	1-5
1.5	silicon photonic systems for quantum computing and communication	1-6
1.6	Silicon photonics chips for machine learning and LiDAR	1-7
1.7	Programmable photonic circuits	1-8
1.8	A typical microwave photonic link	1-10
1.9	Schematic of a microwave photonic filter	1-12

1.10	Various opto-electronic oscillator systems	1-13
1.11	Bulky and integrated microwave photonic systems	1-14
1.12	Schematic of the optical and RF signal processor that we developed in this PhD.	1-16
2.1	Silicon photonic waveguides and their fundamental mode profiles	2-3
2.2	Strip waveguide based directional coupler in silicon photonics . . .	2-5
2.3	Multimode interference coupler in silicon photonics	2-6
2.4	Mechanisms for phase shifting in silicon photonics	2-8
2.5	Various types of heaters in silicon photonics	2-9
2.6	Schematic circuit for heaters' thermal efficiency tests	2-11
2.7	Metal heater thermal efficiency tests	2-12
2.8	Thermal efficiency of side doped heaters with and without EXPO trench	2-13
2.9	Heater designs with improved thermal efficiency	2-13
2.10	Schematic circuit for heaters' time constants tests	2-14
2.11	Measured time waveform of a side doped heater with under etching	2-15
2.12	Frequency measurement results of a side heater with UCUT using a VNA.	2-18
2.13	Frequency measurement results of a side heater with UCUT using a signal generator and an oscilloscope.	2-19
2.14	Heterodyne measurement for phase shifters bandwidth tests	2-21
2.15	Bode plots of various thermal phase shifters	2-21
2.16	DC power supplies	2-22
2.17	Voltage driving and current driving	2-22
2.18	Pulse width modulation	2-22
2.19	Matrix addressing scheme	2-24
2.20	PN and PIN junction	2-25
2.21	PN and PIN modulator model	2-27
2.22	MZ modulator and microring modulator	2-27
2.23	Lateral PIN and vertical PIN photodiodes	2-28
2.24	Tap monitor tests	2-29
2.25	Micro-transfer printing	2-31
2.26	Micro-transfer printing work flowprefabrication of III-V devices .	2-32
2.27	Micro-transfer printing work flow: post processing of fully stacked silicon photonic chips	2-33
2.28	Silicon photonic circuit design work flow	2-34
2.29	Optical coupling schemes	2-36
2.30	Vertical coupling packaging schemes	2-38
2.31	Fiber array curing	2-39
2.32	Assembled RF-DC PCB. (a) RF daughter PCB; (b) DC mother PCB; (c) and (d) Assembled RF-DC PCB.	2-40
2.33	Packaging performance	2-41
2.34	Fully packaged silicon photonic sample	2-42

3.1	Schematic of an MZI	3-3
3.2	Balanced MZI responses	3-3
3.3	Schematic of micro ring resonators	3-5
3.4	Micro ring resonator's filter response	3-5
3.5	Schematic of a double stage MZI	3-8
3.6	Numerical simulation of a double stage MZI	3-10
3.7	Fitting results of a double stage MZI	3-11
3.8	Phase response of a double stage MZI	3-11
3.9	Schematic of a tunable ring resonator	3-12
3.10	Schematic of a tunable ring loaded MZI	3-13
3.11	Schematic of multi-ring loaded MZI	3-13
3.12	Schematic of the filter block in the signal processor	3-14
3.13	Measurement of the rings in the filter block	3-15
3.14	Calibration of the tunable ring resonator with the tap PDs	3-15
3.15	Characterization of the main MZI structure	3-16
3.16	Configuration of the four-ring-loaded MZI	3-17
3.17	Improving the filter's roll-off.	3-17
3.18	Response of a MZI loaded with a critical-coupled ring.	3-18
3.19	Tunable band passed filters.	3-18
4.1	A typical microwave photonic link	4-2
4.2	Schematic of a Mach-Zehnder modulator	4-3
4.3	The figure of merit of a microwave photonic link	4-5
4.4	Linear and non-linear system	4-6
4.5	Nonlinear system characterization	4-7
4.6	Schematic of a typical microwave bandpass filter	4-8
4.7	Principle of the microwave bandpass filter	4-9
4.8	Schematic of a universal RF filter based on SSB modulation	4-10
4.9	Laser beat for RF signal generation	4-11
4.10	Schematic of typical OEO structures	4-12
5.1	Cross section of PN and PIN junction based modulators	5-2
5.2	Schematic of a reconfigurable modulator	5-4
5.3	Modulation curve for various modulators	5-6
5.4	Phasor plot of a reconfigurable modulator	5-7
5.5	Coupling ratio sweep for reconfigurable modulator	5-8
5.6	Coupling ratio and phase sweep for reconfigurable modulator: Intensity modulation	5-9
5.7	Coupling ratio and phase sweep for reconfigurable modulator: Intensity modulation, nonlinearity, loss, and phase modulation range	5-10
5.8	Simulated DC response of a PN junction modulator	5-10
5.9	Fabricated sample and measurement results	5-11
6.1	Schematic of TP-based integration on 200 mm or 300 mm Si photonic wafers in a parallel manner.	6-2

6.2	A schematic of a transfer printed SOA coupon.	6-2
6.3	Process flow of SOA device fabrication on the source InP substrate.	6-3
6.4	A fabricated InP SOA source	6-4
6.5	Process flow of iSiPP50G samples post processing and transfer printing	6-4
6.6	A transfer-printed SOA.	6-6
6.7	Characterization of a SOA	6-6
6.8	Circuits for characterizing cross gain and cross phase modulation of on-chip SOAs.	6-7
6.9	Generated electrical waveform with pump light and probe light.	6-8
6.10	High speed performance of the SOA-MZI based wavelength converter.	6-9
6.11	Schematic of the laser block in the signal processor.	6-10
6.12	Laser tuning results.	6-11
6.13	Laser continuous tuning results.	6-11
6.14	Laser's phase noise and stability.	6-11
7.1	Schematic of the proposed signal processor.	7-2
7.2	A generic optical filter.	7-4
7.3	A phase modulated signal, modulated by a chirp signal.	7-7
7.4	Simulated filtered signal.	7-8
7.5	The layout of the signal processor.	7-9
7.6	Packaged sample	7-10
7.7	RF packaging characterization.	7-10
7.8	Fiber array curing characterization.	7-11
7.9	Laser block tuning results	7-12
7.10	Filter block configuration and turning results.	7-13
7.11	Optical transmitter characterization.	7-13
7.12	Reconfigurable optical modulator characterization.	7-14
7.13	Modulator frequency response.	7-14
7.14	Equalized transmitter response.	7-15
7.15	Microwave bandpass filter.	7-16
7.16	Tunable microwave photonic filter responses.	7-17
7.17	A tunable four band-pass filter.	7-18
7.18	An opto-electronic oscillator demonstrator.	7-18
7.19	Opto-electronic oscillator demonstrator with an off-chip PD.	7-19
7.20	Opto-electronic oscillator demonstrator with an on-chip PD.	7-20
7.21	Opto-electronic oscillator demonstrator with an individual on-chip optical resonant receiver.	7-21
7.22	Modulator block configuration for frequency doubling.	7-23
7.23	Frequency doubling tests setup.	7-24
7.24	Frequency doubling results with an off-chip PD	7-25
7.25	Frequency doubling results with an on-chip PD	7-26
7.26	A demonstrator as an optical wavelength meter or an RF frequency meter.	7-26

7.27 A demonstrator for signal temporal processing.	7-27
7.28 Setup for the noise floor measurement	7-28
7.29 Setup for the SFDR measurement	7-28
7.30 Measured SFDR of this microwave processor	7-29

List of Tables

1.1	Comparison of bulky microwave photonic systems and integrated systems	1-14
2.1	Thermal efficiency of various heaters	2-16
2.2	Thermal efficiency of various heaters with undercut	2-17
2.3	Time constants of various heaters with undercut	2-17
2.4	Frequency measurement results of various heaters with UCUT using a VNA	2-19
2.5	Frequency measurement results of various heaters with UCUT using a signal generator and an oscilloscope.	2-20
7.1	Phase noises of Opto-electronic oscillator demonstrators.	7-22

List of Acronyms

A

ADS Advanced Design System

B

BCB Bisbenzocyclobutene
BPF Band Pass Filter

C

CLIPP ContactLess Integrated Photonic Probe
CMOS Complementary Metal-Oxide-Semiconductor
CROW Coupled Resonator Optical Waveguides
CSSSB Carrier Suppressed Single Sideband Modulation

D

DC Directional Coupler
DFB Distributed Feedback
DUT Device Under Test

E

EAM Electro-absorption Modulator

EDFA	Erbium Doped Fibre Amplifier
EMI	Electromagnetic Interference
EO	Electrical-to-Optical
ESA	Electrical Spectrum Analyzer

F

FDM	Finite-Difference Method
FEM	Finite Element Method
FIR	Finite Impulse Response
FOM	Figure of Merit
FP	Fabry-Perot
FPGA	Field Programmable Gate Arrays
FSR	Free Space Range
FWHM	Full Width at Half Maximum

G

GaAs	Galliumarsenide
GC	Grating Coupler

H

HPF	High Pass Filter
-----	------------------

I

InP	Indium Phosphide
-----	------------------

L

LiDAR	Light Detection And Ranging
LPF	Low Pass Filter

M

MEMS	Micro-Electro-Mechanical Systems
MMI	Multimode Interference
MOVPE	Metal-Organic Vapor-Phase Epitaxy
MRM	Microring Modulator
MUX	Multiplexer
MZI	Mach-Zehnder Interferometer
MZM	Mach-Zehnder modulator

N**O**

OE	Optical-to-Electrical
OEO	Opto-electronic Oscillator
OSA	Optical Spectrum Analyzer

P

PCB	Printed Circuit Board
PD	Photodetector
PDK	Process Design Kits
PDM	Plasma Dispersion Modulator
PDMS	Polydimethylsiloxane
PIC	Photonic Integrated Circuit
PL	Photoluminescence
PWM	Pulse Width Modulation

Q

QKD	Quantum Key Distribution
-----	--------------------------

R

RF Radio Frequency

S

SFDR Spurious-Free Dynamic Range
Si silicon
SiGe silicon-germanium
SMR Sidelobe to Mainlobe Ratio
SNR Signal to Noise Ratio
SOA Semiconductor Optical Amplifiers
SSB Single Sideband Modulation

T

TEC Temperature Controller
TL Tunable Laser
TIA Transimpedance Amplifier

U

UCUT Undercut

V

VNA Vector Network Analyzer

W

WG Waveguide

X

XGM
XPM

Cross Gain Modulation
Cross Phase Modulation

Nederlandse samenvatting

–Summary in Dutch–

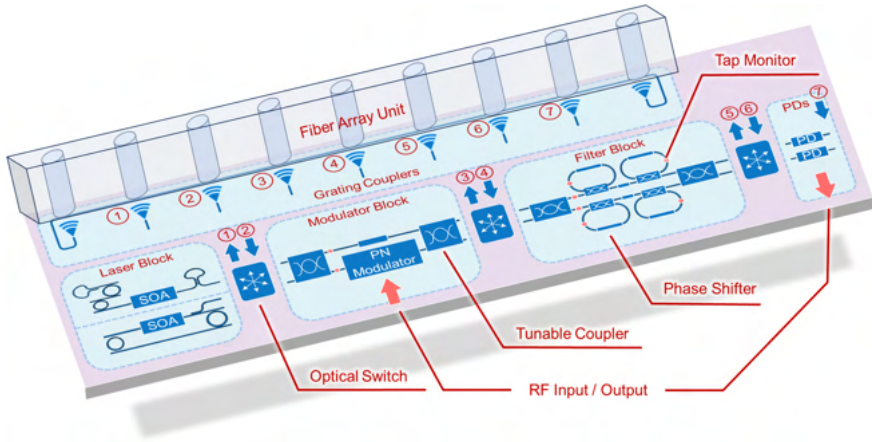
1 Inleiding

Het volume van gegenereerde, verbruikte, gekopieerde en opgeslagen gegevens bereikte 1 zettabyte in 2012 en heeft de weg vrijgemaakt voor een exponentiële toename die naar verwachting 180 zettabytes zal bereiken in 2025. Deze gegevensexplosie stelt aanzienlijke uitdagingen voor datacenters, waarbij een hogere capaciteit en verbeterde energie-efficiëntie worden vereist. Bovendien heeft de proliferatie van grootschalige AI-training de druk op dataverkeer verder verhoogd, met name de scheiding tussen vast verkeer dat wordt overgedragen via optische signalen door vezels en mobiel verkeer dat vertrouwt op draadloze radiofrequente (RF) signalen. Traditioneel worden deze twee signaaltypes afzonderlijk behandeld en verwerkt, wat leidt tot onnodige conversie- en propagatieverliezen, evenals een hogere kostprijs. We hebben een meer veelzijdige aanpak nodig om signalen effectief te verwerken in zowel het RF- als het optische domein.

Silicium fotonische schakelingen worden wijdverspreid gebruikt voor de optische signaaltransmissie en manipulatie van licht op het oppervlak van een chip met behulp van optische golfgeleiders om signalen te transporteren, hogesnelheidsmodulatoren om informatie op een lichtgolf te coderen, en germanium fotodetectoren (PD's) om deze signalen terug te converteren naar het elektrische domein. Bovendien kunnen golfgeleider-gebaseerde interferometers worden ontworpen om het optische signaal en het daarop geplaatste RF-signaal te filteren. Ondersteund door de hoogwaardige productie-infrastructuur van de elektronica is er een duidelijke trend naar een toenemende complexiteit en programmeerbaarheid van schakelingen. Met de integratie van optische faseverschuivers worden extra vrijheidsgraden toegevoegd aan de optische schakelingen, die kunnen worden gebruikt om fabricageonvolkomenheden te compenseren of een grotere regelbaarheid voor verschillende functies te bereiken.

Silicium heeft een indirecte bandkloof, en omdat dit lichtemissie bemoeilijkt, is de integratie van III-V materialen, zoals GaAs en InP, uitgebreid onderzocht. Transferafdrukken komt naar voor als een veelbelovende methode die het gebruik van kostbare III-V epitaxiale substraten optimaliseert zonder aanpassingen aan het fabricageproces van silicium-fotonica.

Omdat optische signalen een enorme bandbreedte kunnen beslaan, wordt foto-



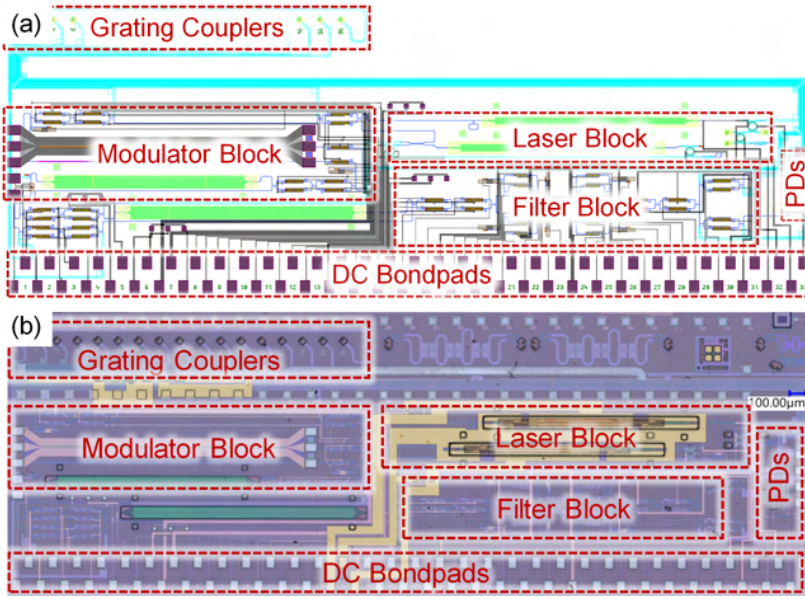
Figuur 1: Schematische voorstelling van de voorgestelde signaalprocessor op één chip.

nica ook gebruikt om hoogwaardige RF-signalen te genereren, manipuleren, transporteren en meten. Dit vakgebied staat bekend als Microwave Photonics (MWP). Door RF-signalen op een optische drager te encoderen met een modulator en het signaal terug om te zetten met een snelle fotodetector, kan een optische verbinding het gemoduleerde RF-signaal via optische media verspreiden, profiterend van een grote bandbreedte en lage propagatieverliezen. Als een optische filter wordt ingevoegd in de optische verbinding, verkrijgt men effectief een microgolffilter. Daarna kan de generatie en multiplexering van een RF-signaal ook worden geïmplementeerd met fotonische schakelingen.

In dit werk hebben we een chip ontworpen, gefabriceerd en getest, die geprogrammeerd kan worden voor het verwerken van zowel optische als microgolffsignalen. We bespreken het ontwerp van de chip, met de verschillende subcircuits: een configureerbare optische modulator die zowel fasemodulatie als intensiteitsmodulatie aankan, twee lasers geïntegreerd met transferafdruk, en een programmeerbare filterbank. We bespreken how we decombinatie van deze circuits kunnen aanwenden voor diverse bewerkingen van optische en microgolffsignalen, waaronder electro-optische en opto-electrische conversie, filteren, en zelfs een opto-electronische oscillator.

2 Chip Layout and Packaging

De schematische weergave van de signaalprocessor wordt getoond in Fig. 1. Zoals te zien is, bestaat deze uit vier hoofdblokken, namelijk een instelbaar laserblok (met 2 lasers), een modulatorblok, een optisch filterblok en een blok met snelle PD's. Het langste optische pad begint met het licht dat wordt gegenereerd door de laserbron en dat vervolgens wordt geleid naar het modulatorcircuit, dat kan worden geconfigureerd voor zowel fase- als intensiteitsmodulatie. Het licht, gemoduleerd



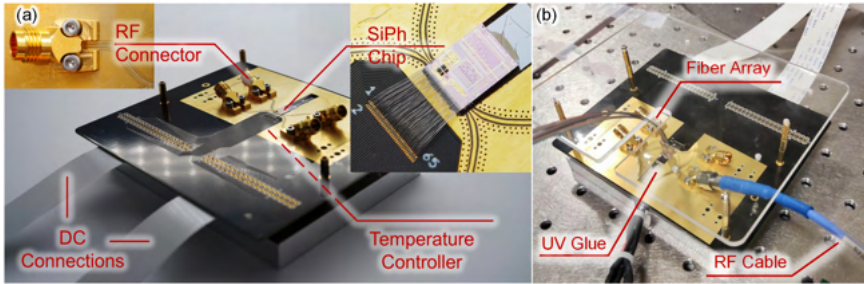
Figuur 2: (a) Lay-out en (b) gefabriceerd monster van de voorgestelde signaalprocessor op één chip.

met een RF-sigitaal, wordt vervolgens doorgevoerd naar het optische filterblok, dat bestaat uit een MZI verzaard met 4 ringresonatoren met instelbare koppeling en aftappunten. Daarna kan het gefilterde lichtsignaal weer worden omgezet naar het microgolfdomein door de snelle PD's.

Alle vier de functionele blokken zijn met elkaar verbonden door optische schakelaars, waardoor het lichtsignaal op elk verbindingspunt kan worden gerouteerd, waardoor de processor kan worden geconfigureerd voor zowel optische als RF-sigitaalverwerking, en waardoor meerdere processors kunnen worden geschakeld over glasvezellinks. De optische schakelaars zelf zijn geïmplementeerd als een-traps or tweetraps MZI's, afhankelijk van de vereisten voor de koppelverhouding.

Het volledige fotonische circuit omvat 15 optische in-/uitgangspoorten, 3 RF-kanalen (1 ingang, 2 uitgangen), 52 optische faseverschuivers op basis van lokale verwarmingselementen en 8 aftappunten. De lay-out en de gefabriceerde monster van de voorgestelde signaalprocessor worden respectievelijk getoond in Fig. 2 (a) en (b). Met deze uitgebreide connectoren is een grondige aanpak voor optische, DC- en RF-verpakking essentieel om de stabiliteit en robuustheid van het systeem te waarborgen.

Een verpakte demonstrator wordt getoond in Fig. 3. Een printplaat (PCB) is ontworpen voor de elektrische verbindingen. De processorchip wordt met de voorkant naar boven op het bord geplaatst, en de bondpads worden verbonden met behulp van draadverbindingen. Om RF-signalen met lage verliezen te propageren,



Figuur 3: Een verpakte demonstratie van de signaalprocessor. (a) Zonder vezelarray-aansluiting; (b) Met een vezelarray bevestigd en een bescherming.

maakt het PCB gebruik van hoogwaardige materialen (Megtron 6) voor de dielektrische lagen, en gebruiken we Rosenberger soldeerloze RF-connectoren. Onder het PCB worden een temperatuurregelaar en een aluminium koellichaam geplaatst om de omgevingstemperatuur van de chip te stabiliseren.

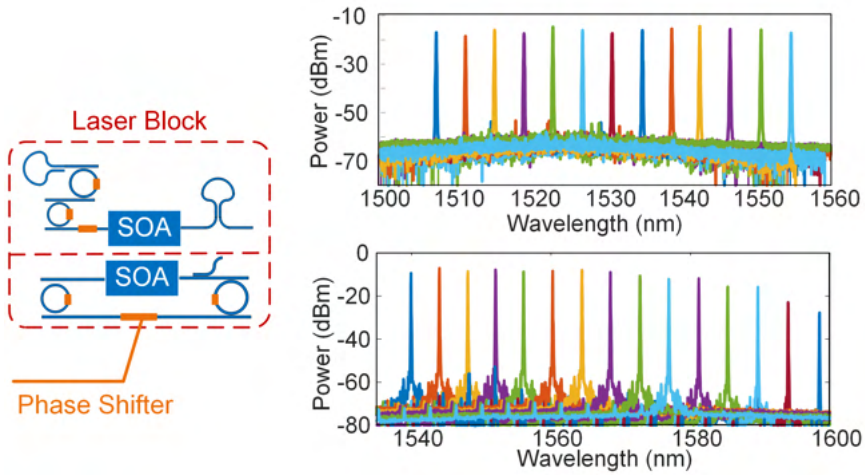
Vervolgens wordt een vezelarray op de silicium-fotonische chip bevestigd. Specifiek werd een 32-kanaals vezelarray met actieve uitlijning gepositioneerd op een referentie golfgeleider en vervolgens op zijn plaats gehouden met UV-uitthardende lijm (NOA 63). Bovendien werd extra UV-lijm toegevoegd om de fragiele draadverbindingen in te kapselen, zoals te zien is in Fig. 3(b). De verpakte chip vertoont hoge robuustheid en reproduceerbaarheid tijdens metingen.

3 Karakterisering

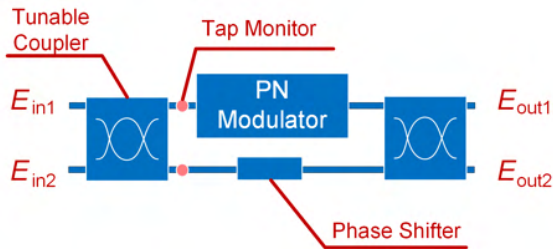
3.1 Micro-transfer-gedrukt laserblok

Het laserblok in de signaalprocessor is ontworpen door Dr. Jing Zhang in de PRG-groep, en het micro-transfer-drukproces werd begeleid door de heer Emadreza Soltanian in de PRG-groep.

In het laserblok zijn er twee verschillende laserholtes, gebaseerd op een Fabry-Pérot (FP) holte en een ringholte, zoals getoond in Fig.4. Voorgefabriceerde SOA's worden overgebracht naar de laserholtes om optische versterking te bieden. Wanneer de versterking van de overgeplaatste SOA hoger is dan de andere geaccumuleerde verliezen in de laserholte, zal het lasen beginnen. In elke laserholte worden twee ringresonatorfilters gebruikt om een Vernier-bandoorlaatfilter te vormen en de longitudinale modi te selecteren. Er bevinden zich drie thermische faseverschuiers in elke laserholte: twee voor de faseafstemming in de ring en één voor de longitudinale fase. Door de fase van de ringen en de optische caviteit aan te passen, kunnen we de geselecteerde longitudinale modus veranderen en de laser-golflengte aanpassen. De resultaten van de lasertuning worden getoond in Fig.4. Het is op te merken dat de FP-laser van de verpakte chip elektrisch kortgesloten bleek te zijn na het draadverbinden, dus de resultaten ervan zijn verkregen van een



Figuur 4: Karakterisering van het laserblok.

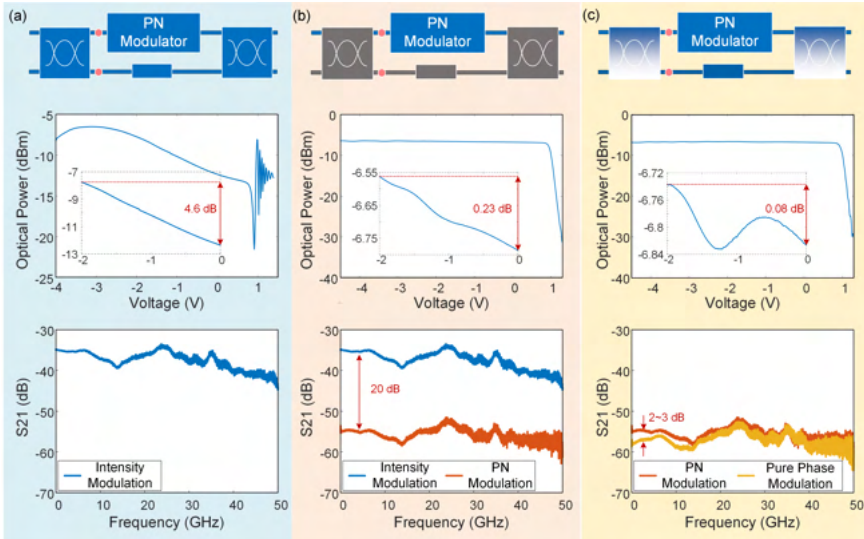


Figuur 5: Schematische voorstelling van het modulatorblok.

andere chip. De twee SOA's die in deze twee lasercaviteiten zijn aangebracht, hebben verschillende fotoluminescentie (PL) pieken rond 1500 nm en 1550 nm, wat leidt tot laserpieken rond respectievelijk 1525 nm en 1575 nm. Uit Fig. 4 blijkt dat beide laserholtes een instelbaarheid van meer dan 50 nm bereiken, en het volledige instelbereik van het laserblok dus kan oplopen tot 90 nm.

3.2 Modulatorblok

Het modulatorblok in de signaalprocessor is een herconfigureerbare modulator, die is geïmplementeerd door een standaard PN-junctie-modulator te integreren in een instelbare MZI, bestaande uit twee instelbare koppelaars (TC) en een faseverschuiver. De schematische weergave ervan wordt getoond in Fig 5. De PN-junctie-modulator fungeert als een fase-modulator, waardoor het RF-sigitaal op de optische drager kan worden geëncodeerd. De andere instelbare componenten, namelijk de TC's en de faseverschuiver, worden gebruikt om de respons van het



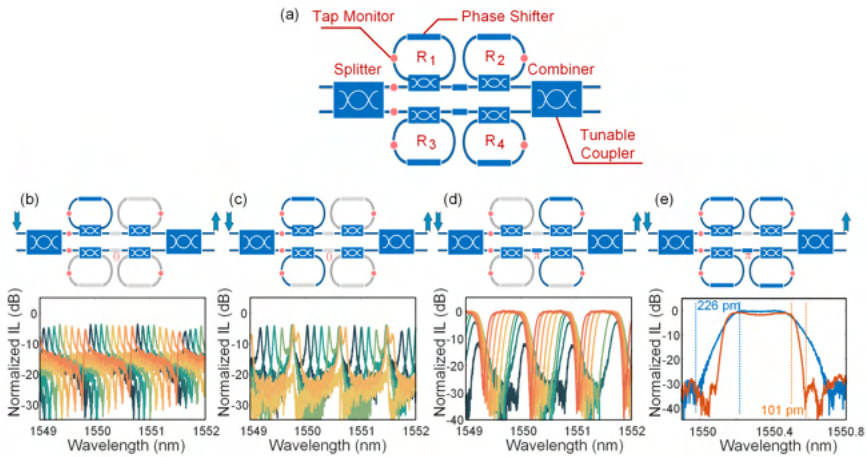
Figuur 6: Karakterisering van het modulatorblok. (a) Geconfigureerd als een intensiteitsmodulator; (b) Geconfigureerd als een fase modulator; (c) Geconfigureerd als een geoptimaliseerde pure fase modulator.

volledige circuit aan te passen. Door de koppelverhoudingen van de TC's en de faseverschuiver te manipuleren, kan een dubbelzijdig gemoduleerd signaal met twee RF-zijbanden (positieve en negatieve frequenties) worden gegenereerd met een instelbare faseverhouding. Dit betekent dat het RF-signaal dat wordt gegenereerd uit het gemoduleerde optische signaal kan overeenkomen met een fase-gemoduleerd signaal, een intensiteit-gemoduleerd signaal, of hun combinatie. Bovendien kan het modulatorblok worden geconfigureerd om de modulatierepons te optimaliseren.

3.3 Filterblok

Het filterblok in de signaalprocessor is een MZI met ringen, dat twee afstembare ringen bevat aan elke arm van een instelbare MZI, zoals getoond in Fig. 7(a). De gekoppelde twee ringen aan elke arm fungeren als een all-pass filter van de tweede orde (indien verliesloos), en de koppelaars van de MZI verdelen licht door de ringen en mengen ze. Het hele filterblok kan worden geprogrammeerd om alle klassieke banddoorlaatfilters te zijn als de koppelverhouding in de MZI 0,5 is. En door de koppelverhoudingen tegelijkertijd af te stemmen, kan dit blok een universeel optisch filter zijn (beperkt door de filterordes).

Verschillende configuraties en reacties van het filterblok worden getoond in Fig.7 (b)(e). Als het faseverschil in de MZI nul is, zullen de ringen scherpe doorlaatbanden introduceren, zoals getoond in Fig.7 (b)-(c). De gefabriceerde ringen laten een 3 dB-bandbreedte van 35 pm zien wanneer ze kritisch zijn gekoppeld.



Figuur 7: Karakterisering van het filterblok. (a) Schematische voorstelling van het filterblok; (b) (c) (d) (e) Verschillende configuraties en reacties van het filterblok.

Als het faseverschil in de MZI wordt ingesteld op π , kan een overgekoppeld ringpaar typische Chebyshev Type II-filters vormen met een vlakke doorlaatband. De metingen laten doorlaatbanden zien met ~ 0.5 dB rimpel in de doorlaatbanden en 30 dB onderdrukking in de stopband (Fig.7d). Door het tweede ringenpaar af te stemmen op de rolloverpunten, wordt een filterrespons van het Chebyshev Type II van hogere orde verkregen, waarbij de overgangsbreedte wordt verbeterd van 226 pm tot 101 pm (Fig. 7e).

3.4 Fotodetectorblok

In de voorgestelde signaalprocessor worden twee verticale PIN-fotodiodes uit het imec Process Design Kit (PDK) gebruikt om het optische signaal om te zetten naar het RF-domein. De verticale PIN-diodes zijn ontworpen met een grote bandbreedte (50 GHz in de handleiding) en een gemiddelde efficiëntie (0,8 A/W in de handleiding).

4 Toepassingen

De single-chip signaalprocessor kan volledig programmeerbare filterrespons bieden (voor zowel optische als RF-signalen), evenals elektrische en optische signaalgeneratie en -detectie. Lasergeneratie (met het laserblok), optische signaalmodulatie (met het laserblok en het modulatorblok), optische signaalfiltering (met het filterblok) en optische signaaldetectie (met het PD-blok) kunnen rechtstreeks worden geïmplementeerd met de functionele blokken van de signaalprocessor. Deze sectie richt zich op de toepassingen voor de verwerking van RF-signalen.

4.1 Instelbaar Microgolf Fotonisch Filter

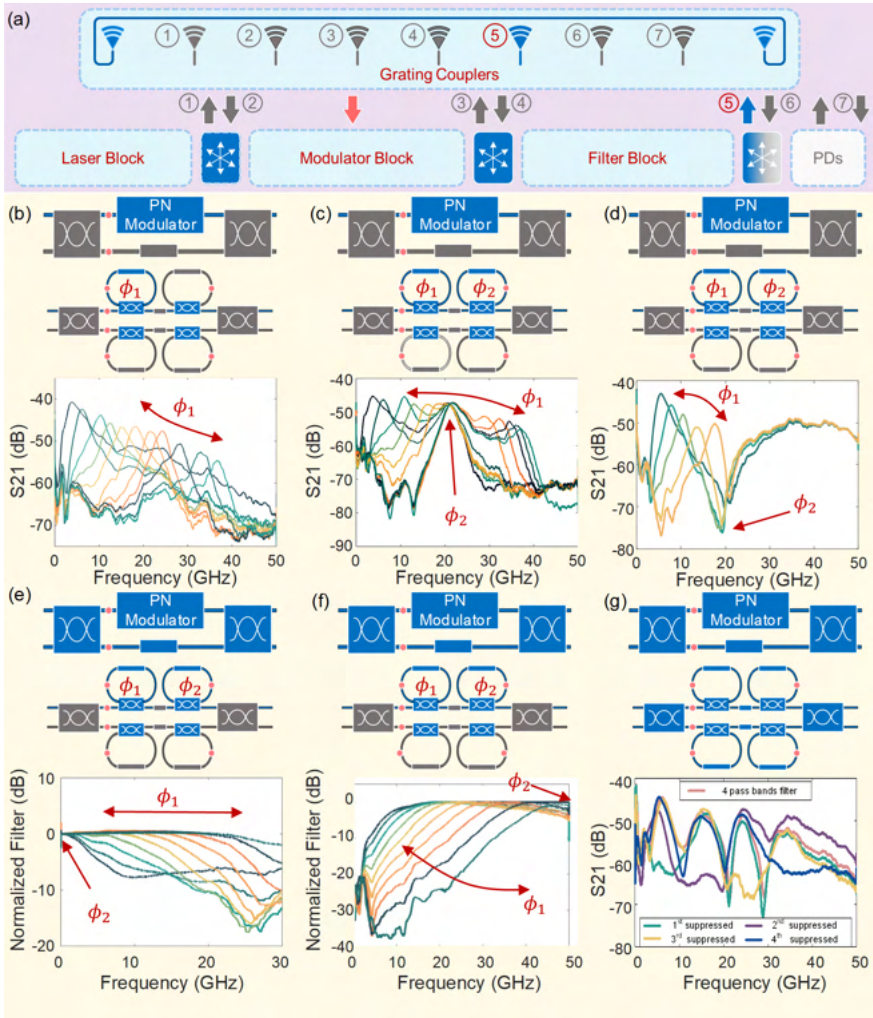
Met de technologie van microgolf-fotonica kan het volledige systeem geavanceerde lineaire filterresponsen van RF-signalen implementeren, zoals getoond in Fig.8. Fig.8 (a) toont de lichtstroom in de signaalprocessor. Het gekoppelde licht wordt ontvangen door een externe PD voor een propere RF-respons. Zoals besproken in het gedeelte over de modulator, kan het licht van de herconfigureerbare modulator RF-zijbanden genereren met instelbare faseverhoudingen wanneer het door de PD wordt ontvangen. Met behulp van herconfigureerbare optische filters kan de RF-filterrespons volledig worden gecontroleerd. Bovendien zijn slechts twee opeenvolgende ringfilters nodig om in het RF-domein een banddoorlaat- of bandstopfilter te bereiken dat equivalent is aan de optische filterrespons van het Chebyshev Type II. Diverse soorten RF-filterresponsen worden getoond in Fig. 8, gerealiseerd door zowel de instelbare modulator als de ringen af te stemmen. Bepaald door de Q -factoren van de ringen, ligt de laagste 3 dB-bandbreedte van de filters rond 3 GHz.

4.2 Instelbare Opto-elektronische Oscillator (OEO)

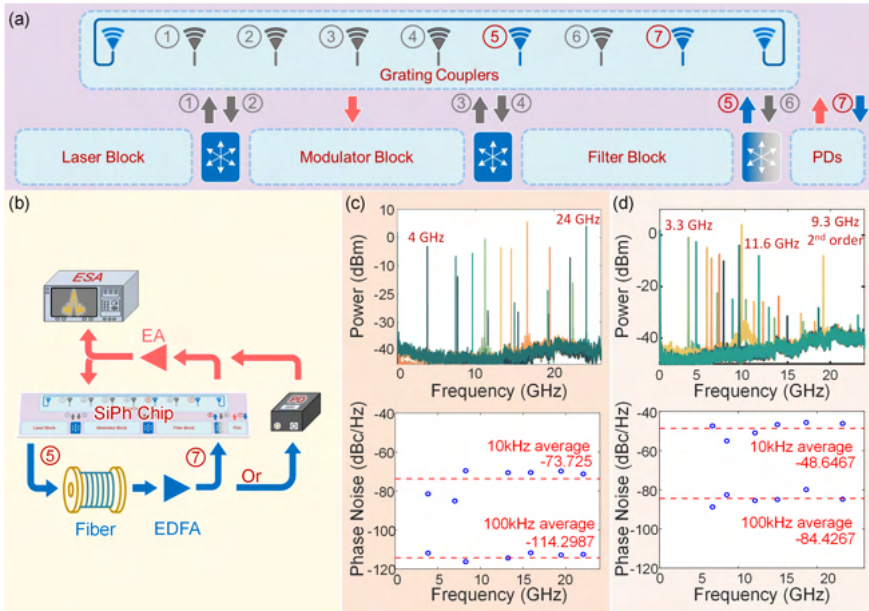
Met extra elektronische versterkers die het verlies van de banddoorlaatfilters compenseren, zoals getoond in de sectie over het microgolf-filter hierboven, kan de gerapporteerde signaalprocessor een OEO vormen met een instelbare centrale frequentie, zoals getoond in Fig.9. Een extra vezellengte is toegevoegd in het lichtpad om een langere oscillatiecaviteit te vormen, wat wordt aangegeven in Fig.9 (b). Met een off-chip PD kunnen RF-signalen worden gegenereerd met een instelbare frequentie van 4 GHz tot 24 GHz en een faseruis van -116 dBc/Hz bij een frequentieafwijking van 100 kHz, zoals getoond in Fig.9 (c). En met de on-chip PD kan het gegenereerde signaal worden afgestemd binnen 3.3 GHz tot 11.6 GHz met een fasegeluid van -84 dBc/Hz bij een frequentieafwijking van 100 kHz, zoals getoond in Fig.9 (d).

4.3 RF Signaal Verdubbeling

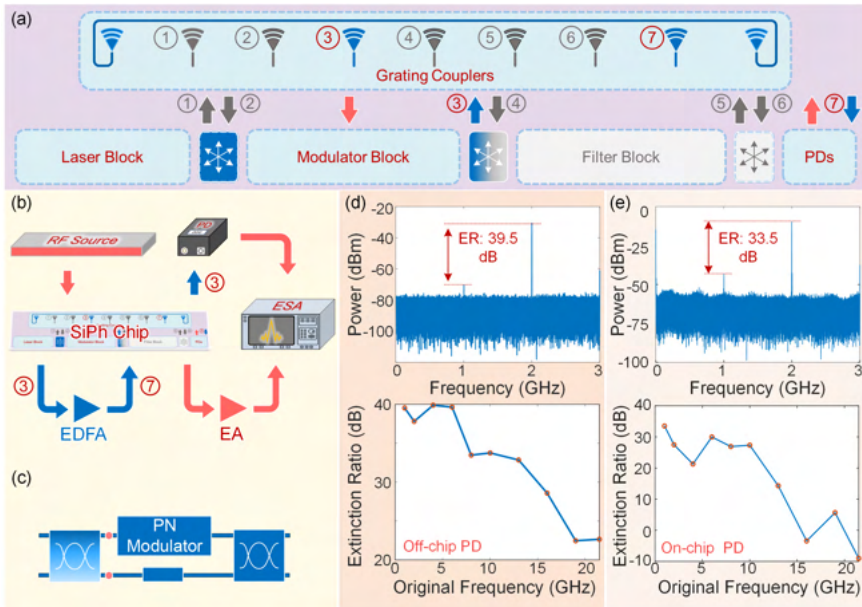
De signaalprocessor kan een RF-frequentieverdubbelingsproces bereiken met behulp van het laserblok, het modulatorblok en het detectieblok, zoals getoond in Fig.10(a). Fig.10(b) toont de meetopstelling voor niet-lineaire RF-responsen. De RF-frequentieverdubbeling wordt bereikt door de Mach-Zehnder-modulator in zijn nulpunt te positioneren, waarbij de verhouding van het tweede-harmonische signaal tot het eerste-orde signaal sterk afhankelijk is van de extinctieverhouding van het gemoduleerde signaal. Aangezien het propagatieverlies van de PN-modulator hoger is dan dat van de faseverschuiver, wordt de splitter van de herconfigureerbare modulators ingesteld op een werkpunt nabij 70:30 om het verliesverschil te compenseren, zoals getoond in Fig.10(c). De frequentieverdubbelingsresultaten met de off-chip PD en on-chip PD worden getoond in Fig.10 (d) en (e) respectievelijk. De resultaten tonen aan dat de extinctieverhouding tussen het tweede-orde



Figuur 8: Instelbaar microwave fotonisch filter. (a) De lichtstroom in de signalprocessor. (b)-(g) Verschillende configuraties van het systeem en de bijbehorende reacties.



Figuur 9: Instelbare opto-elektronische oscillator voor RF-signaalgeneratie. (a) Lichtstroom in de signaalprocessor; (b) Experimentele opstelling met een on-chip PD of een off-chip PD; (c) Experimentele resultaten met een off-chip PD; (d) Experimentele resultaten met een on-chip PD.



Figuur 10: RF-frequentieverdubbeling met de signaalprocessor. (a) Lichtstroom in de signaalprocessor; (b) Experimentele opstelling met een on-chip PD of een off-chip PD; (c) Configuratie van het modulatorblok. Meer licht wordt geleid naar de PN-modulator om het propagatieverlies te compenseren; (d) Experimentele resultaten met een off-chip PD; (e) Experimentele resultaten met een on-chip PD.

signaal (2ω) en het eerste-orde signaal (1ω) tot 40 dB kunnen gaan met off-chip PD, terwijl de RF-kruisspraak de extinctieverhouding met on-chip PD verslechtert.

5 Conclusie

In dit proefschrift presenteren we de eerste single-chip microwave fotonische signaalprocessor gebaseerd op silicium fotonische technologie. Het kan worden geprogrammeerd als een herconfigureerbaar filter voor optische en RF-signalen en biedt elektrisch-naar-optische en optisch-naar-elektrische conversie. De transferdruk laserbronnen stellen het in staat om te werken zonder een externe lichtbron. Meerdere monitor detectoren stellen het systeem in staat om lokaal geconfigureerd te worden. Bovendien toont de processor zijn mogelijkheden voor RF-signaalgeneratie en RF-frequentieverdubbeling. Over het geheel genomen suggereert deze demonstratie een veelbelovende en alomvattende aanpak voor optische en RF-signaalgeneratie, distributie en verwerking, en het potentiële gebruik ervan in datacenters, draadloze en satellietcommunicatie, en andere optische en microgolf toepassingen.

English summary

1 Introduction

The volume of data generated, consumed, copied, and stored reached 1 zettabyte in 2012, and it has paved the way for an exponential increase that is predicted to reach 180 zettabytes by 2025. This data explosion poses significant challenges for data centers, demanding higher capacity and improved power efficiency. Moreover, the proliferation of large-scale AI training has further intensified the pressure on data traffic, particularly the segregation between fixed traffic transmitted via optical signals through fibers and mobile traffic relying on radio frequency (RF) signals with wireless transmission. Conventionally, these two signal types have been handled and processed separately, resulting in unnecessary conversion and propagation losses, as well as increased cost. We need a more versatile approach to effectively handle signals in both the RF and the optical domain.

Silicon photonic circuits have been widely used for optical signal transmission and manipulation of light on the surface of a chip using optical waveguides to transport signals, high-speed modulators to encode information on a lightwave, and germanium photodetectors (PDs) to convert these signals back to the electrical domain. In addition waveguide-based interferometers can be designed to filter out the optical signal as well as the loaded RF signal. Supported by the high-precision manufacturing infrastructure of electronics, there is a clear trend towards increasing circuit complexity and programmability. With the integration of phase shifters, extra degree of freedoms are added into the optical circuits, which can be used to compensate fabrication imperfections or achieve a higher tunability for various responses.

Silicon has an indirect bandgap, and therefore the integration of III-V materials, such as GaAs and InP, has been extensively explored. Transfer printing has emerged as a promising method that optimizes the utilization of costly III-V epitaxial substrates without modifications to the fabrication process of silicon photonics.

Because optical signals can span a massive bandwidth, photonics is used to generate, manipulate, transport, and measure high-speed RF signals. This field is commonly known as Microwave Photonics (MWP). Imprinting RF signals on an optical carrier with a modulator and recovering the signal with a high speed photodetector, an optical link can distribute the modulated RF signal through optical media, benefiting from large bandwidth and low propagating loss. If an optical

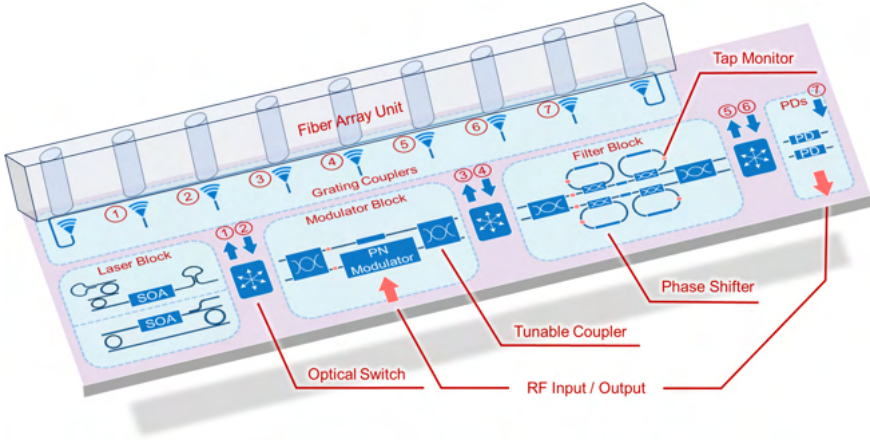


Figure 1: Schematic of the proposed single-chip signal processor.

filter is used in the optical link, a microwave photonic filter is obtained. After that, the generation and multiplexing of an RF signal can also be implemented with photonic circuits.

In this PhD thesis, we propose the first single-chip signal processor built in silicon photonics technology, capable of implementing programmable operations on both optical and RF signals, and converting between the two domains. We discuss the design of the chip, with its different subcircuits: a configurable modulator capable of both phase modulation and amplitude modulation, transfer-printed tunable laser sources, and a programmable optical filter bank. We discuss how we can use the combination of these circuits to implement a variety of functions on both microwave signals and optical signals, including electro-optical and opto-electric conversion, optical and RF signal generation (tunable laser sources and opto-electronic oscillators) and filtering, and RF signal multiplexing.

2 Chip Layout and Packaging

The schematic of our signal processor is shown in Fig.1. As shown, it consists of four main blocks, which are a tunable laser block (with 2 lasers), a modulator block, an optical filter block, and a high-speed PD block. The longest optical path starts with the light generated by the laser source, which is then guided into the modulator circuit, which can be configured for either phase modulation or intensity modulation. The light, modulated with an RF payload signal, will be fed into the optical filter block, which consists of a four-ring-loaded MZI with tunable couplers and tap monitors. After that, the filtered light signal can be converted back into the microwave domain by the high-speed PDs.

All four functional blocks are interconnected by optical switches, allowing the light signal to be routed in or out at each interconnection point, allowing the pro-

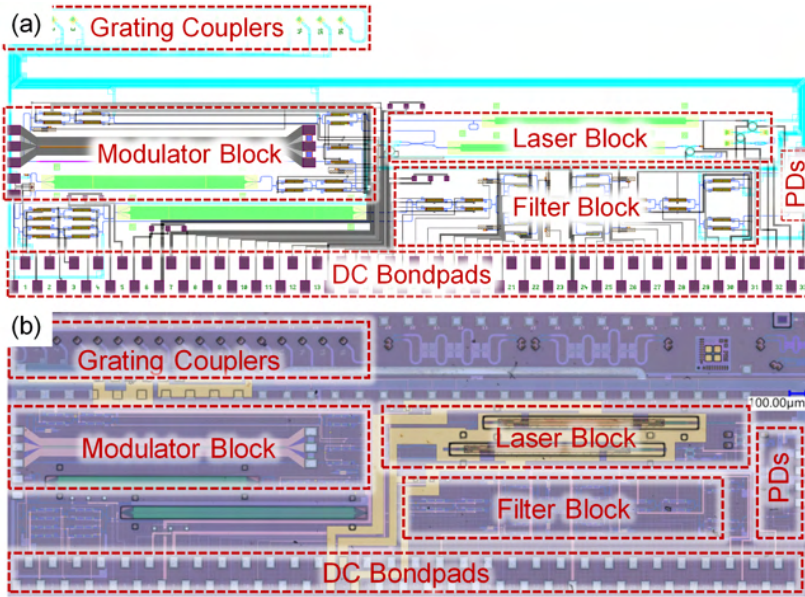


Figure 2: (a) Layout and (b) fabricated sample of the proposed single-chip signal processor.

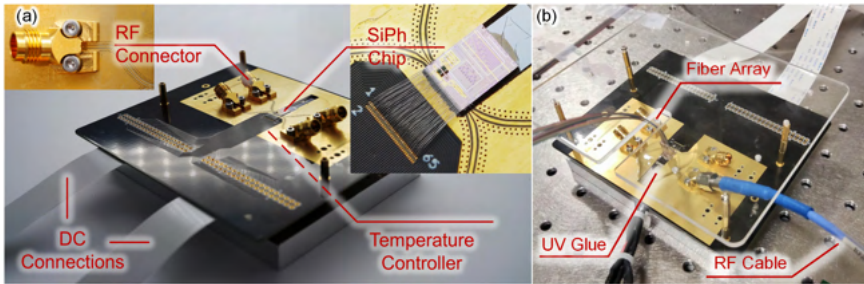


Figure 3: A packaged demonstration of the signal processor. (a) Without fiber array connection; (b) With a fiber array attached and a shelter.

processor to be configured for both optical and RF signal processing, and allowing multiple processors to be cascaded over fiber links. The optical switches themselves are implemented as single-stage MZIs or double-stage MZIs, depending on the coupling ratio requirements.

The entire photonic circuit includes 15 optical input / output ports, 3 RF channels (1 input, 2 outputs), 52 heater-based optical phase shifters, and 8 tap monitors. The layout and fabricated sample of the proposed signal processor are shown in Figs. 2 (a) and (b), respectively. With these massive connectors, a comprehensive optical, DC, and RF packaging approach is essential to ensure the stability and robustness of the system.

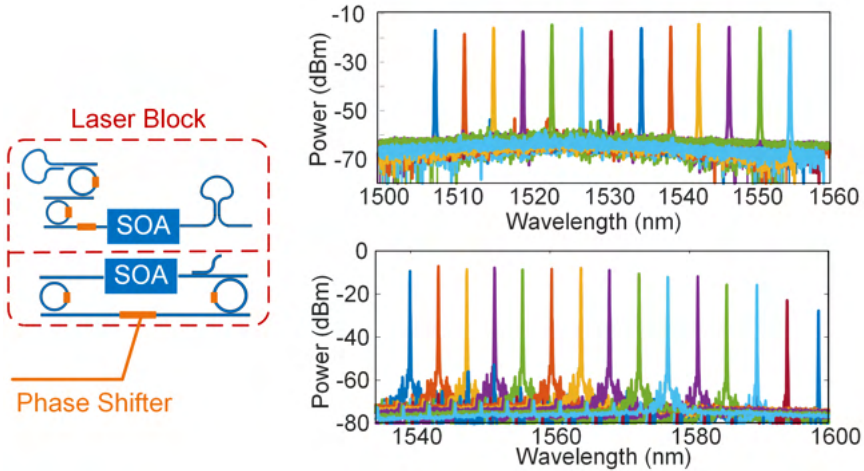


Figure 4: Characterization of the laser block.

A packaged demonstrator is shown in Fig. 3. A printed circuit board (PCB) is designed for the electrical connections. The processor chip is placed face-up on the board, and the bondpads are connected using wirebonding. In order to propagate RF signals with a low loss, the PCB uses high-speed materials (Megtron 6) as dielectric layers, and we use Rosenberger solderless RF connectors for the high-frequency I/O. A temperature controller and an aluminum heat sink are placed underneath the PCB, to stabilize the ambient temperature of the sample.

A fiber array is then cured onto the silicon photonic sample. Specifically, a 32-channel fiber array was positioned with active alignment on the reference waveguide and then fixed in place with UV-curable glue (NOA 63). In addition, additional UV glue is added to encapsulate the fragile bonding wires as shown in Fig. 3(b). The packaged sample shows high robustness and reproducibility during measurement.

3 Characterization

3.1 Micro-Transfer-Printed Laser Block

The laser block in the signal processor was designed by dr. Jing Zhang in the PRG group, and for the micro-transfer-printing process I got guidance by ir. Emadreza Soltanian in the PRG group.

In the laser block, there are two different laser cavities, which are based on a Fabry–Pérot (FP) cavity and a ring cavity, respectively, as shown in Fig. 4. Prefabricated SOAs are transfer-printed into the laser cavities to provide optical gain. When the gain from the printed SOA is higher than the other accumulated losses in the laser cavity, lasing will start. There are two ring resonator filters used in

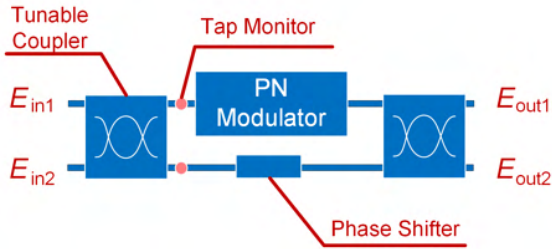


Figure 5: Schematic of the modulator block

each laser cavity to form a Vernier bandpass filter to select the longitudinal modes. There are three thermal phase shifters in each laser cavity: two for the phase tuning in the ring and one for the cavity phase. By tuning the phase of the rings and optical cavity, we can alter the selected longitude mode and tune the lasing wavelength. The laser tuning results are shown in Fig. 4. What to be noted is that the FP laser of our packaged sample turned out to be electrically shorted after the wirebonding, so its results were obtained from another sample. The two SOAs printed in these two laser cavities have different photoluminescence (PL) peaks around 1500 nm and 1550 nm, leading to lasing peaks around 1525 nm and 1575 nm, respectively. From Fig. 4, both laser cavities can achieve a tunability of more than 50 nm, and the full tuning range of the laser block can reach up to 90 nm.

3.2 Modulator Block

The modulator block in the signal processor is a reconfigurable modulator, which is implemented by integrating a standard PN junction modulator into a tunable MZI comprising two tunable couplers (TC) and a phase shifter, and its schematic is shown in Fig 5. The PN junction modulator functions as a phase modulator, allowing for the imprinting of the RF signal onto the optical carrier. The other tunable components, namely the TCs and the phase shifter, are used to adjust the response of the entire circuit. By manipulating the coupling ratios of the TCs and the phase shifter, a double-sideband modulated signal with two RF sidebands (positive and negative frequencies) can be generated with a tunable phase relationship. This means that the RF signal generated from the modulated optical signal can match a phase modulated signal, an intensity modulated signal, or their combination. With this configurability, the modulator block can be configured to optimize the modulation response.

3.3 Filter Block

The filter block in the signal processor is a ring-loaded MZI, which contains two tunable rings on each arm of a tunable MZI, as shown in Fig. 7(a). The cascaded two rings on each arm work as a second-order all-pass filter (if lossless), and the

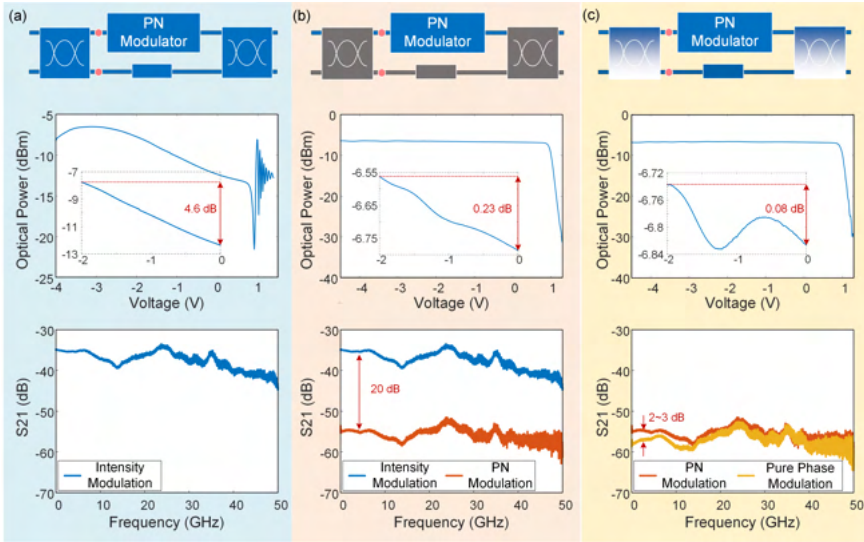


Figure 6: Characterization of the modulator block. (a) Configured as an intensity modulator; (b) Configured as a phase modulator; (c) Configured as an optimized pure phase modulator.

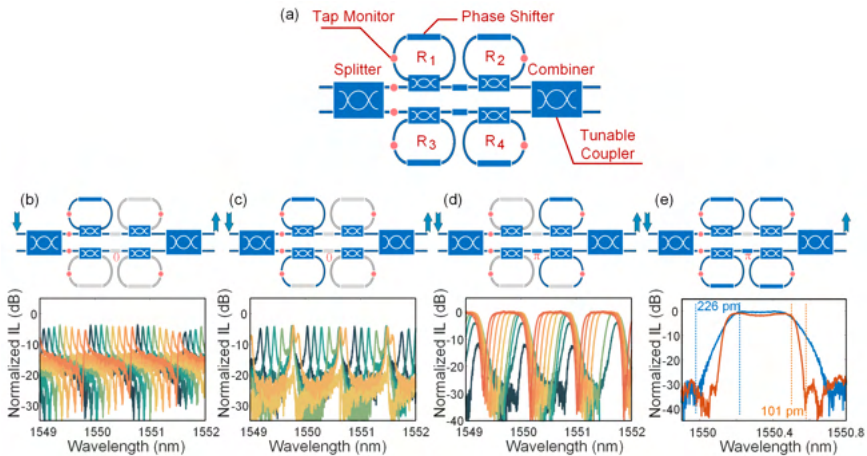


Figure 7: Characterization of the filter block. (a) Schematic of the filter block; (b) (c) (d) (e) Different configurations and responses of the filter block.

splitter and the combiner distribute lights through the rings and mix them up. The whole filter block can be programmed to be all classical bandpass filters if the coupling ratio of the splitter and the combiner is 0.5. And by tuning the coupling ratios simultaneously, this block can be an universal optical filter (limited by the filter orders)

Several configurations and responses of the filter block are shown in Fig. 7 (b)-(e). If the phase difference in the MZI is zero, the rings will introduce sharp pass bands as shown in Fig. 7 (b)-(c). The fabricated rings show a 3 dB bandwidth of 35 pm when critically coupled. If the MZI phase difference is set to π , an over-coupled ring pair can form typical Chebyshev Type II filters with a flat passband. The measurements show passbands with ~ 0.5 dB ripple in passbands and 30 dB stopband rejection (Fig. 7d). By then tuning the second ring pair to the roll-off points, a higher-order Chebyshev Type II filter response is obtained, improving the roll-off bandwidth from 226 pm to 101 pm (Fig. 7e). Other filter responses with up to 4 poles and zeros (corrsponding to the 4 rings) can be tuned.

3.4 PD block

In the proposed signal processor, two vertical Germanium PIN photodiodes from imec process design kit (PDK) are utilized to covert the optical signal into the RF domain. The vertical PIN diodes are designed to have a large bandwidth (50 GHz in manual) and a medium efficiency (0.8 A/W in manual).

4 Applications

The single-chip signal processor can provide a fully programmable filter response (for both optical and RF signals) as well as electrical and optical signal generation and detection. Laser generation (with the laser block), optical signal modulation (with the laser block and the modulator block), optical signal filtering (with the filter block), and optical signal detection (with the PD block) can be implemented directly with the signal processor's functional blocks. This section focuses on the applications for the RF signal process.

4.1 Tunable Microwave Photonic Filter

With the technology of microwave photonics, the full system can implement sophisticated linear filtering responses of RF signals, as shown in Fig. 8. Fig. 8 (a) shows the light flow in the signal processor. The light coupled out is received by an external PD for a clean RF response. As discussed in the modulator section, the light from the reconfigurable modulator can generate RF sidebands with tunable phase relations when received by the PD. With the help of reconfigurable optical filters, the RF filtering response can be fully controlled. Furthermore, to reach a bandpass or band stop filter in the RF domain equivalent to the Chebyshev Type II optical filtering response, only two cascaded ring filters are needed. Various types

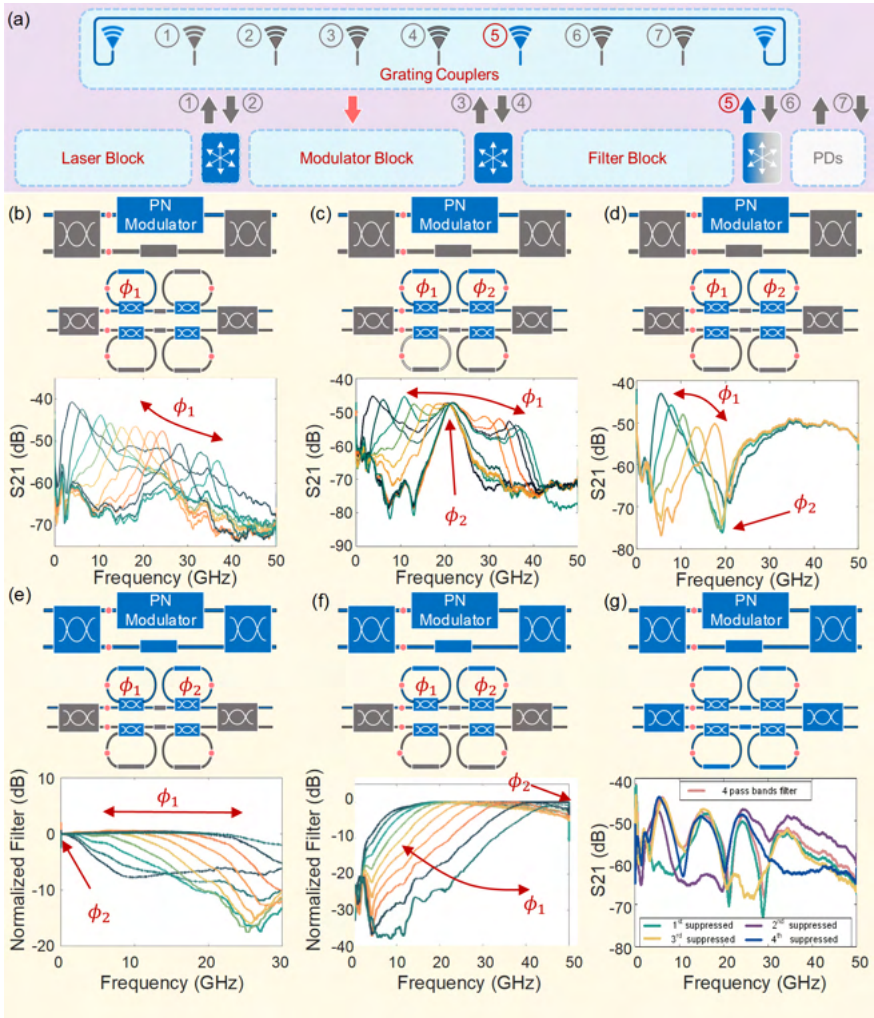


Figure 8: Tunable microwave photonic filter. (a) The light flow in the signal processor. (b)-(g) Different configurations of the system and the corresponding responses.

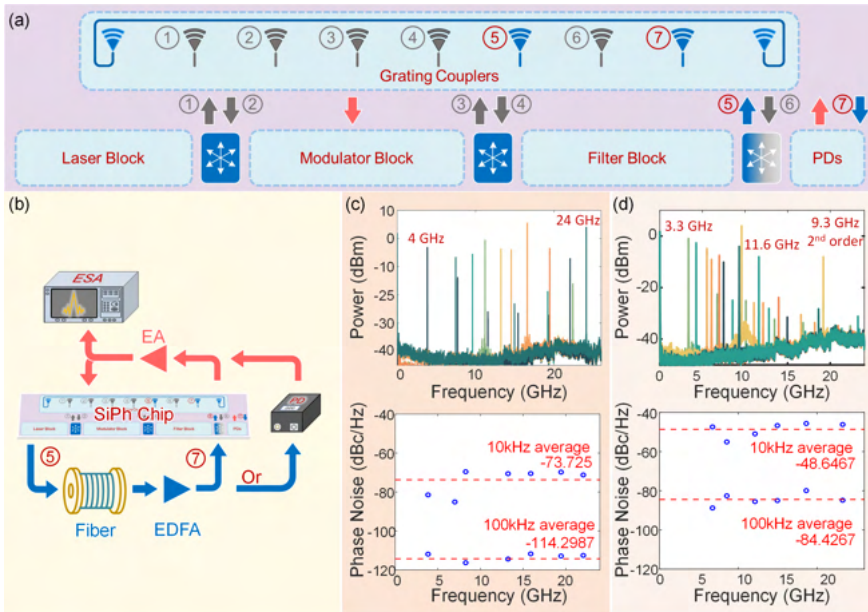


Figure 9: Tunable opto-electronic oscillator for RF signal generation. (a) Light flow in the signal processor; (b) Experimental setup with an on-chip PD or an off-chip PD; (c) Experimental results with an off-chip PD; (d) Experimental results with an on-chip PD.

of RF filtering responses are shown in Fig. 8 realized by tuning both the tunable modulator and the rings. Determined by the Q factors of the rings, the lowest 3 dB bandwidth of the filters lies around 3 GHz.

4.2 Tunable Opto-electronic oscillator

With extra electronic amplifiers compensating the loss of the bandpass filters shown in the microwave filter section above, the reported signal processor can form an OEO with a tunable central frequency as shown in Fig. 9. An extra length of fiber is added in the light path to form a longer oscillation cavity, which is indicated in Fig. 9 (b). With an off-chip PD, RF signals can be generated with a tunable 4 GHz to 24 GHz frequency and -116 dBc/Hz phase noise at 100 kHz offset frequency, shown in Fig. 9 (c). And with the on-chip PD, the generated signal can be tuned within 3.3 GHz to 11.6 GHz with -84 dBc/Hz phase noise at 100 kHz offset frequency, shown in Fig. 9 (d).

4.3 RF Signal Doubling

The signal processor can achieve an RF frequency doubling process using the laser block, modulator block and the detector block, as shown in Fig. 10(a). Fig. 10(b)

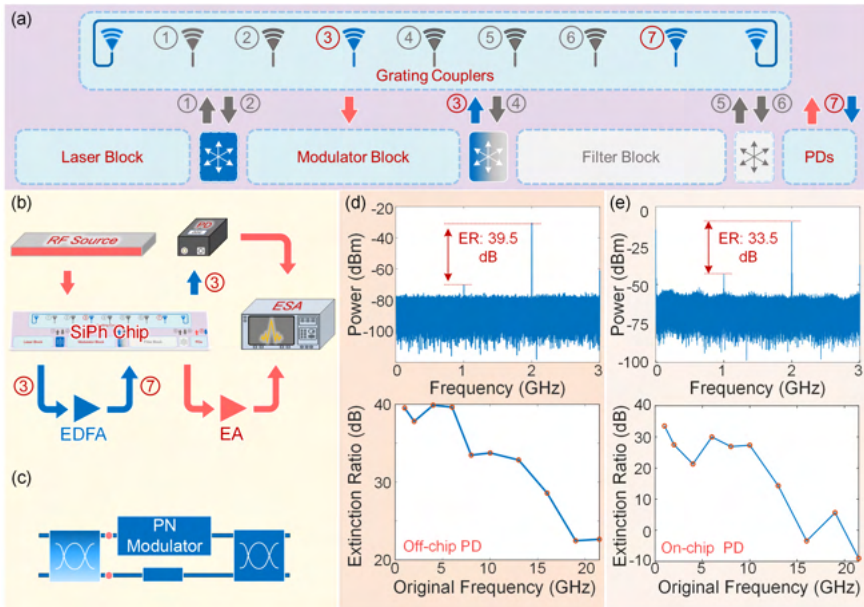


Figure 10: RF frequency doubling with the signal processor. (a) Light flow in the signal processor; (b) Experimental setup with an on-chip PD or an off-chip PD; (c) Modulator block configuration. More light is guided into the PN modulator to compensate its propagation loss; (d) Experimental results with an off-chip PD; (e) Experimental results with an on-chip PD.

shows a measurement setup for the nonlinear RF responses. The RF frequency doubling is achieved by biasing the Mach-Zehnder modulator at its null point, where the ratio of the second harmonic signal to the first order highly depends on the extinction ratio of the modulated signal. Given that the propagation loss of the PN modulator is higher than that of the phase shifter, the reconfigurable modulators' splitter is set to an operating point near 70:30 to compensate the loss difference, as shown in Fig. 10(c). The frequency doubling results with the off-chip PD and on-chip PD are shown in Fig. 10 (d) and (e), respectively. The results show that the extinction ratio between the second-order signal (2ω) and the first-order signal (1ω) can be as high as 40 dB with off-chip PD, while the RF crosstalk degenerates the extinction ratio with the on-chip PD.

5 Conclusion

In this thesis, we present the first single-chip microwave photonic signal processor based on silicon photonic technology. It can be programmed as a reconfigurable filter for optical and RF signals and provides electrical-to-optical and optical-to-electric conversion. Transfer laser sources enable it to operate without an external light source. Multiple monitor detectors allow the system to be configured locally. In addition, the processor demonstrates its capabilities for RF signal generation and RF frequency doubling. Overall, this demonstration suggests a promising and comprehensive approach for optical and RF signal generation, distribution and processing, and its potential use in data centers, wireless and satellite communications, and other optical and microwave applications.

1

Introduction

This work presents a comprehensive technology for a fully integrated single-chip signal processor on a silicon photonic platform. The signal processor is capable of both generation and detection of analog electrical and optical signals, and program a user-defined filter response both in the optical and the microwave domain. Before delving into the specifics of the design or measurement results for the sample, we must address the most crucial question: the need for such a technology. The first chapter will provide an introduction to the concepts and the applications of silicon photonics and microwave photonics, and highlight the underlying motivations behind this project.

1.1 Silicon Photonics

Silicon photonics is a technology that takes advantage of the widespread use of silicon in the semiconductor industry to integrate various optical functions and applications on silicon chips [1–4]. Differently from fiber optics, light signals in silicon photonic circuits are guided and distributed with planar optical waveguides, which can be patterned and etched with the lithography process. Waveguides can form optical interferometers and filters on-chip, and the doping process introduces high-speed electro-optic effects to the waveguides, which become modulators. In addition, doped germanium photodetectors (PDs) can absorb light and convert optical signals into electrical signals. With a complete collection of modulators, filters and PDs, silicon photonic circuits can fully handle the optical signals with

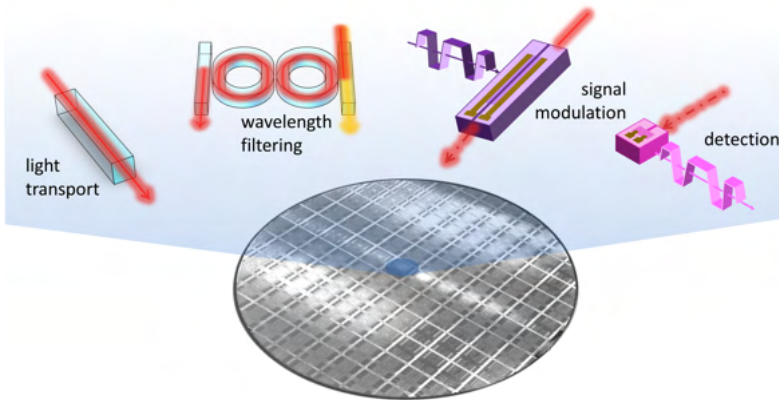


Figure 1.1: Silicon photonic integration circuits. Based on Prof. Wim Bogaerts's course material.

mature semiconductor technology, as shown in Fig. 1.1 [5].

The first research in this area can be traced back to 1980s. In 1985, Silicon-based waveguides, a key component for controlling and guiding optical signals, were first developed by Soref [6]. In 1987, Soref further proposed the concept of electro-optical effects or carrier dispersion effects in silicon, which has become the basis for the widely-used design of optical modulators [7]. Since then, various types of silicon optical passive and active devices have been realized, including directional couplers (DCs) [8], multi-mode interferometers (MMIs) [9], micro ring resonators [10], phase shifters [11], PN and PIN junction modulators [7], grating couplers [12, 13], etc. These passive and active devices provide the building blocks for silicon photonic circuits and systems.

In the early 2000s, the field of silicon photonics gained increased attention from both the research community and industry due to significant improvements in the performance and production of silicon photonic components. These advances were made possible through the development of e-beam and optical lithography technologies [14]. Luxtera developed a 10-Gb/s optical transceiver module that includes a silicon 10-Gb/s modulator, a flip-chip-bonded $1.55\ \mu\text{m}$ III-V laser diode, and a high-speed Ge-on-Si photodiode [15–17]. Researchers also explored new fabrication methods that could be used to produce the silicon photonic devices. The introduction of the complementary metal-oxide-semiconductor (CMOS) compatible processes and the development of the silicon-germanium (SiGe) technology allowed for the integration of electronic and photonic functions on the same chip at high volume, high quality and low cost. [18, 19]. After that, several silicon photonics platforms have been established at research fabs, such as imec, Leti,

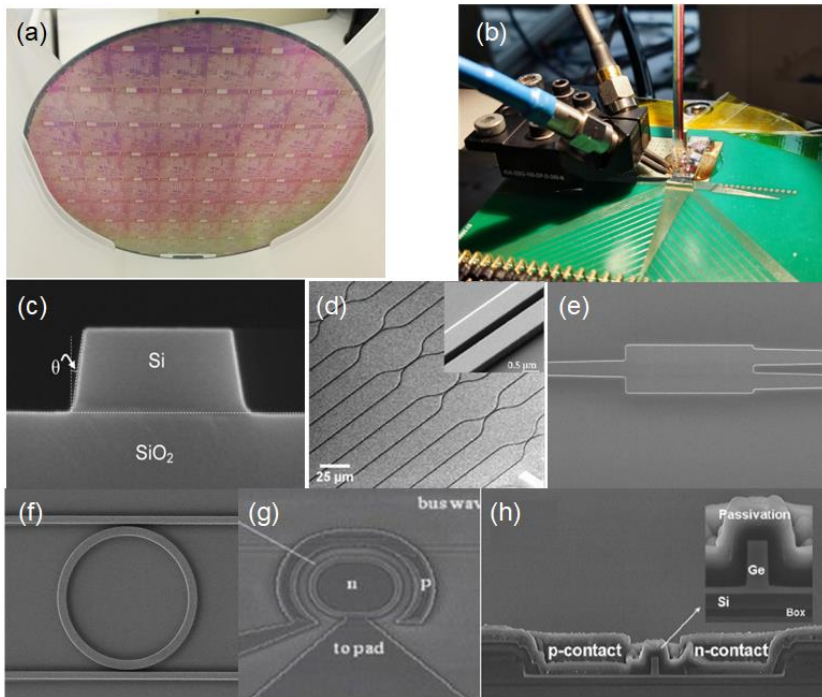


Figure 1.2: Silicon photonic devices. (a) A silicon photonic wafer from project MORPHIC; (b) test environment for a fiber array cured and wirebonded sample. SEM photos for waveguide (c), directional coupler (d), MMI (e), ring resonator (f), ring modulator (g) and photo diodes (h).

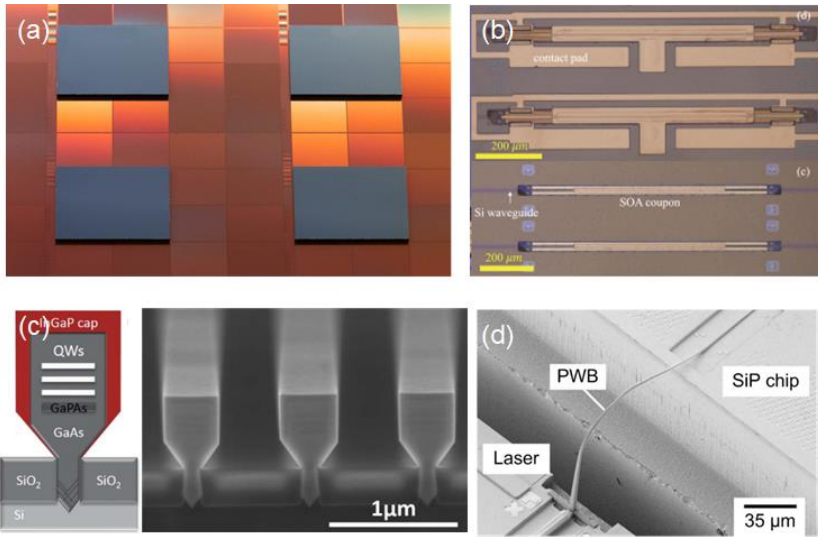


Figure 1.3: Various methods for hybrid integration: (a) Die-to-wafer bonding; (b) micro transfer printing; (c) hetero-epitaxial growth; (d) photonic wirebonding.

AIM photonics, and AMF, bridging the gap between research and the commercial market, and driving silicon photonics integrated circuits into the large-scale and multifunctional phase [1].

At the same time, as an indirect bandgap material, silicon is not suitable for light amplification and lasing. To address this limitation, the integration of III-V materials, such as GaAs and InP, with silicon photonics has been extensively investigated. Various integration techniques for these materials have been proposed, including wafer bonding [20], flip-chip wafer bonding [21], micro-transfer-printing (μ TP) [22], hetero-epitaxial growth [23] and photonic wirebonding [24]. With these technologies, optical amplifiers [25], lasers [26], mode-locked lasers [27] are introduced to the silicon platforms. In this thesis work, we make use of μ TP technology for the integration of optical amplifiers and laser sources, which uses a stamp to transfer devices from the source wafer to a new target silicon photonic sample. More details will be introduced in Chapter 2.2.4.

Over the past decade, silicon photonics integrated circuits (PICs) have achieved astonishing results in a variety of applications. Currently, the largest market and research driver of PICs continues to be data communication systems. In 2022, Intel showed the first industrial level 8×100 Gbps $2 \times$ FR4 silicon photonics transmitter with 8-channels heterogeneously integrated distributed feedback (DFB) lasers, 100 Gbps travelling wave Mach-Zehnder modulators (MZMs) and two multiplexers (MUXs) [28]. And the 800G Pluggable Multisource Agreement (MSA) announced a 800G-LR3 transceiver prototype with 4×112 GBaud PAM4 Electro-absorption

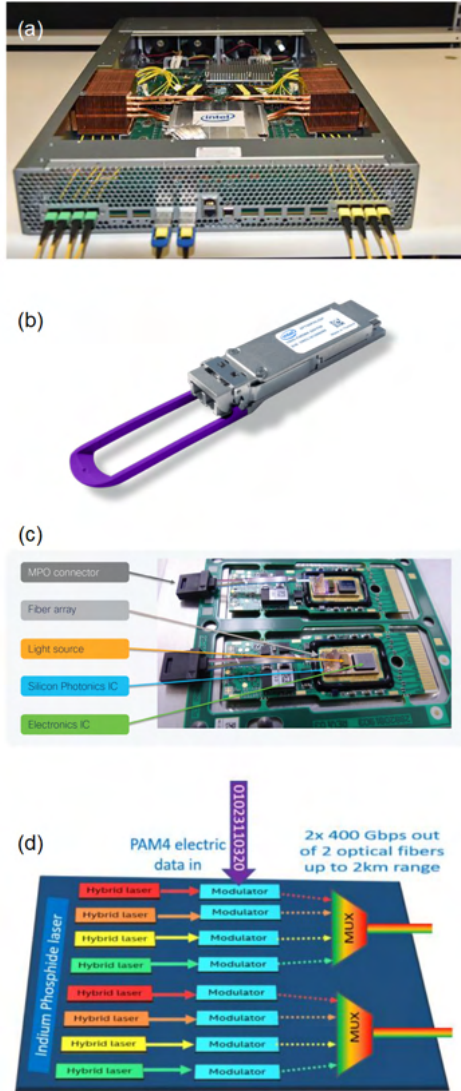


Figure 1.4: silicon photonic transceiver systems. (a) Intel co-packaged optics and silicon photonics switch; (b) Intel® silicon photonics 100G optical transceiver; (c) example of a silicon photonics 100Gbps optical module; (d) schematic of the Intel's 8x100 Gbps 2x4R4 silicon photonics transmitter; figure is from [28].

Modulated laser.

PICs also play an increasingly important role in quantum computing systems and quantum key distribution (QKD) systems, for the small footprint and scalability [31]. University of Bristol presented an arbitrary two-qubit processing system with a large PIC system [29]. Later, Xanadu Photonics showed a full-stack hardware-software system for executing many-photon quantum circuits using a programmable chip [32], which is the first step in scaling chips to reaching the regime of quantum advantage. In the field of quantum communication, A*STAR showed a continuous-variable QKD system demo with a capability of producing a secret key rate of 0.14kbps over a simulated distance of 100 km in fiber [30]. One year later, Università di Padova realized a full daylight QKD systems over a 145 m free-space link in Padua, showing a potential resource for quantum payloads in

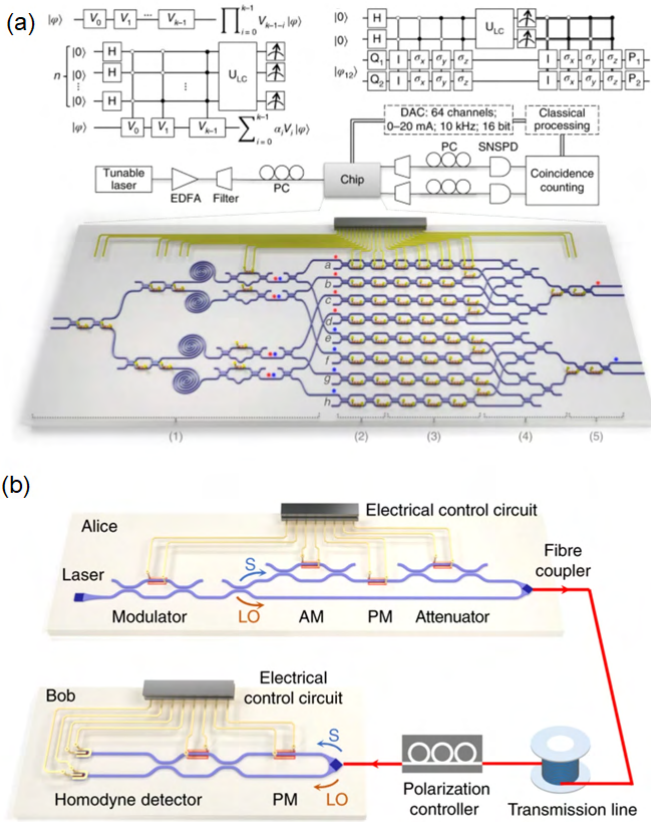


Figure 1.5: silicon photonic systems for quantum computing and communication:(a)Schematic of a silicon photonics arbitrary two-qubit processing system, figure is from [29]; (b) schematic of a silicon photonics CV-QKD system, figure is from [30]

future satellite missions [33].

Deep learning models, such as Dall-E and ChatGPT from OpenAI, have gained significant public attention due to their capabilities in solving complex tasks, including image recognition, language translation, and decision-making problems [36, 37]. However, training these models requires vast computational resources. PICs have paved the way for ultrafast artificial neural networks [38]. Shen and Harris from MIT demonstrated the first PIC for vowel recognition, which consisting of 56 Mach-Zehnder interferometers (MZIs) for optical matrix vector multiplication [34]. Subsequently, Shen established Lightelligence and released the first optical computing product, the Photonic Arithmetic Computing Engine (PACE), which is 800 times faster than current high-end GPUs for specific tasks. In the meantime, deep learning models can also help the design of the silicon photonic devices and systems [39].

Another application area for silicon photonics is sensing and detection. PIC based solid-state light detection and ranging (LiDAR) systems have been widely used for advanced driver-assistance system [35, 40]. In the oil industry, acetone [41], methane [42], carbon dioxide [43] gas detector as well as temperature sensors [44] have been reported with silicon photonic platforms. In health-sensing area,

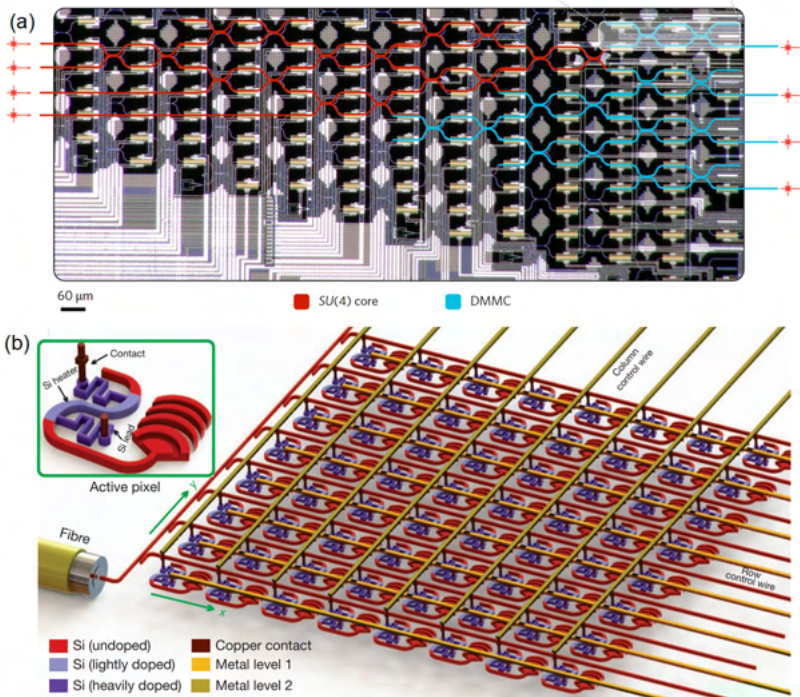


Figure 1.6: Silicon photonics chips for machine learning (a) [34] and LiDAR (b) [35]

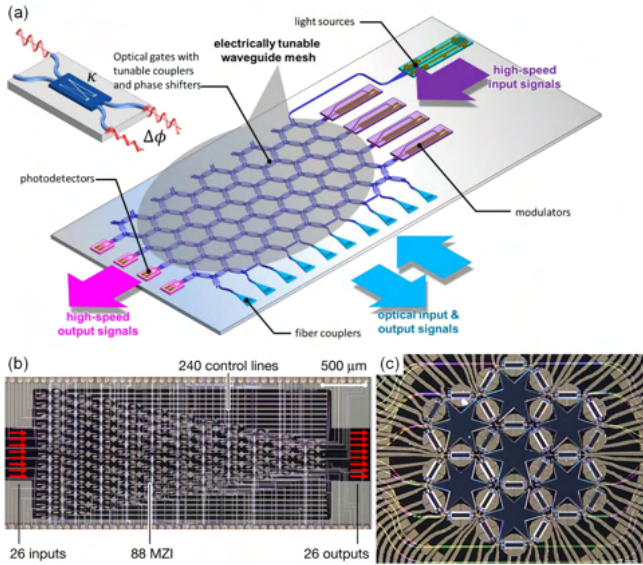


Figure 1.7: Programmable photonic circuits. (a) Schematic of a programmable photonic chip with a hexagonal waveguide mesh, figure is from [48]; (b) a silicon photonic feed-forward mesh, figure is from [34]; (c) a silicon nitride hexagonal mesh, figure is from [49].

PICs have been demonstrated to monitor blood glucose [45], carotid pulse rate [46], aortic stiffness [47] and others.

Currently, most of these PICs, as listed above, are designed for specific applications, and apart from the communication applications, most are still in R&D phase. With increasing complexity, a new generation of photonic circuits can be programmed for a wide variety of functions, similar to Field Programmable Gate Arrays (FPGAs) in the electrical domain [50]. Optical amplitude and phase control at every node are necessary, which can be implemented using MZIs [50] or tunable directional couplers [51] as optical gates. These nodes can be configured into various topologies, such as forward-only meshes and recirculating meshes, each with their own pros and cons for different applications [48, 49]. By incorporating other functional blocks such as modulators and high-speed PDs, programmable PICs have been proposed for applications that require high reconfigurability, such as microwave photonic processors [52], neuromorphic and quantum computation [53] and accelerator for artificial intelligence [34].

With a fully manipulation of light signals on chip, programmable photonic integrated circuits show high flexibility, robustness and scalability. With generic programmability for a wide variety of functions also comes a cost: a large number of optical gates is needed. This can lead to large optical propagation loss, also, the many electrical controls can become complex for the packaging and elec-

tronics. That is why, in this PhD work, we have worked towards a more focused photonic circuit, which is still programmable, but oriented specifically towards signal processing, which can fully make use of all the optical devices. Sporting a combination of an integrated optical modulator, filter and high speed PDs, the signal processor is capable of implementing programmable operations on both optical and radio frequency (RF) signals, and the signal conversion between the two domains.

1.2 Microwave Photonics

Microwave photonics is an application-oriented field that focuses on the interaction between microwaves and light waves to generate, distribute, process, control, and detect microwave signals using photonics technology [52, 54, 55]. The primary motivation for using photonics in microwave applications is the high bandwidth and low loss offered by modern photonics technology. This allows for the implementation of important functions that may not be possible, practical, or cost-effective in the electronic domain, especially as the microwave frequency requirements increase to 60 GHz and beyond. By utilizing the strengths of both microwave and photonics technologies, microwave photonics has enabled the development of advanced systems for various applications, including radar [56], wireless communication (e.g. 5G) [57], sensing [58], satellite links [59], instrumentation [60, 61], and warfare systems.

Today, one of the most commonly used wired media for the distribution of microwave signals, or RF signals, is coaxial cable. However, optical fiber offers several advantages over coaxial cable. First, fiber has significantly lower transmission loss, allowing signals to travel greater distances without degradation. Second, fiber is much lighter and easier to handle and install. Third, fiber is immune to electromagnetic interference (EMI), which can cause noise and distortion in electrical cables. In addition, fiber has a much higher bandwidth (around 40 THz), making it ideal for high-speed data transmission. Finally, optical fiber is much more cost effective than coaxial cable for high speed data transmission. These advantages have motivated researchers to explore the use of optical fibers for RF signal distribution, leading to the development of *microwave photonic links*.

Figure 1.8 illustrates a typical layout of a microwave photonic link. The optical carrier is generated by a laser diode and serves as the optical carrier of the link. A modulator, which can be an intensity modulator or a phase modulator, imprints the RF signal onto the optical carrier. The modulated optical signal can then be transmitted via optical media, such as optical fibers, and eventually detected by a PD. PDs respond to the power of the input light signal, which is proportional

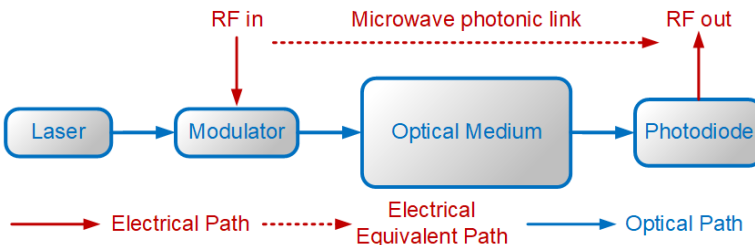


Figure 1.8: A typical microwave photonic link

to the square of the electric field, resulting in a "square law" detection process. Therefore, an RF signal that is recovered by a simple PD will only contain the power envelope information of the modulated light. The recovered signal can be further processed and sent to a microwave receiver or re-radiated as needed. Compared to a coaxial cable with a loss of 3 dB/m, optical fibers enjoy a loss of 0.17 dB/km, making the microwave photonic link promising for the long distance distribution.

In a microwave photonic link, the modulator implements the electrical-to-optical (EO) conversion, an optical medium transmits the optical signal, and the PD implements the optical-to-electrical (OE) conversion. Together they realize the electrical-to-optical-to-electrical conversion and form an electrical transfer function. Ideally, if the transfer function is 1, the recovered RF signal will be equal to the input signal, and the user will not even notice that there is an optical system in between. However, typically, a modulator and a PD will introduce a high RF loss, e.g., 20 dB, and their response is not perfectly linear, which limits the spurious-free dynamic range (SFDR) of the link. In addition, all noise, like the laser source's intensity noise, shot and electrical noise in PDs, environmental effects on the optical medium such as temperature and pressure fluctuations will all contribute to the noise levels of microwave photonic links. Furthermore, optical transmission lines, such as optical fibers, have dispersion effects, which lead to a power penalty. Many studies are being done to optimize or address these imperfections [62–64].

On the other hand, the RF transfer function of the microwave photonic link is highly dependent on the properties of the modulator and optical medium used. Therefore, it is desirable that we can design the modulator and optical medium to achieve a desired transfer function, effectively creating a *microwave photonic filter* [65]. A simple modulator can be a phase modulator or an intensity modulator, while more complex modulators, such as dual drive modulators or dual parallel intensity modulators, can implement single-sideband modulation (SSB), resulting in modulated light with sidebands of different intensity and phase relationships. More details on these modulators and modulation schemes are presented in the Chapter 4.

Optical media can be a free space path, optical fibers, optical filters, nonlinear optical elements, and optical waveguides. These possibilities enable various microwave distributions and filtering responses with a high degree of tunability. In addition, their low loss and large bandwidth enables the formed microwave photonic filters suitable for the processing of millimeter wave (30GHz to 300GHz).

Assuming that a specific microwave photonic filter has a bandpass response for RF frequencies, connecting the output of the PD to the input of the modulator will create a feedback loop, resulting in an *opto-electronic oscillator* (OEO) [68, 69]. Similar to a ring laser, an OEO will self-oscillate and generate an RF signal with one or multiple longitudinal modes if the closed-loop gain is greater than

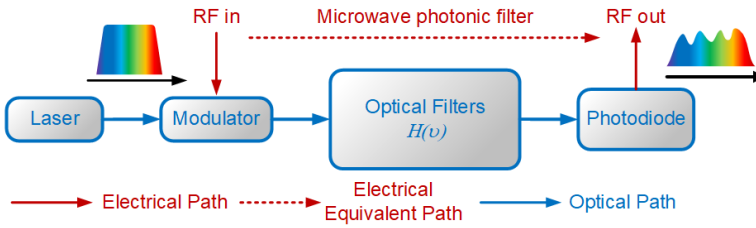


Figure 1.9: Schematic of a microwave photonic filter

zero. The closed-loop gain can be provided by electrical or optical amplifiers. The microwave photonic filter is used to form a relatively long cavity and longitudinal mode selector. The OEO can produce a very stable and high-quality RF signal with tunable frequency and low phase noise. Recently, some ultra-high Q-factor optical filters or some parity-time symmetry breaking circuits are used in OEOs for high-frequency and high-quality RF generation [66, 70, 71].

Another method for generating an RF signal is by utilizing the square-law relationship of the PD, or signal beating in the PD. If two optical signals with frequencies of f_1 and f_2 are fed into a PD, a beat signal with a power envelope signal at a frequency of $|f_1 - f_2|$ can be obtained. One simple way to use this method is to beat two tunable laser diodes directly, but the beaten signal may have phase noise that is the summation of the phase noise in the two lasers. To address this issue, several methods have been proposed to phase-lock the two lasers [72] or use a master laser to slave them [73]. In addition, some nonlinear optical materials, such as a SiN ring can generate multiple wavelengths with a fixed phase relation, but their frequency spacing is typically not tunable [74].

The input RF signal's information is encoded onto the modulated light by the modulator. Therefore, in principle, we can use an optical spectrum analyzer (OSA) to identify an unknown input RF signal. However, the resolution of most OSAs is relatively coarse, resulting in a low measurement resolution for RF signals (e.g., 8 pm to 1 GHz at 1550 nm). A more effective approach is to utilize a tunable microwave photonic filter, similar to an optical sensor interrogator. By monitoring the RF output power of a tunable nonlinear RF filter, we can determine the power and frequency of the RF input with a relatively higher resolution (kHz to MHz) [75].

On the other side, microwave photonic systems are commonly used in optical sensor interrogation systems with high frequency precision and resolution of RF devices (comparing to optical measurement devices). If the optical medium in the microwave photonic filter is sensitive to environmental perturbations, these perturbations will be reflected in the filter's response, which can be measured by a vector network analyzer (VNA) at a resolution of kHz. Alternatively, if the

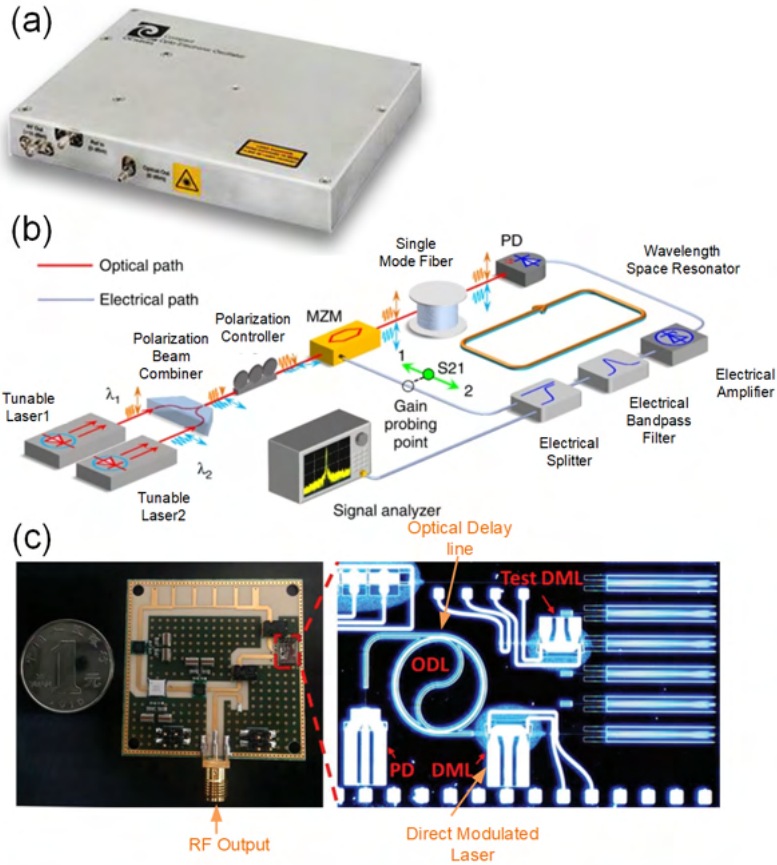


Figure 1.10: Various opto-electronic oscillator (OEO) systems. (a) An OEO module provided by OEwave; (b) A schematic of an OEO, figure reproduced from [66]; (c) A photo of an integrated OEO, figure reproduced from [67]

filter forms an OEO, the perturbations will be reflected in the frequency of the generated RF signal, which can be measured by an electrical spectrum analyzer (ESA) at a resolution of Hz or even in real-time by an oscilloscope. The use of microwave photonic systems enables ultra-high resolution and high-speed interrogation of photonic sensors.

However, conventional microwave photonic systems have several drawbacks. Compared to conventional passive electrical filters and cables, microwave photonic systems require several active components, including at least a laser source and a PD. These active components and their driving systems make the whole system quite bulky and power hungry. In addition, high-speed elements such as modulators and PDs are also costly. Photonic integration involves the integra-

Table 1.1: Comparison of bulky microwave photonic systems and integrated systems

	Discrete microwave photonics	Integrated microwave photonics
Size	Bulky	Integrated system
Stability	Sensitive to stress, temperature, vibration, etc.	Mainly sensitive to temperature
Power Consumption	Individual driving	Driven systems co-integration
Cost	Bulky Laser, modulator, PD...	Integrated on the same chip
Performance	Commercial system	Limited by platform

tion of multiple photonic components on a single chip, resulting in smaller, more efficient, and cost-effective systems, as listed in Table 1.1. This technology has been explored as a promising solution for the development of microwave photonic systems with improved performance and lower power consumption [52]. Different platforms, such as III-V, silicon, and SiN, have been investigated for integrated microwave photonics. Each platform has its advantages and limitations. III-V platforms, such as indium phosphide (InP), are capable of providing optical gain, but their fabrication costs are often high and the yield can be low. In contrast, silicon platforms offer low loss and high compatibility with CMOS processes, allowing for mass production with high yield, but integrating optical gain and lasing can be challenging. While SiN platforms have lower loss, which makes them suitable for long delay lines, their lack of lasers, modulators, and PDs limits their usefulness for microwave photonics. [67].

In the previous section, it was noted that photonic integrated circuits (PICs) are evolving toward higher reconfigurability and integration density. A programmable PIC can enable the implementation of multiple tasks in a microwave photonic integrated system, such as RF signal generation, filtering, processing and detection, resulting in a microwave photonic processor [49, 76]. To achieve a more generic

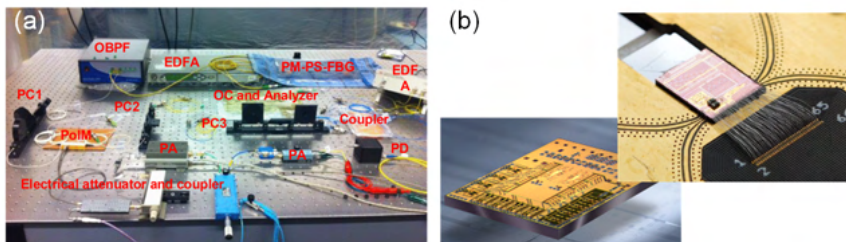


Figure 1.11: (a) A typical bulky microwave photonic system; (b) packaged silicon photonic systems

filtering and processing response, a generic configurable optical filter is required. In recent years, several microwave photonic processors have been proposed using different platforms [76–80]. By linearly mapping the optical filter responses into RF domain with SSB modulation scheme, these processors achieved widely tunable RF filter responses, with a trade-off of an additional 3dB of RF loss and an additional optical filter. Furthermore, except for the III-V platform-based systems, others are not fully integrated with lasers or high-speed PDs.

In this work, we use a silicon photonic chip with a micro-transfer-printed tunable laser to implement a fully on-chip microwave photonic system, taking advantage of both III-V and silicon platforms. We propose a reconfigurable modulator design and a new filter design algorithm that eliminates some of the intrinsic RF loss and complicated optical filter design of conventional methods, which will be discussed in detail in Chapter 7.

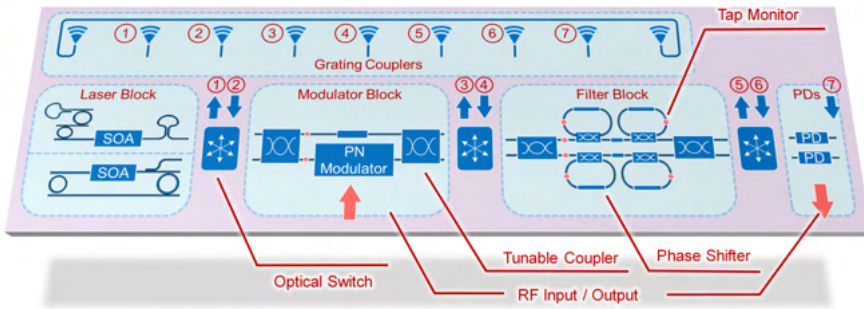


Figure 1.12: Schematic of the optical and RF signal processor that we developed in this PhD.

1.3 Objectives of this thesis

Silicon photonic integrated circuits offer a high degree of configurability and integration density, making them ideal for handling RF signals in complex microwave photonic systems with low cost and high stability. Additionally, these circuits feature high-speed EO and OE devices. Using micro transfer printing technology, tunable lasers can be heterogeneously integrated onto the silicon chips, enabling fully on-chip microwave photonic processing systems. This thesis will provide detailed information on the entire workflow, including optical device design, fabrication, measurement, and packaging for microwave photonic applications such as signal generation, filtering, and detection. A single-chip signal processor is demonstrated, with a schematic shown in Fig. 1.12.

This demonstration shows a promising and comprehensive approach for the generation, distribution, and processing of optical and RF signals and its potential use in data centers, wireless and satellite communication, and other optical and microwave applications.

This thesis work includes the following aspects:

- An exploration of various thermal phase shifters and monitor designs.
- Development of optical, electrical and thermal packaging approaches.
- A reconfigurable modulator circuit which can work as an intensity modulator or a phase modulator with optimized performance.
- A wavelength converter and on-chip tunable lasers based on micro-transfer printing technology.
- A demonstration of a single chip signal processor, with application of programmable optical and RF signals' generation, filtering, processing and detection.

This thesis work involved wide variety of activities, including photonic circuit design and simulation, chip fabrication and post-processing, sample packaging and final characterization.

The research was supported by the projects PhotonICSWARM and MORPHIC, and was carried out in the Photonics Research Group (PRG) at Ghent University-imec. The author thanks Dr. Jing Zhang and Mr. Emadreza Soltanian from PRG for the guidance of micro-transfer printing process, and Dr. Joris Van Kerrebrouck from IDLab for the guidance of high speed PCB design and assembly.

1.4 Outline of this thesis

In this chapter, we reviewed the background of silicon photonics and microwave photonics. A fully integrated microwave photonic processor with a micro-transfer-printed laser is targeted in this thesis.

Chapter 2 focuses primarily on silicon photonic devices. Firstly, the basic units such as optical waveguides, directional couplers, and phase shifters are introduced. Then P(I)N junction and its plasma dispersion effect-based modulators are introduced, followed by a discussion of PDs and different types of monitors. Lastly, a workflow for chip simulation, layout, and packaging is elaborated in this chapter.

Chapter 3 focuses specifically on silicon photonic filters. Balanced MZIs working as optical tunable couplers are explained here, and various types of programmable optical filters are introduced. In Chapter 4, the focus shifts to the principle of microwave photonic systems. Details about RF signal generation, filtering, processing, and detection are presented.

The proposed on-chip signal processing system is the main focus in the following chapters. Chapter 5 introduces a configurable modulator, which is the key component for the proposed system. Chapter 6 discusses micro-transfer-printed amplifiers and lasers on imec iSiPP50G platforms. Chapter 7 elaborates the whole system.

Finally, Chapter 8 discusses several optimization points in future tests and it also presents the main conclusion for the entire thesis.

1.5 Publications

1.5.1 Publications in international journals

1. H. Deng, W. Bogaerts, "Pure phase modulation based on a silicon plasma dispersion modulator", *Optics Express*, 27(19), p.27191-27201 (2019)
2. H. Deng, J. Zhang, E. Soltanian, X. Chen, C. Pang, N. Vaissiere, D. Neel, J. Ramirez, J. Decobert, Ni. Singh, G. Torfs, G. Roelkens, W. Bogaerts, "Single-Chip Silicon Photonic Processor for Analog Optical and Microwave Signals", *Nature* (under review).
3. C. Ma, J. Van Kerrebroeck, H. Deng, S. Sackesyn, E.J.C. Gooskens, B. Bai, J. Dambre, P. Bienstman, "Integrated photonic reservoir computing with an all-optical readout", *Optics Express*, 31(21), pp. 34843-34854 (2023).
4. J. Zhang, L. Bogaert, C.J. Krückel, E. Soltanian, H. Deng, B. Haq, J.Rimbock, J. Van Kerrebrouck, G. Lepage, P. Verheyen, J. Van Campenhout, P. Ossieur, D. Van Thourhout, G. Morthier, W. Bogaerts, G. Roelkens, "Micro-transfer printing InP C-band SOAs on advanced silicon photonics platform for loss-less MZI switch fabrics and high-speed integrated transmitters", *Optics Express*, (2023).

1.5.2 Publications in international conferences

1. H. Deng and W. Bogaerts, "Integrated Reconfigurable Modulator for Microwave Photonic Filtering", 2023 IEEE International Topical Meeting on Microwave Photonics (MWP), China.
2. W. Bogaerts, K. Nagarjun, L. Van Iseghem, X. Chen, H. Deng, I. Zand, Y. Zhang, Y. Liu, A.Y. Takabayashi, H. Sattari, N. Quack, P. Edinger, G. Jo, S.J. Bleiker, K.B. Gylfason, F. Niklaus, A. Kumar Mallik, M. Jezzini, C. Antony, G. Talli, P. Verheyen, J. Beeckman, U. Khan, "Scaling Programmable Silicon Photonic Circuits", SPIE Photonics West OPTO, 12426, United States, pp. 12426-1 (2023).
3. H. Deng, W. Bogaerts, "Configurable Modulator based Optical Carrier Frequency Suppressed Intensity Modulation", IEEE Photonics Society Summer Topicals, Mexico, pp. MB2.3 (2022).
4. W. Bogaerts, X. Chen, H. Deng, L. Van Iseghem, M. Wang, I. Zand, Y. Zhang, Y. Liu, K. Nagarjun, U. Khan, "Programmable Silicon Photonic Circuits", OptoElectronics and Communication Conference / International

- Conference on Photonics in Switching and Computing (OECC / PSC), Japan, pp. TuE4-1 (2022).
5. W. Bogaerts, L. Van Iseghem, X. Chen, I. Zand, H. Deng, M. Wang, K.P. Nagarjun, U. Khan, "Technologies for large-scale programmable photonic circuits", Progress in Electromagnetic Research (PIERS), China, (2022).
 6. W. Bogaerts, L. Van Iseghem, X. Chen, I. Zand, H. Deng, M. Wang, Y. Zhang, Y. Liu, K.P. Nagarjun, U. Khan, "Programmable Silicon Photonic Circuits", International Symposium on Photonic and Electronic Convergence (ISPEC 2021) , (2021).
 7. H. Deng, W. Bogaerts, "Configurable Phase/Amplitude Modulator Circuit based on Silicon Plasma", IEEE International Conference on Group IV Photonics, Spain, (2021).
 8. Y. Zhang, H. Deng, U. Khan, W. Bogaerts, "Comparison between black box and gray box strategies for configuration of feedforward waveguide meshes", Annual Symposium of the IEEE Photonics Society Benelux Chapter, Belgium, (2021).
 9. W. Bogaerts, L. Van Iseghem, M. Wang, H. Deng, X. Chen, I. Zand, K.P. Nagarjun, U. Khan, "Programmable Photonic Circuits", SPIE Photonex, United Kingdom, (2021).
 10. W. Bogaerts, L. Van Iseghem, M. Wang, H. Deng, I. Zand, X. Chen, K.P. Nagarjun, U. Khan, "Programmable Silicon Photonics", International Conference on Solid State Devices and Materials (SSDM) (2021).
 11. W. Bogaerts, M. Wang, X. Chen, H. Deng, I. Zand, L. Van Iseghem, K.P. Nagarjun, U. Khan, "General-Purpose Programmable Photonic Chips", IEEE Photonics Society Summer Topicals, pp. WB2.1 (2021).
 12. W. Bogaerts, L. Van Iseghem, P. Edinger, H. Sattari, A.Y. Takabayashi, X. Chen, H. Deng, P. Verheyen, A. Ribeiro, U. Khan, N. Quack, K.B. Gylfason, "Low-Power Electro-Optic Actuators for Large-Scale Programmable Photonic Circuits", Conference on Lasers and Electro-Optics, pp. STh1Q.4 (2021).
 13. W. Bogaerts, X. Chen, I. Zand, M. Wang, H. Deng, L. Van Iseghem, A. Rahim, U. Khan, "Tutorial: Programmable Integrated Photonics", European Conference on Optical Communication (ECOC), pp. paper Tu4B-1 (3 pages) (2020).

14. W. Bogaerts, X. Chen, M. Wang, I. Zand, H. Deng, L. Van Iseghem, A. Ribeiro, A. Diaz Tormo , U. Khan, "Programmable Silicon Photonic Integrated Circuits", IEEE Photonics Conference (IPC), Canada, pp. ThD2.1 (2020).
15. W. Bogaerts, A. Rahim, X. Chen, L. Van Iseghem, H. Deng, M. Wang, I. Zand, A. Ribeiro, A. Diaz Tormo , U. Khan, "Programmable Photonic Circuits: a flexible way of manipulating light on chips", Frontiers in Optics, United States, (2020).
16. W. Bogaerts, A. Ribeiro, M. Wang, L. Van Iseghem, H. Deng, I. Zand, X. Chen, U. Khan, "Technologies for large-scale programmable photonic circuits", AOS Australian Conference on Optical Fibre Technology (ACOFT) and Australian Conference on Optics, Lasers, and Spectroscopy (ACOLS) 2019, pp. 11200-55 (2019).
17. H. Deng, W. Bogaerts, "Configurable Modulator for Pure Phase Modulation", Photonics North, Canada, pp. PS-87 (2019)

References

- [1] S. Y. Siew, B. Li, F. Gao, H. Y. Zheng, W. Zhang, P. Guo, S. W. Xie, A. Song, B. Dong, L. W. Luo, C. Li, X. Luo, and G. Q. Lo, "Review of Silicon Photonics Technology and Platform Development," *Journal of Lightwave Technology*, vol. 39, pp. 4374–4389, 7 2021.
- [2] W. Bogaerts and L. Chrostowski, "Silicon Photonics Circuit Design: Methods, Tools and Challenges," *Laser & Photonics Reviews*, vol. 12, p. 1700237, 4 2018.
- [3] B. Jalali and S. Fathpour, "Silicon photonics," *Journal of Lightwave Technology*, vol. 24, no. 12, pp. 4600–4615, 2006.
- [4] V. R. Almeida, C. A. Barrios, R. R. Panepucci, and M. Lipson, "All-optical control of light on a silicon chip," *Nature* 2004 431:7012, vol. 431, pp. 1081–1084, 10 2004.
- [5] D. Thomson, A. Zilkie, J. E. Bowers, T. Komljenovic, G. T. Reed, L. Vivien, D. Marris-Morini, E. Cassan, L. Viro, J. M. Fédéli, J. M. Hartmann, J. H. Schmid, D. X. Xu, F. Boeuf, P. O'Brien, G. Z. Mashanovich, and M. Nedeljkovic, "Roadmap on silicon photonics," *Journal of Optics*, vol. 18, p. 073003, 6 2016.
- [6] R. A. Soref and J. P. Lorenzo, "Single-Crystal Silicon: A New Material For 1-3 And 1-6 Fim Integrated-Optical Components," *Electronics Letters*, vol. 21, no. 21, pp. 953–954, 1985.
- [7] R. Soref and B. Bennett, "Electrooptical effects in silicon," *IEEE Journal of Quantum Electronics*, vol. 23, pp. 123–129, 1 1987.
- [8] H. Yamada, T. Chu, S. Ishida, and Y. Arakawa, "Optical directional coupler based on Si-wire waveguides," *IEEE Photonics Technology Letters*, vol. 17, pp. 585–587, 3 2005.
- [9] L. B. Soldano and E. C. Pennings, "Optical Multi-Mode Interference Devices Based on Self-Imaging: Principles and Applications," *Journal of Lightwave Technology*, vol. 13, no. 4, pp. 615–627, 1995.
- [10] B. E. Little, J. S. Foresi, G. Steinmeyer, E. R. Thoen, S. T. Chu, H. A. Haus, E. P. Ippen, L. C. Kimerling, and W. Greene, "Ultra-compact Si-SiO₂ microring resonator optical channel dropping filters," *IEEE Photonics Technology Letters*, vol. 10, pp. 549–551, 3 1998.

- [11] R. L. Espinola, M. C. Tsai, J. T. Yardley, and R. M. Osgood, "Fast and low-power thermo-optic switch on thin silicon-on-insulator," *IEEE Photonics Technology Letters*, vol. 15, pp. 1366–1368, 10 2003.
- [12] N. Eriksson, M. Hagberg, and A. Larsson, "Highly directional grating out-couplers with tailorable radiation characteristics," *IEEE Journal of Quantum Electronics*, vol. 32, pp. 1038–1047, 6 1996.
- [13] D. Taillaert, W. Bogaerts, P. Bienstman, T. F. Krauss, P. Van Daele, I. Moerman, S. Verstuyft, K. De Mesel, and R. Baets, "An out-of-plane grating coupler for efficient butt-coupling between compact planar waveguides and single-mode fibers," *IEEE Journal of Quantum Electronics*, vol. 38, pp. 949–955, 7 2002.
- [14] R. Soref, "The past, present, and future of silicon photonics," *IEEE Journal on Selected Topics in Quantum Electronics*, vol. 12, pp. 1678–1687, 11 2006.
- [15] C. Gunn, A. Narasimha, B. Analui, Y. Liang, and T. J. Sleboda, "A 40Gb CMOS photonics transceiver," <https://doi.org/10.1117/12.702884>, vol. 6477, pp. 181–188, 2 2007.
- [16] G. Masini, S. Sahni, G. Capellini, J. Witzens, J. White, D. Song, and C. Gunn, "Ge photodetectors integrated in CMOS photonic circuits," <https://doi.org/10.1117/12.767035>, vol. 6898, pp. 74–79, 2 2008.
- [17] J. Witzens, G. Masini, S. Sahni, B. Analui, C. Gunn, and G. Capellini, "10Gbit/s transceiver on silicon," <https://doi.org/10.1117/12.786641>, vol. 6996, pp. 258–267, 5 2008.
- [18] W. Bogaerts, R. Baets, S. Member, P. Dumon, S. Member, V. Wiaux, S. Beckx, D. Taillaert, B. Luyssaert, J. Van Campenhout, P. Bienstman, and D. Van Thourhout, "Nanophotonic Waveguides in Silicon-on-Insulator Fabricated With CMOS Technology," *Journal of Lightwave Technology*, vol. 23, no. 1, p. 401, 2005.
- [19] B. Jalali, L. Naval, and A. F. Levi, "Si-Based Receivers for Optical Data Links," *Journal of Lightwave Technology*, vol. 12, no. 6, pp. 930–935, 1994.
- [20] G. Roelkens, J. Van Campenhout, J. Brouckaert, D. Van Thourhout, R. Baets, P. R. Romeo, P. Regreny, A. Kazmierczak, C. Seassal, X. Letartre, G. Hollinger, J. M. Fedeli, L. Di Cioccio, and C. Lagahe-Blanchard, "III-V/Si photonics by die-to-wafer bonding," *Materials Today*, vol. 10, pp. 36–43, 7 2007.

- [21] T. Matsumoto, T. Kurahashi, R. Konoike, K. Suzuki, K. Tanizawa, A. Uetake, K. Takabayashi, K. Ikeda, H. Kawashima, S. Akiyama, and S. Sekiguchi, "Hybrid-integration of SOA on silicon photonics platform based on flip-chip bonding," *Journal of Lightwave Technology*, vol. 37, pp. 307–313, 1 2019.
- [22] J. Zhang, G. Muliuk, J. Juvert, S. Kumari, J. Goyvaerts, B. Haq, C. Op De Beeck, B. Kuyken, G. Morthier, D. Van Thourhout, R. Baets, G. Lepage, P. Verheyen, J. Van Campenhout, A. Gocalinska, J. O'Callaghan, E. Pelucchi, K. Thomas, B. Corbett, A. J. Trindade, and G. Roelkens, "III-V-on-Si photonic integrated circuits realized using micro-transfer-printing," *APL Photonics*, vol. 4, p. 110803, 11 2019.
- [23] A. Y. Liu and J. Bowers, "Photonic integration with epitaxial III-V on silicon," *IEEE Journal of Selected Topics in Quantum Electronics*, vol. 24, 11 2018.
- [24] N. Lindenmann, P. Marin-Palomo, M. R. Billah, C. Koos, A. Nesic, M. Blaicher, M. Moehrle, T. Hoose, P.-I. Dietrich, S. Randel, A. Hofmann, U. Troppenz, and W. Freude, "Hybrid integration of silicon photonics circuits and InP lasers by photonic wire bonding," *Optica*, Vol. 5, Issue 7, pp. 876-883, vol. 5, pp. 876–883, 7 2018.
- [25] B. Haq, S. Kumari, K. Van Gasse, J. Zhang, A. Gocalinska, E. Pelucchi, B. Corbett, and G. Roelkens, "Micro-Transfer-Printed III-V-on-Silicon C-Band Semiconductor Optical Amplifiers," *Laser & Photonics Reviews*, vol. 14, p. 1900364, 7 2020.
- [26] J. Zhang, B. Haq, A. Gocalinska, E. Pelucchi, A. José Trindade, B. Corbett, G. Morthier, G. Roelkens, D. Liang, J. E. Bowers, A. Novack, M. Streshinsky, R. Ding, Y. Liu, A. E. J Lim, G. Q. Lo, T. Baehr-Jones, M. Hochberg, F. Boeuf, S. Cremer, E. Temporiti, M. Fere, M. Shaw, N. Vulliet, D. Ristoiu, A. Farcy, T. Pinguet, A. Mekis, G. Masini, P. Sun, Y. Chi, H. Petiton, S. Jan, J.-r. Manouvrier, C. Baudot, P. Le-Maitre, J. F. Carpentier, L. Salager, M. Traldi, L. Maggi, D. Rigamonti, C. Zaccherini, C. Elemi, B. Sautreuil, L. Verga, H. Stievater, M. W. Pruessner, D. Park, W. S. Rabinovich, R. A. McGill, D. A. Kozak, R. Furstenberg, S. A. Holmstrom, and J. B. Khurgin, "Transfer-printing-based integration of a III-V-on-silicon distributed feedback laser," *Optics Express*, Vol. 26, Issue 7, pp. 8821-8830, vol. 26, pp. 8821–8830, 4 2018.
- [27] A. Hermans, K. Van Gasse, J. Kjellman, C. Caër, T. Nakamura, Y. Inada, K. Hisada, T. Hirasawa, S. Cuyvers, S. Kumari, A. Marinins, R. Jansen, G. Roelkens, P. Soussan, X. Rottenberg, and B. Kuyken, "High-pulse-

- energy III-V-on-silicon-nitride mode-locked laser,” *APL Photonics*, vol. 6, p. 096102, 9 2021.
- [28] H. Yu, D. Patel, W. Liu, Y. Malinge, P. Doussiere, W. Lin, S. Gupta, K. Narayanan, I. Hoshino, M. Bresnehan, S. Sunkoju, D. Mantegazza, R. Herrick, R. Venables, H. Mahalingam, P. Seddighian, A. Fuerst, J. Davis, D. Gold, X. Pan, K. Al-Hemyari, A. Agrawal, Y. Li, X. Zheng, M. Geethachar, M. Favaro, D. Zhu, A. Liu, and Y. Akulova, “800 Gbps Fully Integrated Silicon Photonics Transmitter for Data Center Applications; 800 Gbps Fully Integrated Silicon Photonics Transmitter for Data Center Applications,” 2022.
- [29] X. Qiang, X. Zhou, J. Wang, C. M. Wilkes, T. Loke, S. O’Gara, L. Kling, G. D. Marshall, R. Santagati, T. C. Ralph, J. B. Wang, J. L. O’Brien, M. G. Thompson, and J. C. Matthews, “Large-scale silicon quantum photonics implementing arbitrary two-qubit processing,” *Nature Photonics* 2018 12:9, vol. 12, pp. 534–539, 8 2018.
- [30] G. Zhang, J. Y. Haw, H. Cai, F. Xu, S. M. Assad, J. F. Fitzsimons, X. Zhou, Y. Zhang, S. Yu, J. Wu, W. Ser, L. C. Kwek, and A. Q. Liu, “An integrated silicon photonic chip platform for continuous-variable quantum key distribution,” *Nature Photonics*, 2019.
- [31] E. Pelucchi, G. Fagas, I. Aharonovich, D. Englund, E. Figueroa, Q. Gong, H. Hannes, J. Liu, C. Y. Lu, N. Matsuda, J. W. Pan, F. Schreck, F. Sciarrino, C. Silberhorn, J. Wang, and K. D. Jöns, “The potential and global outlook of integrated photonics for quantum technologies,” *Nature Reviews Physics* 2021 4:3, vol. 4, pp. 194–208, 12 2021.
- [32] J. M. Arrazola, V. Bergholm, K. Brádler, T. R. Bromley, M. J. Collins, I. Dhand, A. Fumagalli, T. Gerrits, A. Goussev, L. G. Helt, J. Hundal, T. Isaacsson, R. B. Israel, J. Izaac, S. Jahangiri, R. Janik, N. Killoran, S. P. Kumar, J. Lavoie, A. E. Lita, D. H. Mahler, M. Menotti, B. Morrison, S. W. Nam, L. Neuhaus, H. Y. Qi, N. Quesada, A. Repeatingon, K. K. Sabapathy, M. Schuld, D. Su, J. Swinarton, A. Száva, K. Tan, P. Tan, V. D. Vaidya, Z. Vernon, Z. Zabaneh, and Y. Zhang, “Quantum circuits with many photons on a programmable nanophotonic chip,” *Nature* 2021 591:7848, vol. 591, pp. 54–60, 3 2021.
- [33] M. Avesani, L. Calderaro, M. Schiavon, A. Stanco, C. Agnesi, A. Santamato, M. Zahidy, A. Scriminich, G. Foletto, G. Contestabile, M. Chiesa, D. Rotta, M. Artiglia, A. Montanaro, M. Romagnoli, V. Sorianello, F. Védovato, G. Vallone, and P. Villoresi, “Full daylight quantum-key-distribution

- at 1550 nm enabled by integrated silicon photonics,” *npj Quantum Information* 2021 7:1, vol. 7, pp. 1–8, 6 2021.
- [34] Y. Shen, N. C. Harris, S. Skirlo, M. Prabhu, T. Baehr-Jones, M. Hochberg, X. Sun, S. Zhao, H. Larochelle, D. Englund, and M. Soljacic, “Deep learning with coherent nanophotonic circuits,” *Nature Photonics* 2017 11:7, vol. 11, pp. 441–446, 6 2017.
- [35] J. Sun, E. Timurdogan, A. Yaacobi, E. Shah Hosseini, and M. R. Watts, “Large-scale nanophotonic phased array,” *Nature*, vol. 493, pp. 195–199, 2013.
- [36] “OpenAI.”
- [37] T. B. Brown, B. Mann, N. Ryder, M. Subbiah, J. Kaplan, P. Dhariwal, A. Neelakantan, P. Shyam, G. Sastry, A. Askell, S. Agarwal, A. Herbert-Voss, G. Krueger, T. Henighan, R. Child, A. Ramesh, D. M. Ziegler, J. Wu, C. Winter, C. Hesse, M. Chen, E. Sigler, M. Litwin, S. Gray, B. Chess, J. Clark, C. Berner, S. McCandlish, A. Radford, I. Sutskever, and D. Amodei, “Language Models are Few-Shot Learners,” *Advances in Neural Information Processing Systems*, vol. 2020-December, 5 2020.
- [38] B. J. Shastri, A. N. Tait, T. Ferreira de Lima, W. H. Pernice, H. Bhaskaran, C. D. Wright, and P. R. Prucnal, “Photonics for artificial intelligence and neuromorphic computing,” *Nature Photonics* 2021 15:2, vol. 15, pp. 102–114, 1 2021.
- [39] W. Ma, Z. Liu, Z. A. Kudyshev, A. Boltasseva, W. Cai, and Y. Liu, “Deep learning for the design of photonic structures,” *Nature Photonics* 2020 15:2, vol. 15, pp. 77–90, 10 2020.
- [40] J. E. Bowers, L. Chang, M. Li, Q. Lin, W. Xie, X. Wang, H. Shu, and K. Vahala, “Silicon Photonic Integrated Circuits for LiDAR,” *2022 IEEE Photonics Conference, IPC 2022 - Proceedings*, 2022.
- [41] H. Niu, P. Yu, P. Yu, Y. Zhu, Z. Jing, P. Li, B. Wang, C. Ma, J. Wang, J. Wu, A. O. Govorov, A. Neogi, Z. M. Wang, Z. M. Wang, and Z. M. Wang, “Mach-Zehnder interferometer based integrated-photonic acetone sensor approaching the sub-ppm level detection limit,” *Optics Express*, Vol. 30, Issue 16, pp. 29665-29679, vol. 30, pp. 29665–29679, 8 2022.
- [42] S. Kamalapurkar, E. J. Zhang, W. M. J. Green, J. S. Orcutt, and L. Tombez, “Methane absorption spectroscopy on a silicon photonic chip,” *Optica*, Vol. 4, Issue 11, pp. 1322-1325, vol. 4, pp. 1322–1325, 11 2017.

- [43] F. Ottonello-Briano, H. Sohlström, C. Errando-Herranz, H. Rödjegård, K. B. Gylfason, and H. Martin, “Carbon dioxide absorption spectroscopy with a mid-infrared silicon photonic waveguide,” *Optics Letters*, Vol. 45, Issue 1, pp. 109–112, vol. 45, pp. 109–112, 1 2020.
- [44] W.-G. Lee, G.-D. Kim, H.-S. Lee, B. T. Lim, S.-S. Lee, C.-H. Park, and H. K. Bae, “Silicon photonic temperature sensor employing a ring resonator manufactured using a standard CMOS process,” *Optics Express*, Vol. 18, Issue 21, pp. 22215–22221, vol. 18, pp. 22215–22221, 10 2010.
- [45] E. Ryckeboer, R. Bockstaele, and R. Baets, “Absorption spectroscopy of glucose based on a silicon photonics evanescent sensor,” *2013 IEEE Photonics Conference, IPC 2013*, pp. 163–164, 2013.
- [46] Y. Li, Y. Li, L. Marais, H. Khettab, Z. Quan, S. Aasmul, R. Leinders, R. Schüler, P. E. Morrissey, S. Greenwald, P. Segers, M. Vanslebrouck, M. Vanslebrouck, R. M. Bruno, P. Boutouyrie, P. O’Brien, M. d. Melis, R. Baets, and R. Baets, “Silicon photonics-based laser Doppler vibrometer array for carotid-femoral pulse wave velocity (PWV) measurement,” *Biomedical Optics Express*, Vol. 11, Issue 7, pp. 3913–3926, vol. 11, pp. 3913–3926, 7 2020.
- [47] L. Marais, H. Khettab, Y. Li, P. Segers, R. Baets, K. Reesink, S. Aasmul, M. De Melis, and P. Boutouyrie, “MEASUREMENT OF AORTIC STIFFNESS BY LASER DOPPLER VIBROMETRY,” *Journal of Hypertension*, vol. 37, p. e88, 7 2019.
- [48] W. Bogaerts, X. Chen, H. Deng, L. Van Iseghem, M. Wang, I. Zand, Y. Zhang, Y. Liu, K. P. Nagarjun, and U. Khan, “Programmable Silicon Photonic Circuits,” *OECC/PSC 2022 - 27th OptoElectronics and Communications Conference/International Conference on Photonics in Switching and Computing 2022*, 2022.
- [49] D. Pérez-López, A. López, P. DasMahapatra, and J. Capmany, “Multipurpose self-configuration of programmable photonic circuits,” *Nature Communications 2020 11:1*, vol. 11, pp. 1–11, 12 2020.
- [50] W. Bogaerts, D. Pérez, J. Capmany, D. A. B. Miller, J. Poon, D. Englund, F. Morichetti, and A. Melloni, “Programmable photonic circuits,” *Nature*, vol. 586, pp. 207–216, 10 2020.
- [51] P. DasMahapatra, J. Capmany, E. Sánchez, D. Pérez-López, and A. M. Gutierrez, “Integrated photonic tunable basic units using dual-drive directional couplers,” *Optics Express*, Vol. 27, Issue 26, pp. 38071–38086, vol. 27, pp. 38071–38086, 12 2019.

- [52] D. Marpaung, J. Yao, and J. Capmany, "Integrated microwave photonics," *Nature Photonics*, vol. 13, pp. 80–90, 2 2019.
- [53] A. Macho-Ortiz, D. Pérez-López, and J. Capmany, "Optical Implementation of 2×2 Universal Unitary Matrix Transformations," *Laser & Photonics Reviews*, vol. 15, p. 2000473, 7 2021.
- [54] J. Yao, "Microwave photonics," *Journal of Lightwave Technology*, vol. 27, pp. 314–335, 2 2009.
- [55] J. Capmany and D. Novak, "Microwave photonics combines two worlds," *Nature Photonics 2007 1:6*, vol. 1, pp. 319–330, 6 2007.
- [56] S. Pan and Y. Zhang, "Microwave Photonic Radars," *Journal of Lightwave Technology*, vol. 38, pp. 5450–5484, 10 2020.
- [57] G. K. Chang and C. Liu, "1-100GHz microwave photonics link technologies for next-generation WiFi and 5G wireless communications," *2013 IEEE International Topical Meeting on Microwave Photonics, MWP 2013*, pp. 5–8, 2013.
- [58] J. Hervás, A. L. Ricchiuti, W. Li, N. H. Zhu, C. R. Fernandez-Pousa, S. Sales, M. Li, and J. Capmany, "Microwave Photonics for Optical Sensors," *IEEE Journal of Selected Topics in Quantum Electronics*, vol. 23, pp. 327–339, 3 2017.
- [59] S. Pan, D. Zhu, S. Liu, K. Xu, Y. Dai, T. Wang, J. Liu, N. Zhu, Y. Xue, and N. Liu, "Satellite Payloads Pay off," *IEEE Microwave Magazine*, vol. 16, pp. 61–73, 9 2015.
- [60] B. Zhu, M. Xue, and S. Pan, "Optical Spectrum Analysis with a Resolution of 6 fm Based on a Frequency-Swept Microwave-Photonic Source," *Optical Fiber Communication Conference (2017), paper M3J.5*, vol. Part F40-OFC 2017, p. M3J.5, 3 2017.
- [61] X. Zou, B. Lu, W. Pan, L. Yan, A. Stöhr, and J. Yao, "Photonics for microwave measurements," *Laser & Photonics Reviews*, vol. 10, pp. 711–734, 9 2016.
- [62] Y. Gu and J. Yao, "Microwave photonic link with improved dynamic range through π phase shift of the optical carrier band," *Journal of Lightwave Technology*, vol. 37, pp. 964–970, 2 2019.
- [63] P. C. Won, W. Zhang, and J. A. Williams, "Self-phase modulation dependent dispersion mitigation in high power SSB and DSB + dispersion compensated modulated radio-over-fiber links," *IEEE MTT-S International Microwave Symposium Digest*, pp. 1947–1950, 2006.

- [64] C. G. Bottenfield, V. A. Thomas, and S. E. Ralph, "Silicon Photonic Modulator Linearity and Optimization for Microwave Photonic Links," *IEEE Journal of Selected Topics in Quantum Electronics*, vol. 25, 9 2019.
- [65] J. Yao, "Photonics to the Rescue: A Fresh Look at Microwave Photonic Filters," *IEEE Microwave Magazine*, vol. 16, pp. 46–60, 9 2015.
- [66] J. Zhang, L. Li, G. Wang, X. Feng, B. O. Guan, and J. Yao, "Parity-time symmetry in wavelength space within a single spatial resonator," *Nature Communications* 2020 11:1, vol. 11, pp. 1–7, 6 2020.
- [67] T. Hao, J. Tang, D. Domenech, W. Li, N. Zhu, J. Capmany, and M. Li, "Toward monolithic integration of OEOs: From systems to chips," *Journal of Lightwave Technology*, vol. 36, pp. 4565–4582, 10 2018.
- [68] R. T. Logan, L. Maleki, and M. Shadaram, "Stabilization of oscillator phase using a fiber-optic delay-line," *Proceedings of the Annual Frequency Control Symposium*, pp. 508–512, 1991.
- [69] L. Maleki, "The optoelectronic oscillator," *Nature Photonics* 2011 5:12, vol. 5, pp. 728–730, 12 2011.
- [70] E. A. Kittlaus, D. Eliyahu, S. Ganji, S. Williams, A. B. Matsko, K. B. Cooper, and S. Forouhar, "A low-noise photonic heterodyne synthesizer and its application to millimeter-wave radar," *Nature Communications* 2021 12:1, vol. 12, pp. 1–10, 7 2021.
- [71] T. Hao, Y. Liu, J. Tang, Q. Cen, W. Li, N. Zhu, Y. Dai, J. Capmany, J. Yao, and M. Li, "Recent advances in optoelectronic oscillators," <https://doi.org/10.1117/1.AP.2.4.044001>, vol. 2, p. 044001, 7 2020.
- [72] L. Goldberg, H. F. Taylor, J. F. Weller, and D. M. Bloom, "Microwave signal generation with injection-locked laser diodes," *Electronics Letters*, vol. 19, pp. 491–493, 6 1983.
- [73] A. C. Bordonalli, C. Walton, and A. J. Seeds, "High-Performance Phase Locking of Wide Line width Semiconductor Lasers by Combined Use of Optical Injection Locking and Optical Phase-Lock Loop," *Journal of Lightwave Technology*, vol. 17, pp. 328–342, 2 1999.
- [74] J. Liu, E. Lucas, A. S. Raja, J. He, J. Riemensberger, R. N. Wang, M. Karpov, H. Guo, R. Bouchand, and T. J. Kippenberg, "Photonic microwave generation in the X- and K-band using integrated soliton microcombs," *Nature Photonics* 2020 14:8, vol. 14, pp. 486–491, 4 2020.

-
- [75] L. A. Bui, “Recent advances in microwave photonics instantaneous frequency measurements,” *Progress in Quantum Electronics*, vol. 69, p. 100237, 1 2020.
- [76] L. Zhuang, C. G. H. Roeloffzen, M. Hoekman, K.-J. Boller, and A. J. Lowery, “Programmable photonic signal processor chip for radiofrequency applications,” *Optica*, vol. 2, p. 854, 10 2015.
- [77] W. Liu, M. Li, R. S. Guzzon, E. J. Norberg, J. S. Parker, M. Lu, L. A. Coldren, and J. Yao, “A fully reconfigurable photonic integrated signal processor,” *Nature Photonics* 2016 10:3, vol. 10, pp. 190–195, 2 2016.
- [78] W. Zhang and J. Yao, “A fully reconfigurable waveguide Bragg grating for programmable photonic signal processing,” *Nature Communications* 2018 9:1, vol. 9, pp. 1–9, 4 2018.
- [79] J. S. Fandiño, P. Muñoz, D. Doménech, and J. Capmany, “A monolithic integrated photonic microwave filter,” *Nature Photonics* 2016 11:2, vol. 11, pp. 124–129, 12 2016.
- [80] X. Guo, Y. Liu, T. Yin, B. Morrison, M. Pagani, O. Daulay, W. Bogaerts, B. J. Eggleton, A. Casas-Bedoya, and D. Marpaung, “Versatile silicon microwave photonic spectral shaper,” *APL Photonics*, vol. 6, p. 36106, 3 2021.

2

Silicon Photonic Components

This chapter offers an overview of the key components utilized in our silicon photonic circuits. It includes an introduction to basic devices such as waveguides, couplers, and active tuning elements such as heaters, photonic resonance junctions, and photodiodes, as well as tapped monitors. We will discuss specifically designed PN, PIN, and PIP doped junctions and their applications in phase shifting and monitoring. In addition, we will give a brief introduction to micro-transfer printing technology. Finally, we will provide a comprehensive workflow for this thesis work, covering the simulation, layout, and packaging solutions utilized in our silicon photonic circuits.

We thank Dr. Yuxi Fang for the help of the characterization of heaters and monitors.

2.1 Passive Components

2.1.1 Waveguides

Waveguides are fundamental structures used to confine and transfer electromagnetic waves from one point to another. They are formed by a core material with a higher refractive index surrounded by a cladding material with a lower refractive index. The possible guided electromagnetic field solutions, known as guided modes, are determined by the waveguide's materials and geometries. These modes are solutions of the Maxwell equations subject to the boundary conditions of the waveguide's size. In the case of silicon photonic waveguides, the high refractive index contrast between silicon (~ 3.5) and silicon dioxide (~ 1.44) enables tight confinement of the fundamental optical modes ($50 \text{ nm} \times 220 \text{ nm}$ for wavelengths around 1550 nm), leading to compact and efficient silicon photonic devices and systems.

An optical mode has two confusing properties, which are the effective refractive index n_{eff} and group index n_g . The effective index is determined by the phase velocity (v_p), which is the velocity of the phase fronts at any frequency components of the mode guided through the waveguide. Equation 2.1 shows how the effective refractive index is calculated [1]:

$$n_{\text{eff}} = \frac{v_c}{v_p} \quad (2.1)$$

Here, v_c is the speed of light in vacuum. The effective index can be roughly estimated using the effective index method, which decouples the 2D waveguide (uniform in the other direction) into two 1D planar waveguides and obtains the refractive index using 1D eigenvalue equations. However, this method becomes inaccurate for complex structures, poorly confined modes, or large index steps [1]. To obtain a more accurate value, numerical methods such as the finite-difference method (FDM), the finite element method (FEM), or film mode matching (FMM) can be used.

The other property of an optical mode is the group index n_g , which is determined by the velocity at which the energy, information, or a wave packet of the mode propagates through the waveguide. Group index is given by:

$$n_g = \frac{v_c}{v_g} = n_{\text{eff}} - \lambda \frac{dn_{\text{eff}}}{d\lambda} \quad (2.2)$$

where v_g is the group velocity of the mode. The group index can be different from the effective index and depends on the dispersion properties of the waveguide material. It is important in designing devices such as optical delay lines, where the delay time is determined by the group velocity.

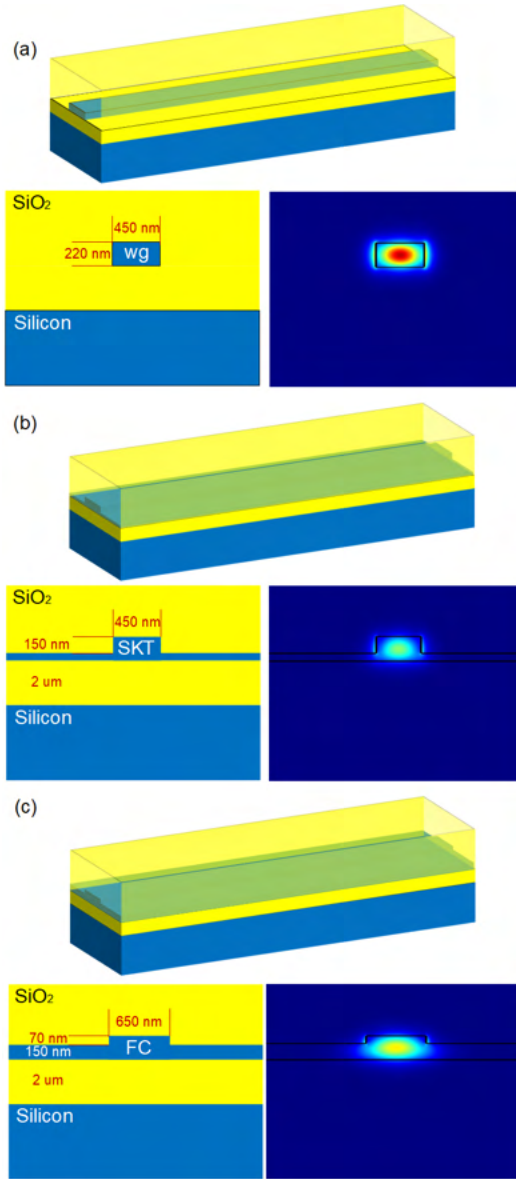


Figure 2.1: Silicon photonic waveguides and their fundamental mode profiles: (a) Strip waveguide; (b) deep etched rib waveguide; (c) shallow etched rib waveguide.

In standard silicon photonic platforms, the core material is silicon and the cladding is silicon dioxide. Therefore, one way to engineer the effective refractive index (n_{eff}) and group index (n_g) of waveguides is by modifying their geometries.

The imec iSiPP50G process offers three etching steps, which can form three kinds of commonly used waveguides, as shown in Fig. 2.1.

Figure 2.1 shows the waveguides and their fundamental TE mode profiles. The mode profiles are obtained from Lumerical Mode Solutions. Fig. 2.1(a) shows a fully etched wire strip waveguide with a width of 450 nm. The mode profile indicates that the mode is confined very well inside the waveguide core, allowing it to have a small low-loss bend radius (5 to 10 μm). Therefore, the strip waveguide is suitable for designing photonic devices for a small footprint. The profile also shows that some energy is located on the waveguide sidewalls, making the sidewall fabrication critical. The sidewall roughness introduced scattering also contributes to the main propagation loss of the waveguide. A wider strip waveguide with a width around 1 μm can offer lower propagation loss and reduced fabrication error, but it is no longer a single-mode waveguide and requires care to avoid exciting higher modes [2].

Figure 2.1(b) and (c) are partially etched rib waveguides, where the 150 nm etched one is defined by SKT layers (in iSiPP50G platform) while the 70 nm etch one is defined by FC layers. It can be seen that the mode confinements are weaker in the rib waveguides, thus the used minimum bend radius is larger, say 10 \sim 15 μm for SKT waveguides and 30 \sim 50 μm for FC (in iSiPP50G platform) waveguides. On the other hand, the guided modes in the rib waveguides distribute less on the sidewalls. This reduces the propagation loss due to sidewall scattering.

These three types of waveguide are commonly used in the design of silicon photonic devices and circuits. Strip waveguides are particularly useful for achieving small footprints in devices and circuits. SKT waveguides, due to their electrical connections within the waveguides, find applications in p and n doped junctions, such as PIN monitors and PN modulators, as discussed in Chapter 2.2.3. FC waveguides, with their low propagation loss, are ideal for making high Q resonators [3, 4] and long-range waveguide connections. However, the bending radius for FC waveguides is quite large, so it is better to taper them into a strip waveguide first and then round out using strip waveguides [5].

Other types of waveguides are also used in silicon photonic circuits, including slot waveguides and sub-wavelength grating waveguides. Slot waveguides can be useful in high-sensitivity sensors, but they usually have a higher propagation loss due to the sidewall roughness. Sub-wavelength grating waveguides offer another degree of freedom in engineering the n_{eff} and n_g of waveguides by tuning the filled factor of the gratings, but their fabrication can be challenging with deep ultraviolet lithography technology in silicon photonics now [6].

In this thesis work, we mostly use strip waveguides to build the filters and connect components for their low bending radius, and use FC rib waveguides to connect the in/out ports with grating couplers for the low propagation loss. SKT waveguides are merely used to form the doped waveguide for the modulations.

2.1.2 Couplers

Silicon photonic couplers are key components in integrated optical systems, distributing the power of light between different waveguides. In this section, three kinds of couplers widely used in our silicon photonic systems will be introduced, which are directional couplers (DCs), multimode interference (MMI) couplers and adiabatic couplers.

Directional Couplers (DC)

DCs use evanescent coupling to transfer light from one waveguide to another. The overlap of evanescent modes causes the light to migrate back and forth between the guides. A typical DC design is shown in Fig. 2.2. Its behavior can be analyzed using coupled mode theory [7]. For instance, two parallel straight strip waveguides can support an odd and an even supermode, as illustrated in Fig. 2.2(d). The cross power coupling of the straight section can be expressed as follows:

$$K_{\text{straight}} = \sin^2(k'l_c) \quad (2.3)$$

where l_c is the coupling length, and the field coupling coefficient k' represents the strength of the coupling per unit length in the straight coupling section. k' is determined by the difference between the effective refractive indices (Δn) of the odd (n_{odd}) and even (n_{even}) supermodes, which is :

$$k' = \frac{\pi}{\lambda} \Delta n = \frac{\pi}{\lambda} (n_{\text{even}} - n_{\text{odd}}) \quad (2.4)$$

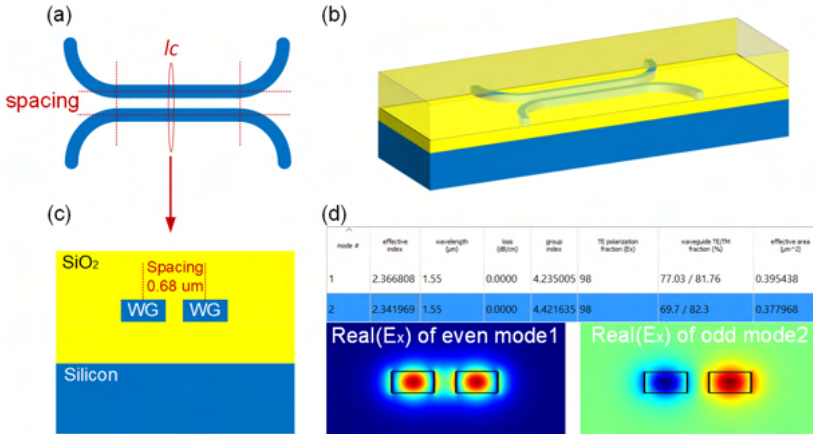


Figure 2.2: Strip waveguide based directional coupler in silicon photonics: (a) Schematic of a typical DC; (b) 3D model of the DC; (c) cross section of the straight part of the DC; (d) Mode properties of the even and odd mode obtained from Lumerical FDE solver.

In the simulation case, $k' = 2.366808 - 2.341969 = 0.024839$.

From Fig. 2.2(a), it can be noticed that a DC also contains two bending sections, which also contribute to the power coupling, noting as k_0 . Thus the full cross power coupling is expressed as:

$$K = \sin^2(k'l_c + k_0) \quad (2.5)$$

These coefficients in Equation 2.5 can be obtained with simulation tools and/or extracted with tested results from previously fabricated devices. Then a DC with specific power coupling ratio can be designed with a coupling length l_c .

Multi Mode Interferometers (MMI)

Another type of commonly used power coupler is an MMI coupler, which generalizes the two-mode interference of a directional coupler to a larger number of guided modes. MMIs are based on the self-imaging principle arising from multi-mode interference in the multimode waveguide [8]. For the designing of a MMI, a critical dimension is its beat length, which is expressed as:

$$L_\pi = \frac{\pi}{\beta_0 - \beta_1} \simeq \frac{4}{3} n_r \frac{w^2}{\lambda_0} \quad (2.6)$$

Here, β_0 and β_1 are the propagation constants of the fundamental and first-order modes of the multimode waveguide, n_r is the effective index, λ_0 is the operating wavelength, and w is the width of waveguide.

Equation 2.4 reveals that the power coupling of a DC is highly dependent on the waveguide refractive index difference, which means that the fabrication pro-

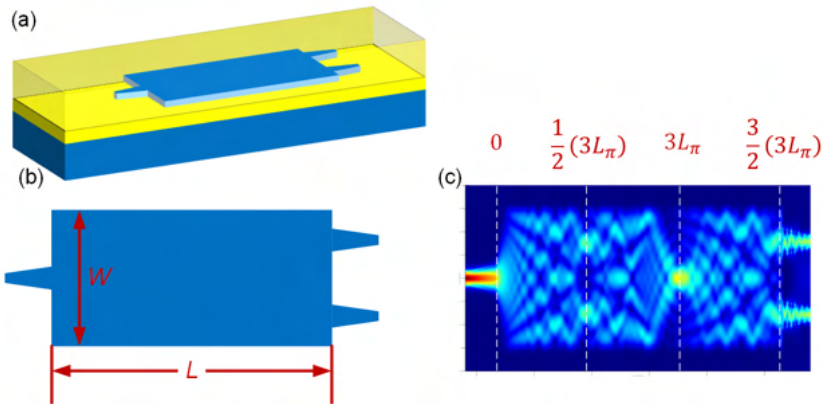


Figure 2.3: A multimode interference coupler in silicon photonics: (a) 3D model of the DC; (b) Schematic of a typical DC; (c) Modes distribution of MMI obtained from Lumerical EME solver.

cess parameters, such as etch depth, core thickness, waveguide width, and waveguide spacing, can significantly affect the device performance. Meanwhile, Equation 2.6 shows that the MMI is more sensitive to the waveguide dimensions such as width and length, which is relatively reliable. Generally, a 50:50 directional coupler can achieve a smaller footprint, lower insertion loss and reflection, while a 50:50 MMI coupler can provide a higher operational bandwidth and robustness [9].

Adiabatic Couplers

Meanwhile, adiabatic couplers are a type of optical coupler that are highly reliable and can convert the mode of a single waveguide into either the even or odd mode of two waveguides with a small gap. Unlike DCs discussed above, adiabatic couplers excite only one mode in the two waveguides and gradually push the modes without any interference, resulting in broad band operation and high robustness [10]. However, their footprints are much longer than normal interference-based couplers, typically around a length of $200 \mu\text{m}$ [11]. Sub-wavelength grating-based adiabatic couplers can offer a 50:50 coupling ratio at a length of $50 \mu\text{m}$, but their fabrication is still challenging [12].

Another way to get a more robust coupler is to add active phase shifters to compensate the fabrication imperfections. A Mach-Zehnder interferometer (MZI) structure with tunable phase shifters can be regarded as a tunable directional coupler. By adjusting the phase shifter, the outputs' power splitting ratios can be tuned as desired. More details will be introduced in Chapter 3. In this thesis work, we mainly use tunable couplers as power couplers, and these tunable couplers show high reliability and also enable the circuits reconfigurability.

2.2 Active Components

2.2.1 Optical phase tuners

Optical phase shifters are essential components for manipulating the phase of light propagating through waveguides [13]. In silicon photonics, various phase-shifting mechanisms can be utilized, including birefringence with liquid crystals, mechanical movement with micro-electro-mechanical systems (MEMS), thermal-optics with heaters, carrier dispersion effects with doped junctions and capacitors, and Pockels effects with some polymers and perovskites. These effects have different strengths and response times, and are suitable for various applications, as shown in Fig. 2.4. In this section, we will mainly focus on heater-based optical phase tuners and illustrate junction-based phase modulators in the next section on modulators.

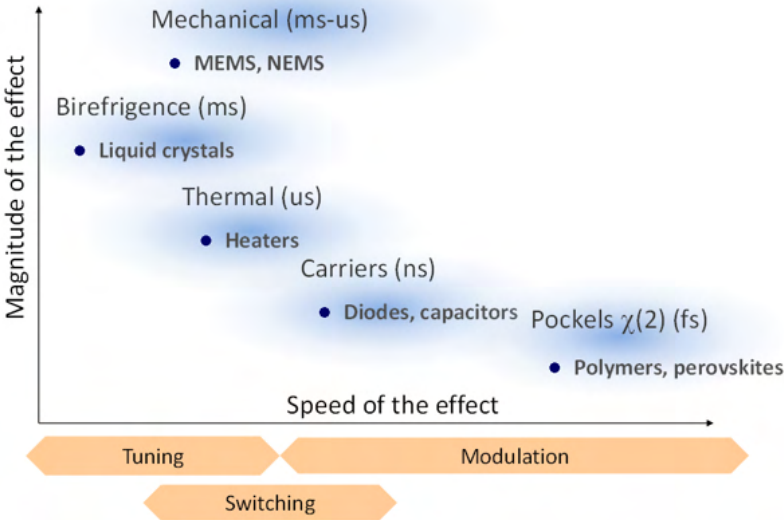


Figure 2.4: Mechanisms for phase shifting in silicon photonics. Figure reproduced from Prof. Wim Bogaerts' course materials.

Due to the high thermo-optic coefficient of silicon ($1.8 \times 10^{-4} K^{-1}$), heaters are suitable for optical phase tuning with high performance and ideally zero insertion loss. In the imec iSiPP50G platform, three types of thermal optical heaters can be designed: top tungsten heaters, side doped heaters, and doped waveguide heaters. Their cross-sections and thermal propagation are shown in Fig. 2.5. As shown in Fig. 2.5(a), a tungsten heater is achieved by depositing a thin wire of tungsten over the waveguide [14]. A side doped heater is implemented by doping one or two silicon resistors next to the main waveguide, as shown in Fig. 2.5(b). It

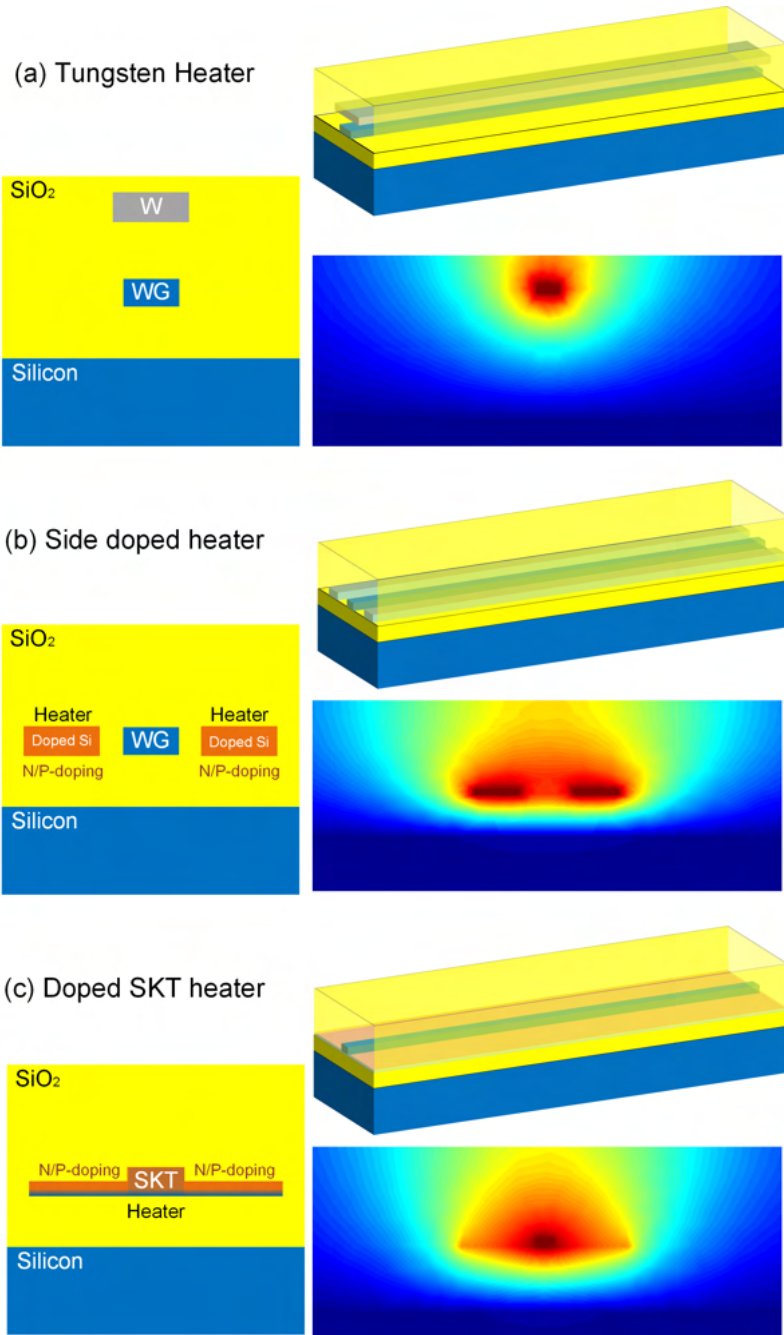


Figure 2.5: Various types of heaters in silicon photonics: (a) Top tungsten heater; (b) doped side waveguide heater; (c) doped SKT waveguide heater.

should be noted that the width of the side resistors and the gap to the main waveguide need to be large enough to avoid optical coupling loss. A more straightforward way is to dope the main waveguide directly, thus requiring a SKT waveguide (i.e., PP doping or PIP doping), as shown in Fig. 2.5(c). To ensure low optical absorption, doping on the SKT waveguide core needs to be weak or even intrinsic.

Thermal efficiency

Generally, the amount of phase shift introduced by a heater can be noted as [15]:

$$\begin{aligned}\Delta\phi &= \frac{2\pi L}{\lambda_0} \left(\frac{dn}{dT} \right) \Delta T \\ &\simeq 2.4\pi \times 10^{-4} \Delta T L |_{\lambda_0=1550nm}\end{aligned}\quad (2.7)$$

Where L is the device length (in m), λ_0 is the free-space wavelength (in m), $\frac{dn}{dT}$ is the thermo-optic coefficient (in $1/K$) and ΔT is the change in temperature (in K). Since ΔT is caused by the heater's heating up, it can be estimated as [16]:

$$\Delta T = \frac{\eta P}{C_p \rho L S} \quad (2.8)$$

where P is the electrical power dissipated by the heater, η is the heater's power efficiency, C_p is the heat capacity of the waveguide (in $J/(kg \cdot K)$), ρ is the material density of the waveguide (kg/m^3), and S is the cross-sectional area of the waveguide (in m^2). Combine equation 2.7 and 2.8 we can get the phase shift as:

$$\Delta\phi \simeq 2.4\pi \times 10^{-4} \frac{\eta P}{C_p \rho S} \quad (2.9)$$

In equation 2.9, $C_p \rho S$ is a constant with a designed silicon waveguide. Thus we can get:

$$\Delta\phi = \eta' P \quad (2.10)$$

where η' can be the heater's thermal-phase efficiency. From equation 2.10, we know that the optical phase shift is only determined by the power delivered to the heater based phase shifter, but not depends on the phase shifter's physical length. For a line resistor (doped heater and tungsten heater), the resistance is higher when the resistor is designed longer and narrower, and the delivered current and power get lower when a fixed voltage applied.

Normally, the efficiency of a heater is expressed as P_π , which is the electrical power required to introduce an optical π phase shift. To measure the introduced phase shifts, an optical interferometer is needed, which can be a microring or an MZI. In this case, we used MZIs for the following tests, as shown in Fig. 2.6. The devices under test (DUT), which are heaters here, and two 50:50 directional couplers form an MZI, with the heaters driven by a tunable DC power source (in

this case, a Keithley 2400 source meter). The light is fed into one input port, and a photodetector is used to collect the output optical power.

For the circuit shown in Fig. 2.6, the transfer function of the optical power can be expressed as:

$$T = 0.5(1 - \cos(\phi)) \quad (2.11)$$

where ϕ is the optical phase shift introduced by the DUT (heater). By keeping the laser output constant and measuring the optical powers from the photodetector, we can extract ϕ and obtain the P_π by checking the readout of the DC power source.

We have measured several types of heaters using the circuit described above. As a demonstration, we present the results of a metal tungsten heater measurement in Fig. 2.7. For this test, we designed and tested a $100 \times 0.3 \mu\text{m}$ metal heater driven by a Keithley. By sweeping the driving voltage, we obtained the optical output power of a power meter, as shown in Fig. 2.7(c). As equation 2.10 shows, the phase shift is proportional to the driving power. Therefore, we also measured the resistance of the tungsten heater, which is shown in Fig. 2.7(d). We observed that the resistance increases with the driving voltage due to heating. Using this resistance data, we then calculated the electrical power delivered and obtained the response shown in Fig. 2.7(e). The curve in Fig. 2.7(e) is consistent with a sinusoidal waveform, as predicted by Equation 2.11, and its signal period reveals the P_π of the designed tungsten heater: $22.36 \text{ mW}/\pi$.

Other types of heaters were also tested using the same method, and the results are presented in Table 2.1. It can be seen that FC waveguide heaters have the lowest thermal efficiency overall, and the doped SKT waveguide heaters have the highest thermal efficiency because they heat up the waveguide directly, but if the doped SKT heater is electrically connected on the sides (as shown in Table 2.1), the efficiency gets lower. A doped SKT waveguide (PIP and PP) will introduce optical absorption loss, while we cannot fully characterize it with such short devices. Tungsten heaters shows a good enough heating efficiency, but their resistance is way lower than other heaters, which means that it will need lower voltage but higher currents for a phase tuning, which commonly causes higher electrical

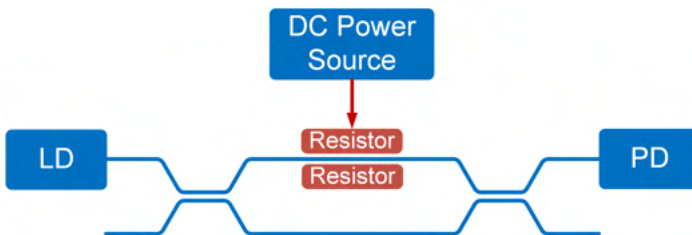


Figure 2.6: Schematic circuit for heaters' thermal efficiency tests. LD: laser diode; PD: photodiode.

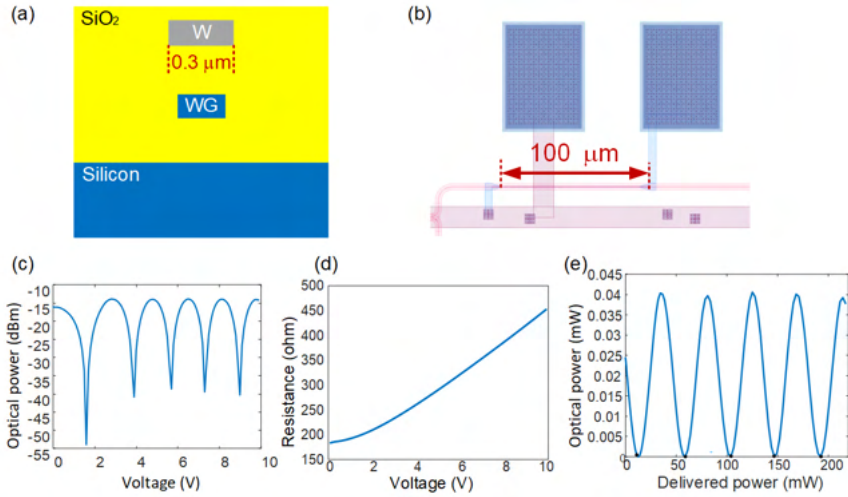


Figure 2.7: Metal heater thermal efficiency tests. (a) The cross section of the metal heater; (b) Layout for the metal heater with electrical bondpads; (c) measured optical power (dBm) versus driving voltage; (d) measured heater resistance versus driving voltage; (e) calculated optical power (mW) versus delivered electrical power (mW).

crosstalk and higher optical phase errors.

Thermal phase shifters are becoming increasingly important in PICs due to their low insertion loss and compatibility with standard CMOS technology. As PICs become larger and more complex, the number of thermal phase shifters required increases, resulting in higher power consumption and thermal crosstalk. To address this issue, researchers are working to develop thermal phase shifters with higher thermal efficiency or lower P_π . One approach to achieve higher thermal efficiency is to reduce thermal leakage by under-etching the substrate and its surroundings to insulate the heater. This method requires additional processing [14]. Another approach is to maximize the use of the heat generated by designing the device so that the light traverses the heater multiple times [17]. These two methods can be combined to achieve even better results.

We designed and tested several thermal phase shifters with the undercut (UCUT) process and top etching (EXPO layer) process from imec, to insulate the heaters, as shown in Fig. 2.9. The comparison between side doped heaters with and without top trench is shown in Fig. 2.8. The EXPO etching improved thermal efficiency, but not significantly. However, devices with UCUT process showed a 3 times improvement in thermal efficiency, as listed in table 2.2. Unfortunately, top etching and undercut cannot be combined in the same device due to design rules.

Among the thermal phase shifters tested, without UCUT, the PIP doped waveguide heaters reached the highest thermal efficiency. With the UCUT process, both

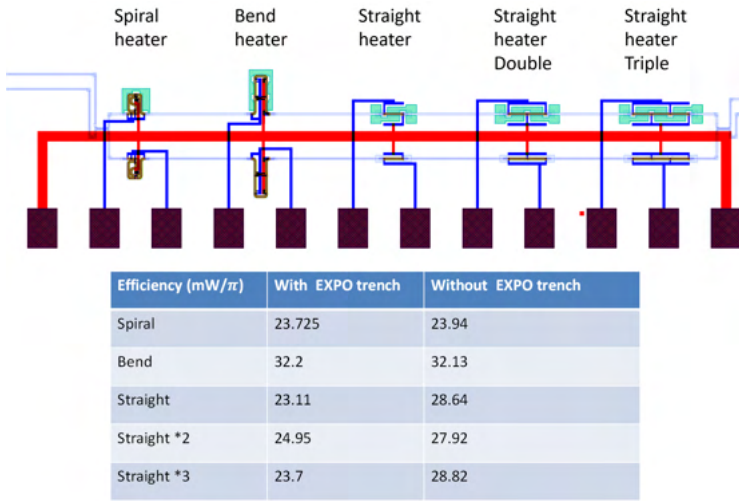


Figure 2.8: Thermal efficiency of side doped heaters with and without undercut

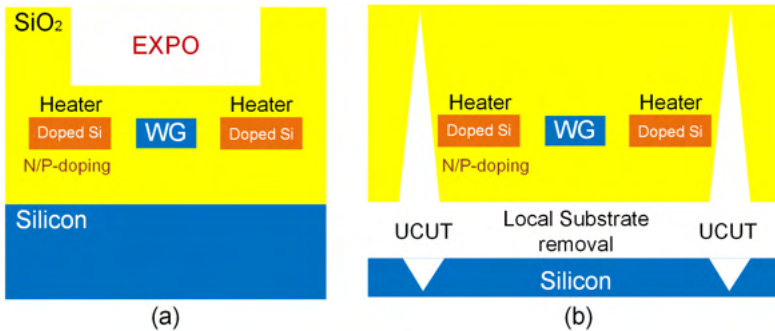


Figure 2.9: Heater designs with improved thermal efficiency. (a) Heater with top-etching (EXPO) process; (b) Heater with under cut (UCUT) process.

side heaters and top heaters can achieve P_π of 8~9 mW/ π , while the PIP doped SKT waveguide heaters with UCUT are also promising, although they have not yet been tested.

Time constant and Modulation speed

Another critical performance of the thermal phase shifter is their time constant, which defined the time required for the heater to reach a steady-state temperature and phase shifts when a constant power is applied. A widely used metric to evaluate the performance of thermal phase shifters, is defined as the product of the thermal time constant and the thermal efficiency $P_\pi\tau$ [16].

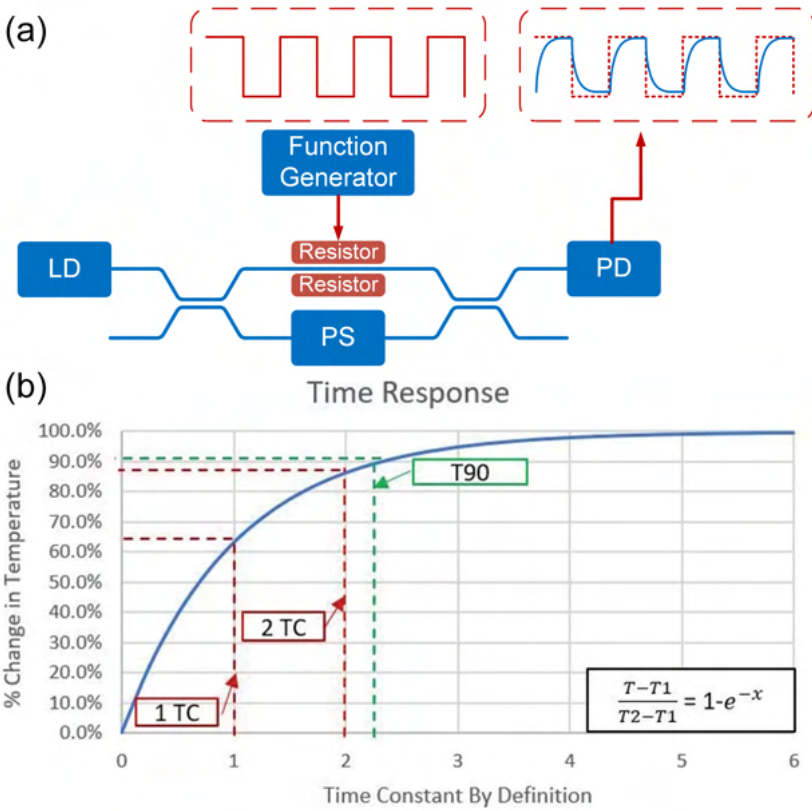


Figure 2.10: (a) Schematic circuit for heaters' time constants. (b) Time constants definition. LD: laser diode; DUT: device under test, heaters here; PS: phase shifter; PD: photodetector.

To reduce $P_\pi\tau$, the heat source needs to be placed as close as possible, thereby reducing the heat flow area. However, this can be challenging when using side doped silicon waveguides or overhead metal heaters, as they can introduce optical loss when placed too close. The Doped SKT waveguide (PP or PIP doped) heaters enjoyed a smaller heat flow area due to the directly heated waveguide, but the doping process introduces potential optical absorption. Processes like UCUT or top etching is another way to reduce the total heat flow area, and lower $P_\pi\tau$ can be reached.

The $P_\pi\tau$ is almost constant unless specific post-processing is implemented. Therefore, heaters with high thermal efficiency or low P_π will have a high time constant τ , indicating that they require a longer time to heat up or cool down, which can be a good or bad thing depending on the application.

To measure the time constants of the heaters discussed above, we used the

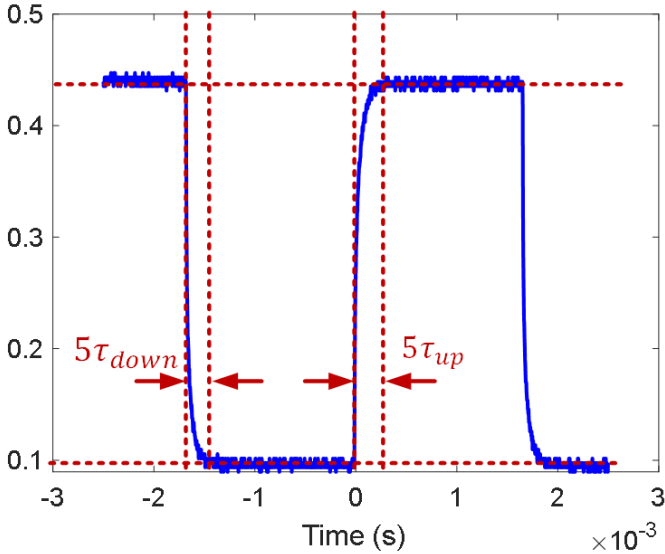


Figure 2.11: Measured time waveform of a side doped heater with under etching

setup shown in Fig. 2.10. A function generator introduced a periodic heating and cooling cycle at 500 Hz, providing enough time for full heat up or cool down. The amplitude of the signal is set as a small signal and the phase shifter on the other arm of the MZI set the bias point at the quadrature point, ensuring the total system is in a linear modulation region. Fig. 2.11 shows one demonstration of the measurement results, and the full results for multiple heaters are presented in table 2.3. As can be seen, there are some discrepancies between the heating time and the cooling time, which should be equal in a first order thermal RC system. One possible reason is that the operational point of the MZI shown in Fig. 2.10(a) is not ideally located at the quadrature point, and the optical nonlinearity distorts the generated AC signal. Another possible reason may be that the amplitude of the input square wave is still too large to satisfy the small signal model. Further measurements and tests are needed.

Table 2.1: Thermal efficiency of various heaters

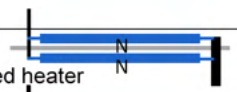
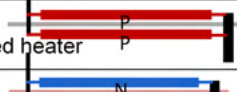
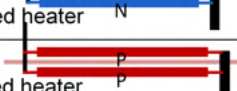
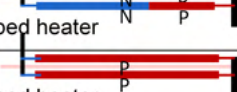
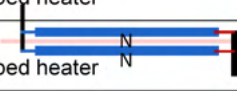
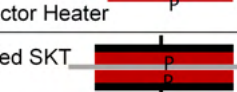
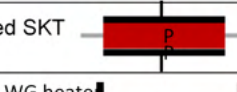
	Length (μm)	Resistance	Without undercut Efficiency (mW /π)
 FC N- doped heater	53	928	32.3
	28	532	38.9
 FC P- doped heater	53	1927	30.6
	28	1070	29.3
 WG N- doped heater	53	1191	miss
	28	534	28.2
 WG P- doped heater	53	2087	28.0
	28	1122	27.6
 WG PN- doped heater	53	--	28.1
	28	--	25.1
 WG PN- doped heater	53	--	25.5
	28	--	26.4
 WG PN- doped heater	53	--	28.2
	28	--	27.6
 WG PN- doped heater	53	--	27.4
	28	--	26.8
 PP Doped SKT 2 connector Heater	53	2115	34.5
	28	1468	32.2
 PP Doped SKT 4 connector Heater	53	1830	37.3
	28	794	36.6
 PIP Doped SKT	53	1018	17.5
	28	1805	17.4
 PP Doped SKT	53	155	19
	28	287.7	18.8
 Tungsten WG heater	100 x 0.3	192	22.36
	100 x 0.6	~100	~20

Table 2.2: Thermal efficiency of various heaters with undercut

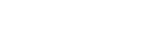
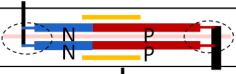
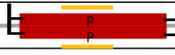
		Length (μm)	Resistance (Ohm)	Efficiency (mW/π)
FC N - doped heater With UCUT		53	928	8.75
		28	532	12.5
FC P - doped heater With UCUT		53	1927	9
		28	1070	13
WG N - doped heater With UCUT		53	1191	10.5
		28	534	12
WG P - doped heater With UCUT		53	2087	13
		28	1122	12.7
SKT PP doped wg heater		53	1018	10.8
		28	1805	10
SKT PP doped side heater		53	155	9
		28	287.7	12

Table 2.3: Time constants of various heaters with undercut

	Heating time 0.1-0.9 (μs)	τ-RC (μs)	Cooling time 0.1-0.9 (μs)
	93.787	42.689	66.45
	16.736	7.6175	20.08
	13.52	6.153	6.153
	114.5	52.13	32.9
	77.85	35.43	71.76

Another parameter used to evaluate the thermal phase shifter's heating speed is its 3 dB bandwidth, $f_{3\text{dB}}$, which is obtained by characterizing the phase shifter as a low-speed phase modulator. The relationship between $f_{3\text{dB}}$ and τ for a pure RC system can be expressed as follows:

$$f_{3\text{dB}} = \frac{0.34}{\tau} \quad (2.12)$$

The frequency response of the thermal phase shifter can reveal more details for the linear responses, and it can be measured using a vector network analyzer (VNA). However, some high-speed VNAs may not handle frequencies lower than 10 MHz, in which case a manual frequency sweep can be done using the setup shown in Fig. 2.6, where the function generator signal would implement a frequency sweep with single frequency sinusoidal waveforms. This is designated as optical homodyne detection. We measured the heaters with and without UCUT. First, we directly use a VNA for measurement, and one set of heater measurement results is shown in Fig. 2.12. As can be seen, the frequency bandwidths are almost unrelated to the heater's length, which is predictable. Some heaters' results are shown in Table 2.4. Then we noticed that, as the frequency range of the VNA we used starts from 30 kHz, this may be too high to get the valid results. Thus we used a function generator and an oscilloscope to implement the frequency sweep. A swept result is shown in Fig. 2.13, which shows that 3 dB bandwidth is around 5 kHz, much lower than the used VNA's frequency range. Then we measured other heaters, and the results are shown in Table 2.5. As can be seen, 3 dB bandwidth of the WG heaters with UCUT are around 3 times smaller than the ones without UCUT, matching the efficiency improvement. However, we can also note that these results cannot match the time constants shown in Table 2.3 and the results measured with VNA shown in Table 2.4.

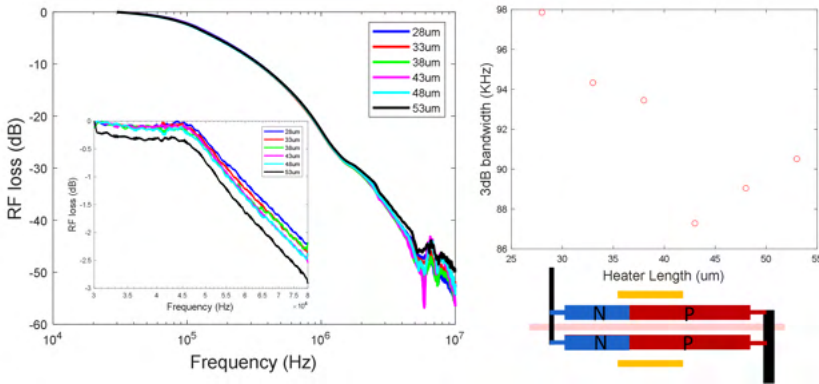


Figure 2.12: Frequency measurement results of a side heater with UCUT using a VNA.

Table 2.4: Frequency measurement results of various heaters with UCUT using a VNA

Length 28 μm	fc-VNA (kHz)
	97.9
	97.3
	99.3
	101.1
	80
	95.2

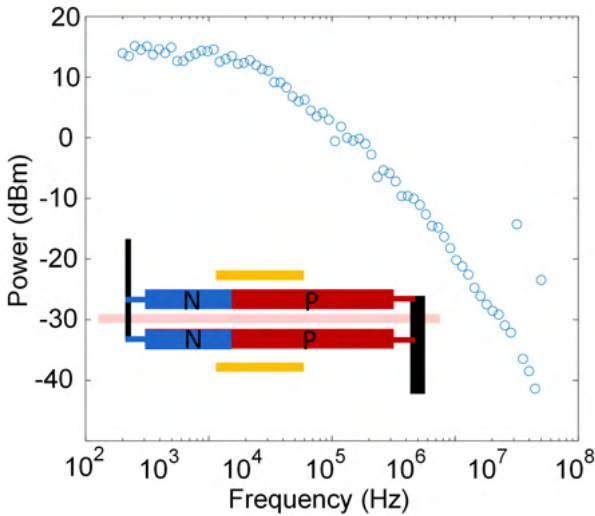


Figure 2.13: Frequency measurement results of a side heater with UCUT using a signal generator and an oscilloscope.

On the other hand, optical heterodyne detection can provide a higher signal-to-noise ratio (SNR) and immune to noise at low frequencies. The measurement setup for optical heterodyne detection is shown in Fig. 2.14. In this setup, the thermal phase shifter (biasing MZI at the quadrature point) and two couplers form a thermal intensity modulator, which modulates the fed-in optical carrier with side-

Table 2.5: Frequency measurement results of various heaters with UCUT using a signal generator and an oscilloscope.

	Length = 28 (μm)	With undercut (KHz)	Without undercut (KHz)	Ratio
	FC side doped N	5.4	28.2	5.2
	FC side doped P	5.4	28.2	5.2
	WG side doped N	6.7	17.5	2.6
	WG side doped P	5.4	14.9	2.7
	WG Side doped N with P connector	6	12.7	2.1
	WG Side doped P with N connector	5.4	14	2.6
	WG Side doped N more	4.8	16	3.3
	WG Side doped P more	4.3	15	3.7
	SKT PP doped with 4 connector	4.7	18.7	4.0
	SKT PP doped with 2 connector	5.9	51.8	8.8
	SKT PP doped	139		

bands spacing at the input RF frequency ω_s ¹. An acousto-optic frequency shifter is used to up-shift the laser carrier by 200 MHz. Thus, the beat signal recovered by the photodiode (PD) will have a copied modulation spectrum centered at 200MHz, as shown in Fig. 2.14. By sweeping the input RF frequency ω_s and calculate the sidelobe to mainlobe ratio (SMR), we can get a normalized frequency response of the thermal phase shifter.

The measured Bode plots of several thermal phase shifters are shown in Fig. 2.15. Unfortunately, these results lacks the lowest frequency points and it cannot match all of previous results. Further measurements needs to be done in future tests.

The Bode plots reveal that thermal phase shifters can function as phase modulators for certain applications. Additionally, the plots are useful for designing the driving systems for these thermal phase shifters.

Driving systems

As the number of phase shifters increases rapidly, the driving systems become more complicated. The fundamental method of driving a heater-based phase shifter is by using a DC power supply, such as the units shown in Fig. 2.16. DC power supplies can be classified as voltage or current supplies, depending on whether the output is set to a constant voltage or a constant current. When only one heater is driven, there is no difference between using a voltage driver or a current driver.

¹Introduction about the modulation sidebands will be detailed in chapter 4

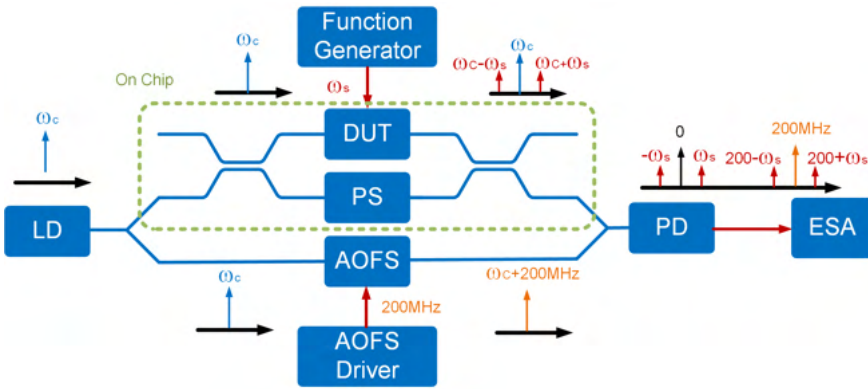


Figure 2.14: Heterodyne measurement for phase shifters bandwidth tests. LD: Laser diode; DUT: device under test, heaters here; PS: phase shifter; AOFS: acousto-optic frequency shifter; PD: photodiode; ESA: electrical spectrum analyzer.

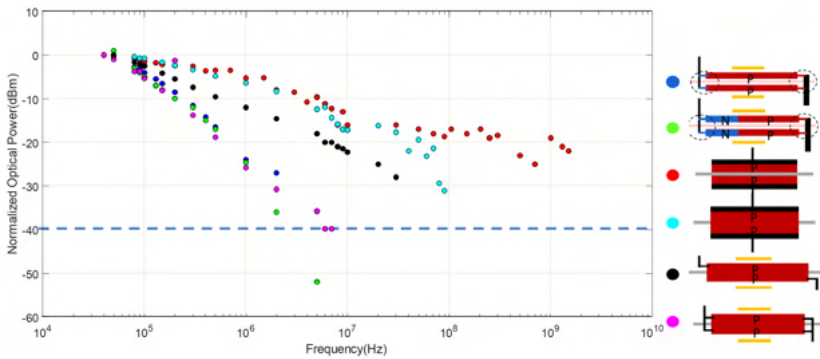


Figure 2.15: Bode plots of various thermal phase shifters (to be finished)

However, when multiple heaters are driven simultaneously and they share a common ground (to reduce the number of used bond pads), voltage drivers introduce electrical crosstalk (in $V_1 - V_2$ terms shown in Fig. 2.17 (a)), while current drivers do not. We use a two-heater driving system to demonstrate this difference in Fig. 2.17.

On the other hand, conventional DC power supplies such as the one shown in Fig. 2.16(a) are bulky and occupy a significant amount of space, making them difficult to scale up. Although there are some multichannel power output modules like the one in Fig. 2.16(b) that can support 32 or 64 channels on a single board, their power delivery capability is limited, which restricts the design of phase shifters. The power module mentioned above can only deliver a maximum of 10 V or 20 mA, which means that a heater with a resistance of 500 ohms is the best fit.

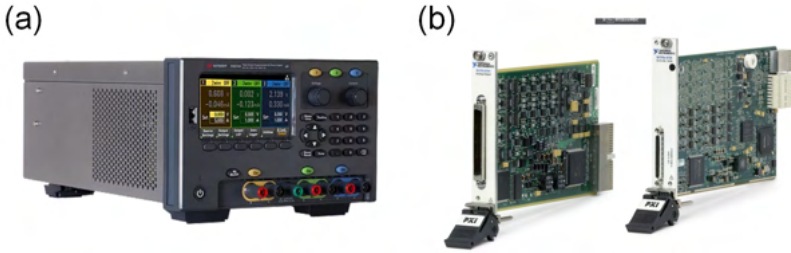


Figure 2.16: DC power supplies. (a) 3 channel power supply E36300 from Keysight; (b) PXI 6739 64 channel analog output module from National Instrument

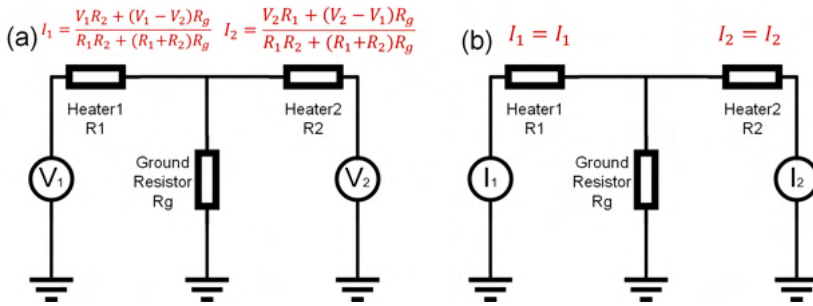


Figure 2.17: Voltage driving and current driving. (a) Voltage driving system for two heaters; (b) Current driving system for two heaters;

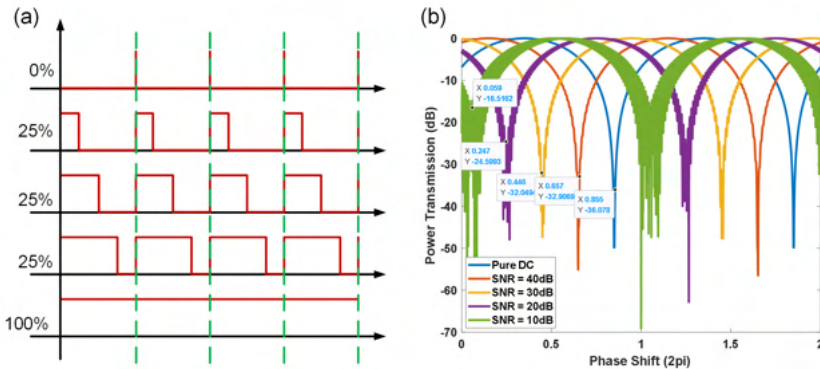


Figure 2.18: (a) Pulse width modulation; (b) MZI extinction ratio with different noise floor

To match the resistance values, we can segment the side-doped heaters according to the table 2.1. In addition, if the driving voltage of the phase shifters can be set within 3.3 V or 5 V, the driving systems can be designed with low cost and compact digital chips.

The DC drive system is reliable but suffers from a drawback: its optical phase response is parabolic with applied voltage or current, unlike the linear response of PWM drive systems [18]. Consequently, the DC drive system requires individual calibration due to variations in heater resistance resulting from manufacturing differences. A solution to this problem is the use of a PWM drive system, which employs a high-frequency square wave signal to supply power to the heater element. The amount of power delivered to the load is proportional to the duty cycle of the digital signal, which the PWM system adjusts to control the phase shift of the phase shifter linearly, as depicted in Fig. 2.18(a). PWM systems have several advantages over DC drive systems, particularly in applications that drive multiple heaters simultaneously and require precise control of phase shift. However, PWM signals cause modulation noise on optical signals, and the frequency responses in Fig. 2.15 show the modulation strength or depth at different frequencies. Thus, the PWM signal's repetition frequency must align with the application specifications. For example, in an optical MZI switches that use phase shifters driven by PWM signals, the PWM-induced phase noise will reduce the switch's extinction ratio, shown in Fig. 2.18(b). The simulation results (a phase noise is added to the phase signal, and the noise power is defined by the signal-noise-ratio (SNR)) in this figure show that when the SNR is greater than 40 dB, the PWM-driven switch can match the DC-driven one, indicating that the PWM signal's speed is adequate. From the SNR and the heater's frequency response, we can get the required driving frequency (f_{PWM}). The PWM resolution is determined by the number of bits in the duty cycle, and thus the shortest signal frequency or the fastest signal speed is $2^{bits} \times f_{PWM}$ (to make sure that the longest signal can still has adequate frequency). Thus, high-bit systems present a challenge to the drive system.

As the size of photonic circuits increases, the number of thermal phase shifters and corresponding drivers also grows rapidly. One potential solution is the use of matrix addressing circuits, which make use of PWM driving and on-chip doped junctions to handle $m \times n$ phase shifters with only $m + n$ drivers, as shown in Fig. 2.19 [19]. However, since time is channelized into n channels, the PWM signal's frequency needs to be n times higher to achieve low noise control, which presents a greater challenge (will increase to GHz) for the PWM generation system.

To summarize, phase shifters with higher time constants are more suitable for PWM driving and matrix addressing, while high-speed phase shifters are better suited for use as modulators, which is mainly discussed in the next section.

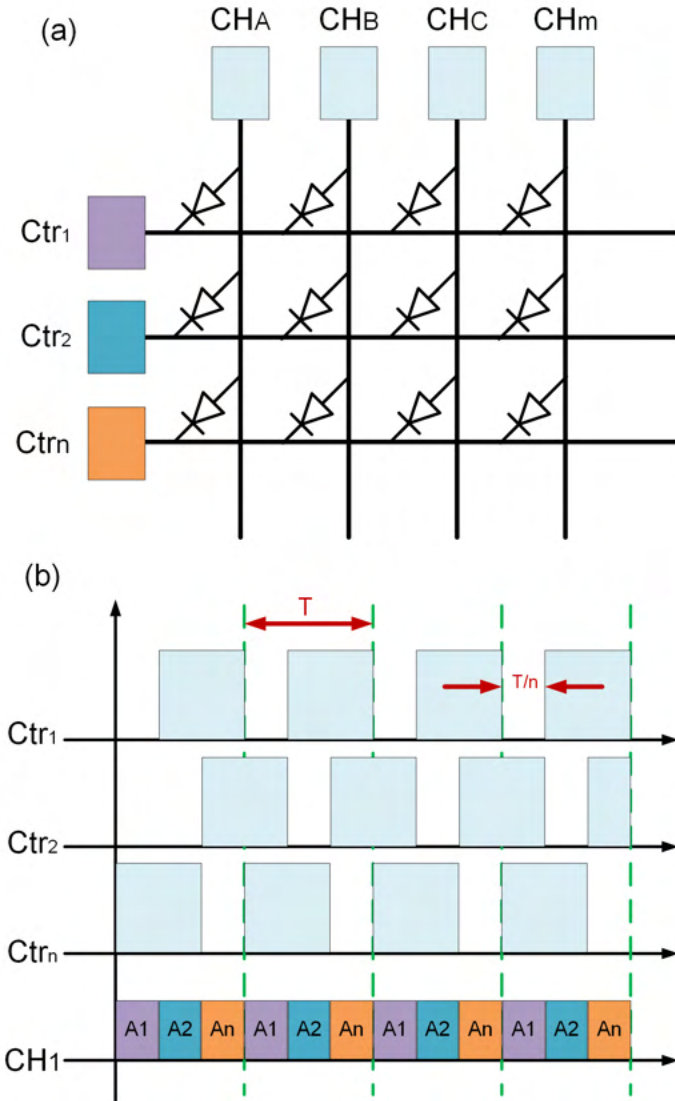


Figure 2.19: Matrix addressing scheme. (a) Schematic of a matrix addressing circuit with m channels and n control lines; (b) Output signals for the control lines and the first channel line

2.2.2 Optical Modulators

Optical modulators play a critical role in photonic systems for imprinting electrical signals onto an optical carrier signal. They are utilized in various applications such as optical communication, sensing, and imaging. Optical modulators are classified into two primary categories: phase modulators and intensity modulators, depending on their mode of operation. Optical phase modulation involves fast phase shifting, as illustrated in Fig. 2.4. Meanwhile, optical intensity modulators can be achieved through phase-to-intensity mapping using interferometers with phase modulators, or plasma absorption effects, Franz-Keldysh effect and quantum-confined stark effect which directly change the intensity of light. In this section, we will mainly focus on modulators based on the plasma dispersion effects, which are the most widely used in silicon photonic circuits. The plasma dispersion effect basically boils down to changing the number of free carriers in the path of the light, which then will affect the phase velocity as well as the absorption.

The most common implementation of such a modulator is by embedding doped regions inside or close to the waveguide core. Shown in Fig. 2.20 are the cross sections of the PN and PIN junctions implemented by doping SKT waveguides. The N plus and P plus layers define a high density but shallow doping, while the N/P body layers define a deep and medium density doping, and the N and P layers are slightly doped. By forward or reversed biasing the PN and PIN junctions, carrier injection or depletion can be achieved, modulating the effective refractive index (n_{eff}) of the waveguide. This is known as the carrier dispersion effect, and the relationship between the carrier density and n_{eff} can be expressed as follows [20]:

$$\Delta n_{\text{eff}} = -5.4 \times 10^{-22} \Delta N^{1.011} - 1.53 \times 10^{-18} \Delta P^{0.838} \quad (2.13)$$

where ΔN and ΔP are the carrier densities of electrons and holes [cm^{-3}]. The carrier densities can be obtained from simulation tools like Lumerical Device or TCAD from Silvaco. In addition, the propagation loss of the doped waveguide is

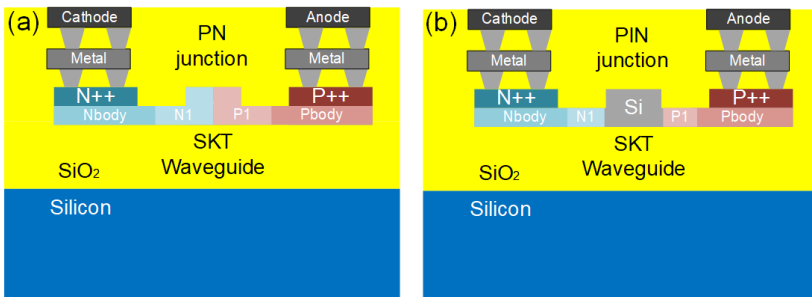


Figure 2.20: PN junction (a) and PIN junction (b)

also related to the carrier density, which can be expressed as:

$$\Delta\alpha = 8.88 \times 10^{-21} \Delta N^{1.167} + 5.84 \times 10^{-20} \Delta P^{1.109} \quad (2.14)$$

Due to the difference in doping levels in the waveguide core, PN junction-based modulators are typically operated in carrier depletion mode, while PIN junction-based modulators are typically operated in injection mode. Carrier depletion is commonly faster (40 GHz) and weaker, while the injection is slower (10 GHz) and stronger. The reason is that the injection modulator dumps a large number of carriers in the intrinsic region, but is limited by recombination times. And the depletion modulator only moves carriers, but the number of available carriers is limited. Fig. 2.21 shows experimental phase and intensity modulation results for a PN and a PIN modulator [21, 22]. The phase change introduced by a phase modulator with a length L can be expressed as:

$$\Delta\phi = \frac{2\pi\Delta n_{\text{eff}}L}{\lambda} \quad (2.15)$$

A FOM of a phase modulator can be the $V_{\pi}L$, where V_{π} is the biased voltage for π phase shift.

By embedding the phase modulators into interferometers, the phase changes introduced by the modulator can be converted into intensity variations, achieving intensity modulation. Different types of interferometers can be used for this purpose, such as MZIs, microrings [23], waveguide Bragg gratings [24, 25], or their combination [26]. Among these, MZMs do not rely on any cavity and can work at all wavelengths, but their modulation strength is relatively low, requiring long modulator lengths (1 to 4 mm). This large footprint becomes a challenge for the RF design of the electrodes and limits the modulation bandwidth of the MZM. A travelling wave MZM can reach up to 45 GHz bandwidth [27], while a lumped MZM can reach 25 GHz [28]. Additionally, the RF termination must be fixed at 50 ohms, which can become a significant heat source when reverse-biasing the PN junction. Microring modulators (MRMs) offer a compact footprint due to their ring cavity. However, they can only operate near resonant wavelengths. And also, MRMs are highly sensitive to temperature variations and even the power of the modulation signal, which requires the use of a feedback control loop to maintain stable operation [29]. Despite these challenges, MRMs have been demonstrated with high-speed modulation up to 50 GHz, making them promising candidates for next-generation photonic systems [30].

In Chapter 4, we will delve into the RF modulation response of the phase modulators and intensity modulators, and discuss ways to optimize them in Chapter 5. However, before that, it is important to introduce the photodiodes and monitors used in silicon photonic circuits, which are critical components for detecting and converting optical signals into electrical signals.

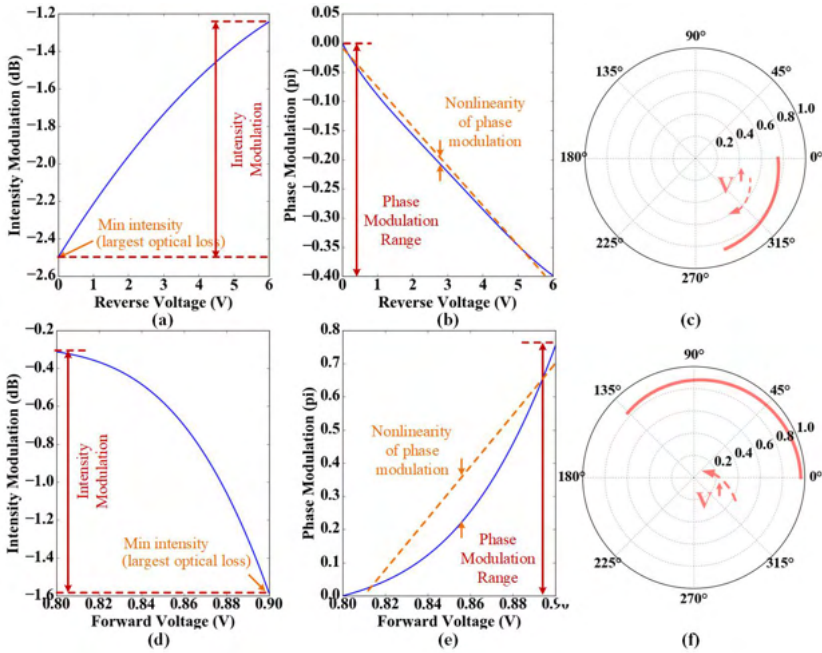


Figure 2.21: (a) Measured intensity modulation and (b) phase modulation response of the used depletion modulator model (0 V to 6 V) [22]; (c) modulation curve of the depletion modulator in polar diagram (0 V to 6 V);(d) Measured intensity modulation and (e) phase modulation response of the used injection modulator model (0.8 V to 0.96 V); (f) modulation curve of the injection modulator in polar diagram (0.8 V to 0.9 V);

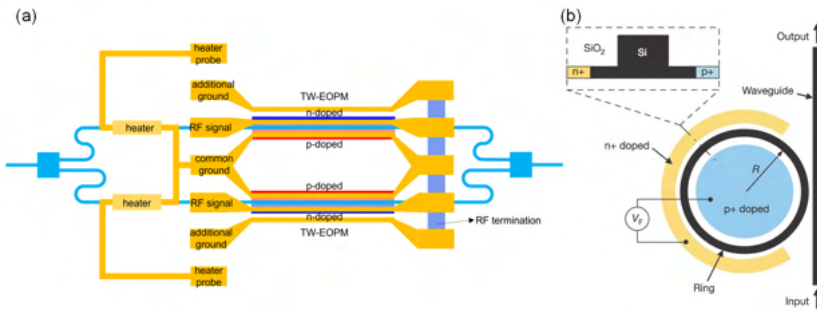


Figure 2.22: (a) An double driven MZ modulator. (b) A microring modulator

2.2.3 Photodiodes and Monitors

Photodiodes typically serve as the final component in photonic links, responsible for the conversion of optical power information into electrical signals, known as O/E conversion [31]. As signal receivers, photodiodes require higher efficiency, larger bandwidth, and lower noise levels. The imec iSiPP50G platform offers two types of photodiodes: silicon germanium vertical PIN junction and silicon germanium lateral PIN junction, depicted in Fig. 2.23 [32]. Vertical PIN diodes can support a larger bandwidth of up to 50 GHz with an efficiency of 0.8 A/W, while lateral PIN diodes can reach a bandwidth of 25 GHz with 1.1 A/W efficiency. Thus, vertical PIN diodes are ideal for strong and fast signal detection, while lateral PIN diodes are preferable for weak and slower signal detection.

In addition to O/E signal conversion, system monitoring is also critical in large-scale photonic circuits to ensure the proper functioning of the system, detect and diagnose any failures or errors, and optimize the performance of the photonic devices [33]. It enables real-time feedback and control of the system, allowing for adjustments and improvements to be made as needed. An effective way to implement a system monitor is to tap a small portion of light from the main light path and feed it into two photodiodes. A schematic and experimental results are shown in Fig. 2.24. Fig. 2.24 shows a typical design for monitoring the bi-directional optical power in the bus waveguide, which ensures the proper functioning of large-scale photonic circuits. The photodiodes provided in the imec iSiPP50G have two ports, one can be used for the main input and the other can be used for calibration using a grating coupler. We conducted a reference test, and the resulting photo current is plotted in Fig. 2.24(c). The gap of the tap is swept, and the results are shown in Fig. 2.24(d), (e), and (f). The results can help determination of the appropriate tap gap to ensure detectable optical power while keeping the coupling as weak as possible. In this application, the bandwidth of the photodiodes is not critical, but higher efficiency and lower dark current are critical, making a lateral PIN diode the preferred choice.

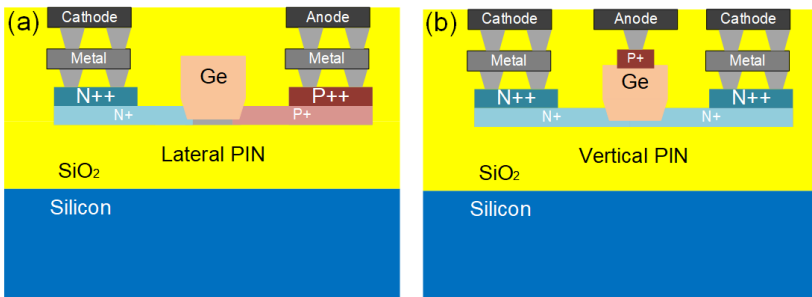


Figure 2.23: Cross section of: (a) A lateral PIN photodiode; (b) A vertical PIN photodiode.

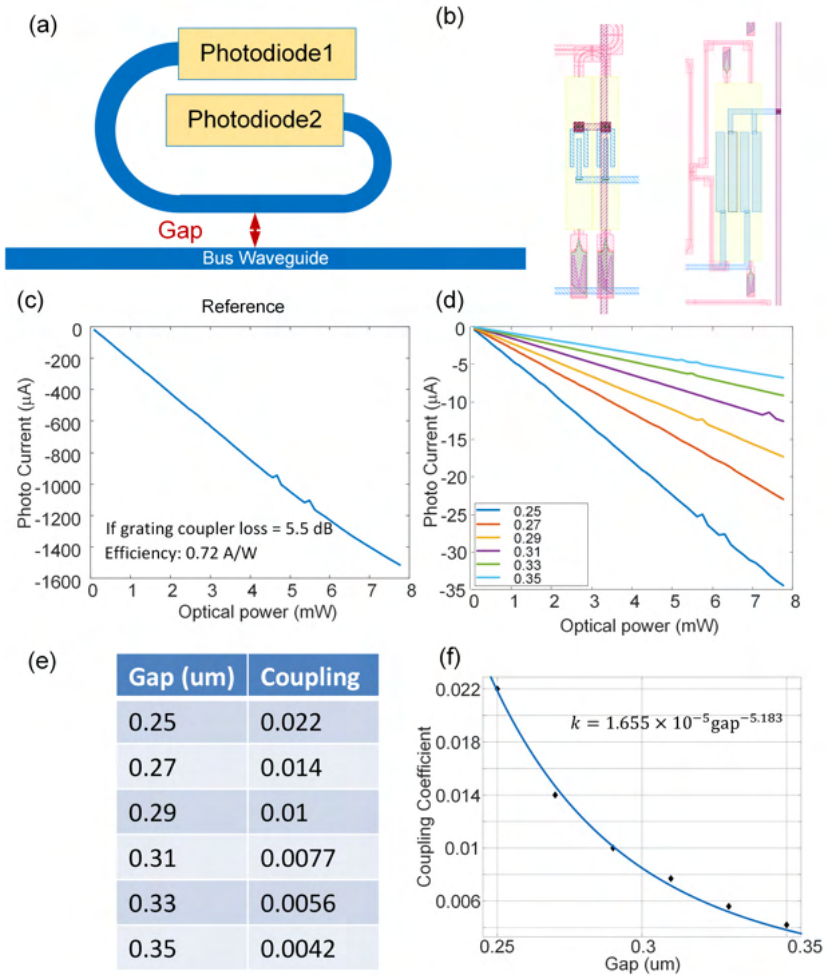


Figure 2.24: Tap monitor tests: (a) A typical tap monitor; (b) a real gds design; (c) photodiode tests with direct grating coupler; (d) photo currents from taps with various gaps (μm); (e) extracted coupling coefficients with different gaps; (f) fitting curve for coupling coefficient vs gaps

The ContactLess Integrated Photonic Probe (CLIPP) is another type of monitor used in silicon photonic circuits. It measures variations in the electric conductance of the waveguide core [34]. However, dedicated electrical readout circuits are required as the signal is weak, and we have not used such devices in our circuits.

Silicon photonic circuits are capable of guiding a light signal through waveguides, imprinting electrical signals onto the light with modulators, manipulating the light with phase shifters, and detecting the light signal with photodiodes. In the next part, we will focus on the laser source hybrid integration on silicon photonic platforms.

2.2.4 Heterogeneous-integrated optical amplifiers

Silicon is an indirect bandgap material, which makes it difficult to provide optical gain or lasing. Therefore, external lasers are often used to characterize photonic circuits, as demonstrated in the previous measurements. However, in mass production, heterogeneous-integrated laser sources are preferred due to their potentially lower cost, smaller footprint, and higher yield. Various integration techniques for laser integration have been proposed, including wafer bonding [35], flip-chip wafer bonding [36], micro-transfer-printing (μ TP) [37], hetero-epitaxial growth [38], and photonic wirebonding [39]. In this section, we will focus on μ TP, which is the integration technique utilized in the main work of this thesis.

Figure 2.26 depicts the schematic of the μ TP process. The stamp is prepared by casting PDMS on a Si master mold that defines post arrays or a single post with the same size and pitch as the device arrays on the source wafer. The stamp is then released from the Si master and laminated on a transparent carrier (glass) wafer. On the III-V source wafer, devices are patterned and protected with an encapsulation layer (usually a photoresist layer), with local openings to access the release layer. The release layer is under etched to release the device. To pick up the device from the native substrate, the PDMS stamp is first aligned and laminated to the desired device or device array and then pulled back at a high velocity, resulting in a relatively high adhesion strength of the device to the stamp, breaking the tethers. The device or device array is then aligned and placed on the target wafer by laminating the stamp to the target wafer and slowly retracting the stamp, resulting in a low adhesion strength between the devices and the stamp. This leaves the device attached to the Si photonics target wafer with the encapsulation layer, either

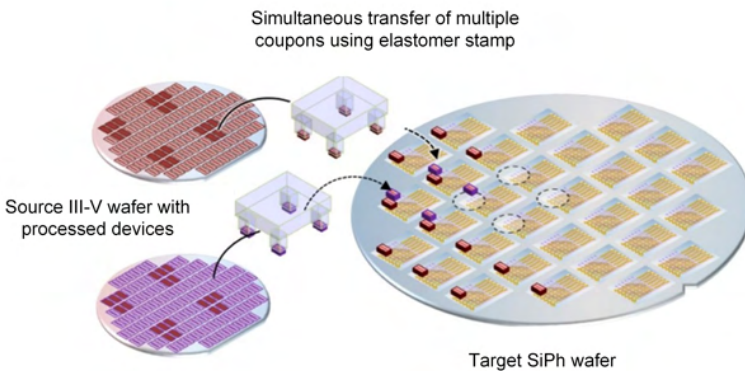


Figure 2.25: Schematic of μ TP-based integration on silicon photonic wafers. Reproduced from [37]

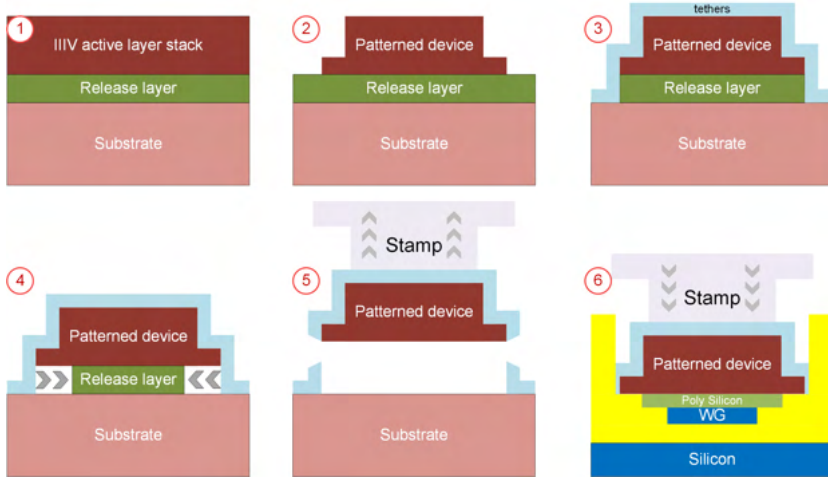


Figure 2.26: Micro-transfer printing work flow: prefabrication of III-V devices on their native substrate and the μ TP integration sequence. Reproduced from [37]

using Van der Waals forces [40] or an adhesive bonding agent [41]. Alignment is achieved by locating the center of co-designed marks on both the source device and the target substrate using a pattern recognition function or eyesight. The process can achieve an alignment accuracy of around $1.5 \mu\text{m}$ when printing devices in large arrays, which can be improved by reducing the array size. The final steps on the Si target wafer involve removing the encapsulation layer and electrically connecting the III-V components to the rest of the circuit.

The transfer printing process for a device onto a bare waveguide is relatively simple, but for the fully stacked iSiPP50G samples from imec, additional post-processing is required. The process flow, as illustrated in Fig. 2.27, involves several steps. First, the LPASS layer of the standard iSiPP50G flow is used in the original design to open a recess for the printed III-V device and the poly silicon layer (normally used for the high-efficiency grating coupler) is designed over the silicon waveguide layer to stack the silicon thickness and facilitate light coupling, as seen in Fig. 2.27(1). Then, using reactive-ion etching and HF etching, the extra silicon dioxide above the silicon waveguide can be removed. After that, a thin layer of benzocyclobutene (BCB) is spray-coated onto the silicon sample as the adhesive bonding agent for the transfer printing process, as shown in Fig. 2.27(2). The III-V device is then printed onto the BCB layer. After printing, the sample experiences an oxygen plasma reactive-ion etching (RIE) etching to remove the tether layer (as previously mentioned), then cured at 280 degrees Celsius. The III-V device is now bonded tightly to the sample, with its electrical ports exposed, as shown in Fig. 2.27(4). Finally, metalization is implemented to connect the III-V

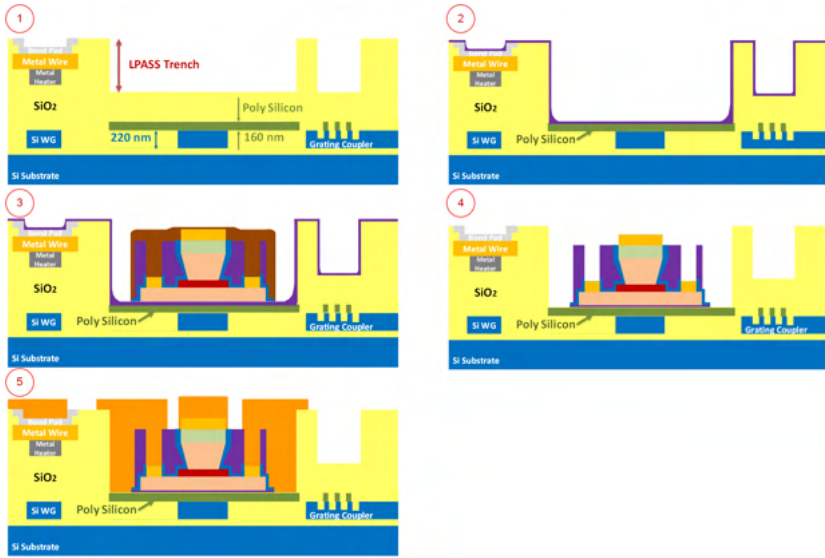


Figure 2.27: Micro-transfer printing work flow: post processing of fully stacked silicon photonic chips

device's electrical ports to the silicon photonic sample's bond pads, as shown in Fig. 2.27(5).

Several III-V semiconductor optical amplifiers (SOAs) have been transfer-printed onto imec iSiPP 50G samples for use as amplifiers or laser sources, and further details and measurement results will be presented in Chapter 7.

So far, all optical components used in this thesis have been introduced. In the next section, we will present the workflow from PIC design to packaging.

2.3 Workflow: from layout to tests

Silicon photonic chips are typically fabricated at research fabs, such as imec (Belgium), AMF (Singapore), AIM photonics (US), and others. One-time fabrication can cost tens of thousands of Euros and take several months to one year's time. Therefore, to achieve more promising results, designers need to be thoughtful during the design stages.

The complete workflow for designing a silicon photonic chip is depicted in Fig. 2.28. It begins with an initial idea, followed by simulations of components and circuits. The simulated circuits are then drawn in a GDS file and fabricated using this file. After a processing time, photonic samples are obtained and can be tested. The testing environment places restrictions on the layout, and the testing results also provide feedback to the initial idea or layout design for the next iteration. Some details will be elaborated below.

Optical device simulation

To build a PIC, the building blocks are the optical components. Often, some of these components are already provided by process design kits (PDK) from fabs. These components have already gone through multiple iterations, and their performance can be obtained from a manual. If a new component is needed and not provided by the PDK, it can be self-designed using simulation tools such as FDTD and EME solvers. These tools allow designers to simulate the behavior of the component (with scatter matrix) and optimize its design parameters before fabrication. It's worth noting that fabrication is never perfect, so component designs should be either robust or can be actively tuned. With the components' scatter matrix, designers can use Lumerical Interconnect or IPKISS Caphe to simulate the whole circuit performance. In our design flow, IPKISS Caphe is a preferred tool due to its tight connection with the physical layout of the circuits. It can expose possible errors in the final physical circuits if the response is not as expected, and allows designers to optimize the design before fabrication.

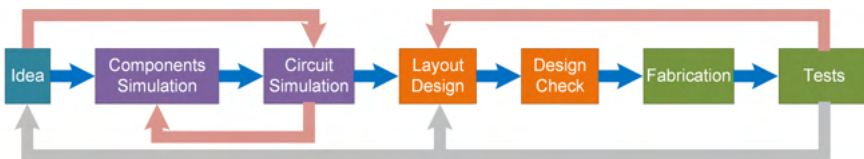


Figure 2.28: Silicon photonic circuit design work flow

Optical and electrical layout design

With all the optical components and their design specifications at hand, designers need to proceed with the layout design of the circuits, including the optical and electrical parts. It is important to note that the fabricated samples may not be available until several months later, the layouts of the samples have to be considered in advance, to ensure that the optical and electrical layouts are compatible with the accessible packaging or measurement setups when the samples arrive.

The general optical layout of a PIC is determined by the used optical components and their optical connection. Connecting waveguides can be standard wire waveguides, which allow for a smaller bend radius, or shallow-etched rib waveguides (FC), which provide lower propagation loss. In some cases, wider multimode wire waveguides (approximately $1\ \mu\text{m}$ width) can also be used to achieve lower insertion loss and lower phase error. The optical input and output (IO) ports depend on the expected packaging and measurement setups. Edge couplers, which have lower loss and higher bandwidth, need to be placed on the sides of the PIC and tested with butt coupling, as shown in Fig. 2.29(a). Grating couplers can be placed freely in the design area, and the light can be coupled vertically to the fiber, as shown in Fig. 2.29(b). However, it should be noted that the fiber probe and its moving stages are bulky, which limits the position of the grating couplers, like they cannot be too close to each other or wire bonds ($\sim 300\ \mu\text{m}$) and they should be on opposite sides if they need to be coupled simultaneously. It is quite challenging to probe more than two fibers to a single chip with normal single-fiber stages. If multiple IOs are required, fiber arrays must be used. In this case, the grating couplers must be positioned regularly following the fiber arrays grid, which is usually $127\ \mu\text{m}$ (but it can be $250\ \mu\text{m}$ or $25\ \mu\text{m}$), as shown in Fig. 2.29(c). A fiber array unit has a width (approximately $2\ \text{mm} + \text{channel_number} \times \text{channel_gap}$) and a thickness (approximately $1\ \text{mm}$ for the substrate and $1\ \text{mm}$ for the lid, and they can be customized), thus it will cover a certain area when aligned with the silicon sample, making it impossible for other probes (optical and electrical) to access the covered area.

The electrical layout of the PIC can be divided into two main parts: RF routing and DC routing. RF routing is used to connect high-speed components such as modulators and photodiodes, and requires short lines to minimize signal loss, parasitic reflections and coupling. RF bond pads also need to match the pitch of expected RF probes, which is typically $100\ \mu\text{m}$. If the RF bond pads are going to be wirebonded and packaged, they should be positioned on the edges of the sample to minimize the length of the bonding wire. In addition to RF routing, DC routing is used for the connections of low speed components like thermo-optic phase shifters and monitors. The DC routing lines can be longer than RF routing lines and they can be placed either on the edges or inside the sample. When wirebonding the DC pads, it is recommended to position them at the edges of the PIC, with

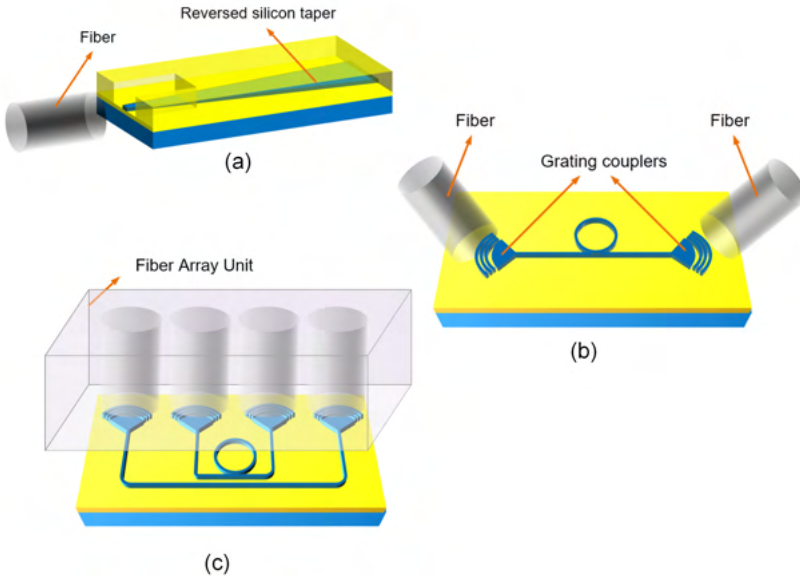


Figure 2.29: Optical coupling schemes: (a) Butt coupling between fibers and edge couplers; (b) vertical coupling between fibers and grating couplers; (c) vertical coupling between fiber array units and grating couplers

a minimum pitch of $100\ \mu\text{m}$. However, a pitch of $200\ \mu\text{m}$ is preferred to avoid fanout of bonding wire to the pads of the printed circuit board (PCB). Finally, it is important to ensure that bond pads are placed at least $300\ \mu\text{m}$ away from grating couplers or fiber array blocks to avoid any conflicts.

In PIC layout design, it is important to consider potential source of crosstalk such as optical, thermal, and electrical coupling. For example, transfer printed lasers are sensitive to all reflections from the entire optical circuit due to the lack of on-chip optical isolators. Therefore, it is recommended to design all components along the optical path with low optical reflection, such as using directional couplers instead of MMIs and low-reflection grating couplers instead of high-efficiency ones.

Some on-chip components, such as the terminations of travelling wave MZM and transfer printed semiconductor optical amplifiers (SOAs), can dissipate a significant amount of electrical power and generate heat in their surrounding areas. As a result, they should be placed far away from thermally sensitive elements like micro rings. While ground pad sharing can reduce the number of bond pads, ground wires can also introduce thermal and electrical crosstalk. Therefore, it is recommended to isolate the ground line for power elements (lasers, phase shifters) and sensitive elements (monitors).

Finally, after spending a considerable amount of time fixing and optimizing the layout, it can be easy to overlook basic errors such as missing waveguides or bond pad overlays. Therefore, it is critical to check the global layout from inputs to outputs before submitting the design.

The submitted design will be merged with other designs to fill a reticle in a multi-project wafer (MPW) run of iSiPP50G. Global density check will also be implemented with the full map. After cleaning all the errors, we can submit the final design and wait for the fabricated samples.

Packaging

Once the sample is received, the next step is to plan the measurement setup. For large-scale samples with multiple optical IOs and numerous electrical connections, it is better to package the sample for robust measurement. This includes optical packaging, electrical packaging, and thermal packaging.

Optical packaging can be accomplished using fibers and fiber array units. These can be either vertically or horizontally glued onto the silicon photonic samples, with precise alignment to the grating coupler(s), as shown in Fig. 2.30. Single fiber gluing requires carefully polished fibers or specifically designed fiber holders, which can be time-consuming and inconvenient to prepare. In contrast, 8 degree polished or 41.5 degree polished fiber arrays have been widely used in industry and are easier to cure due to their self-supporting structure, as shown in Fig. 2.30 (c) and (d).

There are advantages and disadvantages to using 41.5 degree polished (c) or 8 degree polished fiber arrays (d) for optical packaging. Horizontally glued fiber arrays have a larger contact surface with the silicon chip, making the connection much stronger than the vertical one. However, the 41.5 degree polished fiber array relies on total internal reflection on the polished surface, so the reflecting facet surface must remain clean, otherwise, light will be lost on the fiber array surface. Meanwhile, vertically glued 8 degree polished fiber arrays can be fully immersed in epoxy, allowing for extra epoxy to be added to encapsulate other components such as bonding wires. Therefore, the choice of which fiber array to use depends on the packaging requirements. If there are fragile bonding wires and no further probing is needed, vertical curing is preferred. If there is a need for extra probing, such as RF probing, or no extra wires to be protected, curing a horizontal fiber array is a better choice. It should be noted that the use of 41.5 degree polished fiber array will cover one side of the silicon sample, while an 8 degree polished fiber array can be cured vertically.

In our process, we use NOA 63 UV glue for the curing. The curing process for 8 degree polished fiber arrays is straightforward - align the fiber array, drop the UV glue, and cure it with a UV lamp. However, the viscosity of the glue makes it

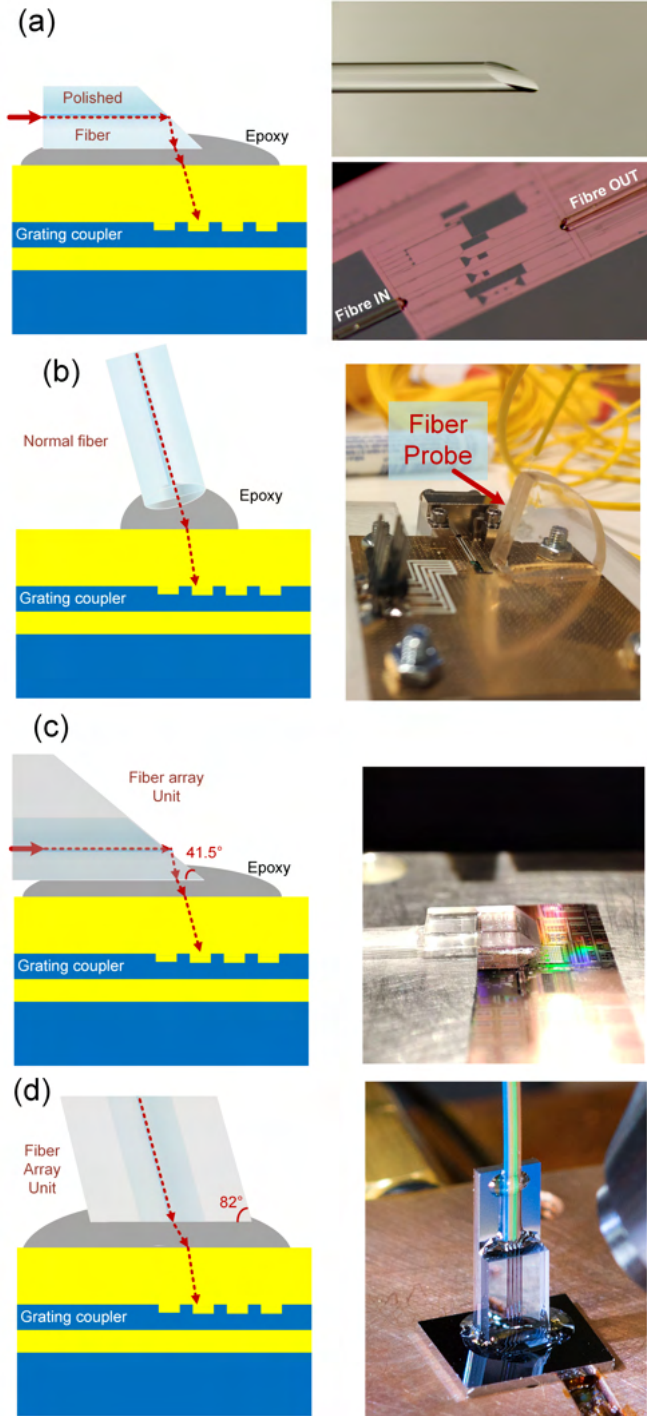


Figure 2.30: Vertical coupling packaging schemes: (a) and (b) Fiber glued horizontally and vertically; (c) and (d) fiber array glued horizontally and vertically.

difficult to control the spreading area, as the minimum drop size for dispensing is large. To address this, we use a method shown in Fig. 2.31 to glue the fiber array with a smaller spreading area. The method involves scratching a small amount of glue onto the back of the fiber array (Fig. 2.31 (3)), which will eventually fill the gap thanks to capillarity (Fig. 2.31(6) and (7)). The glue is then cured with a UV lamp, with a limited spreading distance of around $200\ \mu\text{m}$ (Fig. 2.31(8)). However, this curing process is fragile due to the small contact area. 41.5 degree polished fiber arrays can be bonded much stronger. For them, the UV glue can be dropped on the side of the fiber array, and it will fill the gap. Make sure not to use too much glue as it can immerse the fiber facets and break the total internal reflection. During the curing, the fiber array unit will drift a little bit, due to the glue's curing tensing and exothermic reaction. Thus, we can re-align the fiber array to compensated the drift in the first several seconds (before the glue is fully cured), and shine the UV light off and on, to release the tension and cool down the sample as well. A cured fiber array insertion loss with reference waveguide is shown in Fig. 2.33(a).

Electrical packaging can present a challenge as the number of DC bond pads and RF connectors increase with the scale up of PICs. To fan out the electrical pads on the sample, wire bonding is the most common method used. Metal wires are used to connect the pads on the chip to the pads on a PCB. DC bondpads can be wire-bonded to normal PCBs with FR-4 substrates (fiberglass cloth, flame retardant), which is easy to access. In addition, the normal clearance distance for PCB fabrication is 4 mils (100mm), with a 3 mils (75mm) clearance distance available at a higher cost. A normal FR-4 based PCB is usually used for low speed applications ($<10\ \text{GHz}$), while high-level materials like Rogers or Megtron can be used to fabricate high-speed PCBs at a much higher cost [42].

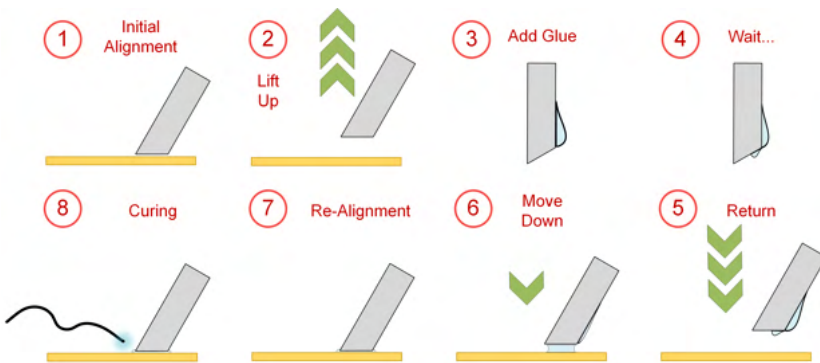


Figure 2.31: Fiber array curing process with small glue spreading

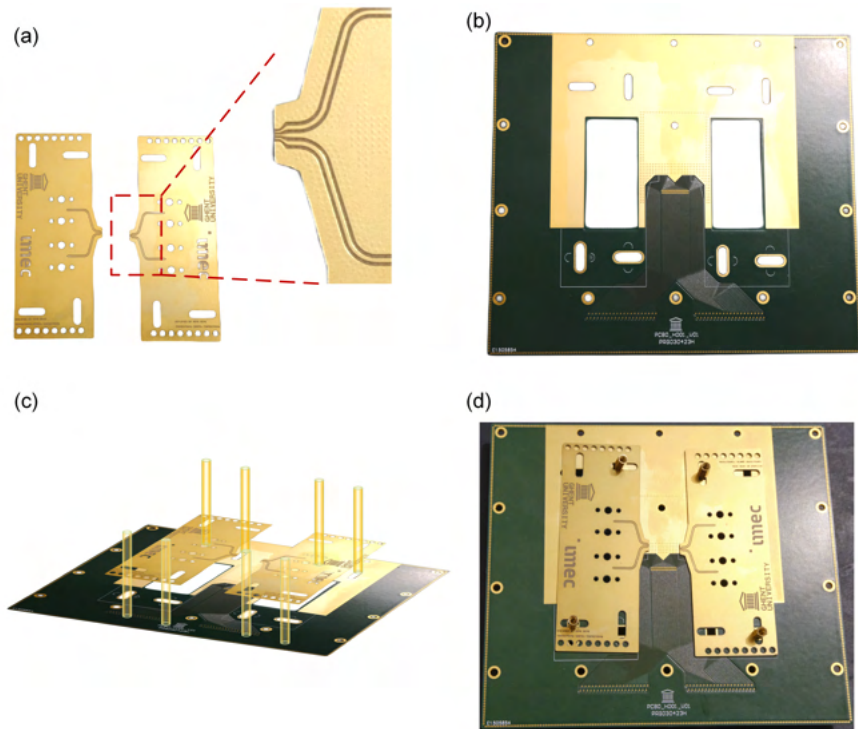


Figure 2.32: Assembled RF-DC PCB. (a) RF daughter PCB; (b) DC mother PCB; (c) and (d) Assembled RF-DC PCB.

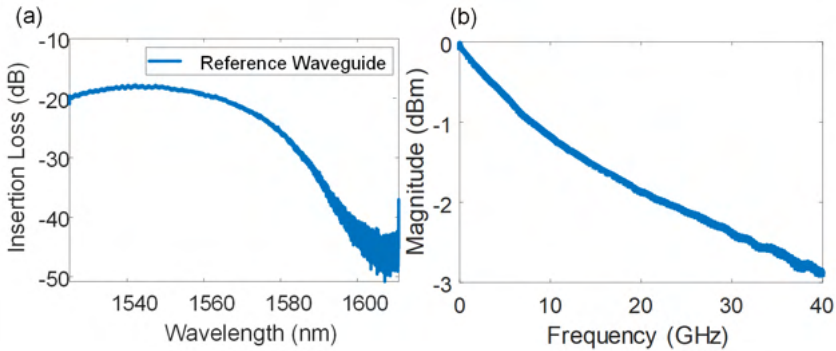


Figure 2.33: (a) UV cured fiber array insertion loss with reference waveguide; (b) reference RF transmission line frequency response

PCB design Normally, a PCB is designed specifically for packaging one photonic circuit. This makes the RF PCB quite costly. To provide a more generic solution and reuse the RF PCB, we propose that the DC PCB can function as a motherboard while the RF PCBs function as daughter-boards, as shown in Fig. 2.32. With this approach, the DC PCB can be designed for a specific PIC while the RF PCB can be screwed on top of the DC PCB for additional RF wire bonding. The RF PCB is designed slightly thinner than the normal photonic chips ($740\ \mu\text{m}$ vs $800\ \mu\text{m}$) to minimize the length of bonding wires. It is fabricated using Megtron 6 materials, while the transmission line is designed as a coplanar waveguide with ground. The copper width and clearance are simulated using PathWave Advanced Design System (ADS) from Keysight. Rosenberger solderless RF connectors are used for the single RF connector, and TR70 from Ardent Concepts can be used for the multi channel RF connectors. Both connectors are solderless and can be reused. A reference RF transmission line test was implemented and it shows that the line has 3 dB loss at 40 GHz with a length of 5 cm, as shown in Fig. 2.33(b).

Thermal packaging Active components such as thermal phase shifters, modulators, and transfer printed SOAs can generate a significant amount of heat on the silicon chip. To address this, thermal vias are incorporated into the design of the DC PCB to improve heat dissipation. In addition, a temperature controller (TEC) with Peltier effect is required to maintain a stable temperature during the measurement process.

Once the sample is fully packaged, it is ready for future testing with improved stability and repeatability. A packaged fully on-chip silicon photonic microwave processor in the Fig. 2.34 as a demo. Before diving into the experimental results, Let's move on to the principles behind the device.

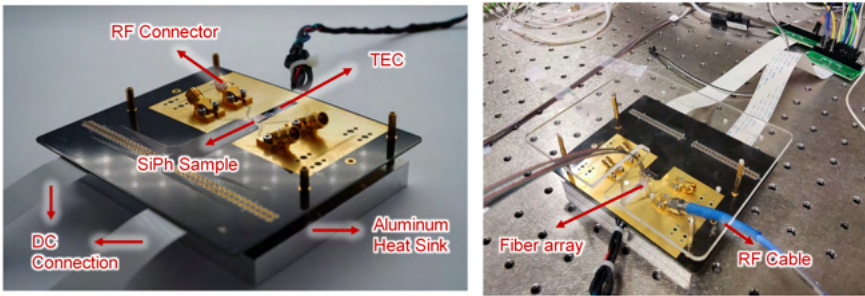


Figure 2.34: Fully packaged silicon photonic sample

2.4 Conclusion

We provided an overview of the key components utilized in our silicon photonic circuits, including an introduction to basic devices such as waveguides, couplers, and active tuning elements such as phase shifters, modulators, and photodiodes, tapped monitors, as well as heterogeneous integrated optical amplifiers.

In optical waveguides, we introduced ridge WG waveguides, SKT rib waveguides and FC rib waveguides, in which WG waveguides have the highest confinement and the FC waveguides enjoy the lowest optical propagation loss. In optical power couplers, DC, MMI and adiabatic couplers were introduced.

As one key component of the silicon photonic circuits, phase shifters were elaborated in this chapter. We explored metal tungsten heaters, doped side heaters and doped SKT waveguide heaters, and we measured their thermal efficiency, time constants and frequency responses. Heaters with undercut process and top-etching process were also characterized, for higher thermal efficiency. Heater driving systems with DC power source, PWM driving and matrix addressing were discussed.

To imprint high-speed signals onto optical carriers, PN junction based phase modulators were introduced. Based on these, MZ modulators and micro-ring modulators, as intensity modulators, were discussed. A reconfigurable modulator design will be introduced in Chapter 5. To recover the high-speed signal, high speed PDs were induced. And these PDs can also be used to monitor the whole integrated photonic circuits.

Micro-transfer printing technology for heterogeneous integration of optical amplifiers in silicon platforms was presented, to introduce optical gain in silicon photonic circuits. Processed SOAs and laser units will be elaborated in Chapter 6.

Finally, we provided the whole workflow for this thesis work, covering the simulation, layout, and packaging solutions utilized in our silicon photonic circuits. In order to get a robust demonstrator, we showed a process of fiber array curing, for optical packaging, a generic design of RF PCB, for electrical packaging, and full TEC integration, for thermal packaging.

References

- [1] G. T. Reed and A. P. Knights, *Silicon photonics : an introduction*. John Wiley, 2004.
- [2] A. Rizzo, A. Rizzo, U. Dave, A. Novick, A. Freitas, S. P. Roberts, A. James, M. Lipson, and K. Bergman, "Fabrication-robust silicon photonic devices in standard sub-micron silicon-on-insulator processes," *Optics Letters*, Vol. 48, Issue 2, pp. 215-218, vol. 48, pp. 215–218, 1 2023.
- [3] D. Adams, G. Madejski, and S. Preble, "High-Q shallow etch silicon micro resonators for optical delay," *IEEE Photonic Society 24th Annual Meeting, PHO 2011*, pp. 871–872, 2011.
- [4] H. Deng, W. Zhang, and J. Yao, "High-speed and high-resolution interrogation of a silicon photonic microdisk sensor based on microwave photonic filtering," *Journal of Lightwave Technology*, vol. 36, pp. 4243–4249, 10 2018.
- [5] s. k. Selvaraja, W. Bogaerts, P. Absil, D. Van Thourhout, and R. Baets, "Record low-loss hybrid rib/wire waveguides for silicon photonic circuits," *Group IV Photonics, 7th International conference, Proceedings*, 2010.
- [6] P. Cheben, R. Halir, J. H. Schmid, H. A. Atwater, and D. R. Smith, "Sub-wavelength integrated photonics," *Nature 2018 560:7720*, vol. 560, pp. 565–572, 8 2018.
- [7] A. Yariv, "Coupled-Mode theory for guided-wave optics," *IEEE Journal of Quantum Electronics*, vol. 9, no. 9, pp. 919–933, 1973.
- [8] L. B. Soldano and E. C. Pennings, "Optical Multi-Mode Interference Devices Based on Self-Imaging: Principles and Applications," *Journal of Lightwave Technology*, vol. 13, no. 4, pp. 615–627, 1995.
- [9] S. Darmawan, C. W. Lee, S. Y. Lee, and M. K. Chin, "A rigorous comparative analysis of directional couplers and multimode interferometers based on ridge waveguides," *IEEE Journal on Selected Topics in Quantum Electronics*, vol. 11, pp. 466–475, 3 2005.
- [10] T. A. Ramadan, R. Scarmozzino, and R. M. Osgood, "Adiabatic couplers: Design rules and optimization," *Journal of Lightwave Technology*, vol. 16, pp. 277–283, 2 1998.
- [11] D. Mao, M. S. Alam, J. Zhang, M. Zhu, P. C. Koh, D. V. Plant, Y. Wang, E. El-Fiky, L. Xu, A. Kumar, M. Jaques, A. Samani, O. Carpentier, and S. Bernal, "Adiabatic Coupler with Design-Intended Splitting Ratio," *Journal of Lightwave Technology*, vol. 37, pp. 6147–6155, 12 2019.

- [12] H. Yun, F. Zhang, Y. Wang, L. Chrostowski, N. A. F. Jaeger, Z. Lu, and S. Lin, "Broadband 2×2 adiabatic 3dB coupler using silicon-on-insulator sub-wavelength grating waveguides," *Optics Letters*, Vol. 41, Issue 13, pp. 3041-3044, vol. 41, pp. 3041–3044, 7 2016.
- [13] H. Sun, Q. Qiao, Q. Guan, and G. Zhou, "Silicon Photonic Phase Shifters and Their Applications: A Review," *Micromachines* 2022, Vol. 13, Page 1509, vol. 13, p. 1509, 9 2022.
- [14] A. Masood, M. Pantouvaki, D. Goossens, G. Lepage, P. Verheyen, J. Van Campenhout, P. Absil, D. Van Thourhout, and W. Bogaerts, "Fabrication and characterization of CMOS-compatible integrated tungsten heaters for thermo-optic tuning in silicon photonics devices," *Optical Materials Express*, vol. 4, p. 1383, 7 2014.
- [15] N. C. Harris, Y. Ma, J. Mower, T. Baehr-Jones, D. Englund, M. Hochberg, and C. Galland, "Efficient, compact and low loss thermo-optic phase shifter in silicon," *Optics Express*, vol. 22, p. 10487, 5 2014.
- [16] S. Liu, J. Feng, Y. Tian, H. Zhao, L. Jin, B. Ouyang, J. Zhu, and J. Guo, "Thermo-optic phase shifters based on silicon-on-insulator platform: state-of-the-art and a review," *Frontiers of Optoelectronics*, vol. 15, pp. 1–21, 12 2022.
- [17] Z. Lu, K. Murray, H. Jayatilaka, and L. Chrostowski, "Michelson Interferometer Thermo-Optic Switch on SOI with a 50- μ W Power Consumption," *IEEE Photonics Technology Letters*, vol. 27, pp. 2319–2322, 11 2015.
- [18] A. Ribeiro, S. Declercq, U. Khan, M. Wang, L. V. Iseghem, and W. Bogaerts, "Column-Row Addressing of Thermo-Optic Phase Shifters for Controlling Large Silicon Photonic Circuits," *IEEE Journal of Selected Topics in Quantum Electronics*, vol. 26, 9 2020.
- [19] A. R. Alves Júnior, U. Khan, and W. Bogaerts, "Matrix addressing silicon photonics phase shifters using heaters with integrated diodes," *European Conference on Integrated Optics (ECIO'2018)*, pp. 63–65, 2018.
- [20] M. Nedeljkovic, R. Soref, and G. Z. Mashanovich, "Free-carrier electrorefraction and electroabsorption modulation predictions for silicon over the 1-14- μ m infrared wavelength range," *IEEE Photonics Journal*, vol. 3, pp. 1171–1180, 12 2011.
- [21] H. Deng and W. Bogaerts, "Pure phase modulation based on a silicon plasma dispersion modulator," *Optics Express*, vol. 27, p. 27191, 9 2019.

- [22] H. Yu, M. Pantouvaki, J. V. Campenhout, D. Korn, K. Komorowska, P. Dumon, Y. Li, P. Verheyen, P. Absil, L. Alloatti, D. Hillerkuss, J. Leuthold, R. Baets, and W. Bogaerts, "Performance tradeoff between lateral and interdigitated doping patterns for high speed carrier-depletion based silicon modulators," *Optics Express*, vol. 20, p. 12926, 6 2012.
- [23] Q. Xu, B. Schmidt, S. Pradhan, and M. Lipson, "Micrometre-scale silicon electro-optic modulator," *Nature* 2005 435:7040, vol. 435, pp. 325–327, 5 2005.
- [24] O. Jafari, H. Sepehrian, W. Shi, and S. Larochele, "High-Efficiency Silicon Photonic Modulator Using Coupled Bragg Grating Resonators," *Journal of Lightwave Technology*, vol. 37, pp. 2065–2075, 5 2019.
- [25] C. Han, Z. Zheng, H. Shu, M. Jin, J. Qin, R. Chen, Y. Tao, B. Shen, B. Bai, F. Yang, Y. Wang, H. Wang, F. Wang, Z. Zhang, S. Yu, C. Peng, and X. Wang, "Slow-light silicon modulator with 110-GHz bandwidth," *Science Advances*, vol. 9, 10 2023.
- [26] R. Li, D. Patel, A. Samani, E. El-Fiky, Z. Xing, M. Sowailem, Q. Zhong, and D. V. Plant, "An 80 Gb/s Silicon Photonic Modulator Based on the Principle of Overlapped Resonances," *IEEE Photonics Journal*, vol. 9, 6 2017.
- [27] M. S. Alam, X. Li, M. Jacques, Z. Xing, A. Samani, E. El-Fiky, P. C. Koh, and D. Plant, "Net 220 Gbps/ λ IM/DD Transmssion in O-Band and C-Band with Silicon Photonic Traveling-Wave MZM," *Journal of Lightwave Technology*, vol. 39, pp. 4270–4278, 7 2021.
- [28] G. Cong, Y. Maegami, M. Ohno, and K. Yamada, "Ultra-compact Non-travelling-wave Silicon Carrier-depletion Mach-Zehnder Modulators Towards High Channel Density Integration," *IEEE Journal of Selected Topics in Quantum Electronics*, pp. 1–1, 2020.
- [29] X. Zheng, E. Chang, P. Amberg, I. Shubin, J. Lexau, F. Liu, H. Thacker, S. S. Djordjevic, S. Lin, Y. Luo, J. Yao, J.-H. Lee, K. Raj, R. Ho, J. E. Cunningham, and A. V. Krishnamoorthy, "A high-speed, tunable silicon photonic ring modulator integrated with ultra-efficient active wavelength control," *Optics express*, vol. 22, p. 12628, 5 2014.
- [30] J. Sun, R. Kumar, M. Sakib, J. B. Driscoll, H. Jayatilika, and H. Rong, "A 128 Gb/s PAM4 Silicon Microring Modulator With Integrated Thermo-Optic Resonance Tuning," *Journal of Lightwave Technology*, vol. 37, pp. 110–115, 1 2019.
- [31] M. Piels and J. E. Bowers, "Photodetectors for silicon photonic integrated circuits," *Photodetectors*, pp. 419–436, 1 2023.

- [32] F. Ferraro, P. De Heyn, M. Kim, N. Rajasekaran, M. Berciano, G. Muliuk, D. Bode, G. Lepage, S. Janssen, R. Magdziak, J. De Coster, H. Kobbi, S. Lardenois, N. Golshani, L. Shiramin, C. Marchese, S. Rajmohan, S. Nadarajan, N. Singh, S. Radhakrishnan, A. Tsiara, P. Xu, A. Karagoz, D. Yudistira, M. Martire, A. H. Shahar, M. Chakrabarti, D. Velenis, W. Guo, A. Miller, K. Croes, S. Balakrishnan, P. Verheyen, Y. Ban, J. Van Campenhout, and P. P. Absil, “Imec silicon photonics platforms: performance overview and roadmap,” <https://doi.org/10.1117/12.2650579>, vol. 12429, pp. 22–28, 3 2023.
- [33] P. Dumais, D. J. Goodwill, D. Celo, J. Jiang, C. Zhang, F. Zhao, X. Tu, C. Zhang, S. Yan, J. He, M. Li, W. Liu, Y. Wei, D. Geng, H. Mehrvar, and E. Bernier, “Silicon Photonic Switch Subsystem with 900 Monolithically Integrated Calibration Photodiodes and 64-Fiber Package,” *Journal of Lightwave Technology*, vol. 36, pp. 233–238, 1 2018.
- [34] S. Grillanda, M. Carminati, F. Morichetti, P. Ciccarella, A. Annoni, G. Ferrari, M. Strain, M. Sorel, M. Sampietro, and A. Melloni, “Non-invasive monitoring and control in silicon photonics using CMOS integrated electronics,” *Optica*, Vol. 1, Issue 3, pp. 129-136, vol. 1, pp. 129–136, 9 2014.
- [35] G. Roelkens, J. Van Campenhout, J. Brouckaert, D. Van Thourhout, R. Baets, P. R. Romeo, P. Regreny, A. Kazmierczak, C. Seassal, X. Letartre, G. Hollinger, J. M. Fedeli, L. Di Cioccio, and C. Lagahe-Blanchard, “III-V/Si photonics by die-to-wafer bonding,” *Materials Today*, vol. 10, pp. 36–43, 7 2007.
- [36] T. Matsumoto, T. Kurahashi, R. Konoike, K. Suzuki, K. Tanizawa, A. Uetake, K. Takabayashi, K. Ikeda, H. Kawashima, S. Akiyama, and S. Sekiguchi, “Hybrid-integration of SOA on silicon photonics platform based on flip-chip bonding,” *Journal of Lightwave Technology*, vol. 37, pp. 307–313, 1 2019.
- [37] J. Zhang, G. Muliuk, J. Juvert, S. Kumari, J. Goyvaerts, B. Haq, C. Op De Beeck, B. Kuyken, G. Morthier, D. Van Thourhout, R. Baets, G. Lepage, P. Verheyen, J. Van Campenhout, A. Gocalinska, J. O’Callaghan, E. Pelucchi, K. Thomas, B. Corbett, A. J. Trindade, and G. Roelkens, “III-V-on-Si photonic integrated circuits realized using micro-transfer-printing,” *APL Photonics*, vol. 4, p. 110803, 11 2019.
- [38] A. Y. Liu and J. Bowers, “Photonic integration with epitaxial III-V on silicon,” *IEEE Journal of Selected Topics in Quantum Electronics*, vol. 24, 11 2018.
- [39] N. Lindenmann, P. Marin-Palomo, M. R. Billah, C. Koos, A. Nestic, M. Blaicher, M. Moehrle, T. Hoose, P.-I. Dietrich, S. Randel, A. Hofmann,

- U. Troppenz, and W. Freude, “Hybrid integration of silicon photonics circuits and InP lasers by photonic wire bonding,” *Optica*, Vol. 5, Issue 7, pp. 876–883, vol. 5, pp. 876–883, 7 2018.
- [40] J. Justice, C. Bower, M. Meitl, M. B. Mooney, M. A. Gubbins, and B. Corbett, “Wafer-scale integration of group III–V lasers on silicon using transfer printing of epitaxial layers,” *Nature Photonics* 2012 6:9, vol. 6, pp. 610–614, 8 2012.
- [41] A. De Groote, P. Cardile, A. Z. Subramanian, A. M. Fecioru, C. Bower, D. Delbeke, R. Baets, u. Roelkens, G. Roelkens, A. Abbasi, P. Cardile, U. Dave, A. De Groote, Y. de Koninck, S. Dhoore, X. Fu, A. Gassenq, N. Hattasan, Q. Huang, S. Kumari, S. Keyvaninia, B. Kuyken, L. Li, P. Mechet, M. Muneeb, D. Sanchez, H. Shao, T. Spuesens, A. Subramanian, S. Uvin, M. Tassaert, K. Van Gasse, J. Verbist, R. Wang, Z. Wang, J. Van Campenhout, X. Yin, J. Bauwelinck, G. Morthier, R. Baets, D. Van Thourhout, E. Menard, K. Lee, D.-y. Khang, R. Nuzzo, J. Rogers, H. Yang, D. Zhao, S. Chuwongin, J.-h. Seo, W. Yang, Y. Shuai, J. Berggren, M. Hammar, Z. Ma, W. Zhou, A. Trindade, B. Guilhabert, D. Massoubre, D. Zhu, N. Laurand, E. Gu, I. Watson, C. J. Humphreys, and M. Daw, “Transfer-printing-based integration of single-mode waveguide-coupled III-V-on-silicon broadband light emitters,” *Optics Express*, Vol. 24, Issue 13, pp. 13754–13762, vol. 24, pp. 13754–13762, 6 2016.
- [42] “What PCB material do I need to use for RF? - EDN.”

3

Silicon Photonic Optical Filters

In this chapter, we will provide an overview of the most widely used optical filters in Silicon photonics. These include basic filters like waveguide Bragg gratings, MZIs, micro-ring resonators, and their combinations, such as double-stage MZIs, tunable ring resonators, and ring loaded MZIs. Specifically, we will focus on a ring-loaded MZI structure, which can be regarded as a first-order arbitrary optical filter. Moreover, a four-ring-loaded MZI with tunable couplers, as an optical filter block in the signal processor, is elaborated and its characterization results are shown.

3.1 Basic silicon photonic optical filters

Optical filters play a critical role in selecting specific wavelengths or frequencies from a broader spectrum of light, which are essential for optical communications and sensing systems. In general, an optical filter can be fully defined by its frequency response, which shows how the amplitude and phase of each frequency component of an incoming signal is affected by the filter [1]. In silicon photonic circuits, there are several types of filters commonly used, including waveguide Bragg gratings, MZIs, micro ring resonators, and arrayed waveguide gratings. These filters can be combined to achieve more complex frequency responses. This section will focus on the fundamental filters, while the next section will introduce the more complex ones.

From the optical filter concept, the most fundamental, most useful, or maybe most useless optical filter is the optical waveguide, which guides light through, with insertion loss and phase shifts for all guided wavelengths. As introduced in Chapter 2.1.1, the dispersion (D) of the waveguide is:

$$D = \frac{1}{c} \frac{dn_{\text{eff}}}{d\lambda} \neq 0 \quad (3.1)$$

leading to a mismatch between n_{eff} and n_g . Here, c is the light speed in vacuum, D is the dispersion of the waveguide, which is commonly < 0 in silicon waveguides.

Optical filters work by splitting the light over two or multiple paths (each with a different or similar amplitude and optical length), and then bringing these paths back together and letting the contributions interfere. The transmission depends on the interference results. Different filters' implementation just use a different way to split the light into paths and different ways to implement the delay lengths.

When light of a specific wavelength, λ , passes through a waveguide of length, L , the resulting phase shift can be expressed as:

$$\phi = \frac{2\pi L n_{\text{eff}}}{\lambda} \quad (3.2)$$

For two lights with a wavelength difference $\Delta\lambda$, the generated phase difference from waveguide dispersion can be calculated by:

$$\begin{aligned} \Delta\phi &= \frac{d\phi}{d\lambda} \Delta\lambda = -\frac{2\pi L}{\lambda^2} \left(n_{\text{eff}} - \lambda \frac{dn_{\text{eff}}}{d\lambda} \right) \Delta\lambda \\ &= -\frac{2\pi L}{\lambda^2} n_g \Delta\lambda \end{aligned} \quad (3.3)$$

The interference transmission on different phase shifts has a period of 2π , thus the optical filters will have a periodic spectrum response, where the period is known as the *free spectral range* (FSR) and can be expressed as:

$$\lambda_{\text{FSR}} \approx \frac{\lambda^2}{n_g L} \quad (3.4)$$

To achieve a desired filter response at a given wavelength, a precise phase shift ϕ is required. However, due to manufacturing imperfections in the waveguide, it is difficult to achieve precise phase shifts. Thermal phase shifters or doped waveguides can be incorporated into the filter design to compensate for these errors and provide filter tunability.

3.1.1 Mach-Zehnder interferometers and tunable optical couplers

An MZI structure is formed by splitting and recombining an optical signal with two arms or two waveguides, and it has been widely used in various applications such as optical switching, modulation, and sensing. The structure of an MZI is shown in Fig. 3.1, in which the splitter and combiner can be optical couplers such as DCs or MMI couplers, while a phase shifter is commonly used to tune the phase difference between these two arms. Depending on the two arms have an equivalent length or not, MZIs can be classified into balanced MZIs and or unbalanced MZIs.

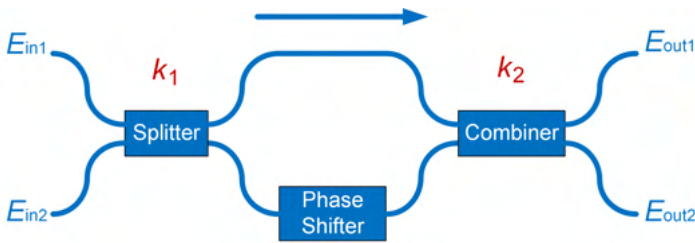


Figure 3.1: Schematic of an MZI

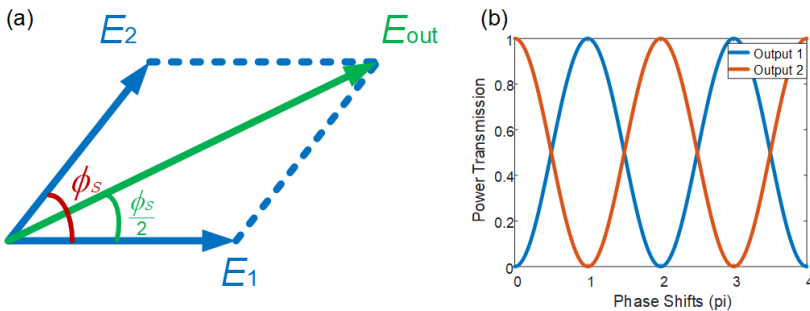


Figure 3.2: Balanced MZI responses: (a) Vector addition of the two arms' signal; (b) optical power transmission vs phase shifts

Balanced MZI The transfer matrix of a balanced MZI can be expressed as:

$$\begin{bmatrix} E_{\text{out1}} \\ E_{\text{out2}} \end{bmatrix} = \begin{bmatrix} \sqrt{(1-\kappa_2)} & j\sqrt{\kappa_2} \\ j\sqrt{\kappa_2} & \sqrt{(1-\kappa_2)} \end{bmatrix} \alpha e^{-j\phi_0} \begin{bmatrix} 1 & 0 \\ 0 & e^{-j\phi_s} \end{bmatrix} \begin{bmatrix} E_{\text{in1}} \\ E_{\text{in2}} \end{bmatrix} \quad (3.5)$$

where E_{out1} and E_{out2} are the electrical field of the MZI's outputs, E_{in1} and E_{in2} are the inputs' electrical field, κ_1 and κ_2 are the splitting ratios of the splitter and combiner, $\alpha e^{-j\phi_0}$ is the waveguide propagation (which is set to 1 for an ideal case), and ϕ_s is the phase shift introduced by the phase shifter. If 50:50 DCs or MMIs are used for the splitter and combiner, the transfer function from E_{in1} to E_{out1} and from E_{in1} to E_{out2} can be expressed as:

$$\mathbf{r} = \frac{E_{\text{out1}}}{E_{\text{in1}}} = \frac{1}{2}[1 - e^{-j\phi_s}] = \sin\left(\frac{\phi_s}{2}\right)e^{-j\frac{\phi_s}{2}} \quad (3.6)$$

$$\boldsymbol{\kappa} = \frac{E_{\text{out2}}}{E_{\text{in1}}} = \frac{1}{2}j[1 + e^{-j\phi_s}] = \cos\left(\frac{\phi_s}{2}\right)e^{-j\left(\frac{\phi_s}{2} - \frac{\pi}{2}\right)} \quad (3.7)$$

From here we can notice that the transmission can be regarded as a moving average filter with a single zero point, and its magnitude follows a sinusoidal relation of $\phi_s/2$, while the output signal's phase is shifted also by $\phi_s/2$. These results can also be explained by the vector addition of the signals in the two arms, which have equal magnitude and a phase difference of ϕ_s , as shown in Fig. 3.2 (a). And we can also get the power transformation of the MZI in the same port and the opposite port, which is:

$$|\mathbf{r}|^2 = \frac{1 - \cos(\phi_s)}{2} \quad (3.8)$$

$$|\boldsymbol{\kappa}|^2 = \frac{1 + \cos(\phi_s)}{2} \quad (3.9)$$

And the response is plotted in Fig. 3.2 (b). It can be noted that the power coupling ratios $|\mathbf{r}|^2$ and $|\boldsymbol{\kappa}|^2$ fully depend on the phase shift ϕ_s , which makes the MZI an *optical tunable coupler* [2]. When $\phi_s = 0$, the two arms of the MZI are fully balanced, and all light from input port 1 is coupled to output port 2, which is called the *cross* state, and when the phase difference $\phi_s = \pi$, the light from input 1 is fully coupled to output 1, called the *bar* state. From Equations 3.6 and 3.7, we can deduce that the two output signal's phases are related. An extra phase shifter can be added on the inputs or outputs to decouple these two outputs' phases.

Because of fabrication imperfections, the power coupling ratio of the splitter and combiner will not be precisely 50%. Setting the power coupling ratio as k , the Equations 3.8 and 3.9 can be rewritten as:

$$|\mathbf{r}|^2 = 1 - 2k + 2k^2 - 2k(1 - k)\cos(\phi_s) \quad (3.10)$$

$$|\boldsymbol{\kappa}|^2 = 2k(1 - k)(1 + \cos(\phi_s)) \quad (3.11)$$

from equations 3.10 and 3.11, we can find out that the bar state can always reach 1 and cross state can reach 0 no matter the value of k , but the bar state can only reach 0 and cross state can reach 1 if $k = 0.5$. On the other hand, this tunable coupler can always reach a 0.5 coupling ratio when:

$$|\boldsymbol{\kappa}|^2 = 2k(1 - k)(1 + \cos(\phi_s)) = 0.5 \quad (3.12)$$

for which the condition is that $4k(1 - k) \geq \frac{1}{2}$, which translate into $0.1464 \leq k \leq 0.8536$. Thus when the coupling ratio of the fabricated couplers vary between 0.15 to 0.85, the tunable coupler can always be tuned to 0.5 coupling ratio.

These two couplers are not necessarily identical, and this working status will be equivalent to the two-stages MZI structure, which will be introduced in Chapter 3.2.1.

Unbalanced MZIs have a difference in waveguide length, ΔL , between the two arms. As a result, signals traveling through the two arms experience a wavelength-dependent phase, leading to a chirped sinusoidal filter response across the optical wavelength range. The FSR of the filter can be calculated using equation 3.4. In contrast, for balanced MZIs, the power transmission is independent of the signal wavelength if the dispersion of the couplers is ignored.

3.1.2 Microring resonators

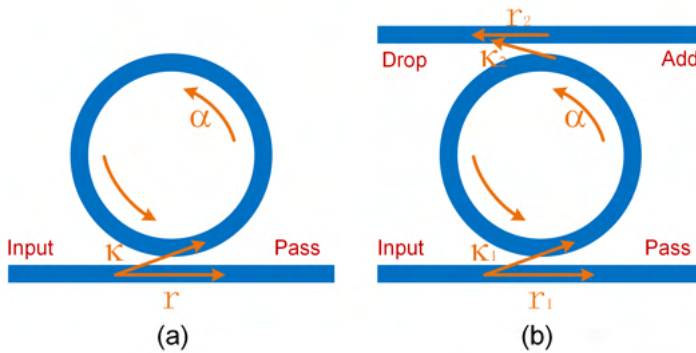


Figure 3.3: Schematic of micro ring resonators: (a) an all-pass ring; (b) an add-drop ring

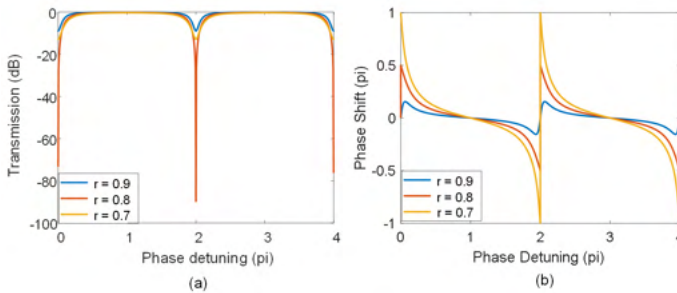


Figure 3.4: Micro ring resonator's filter response: (a) Power transmission; (b) phase response.

A ring resonator can be realized by creating an optical looped waveguide and a coupler (or two) that couples light into (and out of) the looped waveguide [3]. The basic schemes of an all-pass ring resonator and an add-drop ring are shown in Fig. 3.3. For an all-pass ring resonator, the light in the bus waveguide is split by the coupler with a coupling ratio of κ . Then the light in the ring is looped back along the ring waveguide with a power insertion loss of αL , where α is the propagation loss coefficient (in $1/m$) of the waveguide and L is the waveguide length (in m). Then the light in the ring is partially coupled back to the bus waveguide again. Thus, the field transformation can be expressed as:

$$\begin{aligned} \frac{E_{\text{pass}}}{E_{\text{in}}} &= (r - \kappa a e^{-j\phi} \kappa - \kappa r (a e^{-j\phi})^2 \kappa - \kappa r^2 (a e^{-j\phi})^3 \kappa - \dots) \\ &= \frac{r - a e^{-j\phi}}{1 - r a e^{-j\phi}} \end{aligned} \quad (3.13)$$

where ϕ is the phase detuning and also the phase shift that the light experiences as it propagates around the ring and a is the field attenuation. As discussed before, ϕ can be calculated by Eq. 3.2, and the ring's FSR follows equation 3.4. The field attenuation $a^2 = e^{-\alpha L}$.

Equation 3.13 shows that the ring resonator works as an autoregressive filter with a coupled zero-pole pair. Based on it, we can get the power transmission and also the phase response of the all-pass ring. Assuming $a = 0.8$, we can get a ring's filtering responses shown in Fig. 3.4. As can be seen, when $r = a$, the light in the bus waveguide can be fully cancelled out, and the phase jump at the resonant point is π , which is referred as critical coupling state. If $r > a$, the extinction ratio drops and the phase is lower than 2π , which is the undercoupled state. And if $r < a$, the extinction ratio also drops but the phase jump can cover 2π , which is the overcoupled state. In a practical all-pass ring design, the field attenuation a will be around 0.99, which makes it hard to reach a critical coupling or undercoupled states.

For add-drop rings, the field transformations can be expressed as:

$$\frac{E_{\text{pass}}}{E_{\text{in}}} = \frac{r_1 - a r_2 e^{-j\phi}}{1 - r_1 r_2 a e^{-j\phi}} \quad (3.14)$$

$$\frac{E_{\text{drop}}}{E_{\text{in}}} = -\frac{k_1 k_2 \sqrt{a}}{e^{j\frac{\phi}{2}} - a r_1 r_2 e^{-j\frac{\phi}{2}}} \quad (3.15)$$

Comparing equation 3.14 and equation 3.13, we can know that the critical coupling (from the point of view of the input bus waveguide) happens when $r_1 = a r_2$. For a symmetric designed add-drop ring, $r_1 \simeq r_2$, thus it is close to critical coupling and the filtering extinction ratio will be high, as long as a is much larger (closer to 1) than r_1 and r_2 .

From equation 3.14 and equation 3.13, it can be noticed that the microring responses are sensitive to the coupling ratio of the directional coupler. But here too the fabrication imperfection makes it hard to predict the exact behavior of the fabricated coupler. To obtain better control, we replace the DC with the MZI based tunable couplers to achieve a tunable ring resonator, which will be introduced in the next section.

The quality factor (Q factor) is also an important parameter for the ring resonators, which represents the number of oscillations of the optical field before its energy is depleted to $1/e$ of the initial energy [3]. The Q factor can be calculated from the ring power transmission spectrum as:

$$Q = \frac{\lambda_{\text{res}}}{\text{FWHM}} \quad (3.16)$$

where FWHM is the full width at half-maximum of the resonator. The Q factor of a resonator relates directly the loss of the cavity. Thus the all-pass rings will normally have higher Q than the add-drop rings as they only lose light through one coupler instead of two. Likewise, the SKT or FC waveguides (larger bend radius, as a tradeoff), which have lower loss than the WG waveguides, can be used to form the rings for a higher Q factor. The Q-factor also increases with the length of the ring resonator, but the Q will eventually be limited by the waveguide loss [3].

3.2 Complex and reconfigurable optical filters

Achieving a desired optical filtering response is often challenging with simply the basic optical filters we just discussed. To meet specific requirements, it becomes necessary to cascade, parallelize, and combine these basic units to create higher-order and complex optical filter circuits. The use of tunable optical couplers brings configurability to these filter circuits, and enables the compensation of imperfections from fabrication variability or wavelength dispersion. In this section, we will begin by discussing optical tunable couplers, and then introduce tunable microring resonators and ring-loaded MZIs based on the tunable couplers. These filters provide higher order of freedoms to shape a desired filtering response, and finally can be used to form large scale programmable optical circuits, which will be discussed in the next section. Other higher order filters like lattice filters and coupled resonator optical waveguides (CROWs) are not covered in this thesis work, but they are also powerful and widely used.

3.2.1 Optical tunable couplers

As discussed in the previous section 3.1.2, an MZI with two phase shifters can achieve a fully tunable optical power splitting ratio and phase relationship. However, this tuning range highly depends on the coupling ratios k of the couplers used in the MZI, where $k = 0.5$ is required for a full 0 to 1 ratio tuning. To release this requirement, double-stage MZIs are proposed, which is shown in Fig. 3.5. This double-stage MZI can be regarded as an MZI with one tunable coupler and a normal coupler, thus the field transmission matrix can be:

$$\begin{bmatrix} E_{out1} \\ E_{out2} \end{bmatrix} = \begin{bmatrix} \sqrt{(1-k_2)} & j\sqrt{k_2} \\ j\sqrt{k_2} & \sqrt{(1-k_2)} \end{bmatrix} \begin{bmatrix} 1 & 0 \\ 0 & e^{-j\phi_2} \end{bmatrix} \begin{bmatrix} \sqrt{(1-k_1)} & j\sqrt{k_1} \\ j\sqrt{k_1} & \sqrt{(1-k_1)} \end{bmatrix} \begin{bmatrix} E_{in1} \\ E_{in2} \end{bmatrix} \quad (3.17)$$

where k_2 is the power coupling ratio of the normal coupler, k_1 is the power coupling ratio of the tunable coupler, and ϕ_2 is the phase shift from the shifter 2 in Fig. 3.5. Then the field transfer function can be got as:

$$\mathbf{r} = \sqrt{(1-k_1)(1-k_2)} - \sqrt{k_1 k_2} e^{-j\phi_2} \quad (3.18)$$

$$\mathbf{\kappa} = j\sqrt{(1-k_2)k_1} + j\sqrt{k_2(1-k_1)} e^{-j\phi_2} \quad (3.19)$$

Then the optical power transfer functions become:

$$|\mathbf{r}|^2 = (1-k_1)(1-k_2) - 2\sqrt{k_1 k_2(1-k_1)(1-k_2)}\cos(\phi_2) + k_1 k_2 \quad (3.20)$$

$$|\mathbf{\kappa}|^2 = k_1 + k_2 - 2k_1 k_2 + 2\sqrt{k_1 k_2(1-k_1)(1-k_2)}\cos(\phi_2) \quad (3.21)$$

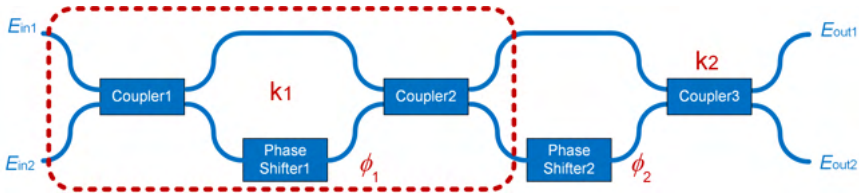


Figure 3.5: Schematic of a double stage MZI

Then we can see that $|\mathbf{r}|^2 + |\boldsymbol{\kappa}|^2 = 1$. In order to get a full tuning range of coupling ratio $[0, 1]$ for the equations 3.20, we can set that $|\mathbf{r}|^2 \in [0, 1]$, thus we get:

$$(1 - k_1)(1 - k_2) - 2\sqrt{k_1 k_2(1 - k_1)(1 - k_2)} + k_1 k_2 = 0 \quad (3.22)$$

$$(1 - k_1)(1 - k_2) + 2\sqrt{k_1 k_2(1 - k_1)(1 - k_2)} + k_1 k_2 = 1 \quad (3.23)$$

Then from equation 3.22, we can get:

$$k_1 + k_2 = 1 \quad (3.24)$$

and from equation 3.23, we can get:

$$k_1 = k_2 \quad (3.25)$$

Here, we can know that, if $k_1 + k_2 = 1$, this circuit can have a high extinction ratio at bar state ($|\mathbf{r}|^2 = 0$) and if $k_1 = k_2$, this circuit can have a zero loss at bar state ($|\mathbf{r}|^2 = 1$).

The first coupler is the tunable coupler discussed above. If we assume that all basic couplers are similar, from equation 3.11 we can get:

$$k_1 = 2k_2(1 - k_2)(1 + \cos(\phi_1)) \quad (3.26)$$

where ϕ_1 is the phase shift from the shifter 1 in Fig. 3.5. Substituting equation 3.26 into 3.24 and 3.25 we can get:

$$\frac{1}{2k_2} = 1 + \cos(\phi_1) \quad (3.27)$$

$$\frac{1}{2(1 - k_2)} = 1 + \cos(\phi_1) \quad (3.28)$$

For a tunable ϕ_1 , we can get:

$$k_2 \in [0.25, 0.75] \quad (3.29)$$

which means that if the power coupling ratio of the fabricated couplers is situated in $[0.25, 0.75]$, the full double-stage MZI's power coupling ratio can be tuned from 0 to 1 by tuning the two phase shifters, which is also indicated in the simulation results in [4].

A numerical simulation of the double-stage MZI structure are shown in Fig. 3.6 to verify the tunability. The figures show a diagonal symmetry, which indicates that the two phase shifters are exchangeable. Figures (a) and (b) are obtained by setting the $k = 0.5$ while in (c) k is set to 0.4 and in (d) k is set to 0.6. It can be seen that all these three states can reach a tuning range from 0 to 1. The axes are the square roots of the phase shifts to match the normal voltage or current power source readout. On the other side, a measured coupling ratio map can be used to fit the parameters of the fabricated circuits, which is shown in Fig. 3.7. As can be seen, the phase offsets, k of the couplers and the phase shifters tuning range are fitted and the fitting quality is quite good.

The parameters of the double-stage MZI can be used to generate a circuit model for the fabricated device, then we can try to explain and guide the tuning scheme during the experiments. It should be noted that all phase differences can be achieved with all achievable power coupling ratios for the two output ports of the double-stage MZI if the light is fed from one input port, as shown in Fig. 3.8. So the double-stage MZI with two phase shifters can also work as a tunable coupler, and the couplers inside are more tolerance with the fabrication errors.

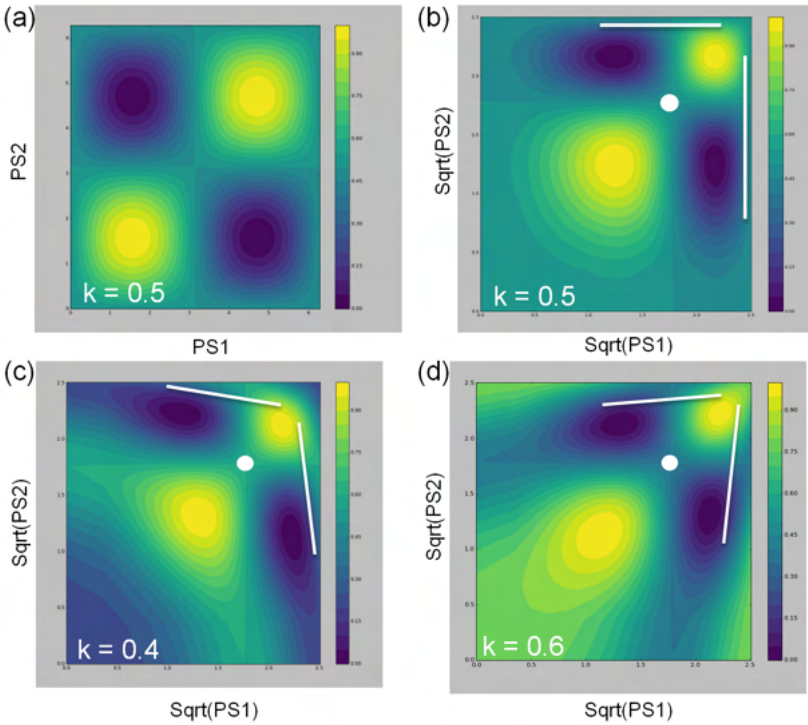


Figure 3.6: Bar state power transmission of a double stage MZI: (a) Phase shifts in linear scale when $k = 0.5$; (b) phase shifts in square root scale when $k = 0.5$; (c) phase shifts in square root scale when $k = 0.4$; (d) phase shifts in square root scale when $k = 0.6$;

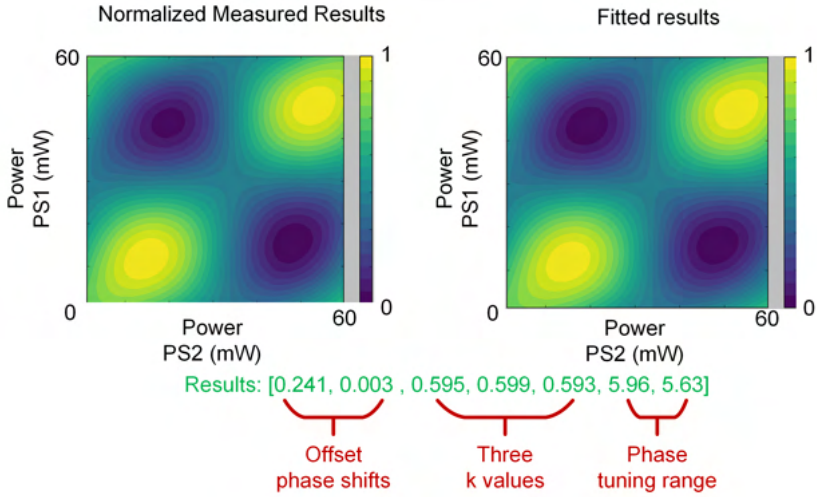


Figure 3.7: Fitting results of a double stage MZI

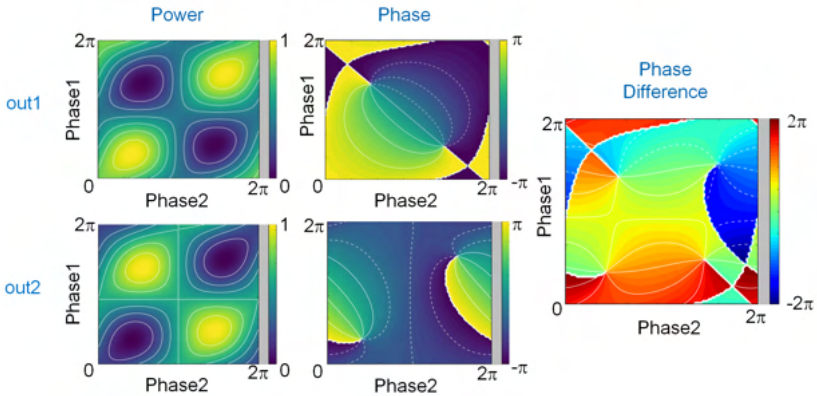


Figure 3.8: Phase response of a double stage MZI

3.2.2 Tunable ring resonators

Normal ring resonators are widely used in silicon photonic circuits, but the filter shape depends on the fabricated coupler, and a coupler with ultra-low coupling ratio is also challenging. To move beyond these limitations, a tunable coupler can be used to replace the directional couplers to form a tunable ring resonator, which is shown in Fig. 3.9. From the discussion in the chapter 3.1.3 we know that the critical coupling state occurs when the k of the tunable coupler is tuned close to 0. This configuration requires the two couplers in the tunable coupler are identical (Equation 3.25), which is normally true when the two couplers are fabricated close together.

With the help of the tunable coupler, the coupling states of the ring can be fully controlled by phase shifter1, shown in Fig. 3.9. What should be noted is that tuning the coupling condition will then also change the round trip phase in the ring, which can be seen in the electrical field transfer function:

$$\frac{E_{\text{out}}}{E_{\text{in}}} = \frac{\sin(\frac{\phi_1}{2})e^{-j(\frac{\phi_1}{2} + \frac{\pi}{2})} - \alpha e^{-j(\phi_1 + \phi_2)}}{1 + \alpha e^{-j(\phi_2)} \sin(\frac{\phi_1}{2})e^{-j(\frac{\phi_1}{2} + \frac{\pi}{2})}} \quad (3.30)$$

where α is the field attenuation and ϕ_1 , ϕ_2 are the phase shifts from the phase shifter 1 and phase shifter 2.

The inclusion of the tunable coupler enables the controlling of the coupling ratio, but it also introduces an additional optical length, which will make the ring longer and therefore reduce its FSR.

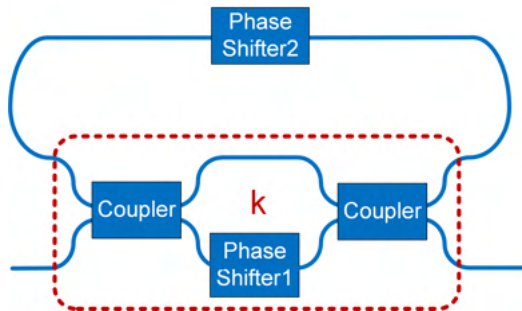


Figure 3.9: Schematic of a tunable ring resonator

3.2.3 Tunable ring-loaded MZI

An MZI filter can be regarded as a moving average filter with a single zero point, and a ring resonator can work as an autoregressive filter with a coupled zero-pole pair, which can be abstracted from their transfer functions (equation 3.6 and equation 3.13) [1]. To reach a more generic filter response, a moving average autoregressive filter is expected, and this can be implemented by a tunable ring-loaded MZI structure.

A typical tunable ring-loaded MZI is shown in Fig. 3.10. In this circuit, three tunable couplers are deployed with a tunable coupling ratio of k_1, k_2 and k_3 , respectively. To be noted that the phases of the two outputs of a tunable coupler are coupled. But because of the two independent phase shifters (phase shifter 1 and phase shifter 2) are introduced, the optical phase states in the circuits can be fully controlled, and the phase shifts from the tunable couplers can be compensated. Thus we can assume that the tunable couplers will not introduce any phase shifts, and get the field transfer function as:

$$\begin{bmatrix} E_{out1} \\ E_{out2} \end{bmatrix} = \begin{bmatrix} \sqrt{(1-k_2)} & j\sqrt{k_2} \\ j\sqrt{k_2} & \sqrt{(1-k_2)} \end{bmatrix} \begin{bmatrix} T_{ring} & 0 \\ 0 & e^{-j\phi_3} \end{bmatrix} \begin{bmatrix} \sqrt{(1-k_1)} & j\sqrt{k_1} \\ j\sqrt{k_1} & \sqrt{(1-k_1)} \end{bmatrix} \begin{bmatrix} E_{in1} \\ E_{in2} \end{bmatrix} \tag{3.31}$$

where T_{ring} is the tunable ring's field response as 3.30.

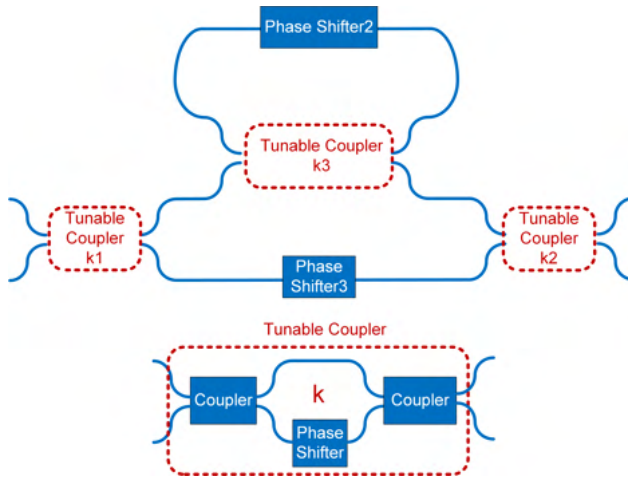


Figure 3.10: Schematic of a tunable ring loaded MZI

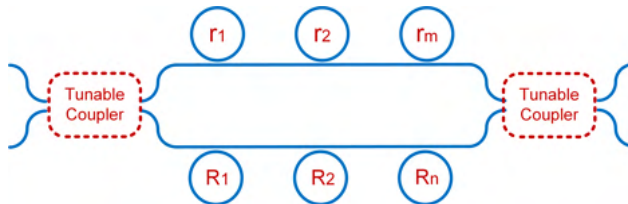


Figure 3.11: Schematic of multi-ring loaded MZI

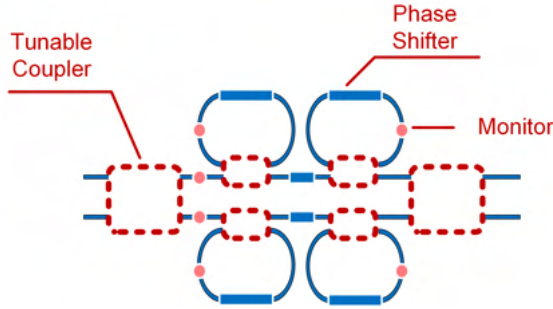


Figure 3.12: Schematic of the filter block in the signal processor

To get a more complex and universal filter configuration, more rings can be added on both arm of the MZI to reach a higher-order filter, as shown in Fig. 3.11. A transfer function like 3.11 can be used to analyze the filter response. If a target transfer function is required, it can also be used to fit the transmission curve with all tunable phase shifters as parameters [5]. However, with the scale-up of the system, the increased degrees of freedom make it hard to fit the fully response.

The ring-loaded MZI can also be regarded as a combination (summation or difference) of two all-pass filters (cascaded ring resonator filters). Classic bandpass filters can be achieved by the sum or difference of two all-pass filters, including Butterworth filters, Elliptic filters, Chebyshev filters, etc. [6]. If a desired response varies between two levels, the bandpass filter design approach can be used by specific MZI coupling ratios, which can turn the maximum and minimum of the MZI's output spectrum (Eq. 3.24 and Eq. 3.25). A more generic filter design can be achieved with the characteristic function approach [1]. While in the fabricated samples, the ring resonators cannot be lossless (say $\alpha < 1$ in Equation 3.30) and then the whole filter will have a FSR, which can be calculated with Equation 3.4.

Characterization of a four ring-loaded MZI For the signal processor described further in this thesis work, we deployed a four ring-loaded MZI structure as an optical filter. The schematic of the filter block is shown in Fig. 3.12. As can be seen, there are two tunable ring resonators on each arm of the MZI, and the MZI is also formed with two tunable couplers as the splitter and combiner. Several tapped PDs are set to monitor the ring resonators coupling status, as well as the configuration of the complete filter.

The characterization of the ring-loaded MZI starts by measuring the ring resonators. By tuning the splitter and the combiner's coupling ratio κ to either 0 or 1, we can measure the transmission of a single ring. The measurement setup is shown in Fig. 3.13(a), and the results are shown in Fig. 3.13(b)-(e). As can be seen, these four rings show an FSR of 0.86 nm or 107.5 GHz. Due to the embedded tunable coupler, the ring's length is relatively large and the FSR is small. A larger FSR can be achieved with a more compact tunable coupler.

The full width at half-maximum (FWHM) or 3 dB bandwidth of the measured ring resonators in their critical coupling states are 30.7 pm, 35.8 pm, 35.8 pm, 43.6 pm, corresponding to quality (Q) factors of 50489, 43296, 43296, 35550, respectively. The tap PDs introduce extra loss in the ring cavities, which will limit the Q factor of the rings. The

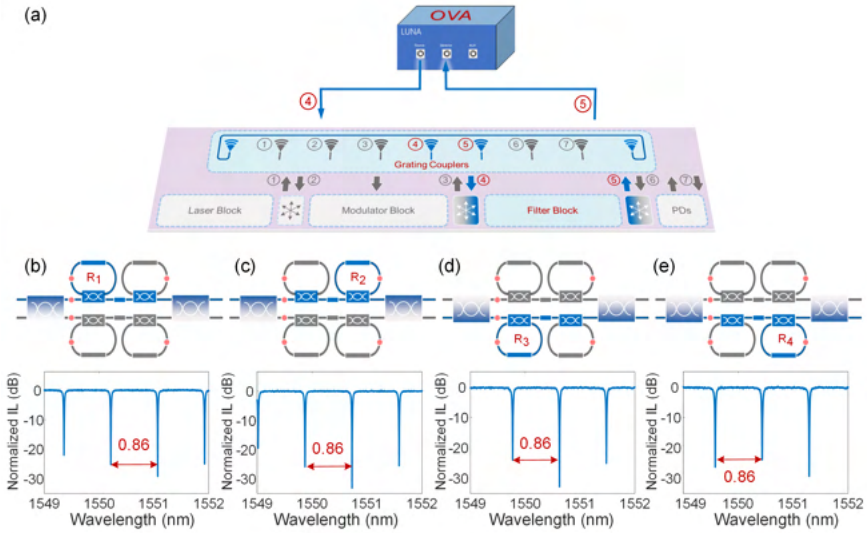


Figure 3.13: (a) The measurement setup for the filter block; (b) Ring 1 measurement configuration and results; (c) Ring 2 measurement configuration and results; (d) Ring 3 measurement configuration and results; (e) Ring 4 measurement configuration and results.

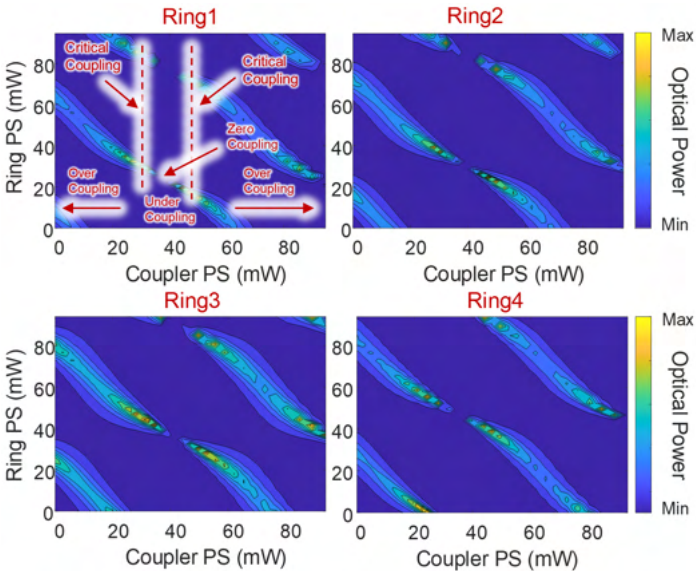


Figure 3.14: Tap monitor reading while tuning the phase shifters for a fixed optical wavelength of 1552nm. Coupler PS: phase shifter in the tunable coupler (ϕ_1). Ring PS: phase shifter in the ring (ϕ_2).

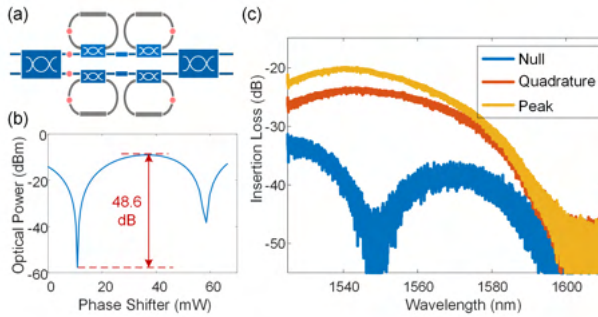


Figure 3.15: Characterization of the main MZI structure. (a) The configuration of the MZI measurement. (b) The transmission while sweeping the phase shifter on one arm of the MZI. (c) The spectrum response of the MZI biasing at null point, quadrature point and peak point.

PDs help to monitor the ring status, but they are not strictly necessary if the circuit is fully calibrated and isolated.

The tap PDs couple a percentage of light ($\sim 2\%$) out of the ring and are monitored with an electrical current meter. The monitored photocurrents in the ring can help to calibrate the phase shifters (ϕ_1 and ϕ_2). We swept the phase shifters' electrical power in the tunable coupler (ϕ_1) and the ring (ϕ_2), the PD readings are shown in Fig. 3.14. As shown in the figure, the peak points indicate that the rings are at their critical coupling states, which can hold the highest optical energy. Then the region in between is the undercoupled state, and the central lowest point is the 0-coupling state, where no light is coupled into the rings. The outer regions are overcoupled states. As can be seen, with the help of the in-line monitors, these ring resonators can be calibrated locally, without requirements of extra optical devices. From these measurements we can also extract that the phase shifter's thermal efficiency is around $28 \text{ mW}/\pi$, so now we can use this information to fit all phase delays.

With the locally calibrated phase shifters, we can tune the coupling ratios of all rings to 0 to calibrate the main MZI response, which is shown in Fig. 3.15. When sweeping the phase shifter on one MZI arm, the MZI can reach an extinction ratio of 48.6 dB at 1550 nm at cross state, as shown in Fig. 3.15(b). And the optical spectrum responses with different phase states are shown in Fig. 3.15(c). As can be seen, the highest extinction ratio can only be kept in a small wavelength range due to the dispersion of the used directional couplers.

Based on this calibration data, the whole filter now can be configured with these phase shifters. First, a Chebyshev type II type bandpass filter is defined, as shown in Fig. 3.16. In this filter configuration, only two rings (R2 and R4) are overcoupled to act as all-pass filters, and the other two rings are switched off ($\kappa = 0$), as shown in Fig. 3.16(a). By tuning R2's ring phase, we can get a bandpass filter with a tunable bandwidth, as shown in Fig. 3.16(b). The filter transmission profile shows a passband ripple of 0.5 dB, a roll-off transition of around 210 pm and an extinction ratio of 32 dB. Because of the gradual roll-off, this bandpass filter introduces extra insertion loss when it is too narrow. When the filter bandwidth is narrowed to around 120 pm, the filter introduces 10 dB extra loss. Setting the ring to critical coupling can help to get a sharper roll-off. As can be seen in Fig. 3.16(c), if R2 is kept over coupled and R4 is tuned to be critically coupled, the bandpass filter can have a narrower (50 pm) bandwidth and a lower loss (3 dB extra loss). And if these two

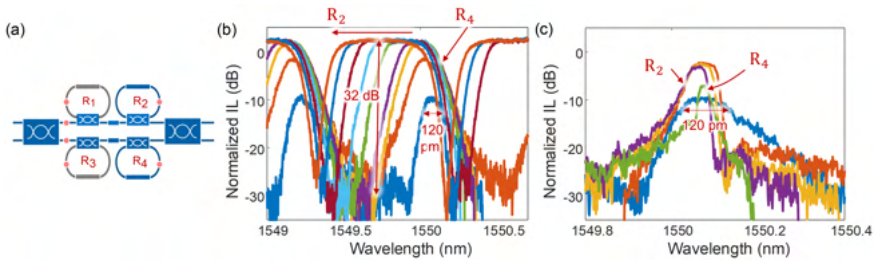


Figure 3.16: Configuration of the four-ring-loaded MZI. (a) The configuration of the filter block for a tunable bandpass filter. (b) A tunable bandpass filter response. Two rings are over coupled. (c) A tunable bandpass filter response with narrower passbands. Two rings are tuned from over coupled to under coupled.

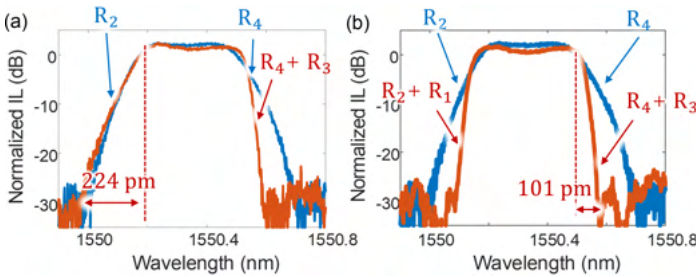


Figure 3.17: Improving the filter's roll-off. (a) R3 is added to improve the roll-off. (b) R1 and R3 are added to improve the roll-off.

rings are both critically coupled, the filter passband can be as narrow as 29.5 pm with a loss of 7 dB.

The roll-off transition can also be improved with a higher-order filter. As can be seen in Fig. 3.17, extra cascaded ring filters (R1 and R3) can help to increase the all-pass filter order and reach a narrower roll-off transition (from 224 pm to 101 pm). Thus, if higher order filters are required, more ring filters can be added on both arms.

When the ring filters are critically coupled, the ring loss can no longer be neglected and the rings are no longer all-pass filters. If the splitter and combiner's κ of the filter block is set to 0 or 1, the rings act as independent tunable band-stop filters, as shown in Fig. 3.13 (b)-(e). When the splitter and combiner's coupling ratios of the filter block is set to 0.5, forming a good MZI, the responses of the MZI with a critically coupled ring are shown in Fig. 3.18. It can be seen that a bandpass filter with a Fano resonance is achieved when the MZI is biased at null point in Fig. 3.18(c). By tuning the ring phase, a tunable bandpass filter is achieved, as shown in Fig. 3.19(a). And if two rings are used, then we can get two pass bands which can be independently tuned, shown in Fig. 3.19(b). The 3 dB bandwidth of these passbands from R1 are around 35 pm, which is slightly larger than the 3 dB bandwidth of R1 (30.7 pm).

In conclusion, the tunable-ring-loaded MZI based filter of our signal processor can in principle be configured for arbitrary magnitude responses (limited by the performance of fabricated circuits). We have shown measurement results with bandstop filters (with

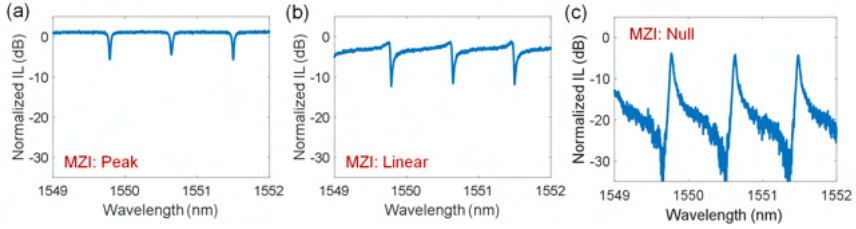


Figure 3.18: Response of a MZI loaded with a critical-coupled ring. (a) MZI biased at peak point; (b) MZI biased at linear point; (c) MZI biased at null point;.

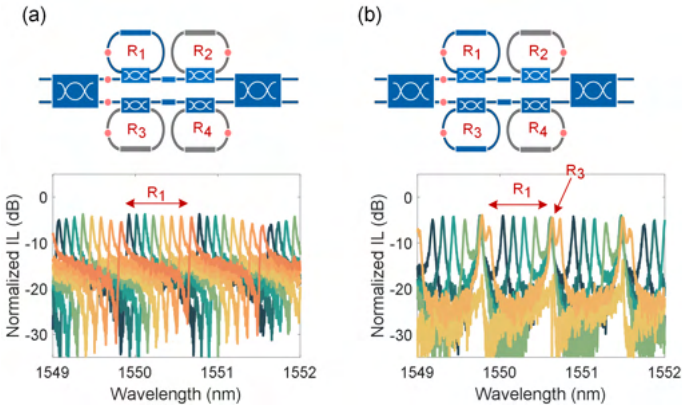


Figure 3.19: Tunable band passed filters. (a) A tunable bandpass filter; (b) An independently tunable two pass-band filter.

single rings), bandpass filters (Ring-loaded MZI with critical coupled rings), and flat-top Chebyshev type II type bandpass filters (Ring-loaded MZI with over coupled rings). Thanks to all the tap PDs, the system can be monitored and calibrated locally.

3.3 Conclusion

Utilizing basic components, like optical waveguides and couplers, we can build optical filters to tailor optical signals in silicon photonic circuits. The transmission of the optical filters depends on the phase delay and interference at the frequencies, but it cannot be fully predicted because of fabrication variance and environment perturbations.

Optical phase shifters are used to introduce degree of freedoms to tune these optical filters. A tunable MZI structure, with two phase shifters, can form a tunable coupler, which can tune the coupling ratio and phase relations between its two outputs. With tunable couplers, we can built tunable ring resonators and tunable ring-loaded MZIs. Tunable ring-loaded MZIs are considered to be universal tunable optical filters.

In this thesis work, we deploy a four ring-loaded MZI in the signal processor. The ring-loaded MZI itself shows an universal tunable optical filtering responses, and it will also help to build a widely tunable RF filter, which details will be shown in Chapter 7.

References

- [1] C. K. Madsen and J. H. Zhao, "Optical Filter Design and Analysis," *Optical Filter Design and Analysis*, 6 1999.
- [2] D. A. B. Miller, "Perfect optics with imperfect components," *Optica*, Vol. 2, Issue 8, pp. 747-750, vol. 2, pp. 747–750, 8 2015.
- [3] W. Bogaerts, P. D. Heyn, T. V. Vaerenbergh, K. D. Vos, S. K. Selvaraja, T. Claes, P. Dumon, P. Bienstman, D. V. Thourhout, and R. Baets, "Silicon microring resonators," *Laser & Photonics Reviews*, vol. 6, pp. 47–73, 1 2012.
- [4] M. Wang, A. Ribero, Y. Xing, and W. Bogaerts, "Tolerant, broadband tunable 2×2 coupler circuit," *Optics Express*, vol. 28, p. 5555, 2 2020.
- [5] M. Wang, X. Chen, U. Khan, and W. Bogaerts, "Programmable wavelength filter with double ring loaded MZI," *Scientific Reports 2022 12:1*, vol. 12, pp. 1–12, 1 2022.
- [6] A. N. Willson and H. J. Orchard, "Insights into Digital Filters Made as the Sum of Two Allpass Functions," *IEEE Transactions on Circuits and Systems I: Fundamental Theory and Applications*, vol. 42, no. 3, pp. 129–137, 1995.

4

Microwave Photonics

Microwave photonics is an application-oriented field that focuses on the interaction between microwaves and light waves to generate, distribute, process, control, and detect microwave signals using photonics technology. In this thesis work, we propose a signal processor with microwave photonic technology to handle microwave signals. In this chapter, we give an overview of this technology, and focus on microwave signal distribution, filtering and generation. Detailed principles in these applications will be elaborated, with a focus on the use of integrated photonic circuits.

4.1 Microwave Photonic Link

Microwave photonic links use optical fibers instead of coaxial cable to distribute a radio-frequency (RF) signal, with the advantage of low propagation loss, high bandwidth, immunity to electro-magnetic interference (EMI) and low cost. As shown in Fig. 4.1, a typical microwave photonic link will include a laser, a modulator, an optical medium and a photodetector (PD). The laser generates a continuous-wave (CW) light signal, which can be expressed as $E_c = e^{-j(\omega_c t)}$, as a carrier. On this carrier, an RF signal $E_s = V_{dc} + V_s \cos \omega_s t$, is modulated.

4.1.1 Intensity Modulation

If an intensity modulation is implemented with the modulator, the modulated light signal can be expressed as:

$$\begin{aligned} E_{im} &= m(V_{dc} + V_s \cos \omega_s t)e^{-j(\omega_c t)} \\ &= \frac{mV_s}{2}e^{-j(\omega_c t - \omega_s t)} + mV_{dc}e^{-j(\omega_c t)} + \frac{mV_s}{2}e^{-j(\omega_c t + \omega_s t)} \end{aligned} \quad (4.1)$$

where m is the modulation efficiency. Then the modulated signal is distributed through the optical medium (commonly free space or optical fiber), and eventually received by a PD. If the optical medium is perfectly lossless and non-dispersive (e.g., vacuum), the photocurrent of the PD becomes:

$$\begin{aligned} I_{PD} &= \mathcal{R}E_{im} \times E_{im}^* \\ &= \mathcal{R}m^2(V_{dc}^2 + 2V_{dc}V_s \cos \omega_s t + V_s^2 \cos^2 \omega_s t) \end{aligned} \quad (4.2)$$

where \mathcal{R} is the efficiency of the PD (in A/W). From this we can discern:

- A DC component: $\mathcal{R}m^2V_{dc}^2$
- A recovered first-order component: $2\mathcal{R}m^2V_{dc}V_s \cos \omega_s t$
- A second-order harmonic component: $\mathcal{R}m^2V_s^2 \cos^2 \omega_s t$

Then we can get the RF signal back at the output of the PD.

But, an optical fiber has loss and dispersion, which will introduce a phase difference between the sidebands ($\omega_c - \omega_s$ and $\omega_c + \omega_s$). Then this phase difference will make the system behave as a two-tap finite impulse response (FIR) filter and therefore attenuate the recovered first-order signal, which is called the dispersion penalty [1]. A way to get rid of

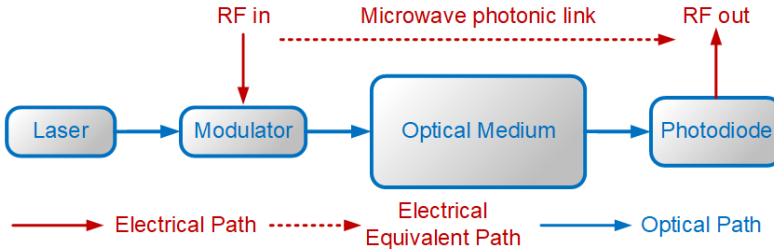


Figure 4.1: A typical microwave photonic link

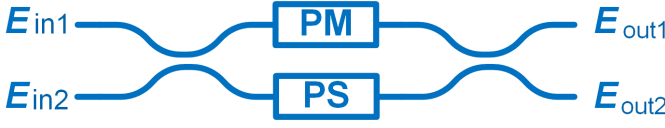


Figure 4.2: Schematic of a Mach-Zehnder modulator

this penalty is using a single-sideband modulation (SSB), which is implemented with an extra optical filter or a complex optical modulator.

4.1.2 Phase Modulation

Alternative, if the modulator is a phase modulator, then the modulated signal is:

$$\phi_m = \frac{V_{dc} + V_s \cos \omega_s t}{V_\pi} \pi \quad (4.3)$$

Where V_π is the applied voltage for which the modulator induces a π phase shift.

With the help of the Bessel expansion of the first kind, the signal at the output of the phase modulator can be expressed as:

$$\begin{aligned} E_{pm} &= e^{-j(\omega_c t + \frac{V_{dc} + V_s \cos \omega_s t}{V_\pi} \pi)} \\ &= \sum_{n=-\infty}^{\infty} j^n J_n \left(\frac{\pi}{V_\pi} V_s \right) e^{-j(\omega_c t + n\omega_s t + \frac{V_{dc}\pi}{V_\pi})} \\ &\simeq j J_1 \left(\frac{\pi}{V_\pi} V_s \right) (e^{-j(\omega_c t + \omega_s t + \frac{V_{dc}\pi}{V_\pi})} + e^{-j(\omega_c t - \omega_s t + \frac{V_{dc}\pi}{V_\pi})}) + J_0 e^{-j(\omega_c t + \frac{V_{dc}\pi}{V_\pi})} \end{aligned} \quad (4.4)$$

where only the first order sidelobes are kept. High order sidelobes will be orders of magnitude smaller when the modulation signal is small (small signal model).

If this signal is fed into the PD directly, the outputs will be as simple as:

$$I_{PD} = \mathcal{R} E_{pm} \times E_{pm}^* = \mathcal{R} \quad (4.5)$$

which confirms that the PD cannot directly detect optical phase information.

Extra interferometers can be added to retrieve the modulated phase information. In silicon photonic circuits, PN or PIN based phase modulators can form an Mach-Zehnder modulator (MZM) or micro-ring modulators.

If one of those phase modulators is put in an ideal balanced MZI, a single-drive MZM is formed, as shown in Fig. 4.2. If the directional coupler's coupling ratio is κ , the output field can be expressed as:

$$\begin{bmatrix} E_{out1} \\ E_{out2} \end{bmatrix} = \begin{bmatrix} \sqrt{(1-\kappa)} & j\sqrt{\kappa} \\ j\sqrt{\kappa} & \sqrt{(1-\kappa)} \end{bmatrix} \begin{bmatrix} e^{-j\phi_m} & 0 \\ 0 & e^{-j\phi_s} \end{bmatrix} \begin{bmatrix} \sqrt{(1-\kappa)} & j\sqrt{\kappa} \\ j\sqrt{\kappa} & \sqrt{(1-\kappa)} \end{bmatrix} \begin{bmatrix} E_{in1} \\ E_{in2} \end{bmatrix} \quad (4.6)$$

in which ϕ_s represents the relevant phase difference between the two arms (tuned by the phase shifter), and ϕ_m is the phase shift introduced by the modulator, which can be expressed as Equation 4.3 (The DC-introduced phase shifts can be compensated by ϕ_s).

Assuming the light signal $E_{\text{in1}} = e^{-j(\omega_c t)}$ is fed from input 1, the modulated light signal at the bar output can be expressed as:

$$E_{\text{out1}} = [(1 - \kappa)e^{-j\phi_m} - \kappa e^{-j\phi_s}]E_{\text{in1}} \quad (4.7)$$

Substitute Equation 4.4 into Equation 4.7, we get

$$\begin{aligned} E_{\text{out1}} &= [(1 - \kappa)J_0\left(\frac{\pi}{V_\pi}V_s\right) - \kappa e^{-j\phi_s}]e^{-j(\omega_c t)} + \\ & j(1 - \kappa)J_1\left(\frac{\pi}{V_\pi}V_s\right)(e^{-j((\omega_c - \omega_s)t} + e^{-j((\omega_c + \omega_s)t)}) \\ & = A_0 e^{-j\phi_{A_0}} e^{-j(\omega_c t)} + jA_1(e^{-j((\omega_c - \omega_s)t)} + e^{-j((\omega_c + \omega_s)t)}) \end{aligned} \quad (4.8)$$

The gain of the carrier and the upper and lower modulated sideband are give by

$$\begin{aligned} A_0 e^{-j\phi_{A_0}} &= (1 - \kappa)J_0\left(\frac{\pi}{V_\pi}V_s\right) - \kappa e^{-j\phi_s} \\ A_1 &= (1 - \kappa)J_1\left(\frac{\pi}{V_\pi}V_s\right) \end{aligned} \quad (4.9)$$

When the modulated light signal is received by a PD, we get the photocurrent which can be expressed as:

$$\begin{aligned} I_{\text{PD}} &= \mathcal{R}E_{\text{out1}}E_{\text{out1}}^* \\ &= \mathcal{R}[A_0 e^{-j\phi_{A_0}} e^{-j(\omega_c t)} + jA_1(e^{-j((\omega_c - \omega_{\text{rf}})t - \phi_{\text{rf}})} + e^{-j((\omega_c + \omega_{\text{rf}})t + \phi_{\text{rf}})})] \\ &\times [A_0 e^{j\phi_{A_0}} e^{j(\omega_c t)} - jA_1(e^{j((\omega_c - \omega_{\text{rf}})t - \phi_{\text{rf}})} + e^{j((\omega_c + \omega_{\text{rf}})t + \phi_{\text{rf}})})] \\ &= \mathcal{R}[A_0^2 + 2A_1^2 - 4A_0A_1 \sin(A_0) \cos(\omega_{\text{rf}}t + \phi_{\text{rf}}) + 2A_1^2 \cos(2\omega_{\text{rf}}t + 2\phi_{\text{rf}})] \\ &= \mathcal{R}[I_{\text{DC}} + I_1^{st} + I_2^{nd}] \end{aligned} \quad (4.10)$$

Here \mathcal{R} is PD's responsibility. Then we can calculate that the field amplitude of the recovered RF signal at the original frequency ω_s is (with Eq.4.9)

$$I_1^{st} = \mathcal{R}[-4A_0A_1 \sin(\phi_{A_0})] = 4\mathcal{R}\kappa(1 - \kappa)J_1\left(\frac{\pi}{V_\pi}V_s\right) \sin(\phi_s) \quad (4.11)$$

For a balanced MZM with normal 50:50 directional couplers as splitter and combiner, the output field amplitude becomes:

$$I_1^{st} = \mathcal{R}J_1\left(\frac{\pi}{V_\pi}V_s\right) \sin(\phi_s) \quad (4.12)$$

which is determined by the offset phase shift ϕ_s . When $\phi_s = \pi/2$ or $3\pi/2$, the RF signal is maximized, and this operational point is the MZM's quadrature point. When $\phi_s = 0$, there won't be any light from output port 1 and this is the MZM's null point. When $\phi_s = \pi$, all light comes out of output port 1 but no RF signal at the original frequency recovered, because this is the MZM's peak point.

4.1.3 Imperfect Modulators

Till now we considered the intensity modulator and the phase modulator in the microwave photonic links to be perfect, so they do not introduce any unwanted phase modulation or intensity modulation, respectively. However, this is not always true, especially for silicon



Figure 4.3: The figure of merit of a microwave photonic link.

modulators. The carrier dispersion effect-based modulators and electro-absorption modulators (EAM) both introduce phase and intensity modulation simultaneously [2, 3]. Chapter 5 will introduce a reconfigurable modulator design to compensate these imperfections. With this modulator circuit, an imperfect modulator can be transformed into a near-perfect phase modulator or near-perfect amplitude modulator, at the cost of a constant insertion loss. Because we have such a compensation mechanism at our disposal, we can perform all derivations in this chapter based on perfect modulators, without loss of generality.

4.1.4 Figures of Merit

The figure of merit (FoM) for a microwave photonic link is a metric used to evaluate the overall performance of the link. It typically combines various key parameters to provide a comprehensive assessment of the system. The specific formulation of the figure of merit may vary depending on the application and requirements, but common parameters considered, except for its 3 dB bandwidth, in the evaluation of a microwave photonic link include the link gain, noise figure, and linearity. These concepts are shown in Fig. 4.3.

RF Gain. As shown in Fig. 4.3, if the input RF signal has a power of P_{in} and the recovered RF signal at the output has a power of P_{out} , the RF gain G_{RF} can be calculated as

$$G_{RF} = \frac{P_{out}}{P_{in}} \quad (4.13)$$

$$G_{RF}(\text{dB}) = P_{out}(\text{dBm}) - P_{in}(\text{dBm})$$

Noise Figure. Figure 4.3 shows the noise power at the input N_{in} and output N_{out} . The link noise figure (NF) is defined as the quotient between the signal to noise ratio (SNR) at the input and the SNR at the output, given by

$$\begin{aligned} \text{NF} &= 10 \log \frac{\text{SNR}_{in}}{\text{SNR}_{out}} \\ &= 10 \log \frac{P_{in}/N_{in}}{P_{out}/N_{out}} \\ &= -G_{RF}(\text{dB}) + N_{out}(\text{dBm}) - N_{in}(\text{dBm}) \end{aligned} \quad (4.14)$$

where we substitute Eq. 4.13.

Ideally, if the microwave photonic system does not introduce any noise, we will have $N_{out} = G_{RF}N_{in}$ and then $\text{NF} = 0$ dB. However, the electronic and photonic devices in the link, such as laser, photodetector, electronic components, add extra noise in the system. This implies that, in general, $N_{out} = G_{RF}N_{in} + N_{add}$, where N_{add} is the power of additional noise sources at the system output. The most important noise contributions in this system

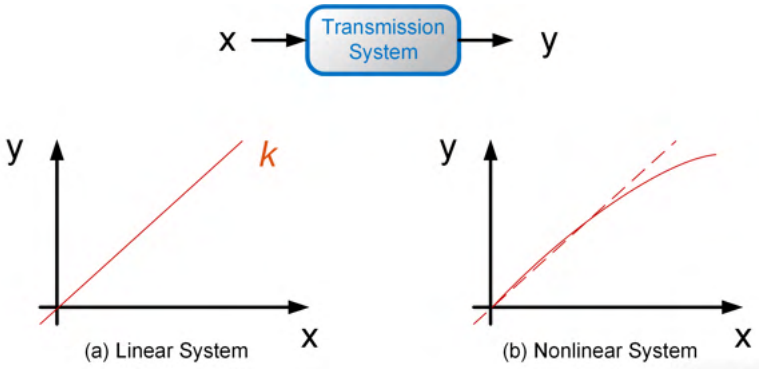


Figure 4.4: Linear (a) and non-linear (b) system.

are the thermal noise, the laser relative intensity noise (RIN), and the shot noise of the photodetector. More detailed information can be found in [4].

Linearity and Spurious-Free Dynamic Range. If the transmission system is ideally linear, the output signal Y can be easily expressed as $Y = kX$, where k is the transfer function of the system and X is the input signal, as shown in Fig 4.4(a). When the input signal is an RF signal with a frequency of ω_s , the output signal will also just have one frequency component ω_s .

However, in reality, the transmission system cannot not be perfectly linear. When x and y are small, the curve is close to a straight line, but not 100% straight. Whether or not the designer realizes it, there are nonlinearities. When x and y are large, however, the nonlinearities are highly visible, as shown in Fig 4.4(b). Here, we can do a Taylor expansion on the transfer function, and the output signal can be like:

$$Y = k_0 + k_1X^1 + k_2X^2 + k_3X^3 + \dots \quad (4.15)$$

If the input signal X has a frequency of ω_s , the output signal will have the fundamental signal ω_s , and a series of harmonics ($2\omega_s, 3\omega_s, 4\omega_s\dots$), as shown in Fig 4.3. These harmonics are responsible for the signal distortion and noise.

Harmonics are commonly easy to filter out since their frequencies are relatively far from useful signals bands. More troubles come when the input signal has multiple frequency components. If the input signal X is a two tone signal with frequency components of ω_a and ω_b :

$$X = x_a + x_b \quad (4.16)$$

The output signal can be expressed with terms:

$$\begin{aligned} (0^{th} \text{ order}) Y_0 &= k_0 \\ (1^{st} \text{ order}) Y_1 &= k_1X = k_1(x_a + x_b) \\ (2^{nd} \text{ order}) Y_2 &= k_2X^2 = k_2(x_a^2 + x_b^2 + 2x_ax_b) \end{aligned} \quad (4.17)$$

In the 2^{nd} order, x_a^2 has frequency $2\omega_a$, and x_b^2 has frequency $2\omega_b$, which are harmonics. The term x_ax_b shows a combination of two fundamental frequencies, and they have frequency $\omega_a + \omega_b$ and $|\omega_a - \omega_b|$, which are called intermodulation products (IM).

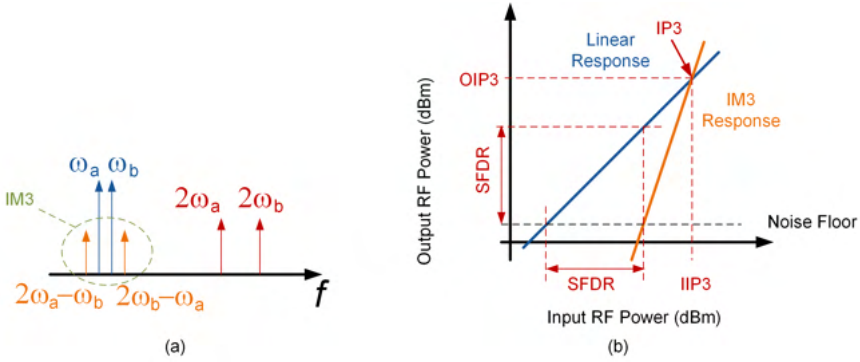


Figure 4.5: (a) Frequencies generated by a two-tone input signal applied to a nonlinear device and non-linear device. (b) Output power versus input power of a system.

If the x_a and x_b are in the same band, ω_a and ω_b will be close, and then these 2^{nd} order IM products or IM2 can be filtered out, like harmonics. However, in the 3^{rd} order outputs:

$$(3^{rd} \text{ order})Y_3 = k_3 X^3 = k_2(x_a^3 + 3x_a x_b^2 + 3x_a^2 x_b + x_b^3) \quad (4.18)$$

Here, the term $x_a x_b^2$ has frequency component $2\omega_b - \omega_a$, and the term $x_a^2 x_b$ has frequency component $2\omega_a - \omega_b$, which are called third-order intermodulation products (IM3). IM3 will be too close to ω_a and ω_b to be filtered out, as shown in Fig. 4.5(a), and will cause unrecoverable jamming and interferences to the recovered signal. With a similar situation, IM5, IM7 will also be hard to filter out, but they are much weaker than IM3, and we will not take them into account in this thesis work.

A commonly used specification to evaluate the linearity of a system is the spurious-free dynamic range (SFDR), which indicates the dynamic range of the input RF power that the linear response is detectable (higher than the noise floor) and the IM3 is not detectable (lower than the noise floor). More details on the linearity of a microwave photonic link can be found in [5]. A system with higher linearity will have a lower IM3 with the same input RF power, resulting in a higher SFDR.

In a normal microwave photonic link, an optical modulator is necessary to imprint the RF signal, which is inherently a nonlinear device, and it will reduce the SFDR. In this thesis, we will introduce a reconfigurable modulator in Chapter 5. The modulator makes use of the nonlinearity of the intrinsic PN junction (intensity and phase modulation) to compensate the nonlinearity of the sinusoidal response of the MZI modulator, resulting in an improved SFDR.

4.2 Microwave Photonic Filter

Microwave filters are essential components in modern communication, radar, and electronic systems that operate at microwave (3 to 30 GHz) and millimeter-wave frequencies (30 to 300 GHz). Traditional microwave filters are made up of passive components like capacitors, inductors, and resistors or active components like transistors or operational amplifiers to achieve the desired filter characteristics. However, it is quite challenging to attain both high frequency operation and a large bandwidth. These bottlenecks can be easily released with microwave photonic filters. Also, extra degrees of freedom introduced in optical domain bring a high reconfigurability to the filtering responses.

As discussed in the previous section, microwave photonic links can distribute the RF signal over the optical medium, by imprinting the RF signal on an optical carrier. As shown in Equation 4.1 and Equation 4.4, single-frequency RF signal will create two sidelobes on both sides of the optical carrier frequency. If we assume the system is a linear system, a broadband RF signal will then create two sidebands. The recovered RF signal from the PD is generated from the beat signal between the sidebands and the optical carrier. Thus, if an optical filter alters the intensity or phase transmission of the sidebands or the carrier, the recovered RF signal will be reshaped and a microwave photonic filter response is obtained.

In a fiber-based system, optical filters commonly used for microwave photonic filtering can be fiber Bragg gratings, dispersion compensating fibers, or arrayed waveguide gratings [6]. To reach a higher flexibility, programmable optical filters such as WaveShaper (Finisar, II-VI [7]) are also widely used in microwave photonic filter systems [8]. In integrated photonic circuits, the filters can be implemented as MZIs, micro ring resonators and their combinations. All these optical filters can be electrically tuned. Compared to classical electronic RF filters, microwave photonic filters enjoy higher operational bandwidth and higher reconfigurability. But due to the electrical-to-optical and optical-to-electrical conversion, the RF gain of a microwave photonic filter is usually very low (RF loss is high).

An typical tunable microwave bandpass filter can be achieved using an optical phase modulator and an optical notch filter (say, a critically coupled all-pass ring filter) in a microwave photonic link, which is shown in Fig. 4.6. From Equation 4.5, we can know that, if there is no optical filter in the link, there will not be any RF signal generated from the PD outputs, for all RF frequency components will be cancelled out. However, due to the added optical notch filter, one sideband of the modulated light signal will be filtered and one frequency component cannot be fully cancelled out, resulting in a bandpass filtering response, as shown in Fig. 4.7. The RF central frequency of the passband will be determined by the

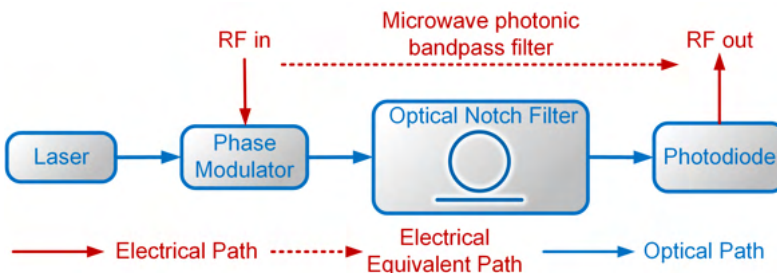


Figure 4.6: Schematic of a typical microwave bandpass filter.

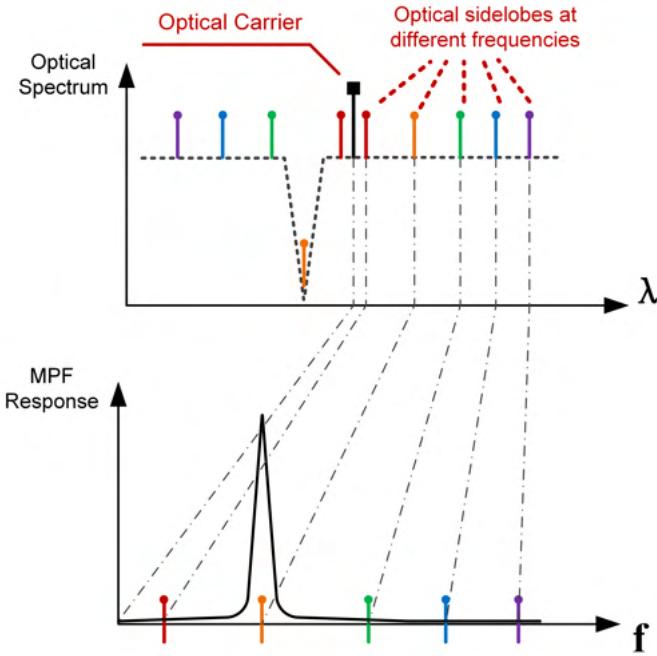


Figure 4.7: Principle of the microwave bandpass filter.

optical frequency difference of the notch filter and the optical carrier, and the bandwidth of the RF filter will highly depends on the bandwidth of the optical notch filter.

As discussed in Chapter 3.2.3, ring-loaded MZI structures can implement general classic bandpass filters in the optical domain, which have been used in integrated microwave photonic filters to implement an universal RF filtering response [9, 10]. However, this type of filter is hard to synthesis in the RF domain if used in a microwave photonic link as described in Fig. 4.1. A simpler way to map the optical response into the RF domain is to use the SSB modulation approach, which can be realized by complex modulators [10] or additional optical filters [9]. The schematic will be like in Fig. 4.8. Here we can simply assume that an intensity modulator is used to obtain SSB modulation, for the phase relation between the optical carrier and the sidelobes will be covered by the optical filter later. Thus, the electrical field of the modulated signal at point A (after the SSB modulator, with only the upper sideband remaining) can be expressed as:

$$E_A = m' V_{dc} e^{-j(\omega_c t)} + \frac{m' V_s}{2} e^{-j(\omega_c t + \omega_s t)} \tag{4.19}$$

where m' is the SSB modulation efficiency.

We can set the optical filter's response at the upper sideband to be $U e^{-j\phi_U}$ (U can be frequency-dependent). Then the filtered field of the modulated signal at point B (after the filter) will be:

$$E_B = m' V_{dc} e^{-j(\omega_c t)} + U \frac{m' V_s}{2} e^{-j(\omega_c t + \omega_s t + \phi_U)} \tag{4.20}$$

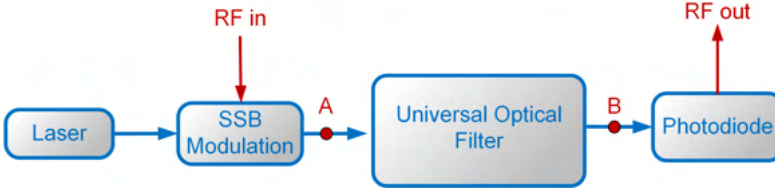


Figure 4.8: Schematic of a universal RF filter based on SSB modulation.

Therefore the photocurrent from the PD can be expressed as:

$$\begin{aligned}
 I &= \mathcal{R} E_B E_B^* \\
 &= \mathcal{R} [(m' V_{dc})^2 + (U \frac{m' V_s}{2})^2 + m'^2 V_{dc} U V_s \cos(\omega_s t + \phi_U)]
 \end{aligned} \tag{4.21}$$

From Equation 4.21, we notice that the optical response $U e^{-j\phi_U}$ of the optical filter is a linear factor applied to the RF signal $V_s \cos(\omega_s t)$. Thus if the optical filter is a universal filter (i.e. of which the response can be arbitrarily configured), the generated RF filter will also be universal.

However, this scheme asks for SSB modulation, which is complicated and introduces extra optical and RF loss. And a universal filter, like a ring-loaded MZI structure discussed in Chapter 3.2.3, is also hard to configure, especially when the system gets scaled up to a large number of rings. In this thesis work, we propose a novel way, using the reconfigurable modulator, combined with simple cascaded ring filters, to reach an equivalent universal RF filter, which will be introduced in the Chapter 7.

4.3 RF signal Generation

RF signal generation, especially with high frequency and low phase noise, is quite challenging with normal electronic devices. Microwave photonics can also contribute to this function.

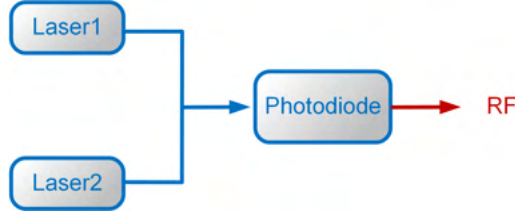


Figure 4.9: Laser beat for RF signal generation

4.3.1 Laser Beating

The most straightforward method for generating a RF signal in an optical way is to beat two laser sources in a PD. For instance, two free-run lasers are fed into a PD, as shown in Fig. 4.9, which can be expressed as:

$$\begin{aligned} E_1 &= e^{-j(\omega_1 t + \Delta\phi_1)} \\ E_2 &= e^{-j(\omega_2 t + \Delta\phi_2)} \end{aligned} \quad (4.22)$$

Where ω_1 and ω_2 are the lasers' frequency, and $\Delta\phi_1$ and $\Delta\phi_2$ are the lasers' phase noise. Then, The output of the PD can be calculated as:

$$\begin{aligned} I &= \mathcal{R}(E_1 + E_2)(E_1^* + E_2^*) \\ &= \mathcal{R}[2 + 2 \cos((\omega_1 - \omega_2)t + \Delta\phi_1 - \Delta\phi_2)] \end{aligned} \quad (4.23)$$

For two free-running lasers, $\Delta\phi_1$ and $\Delta\phi_2$ are two independent random numbers, thus the two phase noise contributions are added on the generated RF signal $\cos((\omega_1 - \omega_2)t)$, which will result in too high phase noise for some RF applications.

But if these two lasers are phase locked or slaved by one master laser, their phase noise will not be uncorrelated anymore, and the generated RF signal will not suffer from the high phase noise of the lasers [6]. Alternatively, these laser sources can originate from one frequency comb, which also has locked phase relations, and thus the generated RF signal can also enjoy low phase noise [11].

4.3.2 Opto-Electronic Oscillator

Apart from laser beating, we can also build an oscillating cavity to generate an RF signal. Similar to a ring laser, if we have a closed RF transmission loop, an RF filter to select the mode, and enough RF gain to compensate the propagation loss, we can obtain an RF oscillator. However, the propagation loss of normal coaxial cables is quite high, which limits the length of the cavity and therefore limits the generated RF signal's phase noise performance. Thanks to the low propagation loss of optical fibers, a microwave photonic

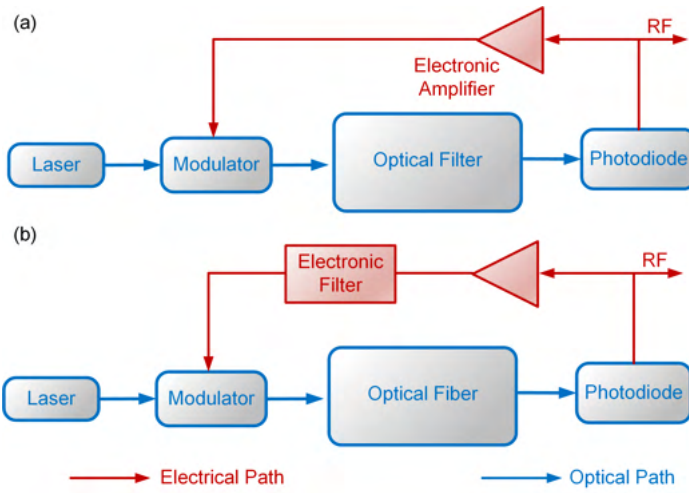


Figure 4.10: Schematic of typical OEO structures. (a) With a microwave photonic filter; (b) With an additional electronic filter.

link and a filter can be a solution. Such an oscillating cavity contains electronic devices as well as optical devices, and it is therefore called an Opto-Electronic Oscillator (OEO).

A typical OEO schematic is shown in Fig. 4.10. As can be seen, the optical path forms a microwave photonic link or filter, and the generated RF signal is fed into an electronic amplifier to be boosted, and then goes to the modulator to close the loop. A electronic filter can be added in the loop to further select the mode to reach a high mainlobe-to-sidelobe ratio (MSR), but it is not strictly necessary due to the mode competition. With the help of the optical fiber, the cavity can be several kilometers long to generate an RF signal with low phase noise.

Traditional OEO structures with fiber-based devices are quite bulky compared with electronic signal generators. Photonic integration can significantly reduce the footprint of the system, but the propagation loss of all the photonic integration platforms cannot be as low as the loss of an optical fiber. And the kilometers-long optical path is also hard to achieve in electronic or photonics integrated circuits. So, a fully on-chip OEO for RF generation cannot yet realize an advantage compared with electronic devices [12, 13]. So, in this thesis work, we will use our signal processor and combine both systems, with all photonic components integrated on a single chip, and couple light out of chip with a length of fiber, to reach a small footprint as well as a low-phase-noise RF signal. The results will be shown in Chapter 7.

Another challenge of using integrated photonic circuits is that the Q factor of the on-chip optical filters is not high enough, or the bandwidth of the optical filters (around GHz) is too wide to select a single longitude mode of the RF signal if the entire cavity is too long (MHz spacing). Due to the mode competition, it is not really necessary to use a narrow enough RF filter to get a single mode oscillation, but the stability and the side-mode attenuation of the system will be better with a narrower filter band.

One way to get a single mode OEO with a longer optical path is to use a parity-time symmetry breaking loop [14–16]. When the symmetry is broke, one mode will be highly

pumped and the neighboring modes will be highly attenuated, which shows outstanding mode selecting performance without adding extra filters. This principle works in both optical laser cavities and OEO cavities. The signal processor in this thesis work can in principle work in this way, and this could be an idea for a future experiment.

4.3.3 Frequency Multiplication

On the other hand, the microwave photonic filter can also work as an RF frequency multiplier. As shown in Equation 4.11, for an MZM, when we bias an MZM on the peak point ($\phi_s = \pi$) or the null point ($\phi_s = 0$), the original frequency components ω_s will be attenuated while the second harmonics (at $2\omega_s$ and $-2\omega_s$) remain, resulting in a frequency doubling of the applied signal. However, due to the extra loss of the embedded silicon modulator, the original frequency cannot be suppressed perfectly with a normal designed MZM. With the reconfigurable modulator, which will be introduced in Chapter 5, the first-order signal can be suppressed close to the noise floor and a high second-order to first order ratio is achieved (40 dB). Moreover, if the full microwave photonic filter is configured to filter out specific RF harmonics, an arbitrary RF multiplier can be achieved. This could serve an idea for future experiments.

4.4 Conclusion

Microwave photonics is a technology that using photonics approaches to generate, distribute, process, control, and detect microwave signals. The capacity of large bandwidth of optical signals, the availability of low-loss optical transport media, and the immunity of EMI show the benefits of handling RF signals using photonic technology.

In this chapter, we introduced the principle of microwave photonic links, which distributes RF signals through an optical medium. If the optical medium is not flat (in magnitude and phase) over the frequency range of the loaded RF signal, the recovered RF signal will also load the transmission response of the optical medium. Therefore, the entail microwave photonic link acts a RF filter, and it will become a reconfigurable RF filter if a programmable optical filter is used as the optical medium.

The generation of RF signals can also be implemented with photonic systems. Laser beating can be a straightforward method, but the generated RF signal will suffer from high phase noise, if the original lasers are not phase locked. An OEO, formed by closing the loop between the output of a microwave photonic link and its input, can be a good approach for RF signal generation, with a low phase noise.

In addition, a frequency-doubled signal can be obtained by the controlling of the bias point of the MZM in the microwave photonic link. With the help of potential optical filters, high-order frequency multiplication can be achieved.

In this thesis work, we propose a signal processor, which is capable of the generation, filtering and doubling of RF signals. A full microwave photonic link is built fully on chip, and a ring-loaded MZI is used in the optical path to form a reconfigurable microwave photonic filter. Together with off-chip amplifiers (optical and electrical), we demonstrate a tunable OEO for RF signal generation. Thanks to a reconfigurable modulator design in the system, the processor can also be used for frequency doubling. More details will be shown in Chapter 7.

References

- [1] A. Hilt, E. Udvary, and T. Berceci, "Harmonic distortion in dispersive fiber-optical transmission of microwave signals," *MWP 2003 - Proceedings, International Topical Meeting on Microwave Photonics*, pp. 151–154, 2003.
- [2] R. Soref and B. Bennett, "Electrooptical effects in silicon," *IEEE Journal of Quantum Electronics*, vol. 23, pp. 123–129, 1 1987.
- [3] T. Bo and H. Kim, "Generalized model of optical single sideband generation using dual modulation of DML and EAM," *Optics Express*, Vol. 28, Issue 19, pp. 28491–28501, vol. 28, pp. 28491–28501, 9 2020.
- [4] I. Gasulla, J. Capmany, A. J. Seeds, K. J. Williams, V. J. Urick, M. S. Rogge, F. Bucholtz, P. S. Devgan, and J. D. McKinney, "Analytical model and figures of merit for filtered Microwave photonic links," *Optics Express*, Vol. 19, Issue 20, pp. 19758–19774, vol. 19, pp. 19758–19774, 9 2011.
- [5] J. Yao and J. Capmany, "Microwave photonics," *Science China Information Sciences* 2022 65:12, vol. 65, pp. 1–64, 8 2022.
- [6] J. Yao, "Microwave photonics," *Journal of Lightwave Technology*, vol. 27, pp. 314–335, 2 2009.
- [7] "WaveShaper® 1000A Programmable Optical Filter — Coherent Corp."
- [8] H. Deng, S. Fu, M. Tang, and D. Liu, "Electronically reconfigurable bandpass microwave photonic filter using a windowed optical frequency comb," *Journal of Optics (United Kingdom)*, vol. 17, no. 3, 2015.
- [9] X. Guo, Y. Liu, T. Yin, B. Morrison, M. Pagani, O. Daulay, W. Bogaerts, B. J. Eggleton, A. Casas-Bedoya, and D. Marpaung, "Versatile silicon microwave photonic spectral shaper," *APL Photonics*, vol. 6, p. 36106, 3 2021.
- [10] J. S. Fandiño, P. Muñoz, D. Doménech, and J. Capmany, "A monolithic integrated photonic microwave filter," *Nature Photonics* 2016 11:2, vol. 11, pp. 124–129, 12 2016.
- [11] J. Liu, E. Lucas, A. S. Raja, J. He, J. Riemensberger, R. N. Wang, M. Karpov, H. Guo, R. Bouchand, and T. J. Kippenberg, "Photonic microwave generation in the X- and K-band using integrated soliton microcombs," *Nature Photonics* 2020 14:8, vol. 14, pp. 486–491, 4 2020.
- [12] W. Zhang and J. Yao, "Silicon Photonic Integrated Optoelectronic Oscillator for Frequency-Tunable Microwave Generation," *Journal of Lightwave Technology*, Vol. 36, Issue 19, pp. 4655–4663, vol. 36, pp. 4655–4663, 10 2018.
- [13] T. Hao, Y. Liu, J. Tang, Q. Cen, W. Li, N. Zhu, Y. Dai, J. Capmany, J. Yao, and M. Li, "Recent advances in optoelectronic oscillators," <https://doi.org/10.1117/1.AP.2.4.044001>, vol. 2, p. 044001, 7 2020.
- [14] L. Feng, Z. J. Wong, R. M. Ma, Y. Wang, and X. Zhang, "Single-mode laser by parity-time symmetry breaking," *Science*, vol. 346, pp. 972–975, 11 2014.
- [15] J. Zhang, L. Li, G. Wang, X. Feng, B. O. Guan, and J. Yao, "Parity-time symmetry in wavelength space within a single spatial resonator," *Nature Communications* 2020 11:1, vol. 11, pp. 1–7, 6 2020.
- [16] L. Wang, X. Xiao, L. Xu, Y. Liu, Y. Chen, Y. Yu, and X. Zhang, "On-chip tunable parity-time symmetric optoelectronic oscillator," <https://doi.org/10.1117/1.APN.2.1.016004>, vol. 2, p. 016004, 1 2023.

5

Reconfigurable Modulator

In this chapter, we present a reconfigurable modulator design, which consists of two tunable couplers, a PN junction-based modulator, and a thermal phase shifter. As a modulator component, this circuit can be configured to be a phase modulator, or an intensity modulator, with optimized modulation performance for various applications. As a key device in the signal processor (main work of this thesis), it not only provide a reconfigurable electrical-to-optical conversion, but it also enables the universal RF filtering with double sideband modulation.

5.1 Introduction

As introduced in chapter 2.2.2, the modulator most commonly used in silicon photonic circuits is the P(D)N junction-based phase modulator, and the generated phase modulation can easily be converted to intensity modulation using interferometric circuits, such as the MZI and microring resonators [1, 2]. The refractive index in silicon waveguides depends on the density of free carriers, which is commonly known as the plasma dispersion effect [3]. By removing or injecting the free carriers in a silicon waveguide core, a plasma dispersion modulator (PDM) can change the refractive index of the waveguide and induce a phase shift in the guided light. The mechanism for changing the carrier density can be based on a carrier depletion (PN junction) or carrier injection (PIN junction), which the cross sections are shown in Fig. 5.1.

However, as shown in Equation 2.14 and in Fig. 2.21, a spurious intensity modulation always accompanies the phase modulation, which can be a problem in coherent communication systems that make use of complex multilevel quadrature modulation formats, as well as analog applications such as microwave photonics. In other material systems, pure phase modulators based on the Pockels effect are preferred, but this effect is not present in silicon.

To realize a pure phase modulation in a silicon photonics platform one can use the thermal effect or introduce new materials with a strong electro-optic effect. In [4], a silicon-organic hybrid modulator is used to implement a pure phase modulation, and demonstrated a 16QAM system at 112 Gbit/s with a BER of 5.1×10^{-5} . However, this silicon organic hybrid integration is not compatible with all silicon photonics platforms. In [5], a thermo-optic phase shifter was used with no extra absorption, but its modulation bandwidth is limited to a few MHz.

Also, with the rising popularity of coherent communication formats and microwave photonics, the requirements on the modulators are becoming more diverse: Some applications need intensity modulation while others need phase modulation, and this with different dynamic range and linearity.

In this chapter, we will introduce a reconfigurable modulator circuit, which can be tuned to work as either an intensity modulator or a phase modulator [6, 7]. The configurable modulator is implemented by embedding a standard PN junction modulator into a tunable MZI which consists of two tunable couplers and a phase shifter. By tuning the tunable couplers and the phase shifter, the phase and amplitude response of the modulator circuit

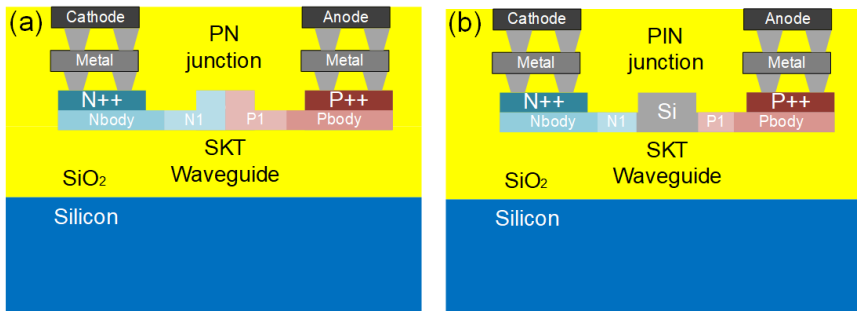


Figure 5.1: Cross section of PN and PIN junction based modulators: (a) PN junction; (b) PIN.

can be reconfigured, adjusting the phase modulation range, intensity modulation range, insertion loss and modulation nonlinearity. Experimental results show that it can work as a phase modulator with a phase change of 0.3π , or as an intensity modulator with a 13 dB extinction ratio, within a reversed DC bias voltage from 0 to 10 V, while it can also provide a pure phase modulation with a spurious intensity modulation of 0.06 dB within the same voltage range.

5.2 Optical design and principle

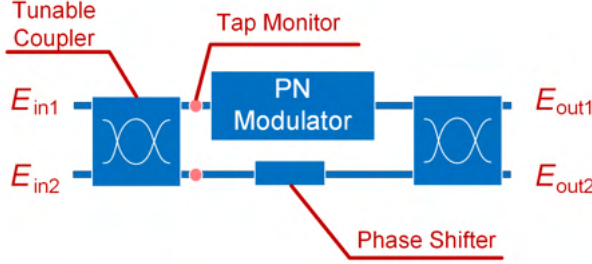


Figure 5.2: Schematic of a reconfigurable modulator

The schematic of the reconfigurable modulator is shown in Fig. 5.2, in which the tunable couplers are implemented with a double-stage MZI structure, introduced in Chapter 3.2.1, and the phase shifter we use is a thermal phase shifter, introduced in Chapter 2.2.1. The double-stage-MZI based tunable coupler can reach a 0 to 1 coupling ratio tuning, with a high tolerance to fabrication variation.

When we describe the modulator response as $\alpha(V)e^{-j\phi_m(V)}$, the transformation matrix of the reconfigurable modulator using a balanced MZI can be calculated as [6]:

$$\begin{bmatrix} E_{out1} \\ E_{out2} \end{bmatrix} = \begin{bmatrix} \sqrt{(1-\kappa_2)} & j\sqrt{\kappa_2} \\ j\sqrt{\kappa_2} & \sqrt{(1-\kappa_2)} \end{bmatrix} e^{-j\frac{Ln_{eff}\omega_c}{c}} \begin{bmatrix} \alpha(V)e^{-j\phi_m(V)} & 0 \\ 0 & e^{-j\phi_s} \end{bmatrix} \begin{bmatrix} E_{in1} \\ E_{in2} \end{bmatrix} \quad (5.1)$$

where c is the light speed in vacuum, L is the waveguide length, n_{eff} is the effective refractive index of the waveguide and ω_c is the angular frequency of the optical carrier. For an ideal case (no loss and no dispersion), this propagation factor can be set as 1.

Then the modulated light signal can be expressed as

$$E_{out1} = [\sqrt{(1-\kappa_1)(1-\kappa_2)}\alpha(V)e^{-j\phi_m(V)} - \sqrt{\kappa_1\kappa_2}e^{-j\phi_s}]E_{in1} \quad (5.2)$$

According to Equation 3.26, the reconfigurable modulator will have the lowest insertion loss from port in1 to port out1 when $\kappa_1 = \kappa_2$, if the insertion loss of the modulator can be ignored. With a noticeable lossy modulator, κ_1 will have to be slightly smaller than κ_2 to make sure that the light can have a totally destructive interference at output port 2. But to have a simpler description, we still set $\kappa_1 = \kappa_2 = \kappa$ here, then Equation 5.2 become:

$$E_{out1} = [(1-\kappa)\alpha(V)e^{-j\phi_m(V)} - \kappa e^{-j\phi_s}]E_{in1} \quad (5.3)$$

Ideal pure phase modulator Now, if we assume that $\alpha(V)$ is constant, which means that the modulator does introduce extra insertion loss but no spurious intensity modulation, then Equation 5.3 can be expanded like Equation 4.8 (with an extra loss factor α):

$$\begin{aligned}
E_{\text{out1}} &= [(1 - \kappa)\alpha J_0(\frac{\pi}{V_\pi} V_s) - \kappa e^{-j\phi_s}] e^{-j(\omega_c t)} + \\
& j(1 - \kappa)\alpha J_1(\frac{\pi}{V_\pi} V_s) (e^{-j((\omega_c - \omega_s)t} + e^{-j((\omega_c + \omega_s)t)}) \\
& = A_0 e^{-j\phi_{A_0}} e^{-j(\omega_c t)} + jA_1 (e^{-j((\omega_c - \omega_s)t)} + e^{-j((\omega_c + \omega_s)t)})
\end{aligned} \tag{5.4}$$

and now:

$$\begin{aligned}
A_0 e^{-j\phi_{A_0}} &= (1 - \kappa)\alpha J_0(\frac{\pi}{V_\pi} V_s) - \kappa e^{-j\phi_s} \\
A_1 &= (1 - \kappa)\alpha J_1(\frac{\pi}{V_\pi} V_s)
\end{aligned} \tag{5.5}$$

From here. it can be seen that the phase relation between the sidelobes is fixed, while the optical carrier's phase state can be tuned thanks to the MZI interference.

When this modulated light signal is received by a photodetector (PD), we can get the photocurrent with the square law detection, which can be expressed as:

$$\begin{aligned}
I_{\text{PD}} &= \mathcal{R} E_{\text{out1}} E_{\text{out1}}^* \\
&= \mathcal{R} [A_0 e^{-j\phi_{A_0}} e^{-j(\omega_c t)} + jA_1 (e^{-j((\omega_c - \omega_{\text{rf}})t - \phi_{\text{rf}})} + e^{-j((\omega_c + \omega_{\text{rf}})t + \phi_{\text{rf}})})] \\
&\times [A_0 e^{j\phi_{A_0}} e^{j(\omega_c t)} - jA_1 (e^{j((\omega_c - \omega_{\text{rf}})t - \phi_{\text{rf}})} + e^{j((\omega_c + \omega_{\text{rf}})t + \phi_{\text{rf}})})] \\
&= \mathcal{R} (A_0^2 + 2A_1^2 - 4A_0 A_1 \sin(A_0) \cos(\omega_{\text{rf}} t + \phi_{\text{rf}}) + 2A_1^2 \cos(2\omega_{\text{rf}} t + 2\phi_{\text{rf}}))
\end{aligned} \tag{5.6}$$

where \mathcal{R} is the responsibility of the used PD.

Then we can know that the field amplitude of the recovered RF signal at the original frequency will be:

$$\begin{aligned}
I_{1st} &= -4\mathcal{R} A_0 A_1 \sin(\phi_{A_0}) \cos(\omega_{\text{rf}} t + \phi_{\text{rf}}) \\
&= 4\mathcal{R} \kappa (1 - \kappa) \alpha J_1(\frac{\pi}{V_\pi} V_{\text{rf}}) \sin(\phi_s) \cos(\omega_{\text{rf}} t + \phi_{\text{rf}})
\end{aligned} \tag{5.7}$$

which is determined by the coupling ratio of the tunable couplers κ and the phase shifter's phase change ϕ_s .

Phase modulator with spurious intensity modulation Let's now look at the more realistic scenario, where the $\alpha(V)$ is not a constant but varies with input voltage, so the modulator will induce both phase modulation and intensity modulation simultaneously. The simplest case is that the propagation loss is proportional to the applied voltage, as:

$$\alpha(V) = \alpha_0 + mV_s \cos(\omega_s t) \tag{5.8}$$

where α_0 is the static loss factor, m is the modulation efficiency. Then the Equation 5.3 becomes:

$$\begin{aligned}
E_{\text{out1}} &= [(1 - \kappa)\alpha(V) e^{-j\phi_m(V)} - \kappa e^{-j\phi_s}] E_{\text{in1}} \\
&= [(1 - \kappa)\alpha_0 e^{-j\phi_m(V)} - \kappa e^{-j\phi_s}] E_{\text{in1}} + (1 - \kappa)mV_s \cos(\omega_s t) e^{-j\phi_m(V)} E_{\text{in1}} \\
&\simeq [(1 - \kappa)(\alpha_0 J_0(\frac{\pi}{V_\pi} V_s) + jmJ_1(\frac{\pi}{V_\pi} V_s)) - \kappa e^{-j\phi_s}] e^{-j(\omega_c t)} + \\
&(1 - \kappa)(j\alpha_0 J_1(\frac{\pi}{V_\pi} V_s) + \frac{m}{2} J_0(\frac{\pi}{V_\pi} V_s)) (e^{-j((\omega_c - \omega_s)t} + e^{-j((\omega_c + \omega_s)t)})
\end{aligned} \tag{5.9}$$

where higher order sidelobes are ignored.

If this intensity and phase modulated signal is fed into a PD, the photocurrent will be expressed as:

$$I = \mathcal{R}E_{\text{out}1}E_{\text{out}1}^*$$

$$I_{1st} = 2\mathcal{R}(1 - \kappa)[2\kappa\alpha_0J_1 \sin(\phi_s) + m(\alpha_0(1 - \kappa)(2J_1^2 + J_0^2) - \kappa J_0 \cos(\phi_s))] \cos(\omega_s t) \quad (5.10)$$

In this equation, ϕ_s can vary in the range of $(0, 2\pi)$, while κ should be in the range of $(0, 0.5)$, such that more light should be coupled into the modulator than into the reference arm with the static phase shifter. To suppress the intensity modulation, I_{1st} can be minimized by tuning the κ and ϕ_s when m is determined.

An intuitive way to understand the behavior of this tunable modulator circuit is through the use of phasor diagrams. The modulus variation of the light vector reflects intensity modulation, and the rotation of the light vector shows the phase modulation. Thus, a pure phase modulator will have modulation on a circle, as shown in Fig. 5.3(a). For a PN junction based modulator, when the applied reversed voltage increases, the carrier density in the waveguide will get lower and the absorption will get lower as well, making the phasor longer, as shown in Fig. 5.3(b). For PIN junction-based modulator, when the applied forward voltage increases, the carrier density in the waveguide gets higher and the absorption increases, as shown in Fig. 5.3(c). Therefore, the modulation curves of PN and PIN modulators deviate from the circle.

When the modulator is embedded in an MZI structure, part of the light is guided through the modulator while the rest will experience a static phase shift before the two parts are again combined. Fig. 5.4 shows phasor plots of the reconfigurable modulator with a PN junction. The output amplitude is the magnitude of the phasor, while the output phase rotation is indicated by the angle of the phasor. The phasor of the modulator arm τ_1 is drawn in red, while the phasor of the phase shifter arm τ_2 is drawn in blue. The sum of the phasors, corresponding to the output signal, is drawn in green. The relative magnitude and orientation of the red and blue phasor is determined by the κ_1, κ_2 of the TCs and ϕ_s of the static phase shifter. When the carrier depletion modulator is being modulated, the red phasor will move. For instance, with a carrier depletion modulator rotates τ_1 clockwise and increases in amplitude, as shown as the red curve. As a result, the angle between τ_1 and τ_2 changes, which has an effect on the intensity of the sum of the two phasors. When the magnitude and phase of the blue phasor is properly chosen, the reconfigurable modulator can be set

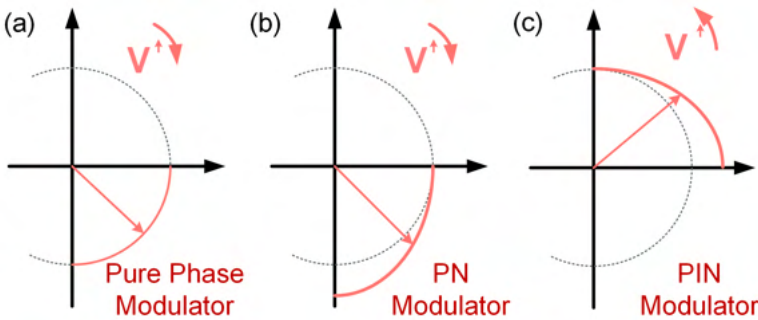


Figure 5.3: Modulation curve for pure phase modulator (a), PN junction modulator (b), and PIN junction modulator (c).

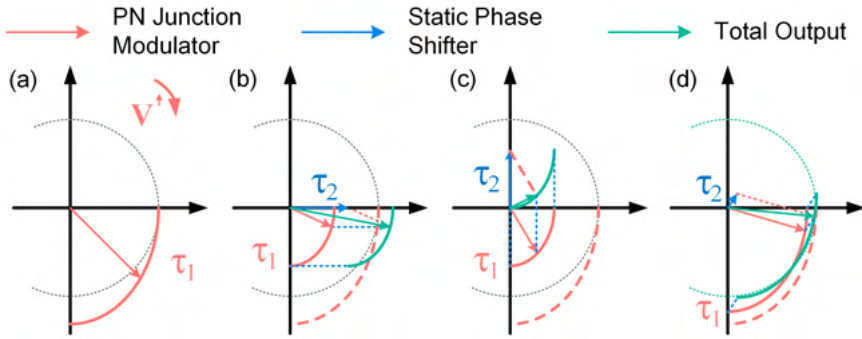


Figure 5.4: Phasor diagrams for a carrier depletion modulator based configurable modulator. (a) All light feeds into the PN junction modulator; (b) half of the light feeds into the modulator and the other half goes into the phase shifter with zero phase shift; (c) A condition for intensity modulation; (d) A condition for pure phase modulation.

as an intensity modulator (Fig. 5.4(c)) and optimized pure phase modulator (Fig. 5.4(d)). Other optimization targets like better linearity or a larger phase modulation range can also be achieved with a similar method.

From the phasor plots, we can also get that the optimization depends on the modulation signal voltage swing, or the phase range covered. A larger phase range will lead to a larger residual intensity variance. Thus, in a normal small signal model, the spurious intensity modulation can be suppressed to near 0, while in large signal model, this optimization can help, but cannot reach a real pure phase modulation.

5.3 Simulation and Tested results

To implement a simulation, a physical depletion modulator model with $1000 \mu\text{m}$ length is constructed, and its direct current response is shown in Fig. 2.21(a) and 2.21(b) [8]. As can be seen, for reverse biased voltage from 0 to 6 V, the depletion modulator provides a 0.4π phase modulation (from 0° to -71.7°) and a 1.26 dB spurious intensity modulation (from 0.75 to 0.87).

From Equation 5.2, we can find three degrees of freedom, κ_1 , κ_2 and ϕ_s to minimize the intensity modulation. First we performed a sweeps of κ_1 and κ_2 at fixed ϕ_s . Fig. 5.5 (a) and 5.5(b) show the modulation at $\phi_s = 0$ and $\phi_s = -0.2\pi$. The contour line shows the intensity modulation, where lower values are better. From Fig. 5.5(a), it can be found that two areas have lower intensity modulation than the other parts. Area 1 is located near $\kappa_1 = 1$ or $\kappa_2 = 1$, where nearly no light is fed to the depletion modulator, which will result in little or no modulation at all. Area 2 is more useful, where κ_1 and κ_2 are somewhat lower than 0.5. Comparing Fig. 5.5(a) and 5.5(b), we can find that different ϕ_s lead to different varying range, but the target area still locates at a similar area. In addition, the figures show a symmetry between κ_1 and κ_2 , and this symmetry allows us to set $\kappa = \kappa_1 = \kappa_2$ for the remainder of the discussion and then sweep κ (from 0.02 to 0.49), and ϕ_s (from $-\pi$ to π) to investigate how the intensity modulation changes, and the simulation results are shown in Fig. 5.6. Again, the contour line shows the intensity modulation. A,B,C,D represent four different operating points and their corresponding polar diagrams. Red curves show the modulation curve of the PN junction modulator and the green ones show the modulation curve of the reconfigurable MZI modulator. In a crescent region, the minimum spurious intensity modulation can be suppressed down to 0.023 dB variance minimally, as shown at the operation point A and in Fig.5.8. At point B, the modulation curve shows a large intensity modulation, but with a small phase modulation, turning the reconfigurable modulator into an intensity modulator. At point C, it can be seen that the total insertion loss is reduced, but the phase modulation range is also significantly suppressed. At point D, the modulation curve is close to the zero point, and phase modulation of more than π phase

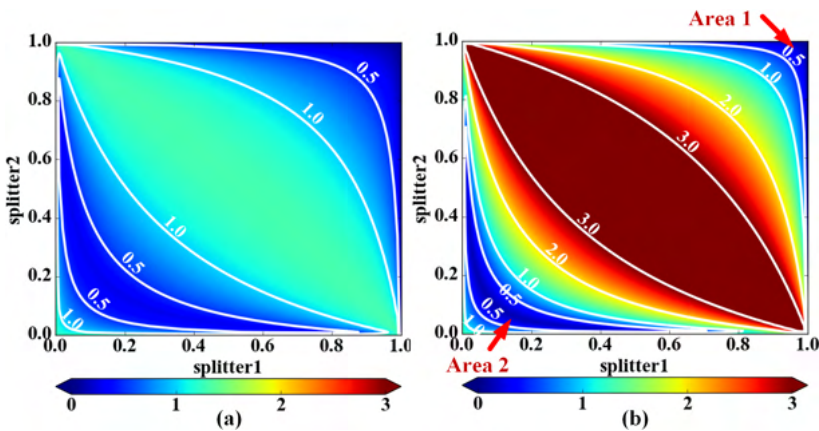


Figure 5.5: (a) Intensity modulation with PN junction modulator: sweep κ_1 and κ_2 at $\phi_s = 0$; (b) Intensity modulation with PN junction modulator: sweep κ_1 and κ_2 at $\phi_s = -0.2\pi$.

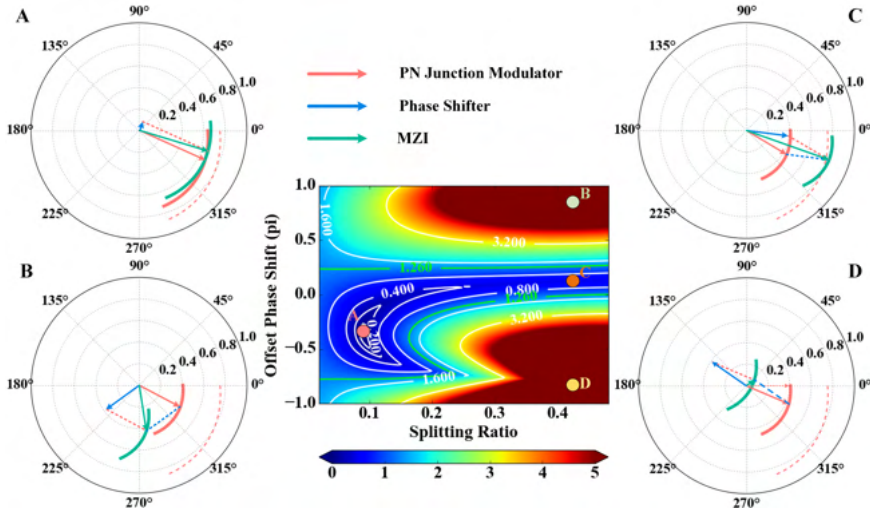


Figure 5.6: Simulation results with PN junction modulator for minimal spurious intensity modulation: sweep splitting ratio and offset phase shifts. Operation points: A: $\kappa = 0.092$ and $\phi_s = -0.384\pi$; B: $\kappa = 0.42$ and $\phi_s = 0.8\pi$; C: $\kappa = 0.42$ and $\phi_s = 0.05\pi$; D: $\kappa = 0.42$ and $\phi_s = -0.8\pi$.

range is achieved, which makes the modulator suitable for binary π phase modulation.

From Fig.5.6, it can be seen that different operation points lead to different phase modulation ranges, optical losses, and nonlinearities. The other performance metrics are plotted in Fig. 5.7. Fig. 5.7(a) shows the spurious intensity modulation as shown in Fig. 5.6. Fig. 5.7(b) indicates the nonlinearity of the phase modulation, which is defined by the maximum phase deviation from a fitted straight line over the phase modulation range, and it should be as low as possible for many microwave photonic applications. Fig. 5.7(c) expresses the minimum intensity (i.e the lowest optical transmission during modulation), which should be as high as possible. Fig. 5.7(d) elaborates the phase modulation range. In addition, the green curves in those figures are the characteristics of the bare depletion modulator model that we used, which are 1.26 dB intensity modulation, 0.058 nonlinearity, 0.750 minimum intensity and 0.398 π phase modulation. According to Fig. 5.7, we can determine the operation point to implement a phase modulator with required performance.

The green curve in Fig. 5.8 shows a modulation curve for pure phase modulation (as operation point A in Fig.5.6), with a intensity variance of 0.02 dB, 0.040 nonlinearity, a phase modulation range of 0.41 π and 1 dB extra optical loss. If a large modulation range is needed, several of these configurable modulator circuits can be cascaded to achieve a larger modulation range with a low spurious intensity modulation. These cascaded modulators can be driven from the same high-speed signal, not complicating the electrical control.

We fabricated this reconfigurable modulator circuit in IMEC’s iSiPP50G platform [9]. A photo is shown in Fig. 5.9(a). The phase shifters of the tunable couplers are driven by PXI chassis multi-channel driver, and the optical status is monitored by two tap PDs. By monitoring the optical power on each arm of the MZI, we can roughly know the configuration of the system. Then optimization algorithms, like gradient decent method, can be

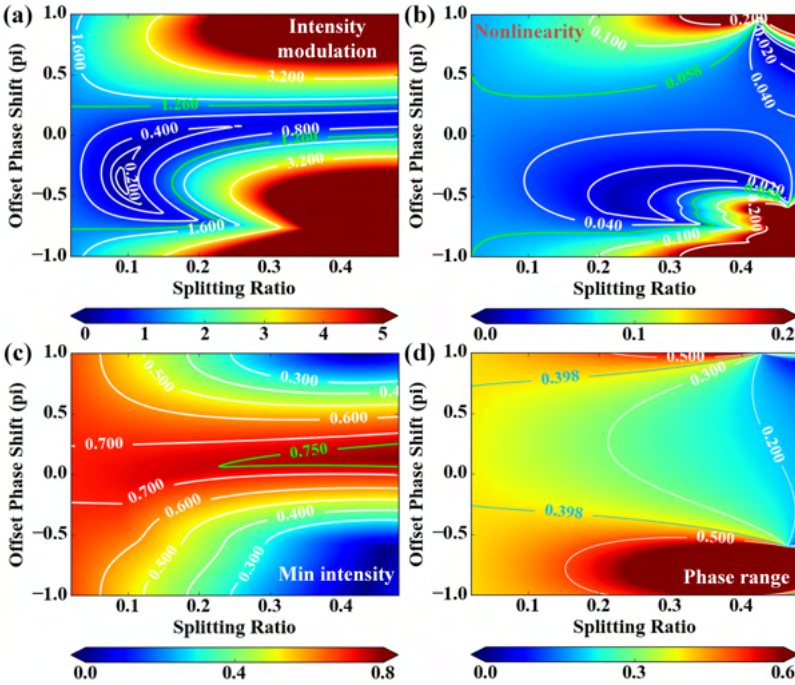


Figure 5.7: Simulation results with PN junction modulator within 0 V to 6 V. (a) spurious intensity modulation; (b) nonlinearity of phase modulation; (c) minimal intensity; (d) phase modulation range. Green curve show the performance of the used depletion modulator.

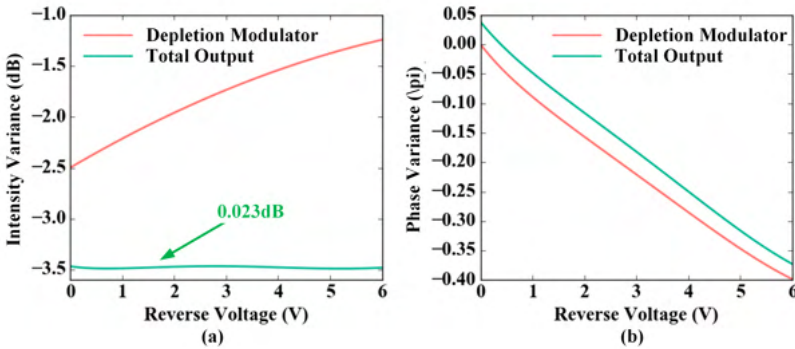


Figure 5.8: DC response of a PN junction modulator (red) and the configurable MZI modulator working at $\kappa_1 = \kappa_2 = 0.092$ and $\phi_s = -0.384\pi$ (green).

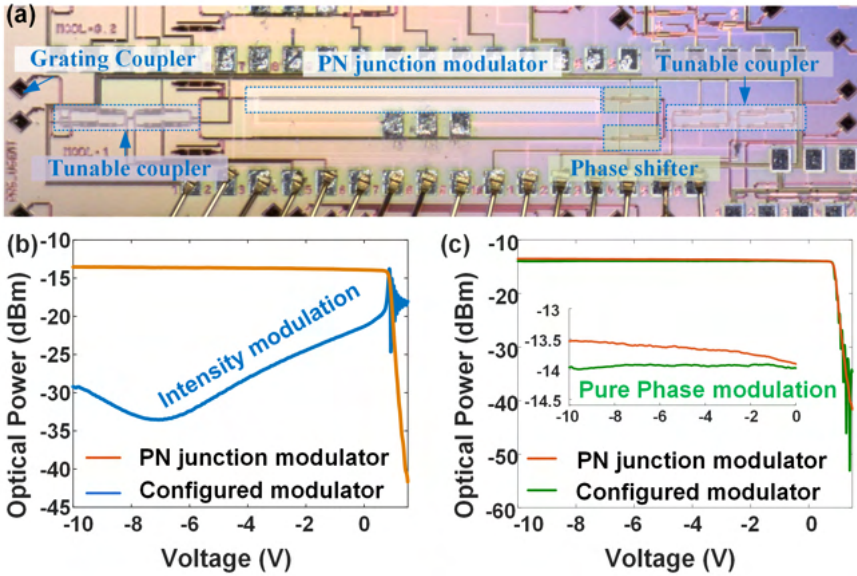


Figure 5.9: (a) Photo of the fabricated circuit; (b) DC response of the modulator as phase modulator and as intensity modulator; (c) DC response of the modulator as pure phase modulator. The orange line: phase modulator. The blue line: intensity modulator. The green line: pure phase

deployed to find the optimum operational points.

Figure 5.9(b-c) show the output power as function of drive voltage for three working states of the modulator. The voltage swing is set from -10 V to +1.5 V. From -10 V to 0.7 V (threshold voltage of PN junction) the PDM works as a depletion modulator, and with a higher voltage it works as an injection modulator. In Fig. 5.9(b), the orange line shows the circuit response as the "naked" PN junction modulator response, where the coupling ratio κ of the tunable couplers is set to 0 and all light goes through the PDM. As shown, the insertion loss, and therefore the intensity modulation of the PDM increases gradually from -10 V to 0.7 V, and increases dramatically after 0.7 V, which matches the threshold voltage of a PN junction. When the κ of the tunable coupler is set to near 0.5, the full circuit works as an intensity modulator, and the DC response is the blue curve. The bias point of the MZI can be tuned by the phase shifter. The extinction ratio of the MZI is more than 12dB. Fig. (c) shows another working state (in green), where the response is optimized for pure phase modulation. As shown, the intensity change in the reverse biased region is reduced from 0.5 dB to around 0.06 dB, but in the forward bias this setting will generate some interference, indicating that we are indeed sending light through both arms of the MZI to compensate the spurious intensity modulation in reverse bias.

As a proof of concept, the PN junction modulator is not delicately designed for high-speed applications. The 3 dB bandwidth of the fabricated modulated is limited to around 4 GHz. A better iterated modulation design is implemented as a modulator block in the fully integrated signal processor design, where details will be shown in Chapter 7, and scaled-up versions (Dual and quad parallel MZM) have been fabricated and will be characterized in

the future.

5.4 Conclusion

In this chapter, we introduced the reconfigurable modulator design, which can be configured as an intensity modulator or a phase modulator. The modulation performance can be further optimized for specific requirements, such as pure phase modulation. On the other hand, the reconfigurable modulator can create a modulated light signal with a tunable carrier frequency (in amplitude and phase), which is the intrinsic reason of the tuning in intensity modulation and phase modulation, and it also enable the universal RF filter with double sideband modulation, which details will be introduced in Chapter 7.

References

- [1] J. Witzens, “High-Speed Silicon Photonics Modulators,” *Proceedings of the IEEE*, vol. 106, pp. 2158–2182, 12 2018.
- [2] W. Bogaerts, P. D. Heyn, T. V. Vaerenbergh, K. D. Vos, S. K. Selvaraja, T. Claes, P. Dumon, P. Bienstman, D. V. Thourhout, and R. Baets, “Silicon microring resonators,” *Laser & Photonics Reviews*, vol. 6, pp. 47–73, 1 2012.
- [3] R. Soref and B. Bennett, “Electrooptical effects in silicon,” *IEEE Journal of Quantum Electronics*, vol. 23, pp. 123–129, 1 1987.
- [4] M. Lauer mann, R. Palmer, S. Koeber, P. C. Schindler, D. Korn, T. Wahlbrink, J. Bolten, M. Waldow, D. L. Elder, L. R. Dalton, J. Leuthold, W. Freude, and C. Koos, “Low-power silicon-organic hybrid (SOH) modulators for advanced modulation formats,” *Optics Express*, vol. 22, p. 29927, 12 2014.
- [5] N. C. Harris, Y. Ma, J. Mower, T. Baehr-Jones, D. Englund, M. Hochberg, and C. Galland, “Efficient, compact and low loss thermo-optic phase shifter in silicon,” *Optics Express*, vol. 22, p. 10487, 5 2014.
- [6] H. Deng and W. Bogaerts, “Pure phase modulation based on a silicon plasma dispersion modulator,” *Optics Express*, vol. 27, p. 27191, 9 2019.
- [7] H. Deng and W. Bogaerts, “Configurable Phase/Amplitude Modulator Circuit based on Silicon Plasma Dispersion,” *IEEE International Conference on Group IV Photonics GFP*, vol. 2021-December, 2021.
- [8] H. Yu, M. Pantouvaki, J. V. Campenhout, D. Korn, K. Komorowska, P. Dumon, Y. Li, P. Verheyen, P. Absil, L. Alloatti, D. Hillerkuss, J. Leuthold, R. Baets, and W. Bogaerts, “Performance tradeoff between lateral and interdigitated doping patterns for high speed carrier-depletion based silicon modulators,” *Optics Express*, vol. 20, p. 12926, 6 2012.
- [9] M. Pantouvaki, S. A. Srinivasan, Y. Ban, P. De Heyn, P. Verheyen, G. Lepage, H. Chen, J. De Coster, N. Golshani, S. Balakrishnan, P. Absil, and J. Van Campenhout, “Active Components for 50 Gb/s NRZ-OOK Optical Interconnects in a Silicon Photonics Platform,” *Journal of Lightwave Technology*, vol. 35, pp. 631–638, 2 2017.

6

Micro-Transfer-Printing SOA and Lasers

In this chapter, we will briefly introduce the transfer printing process on the imec iSiPP50G platform, and show some demonstrators with transfer printed SOAs. An SOA-MZI is implemented, which can be used for wavelength conversion based on cross-gain and cross-phase modulation. In addition, we processed and characterized two tunable lasers. Dr. Jing Zhang provides the laser designs. III-V lab design and fabricate the SOA coupons. Meanwhile, the release of SOA coupons and the pre-processing of silicon photonic samples are implemented by ir. Emadreza Soltanian. The author manages the transfer printing process, metal lift-off, and system characterization.

6.1 Micro-Transfer-Printing Process on iSiPP50G

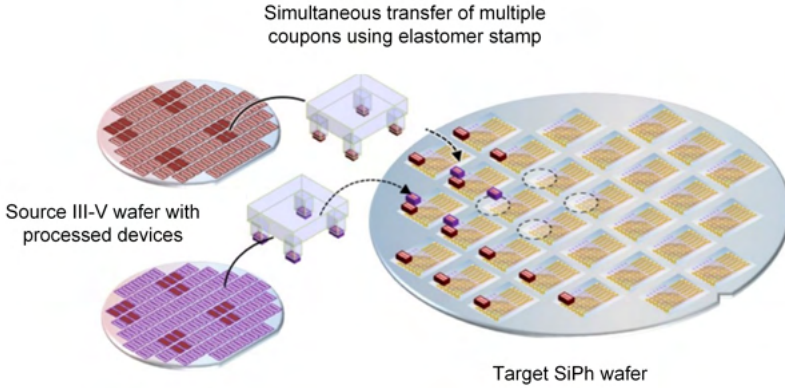


Figure 6.1: Schematic of μ TP-based integration on 200 mm or 300 mm Si photonic wafers in a parallel manner. Figure is regenerated from dr. Jing Zhang.

As shown in the previous chapters, silicon photonic circuits bring together a wider variety and greater number of optical components to achieve complex functionalities. However, silicon, as an indirect bandgap material, cannot provide optical gain, which limits the scaling towards larger and more complex circuits. III-V materials, on the other hand, are ideal for optical amplification. Several heterogeneous III-V-on-Si integration techniques have already been proposed, such as flip-chip integration, wafer bonding, micro-transfer-printing (μ TP) and hetero-epitaxial growth [1]. Among these technologies, μ TP shows great potential for scalable, economical and flexible integration of III-V SOA on silicon photonic platforms.

Process of SOA coupons The μ TP technique uses a stamp to pick up a prefabricated SOA coupon from a III-V source wafer and print it on to the target position of the silicon photonic sample (or wafer). The basic concept is shown in Fig. 6.1, and a schematic of a transfer printed device is shown in Fig. 6.2. In this process, SOA devices, termed "coupons",

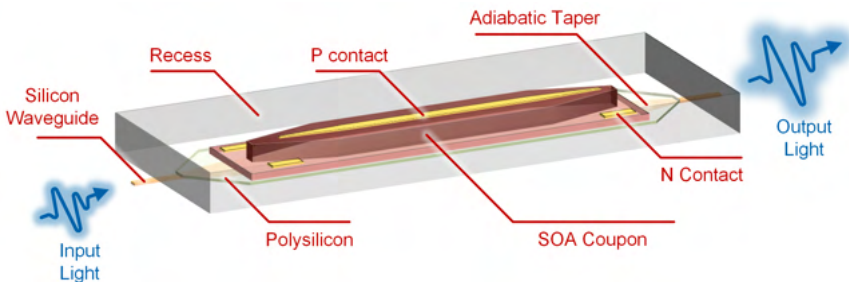


Figure 6.2: A schematic of a transfer printed SOA coupon.

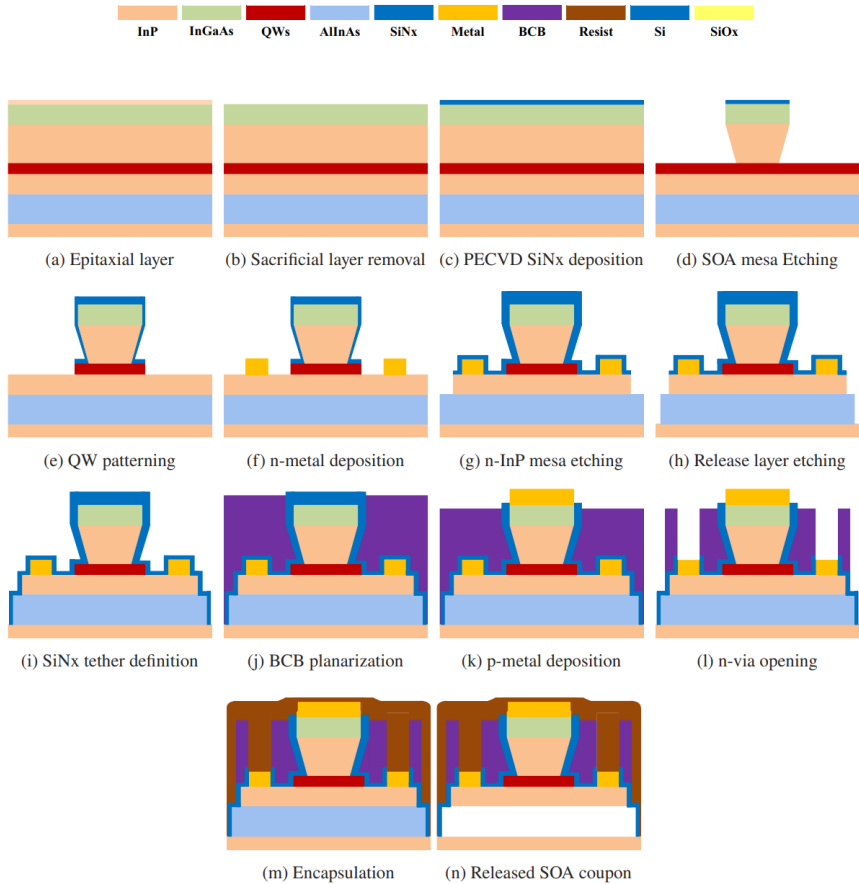


Figure 6.3: Process flow of SOA device fabrication on the source InP substrate. Figure is regenerated from [2].

are fabricated on a 2” wafer of InP epitaxial layer stack, grown by metal-organic vapor-phase epitaxy (MOVPE), which the process flow is shown in Fig. 6.3. In this thesis work, all SOA coupons are fabricated by III-V lab in France. A release layer is incorporated underneath the SOA device layer stack. After the devices are patterned, the release layer is selectively etched, resulting in free-standing components held in place by tethers. The concept is as shown in Fig. 6.3(l) and the fabricated sample SEM and microscope images are shown in Fig. 6.4.

Post-process of silicon photonic chips As a fully stacked silicon photonic platform, optical waveguides on the imec iSiPP50G platform are covered with silicon dioxide. Thus, a localized back-end opening (recess) is necessary to allow the SOA coupon to be laminated on the waveguide. The processing flow is shown in Fig. 6.5. During the photonic circuit

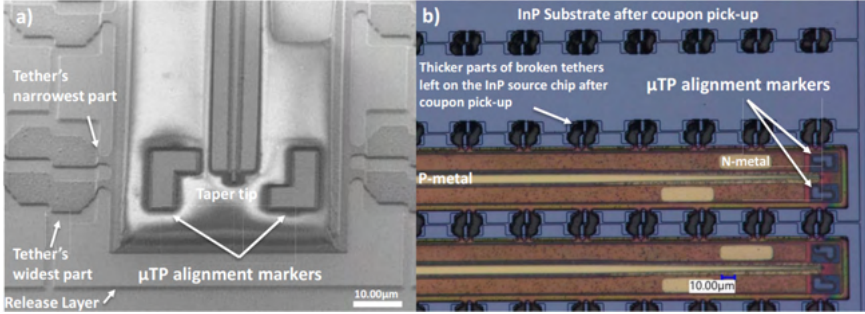


Figure 6.4: A fabricated InP SOA source: a) Side-view SEM image, b) Top-view microscope image. Figures are regenerated from [2].

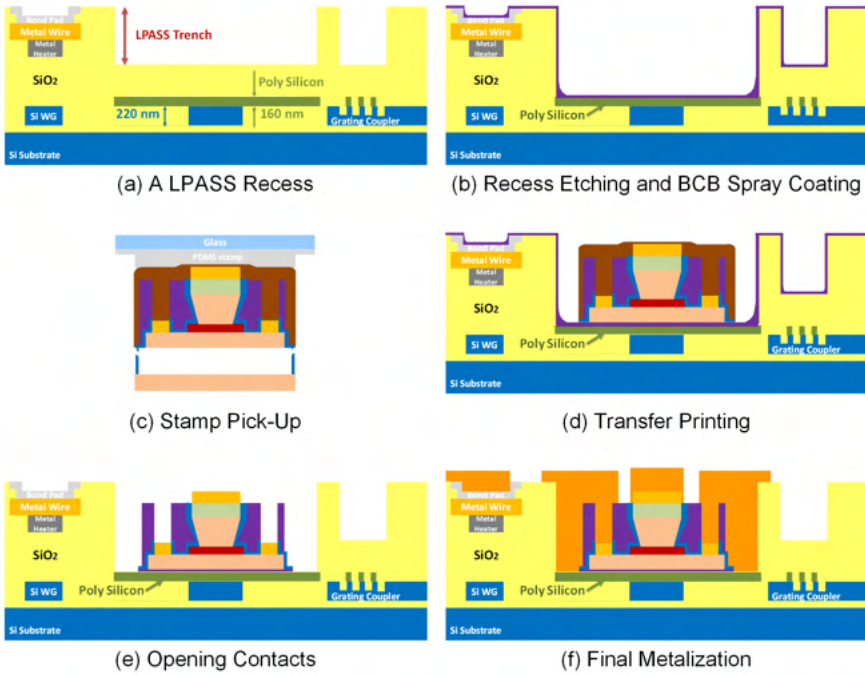


Figure 6.5: Process flow of *iSiPP50G* samples post processing and transfer printing.

design, a poly-crystalline silicon layer is added on top of silicon waveguide, to increase the local silicon thickness to around 380 nm. At the end of the iSiPP50G process flow, the back-end-of-line (BEOL) dielectric stack above the poly-Si waveguide is etched back locally to define a recess, stopping approximately 2.5 μ m above the waveguide, as shown in Fig. 6.5(a).

During the post-processing in the Ghent University clean room, a combination of dry-etch (by RIE) and wet-etch (by BHF) is applied to the chip to remove the remaining 2.5 μ m thick silicon dioxide in the recess. Then, a thin divinylsiloxane bisbenzocyclobutene (DVS-BCB) adhesive layer with a thickness of 150 nm was spray-coated to enhance the bonding strength between the III-V SOA and the underlying Si-waveguide, as shown in Fig. 6.5(b).

Micro-transfer printing process After the post process of the silicon photonic chip, a polydimethylsiloxane (PDMS) stamp is laminated against the released SOA coupons. When the stamp is rapidly pulled away, the coupons adhere due to strong bonding, break the tethers, transferring the devices to the stamp, as shown in Fig. 6.5(c). After pick-up, the stamp now carrying the device (either single or array), is aligned to the destination wafer using pattern recognition through the transparent PDMS stamp. The printing process entails laminating the stamp to the target wafer and retracting it slowly, using a shear force, ensuring the coupons adhere in the target recess, as shown in Fig. 6.5(d). After the process, a selective etching was applied to expose the metal contacts of the SOA devices, and one lift-off metallization step is performed to connect the transfer-printed components with the bondpads on the original silicon photonic sample, which are shown in Fig. 6.5(e) and (f) [3].

In the thesis work, the SOA coupons were fabricated in III-V lab in France, the post processes of silicon photonic samples were implemented by ir. Emadreza Soltanian, and I did the transfer printing process for all the samples.

6.2 SOA Characterization

To characterize transfer-printed SOAs on iSiPP50G samples, several optical circuit designs with embedded SOAs are implemented.

6.2.1 Gain

The simplest design is a straight waveguide to test the gain or loss of the transfer printed SOA coupons. A processed sample is shown in Fig. 6.6, and the used SOA coupons are shown in Fig. 6.4. A light signal from an off-chip laser is coupled into the sample, and the output is fed into a power meter. The SOA coupon is driven by a current source (Keithley). The IV curve is shown in Fig. 6.7(a). By tuning the drive current, the SOA can work as an optical absorber (Gain <0) or an optical amplifier. The result is shown in Fig. 6.7(b). As shown, the SOA become transparent at a driving current of 80 mA, with a power consumption of 140 mW. The input optical power off-chip is 10 dBm. The SOA can provide a higher gain for a lower optical input power [4]. The temperature control of the SOA is very important in such experiments, as the SOA produces a substantial amount of heat, and its efficiency drops with higher temperatures. In this measurement, the sample is put on an aluminum plate with a temperature controller (TEC), which is set at 20 °C.

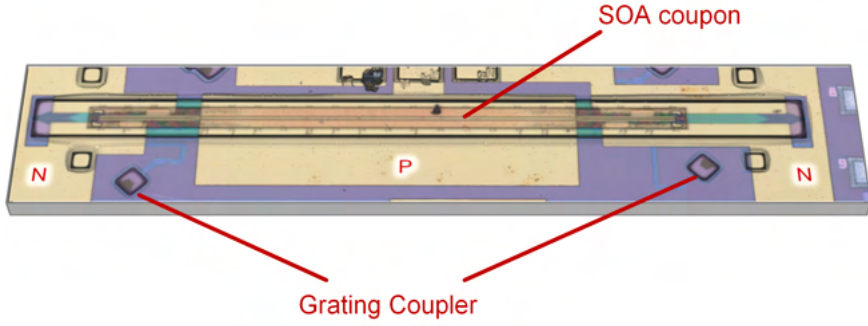


Figure 6.6: A transfer-printed SOA.

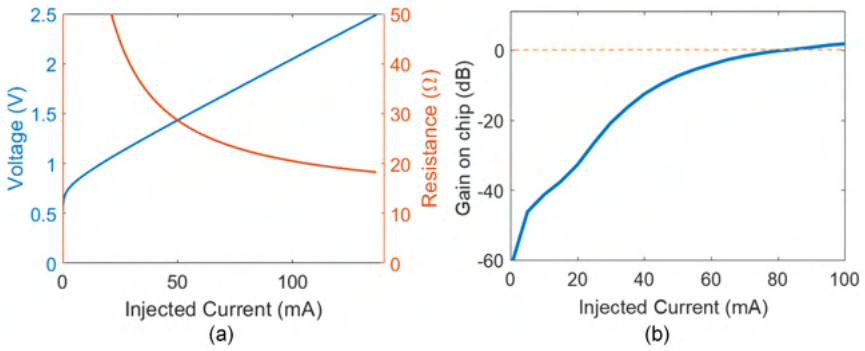


Figure 6.7: Characterization of a SOA. (a) Driving current vs voltage and resistance; (b) Driving current vs optical gain.

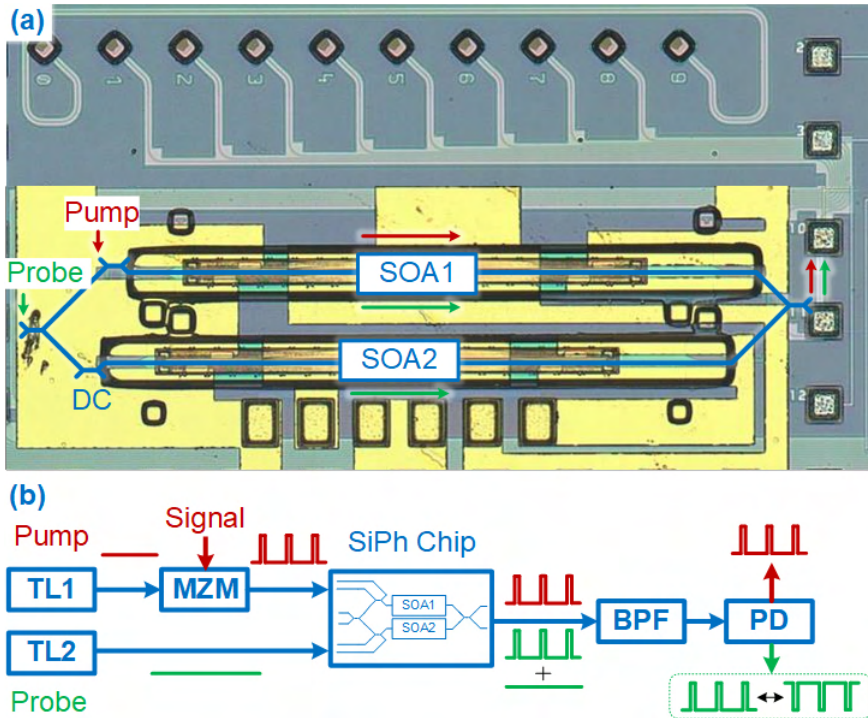


Figure 6.8: Circuits for characterizing cross gain and cross phase modulation of on-chip SOAs. (a) SOA-MZI circuit on chip. SOA: semiconductor optical amplifier; DC: directional coupler; (b) Schematic of the wavelength converter. TL: tunable laser; IM: intensity modulator; BPF: bandpass filter; PD: photodetector.

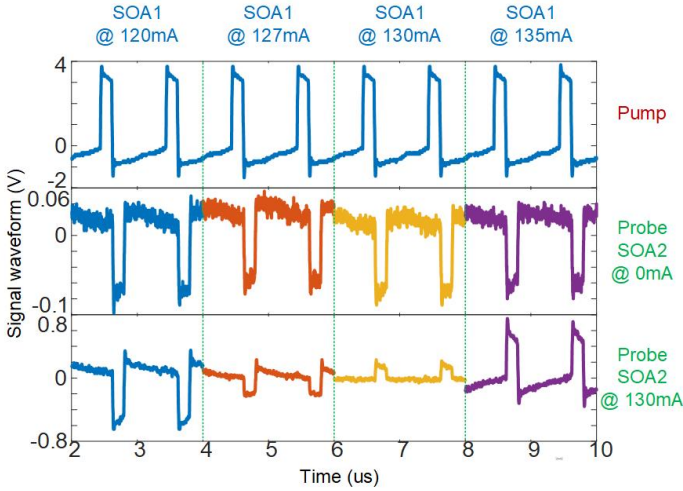


Figure 6.9: Generated electrical waveform with pump light and probe light.

6.2.2 Cross-Gain and Cross-Phase Modulation

SOAs can be used as an optical wavelength converter or optical gate, utilizing its cross-gain modulation (XGM) and cross-phase modulation (XPM).

Device description Here, we used μ TP to integrate two SOAs into both arms of an MZI structure [5]. The processed chip is shown in Fig. 6.8(a). The MZI circuit consists of a DC splitter and combiner, with two balanced arms each containing an SOA. Each arm also has an additional DC allowing us to inject a signal into one arm only. Two SOAs are transfer printed to both arms, to provide optical amplification/absorption, nonlinearity as well as phase tuning. All the optical input/output ports are connected to a grating array for multiple-input multiple-output measurements. Fig. 6.8(b) shows the schematic of the wavelength converter. An external tunable laser (TL1) is used as pump light, whose intensity is modulated by an electrical square wave signal. The pump light is directly fed into the North arm (SOA1). The other tunable laser (TL2), the probe, is coupled to the input of the MZI and passes through both SOAs on the chip. At the output, an external optical bandpass filter (BPF) allows us to select the pump or probe light going to the photodetector.

In this scheme, the pump light and part of the probe light are simultaneously fed into SOA1, so the probe light would be amplitude modulated and phase modulated by the pump. The other fraction of the probe light goes through SOA2 and then interferes with the modulated probe light in the DC combiner. If SOA2 is not driven or is reversed biased, it would show a high absorption and operate as a photodiode, and the probe light in the South arm would be lost. In this case, the wavelength conversion signal recovered from the PD will be the XGM signal. If the SOA2 is driven in forward bias, providing gain, the phase difference in the MZI is now determined by the drive currents of both SOA1 and SOA2. Because of the interference in the combiner, the modulated phase information can be converted to intensity. Thus the wavelength converted signal from the PD will be a combination of the XGM and XPM signal, and with the correct phase delay they can reinforce each other. The

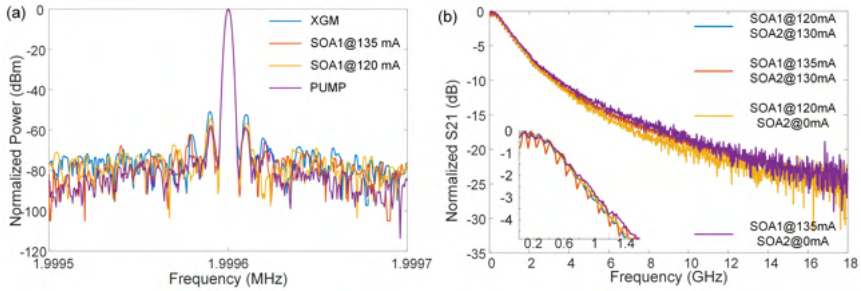


Figure 6.10: High speed performance of the SOA-MZI based wavelength converter. (a) Spectrum of the wavelength converted signal and pump signal. XGM is SOA2 off and the others are SOA2 on; (b) Frequency response of the wavelength converter.

measurement results show that the combined signal can have a better mainlobe-to-sidelobe ratio (MSR) than the XGM-only signal.

XGM and XPM results We implemented the experiments using two external tunable lasers, an intensity modulator and a tunable BPF, as shown in Fig. 6.8(b). The pump laser was set at 1550 nm, and the probe laser at 1555 nm. A square wave with a duty cycle of 20% was used to modulate the pump light. A tunable optical filter (Finisar waveshaper) was used as the BPF. By passing the 1550 nm pump light, we can monitor the original waveform with an oscilloscope and use it as a reference, shown in the top plot in Fig. 6.9. Then the BPF was set to 1555 nm and the wavelength converted signal was received by the PD and shown in the second and third plot of Fig. 6.9. The second plot's waveform is acquired with the SOA2 switched off, which makes it an optical absorber. The injection current of the SOA1 has little effect on the waveform, while the inverted waveform verifies that this signal is generated by the XGM in SOA1. The third plot shows the additional effect of the phase difference of the MZI. By tuning the injection current of the SOA1 (the four different colors), the waveform can be flipped to its original state, indicating that it is generated by a combination of XGM and XPM in SOA1.

Mainlobe-to-sidelobe ratio Then we applied a 2 MHz sinusoidal modulation on the pump light, and used an electrical spectrum analyzer to monitor the output of PD. The results are shown in Fig. 6.10(a). As can be seen, the XGM-only signal shows the worst mainlobe-to-sidelobe ratio (MSR), while the combined XPM-XGM signals' MSR are approaching the level of the pump signal. This means the SOA-MZI wavelength converter circuits performs better than a standalone SOA.

Frequency bandwidth The frequency responses of the wavelength converter are measured by a vector network analyzer in different driving states. The results are shown in Fig. 6.10(b), where we see that the curves are mostly overlapped. We also see that the 3 dB bandwidth of the fabricated SOAs are limited to 1 GHz. This may due to the low current density of the drive current, while the current is limited up to around 150 mA to avoid burning.

6.3 Lasers

The main target of transfer-printing SOAs on photonic circuits is to introduce on-chip laser sources [3]. With the help from dr. Jing Zhang, we have two tunable laser designs for the final signal processor, which contains two tunable laser designs.

There are two different laser cavities designed in the laser block for the signal processor, which are based on a Fabry–Pérot (FP) cavity and a ring cavity laser, respectively, as shown in Fig. 6.11. Two ring resonator filters with bend radius of 25 μm and 27 μm are used in each laser cavity to form a Vernier bandpass filter to select the longitudinal modes. The prefabricated SOA coupons are then transfer printed into the laser cavities to provide optical gain. When the gain from the printed SOA is higher than the other accumulated losses in the laser cavity, the lasing will start.

Wavelength tuning There are three thermal phase shifters in each laser cavity: two for the phase tuning in the ring and one for the cavity phase. If we just tune the phase in one ring resonator, the laser wavelength will be tuned with a spacing of the other ring’s FSR (around 4 nm in this implementation) because of the Vernier effect. The tuning results are shown in Fig. 6.12. To be noted is that the results of the FP laser and the ring laser are from different samples, because we accidentally shorted one device. We also used two types of coupons for both experiments, which have different photoluminescence (PL) peaks around 1500 nm and 1550 nm, leading to lasing peaks around 1525 nm and 1575 nm, respectively. From Fig. 6.12, both laser cavities can achieve a tunability of more than 50 nm.

A proper tuning of the three phase shifters in the laser cavities can cover a continuous wavelength range, and the ring laser tuning results are shown in Fig. 6.13. The wavelength tuning results per FSR of the ring are shown in Fig. 6.12, and the tuning within an FSR are shown in Fig. 6.13(a), which are measured with an optical spectrum analyser (OSA). However, the resolution of the used OSA is only 30 pm. A higher wavelength/frequency resolution measurement can be implemented with an electrical spectrum analyser (ESA). Here, we introduced a reference laser source, and beat the laser source on-chip, to generate an RF signal, whose frequency is the difference of the two lasers, as described in Chapter 4.3. The tuning results are shown in Fig. 6.13(b). As can be seen, the laser wavelength can be continuously tuned within around 7 GHz (56 pm), and jump a gap around 12 GHz (96 pm). When compared to a commercial laser source (Syntune laser, S3500, with a 50GHz spacing), this discontinuity meets our system’s requirements.

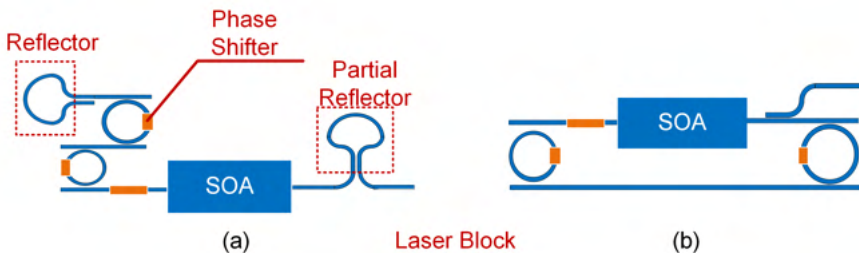


Figure 6.11: Schematic of the laser block in the signal processor. (a) A Fabry–Pérot cavity laser; (b) A ring cavity laser. SOA: Semiconductor optical amplifier. Designed by dr. Jing Zhang

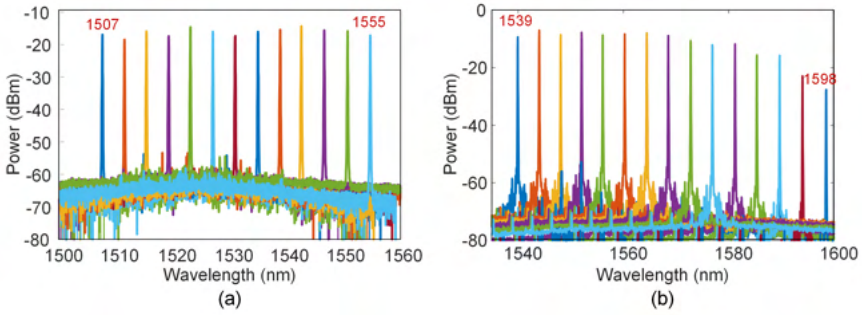


Figure 6.12: Laser tuning results. (a) Using the Fabry–Pérot cavity laser; (b) Using the ring cavity laser. The results are measured from grating couplers.

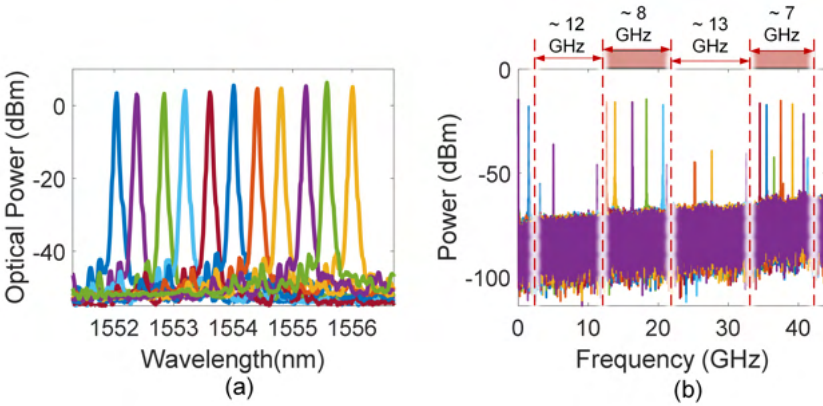


Figure 6.13: Laser continuous tuning results. (a) Tuning within 4 nm, measured with an optical spectrum analyzer; (b) Laser beating results, measured with an electrical spectrum analyzer.

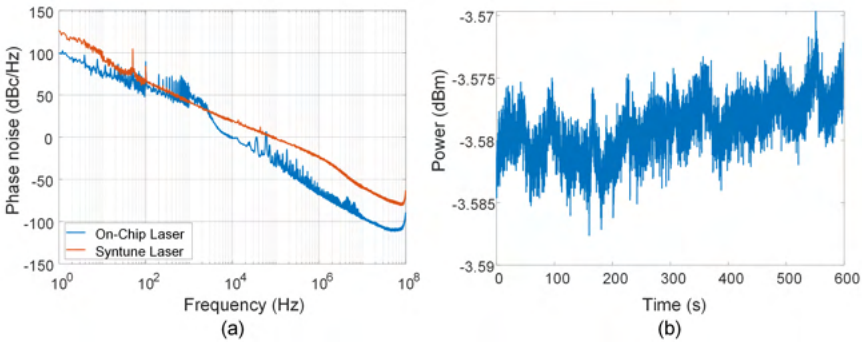


Figure 6.14: Laser's phase noise and stability. (a) Phase noise of the ring laser. (b) Stability test of the ring laser.

Phase noise The phase noise of the ring laser is shown in Fig. 6.14(a), which is measured by an OEwave OE4000 optical phase noise test system. The estimated instantaneous linewidth is 283 kHz. The orange curve is from a commercial laser source (Syntune laser, S3500). Our on-chip laser shows an overall lower phase noise. The stability of the output power is shown in Fig. 6.14(b), from which we can find that the output power of the laser varies with only 0.015 dB within a 600 second timeframe.

6.4 Conclusion

In this chapter, we gave an introduction to the heterogeneous integration of SOA coupons on silicon photonic circuits using the micro-transfer-printing process. And also, we designed a straight waveguide, and an SOA-MZI structure, to characterize the optical gain, and XGM and XPM of the printed SOA coupons.

After that, two tunable laser designs were processed and characterized. Both lasers with different types of SOA coupons showed a tuning range of 50 nm, with lasing peaks around 1525 nm and 1575 nm, respectively. The phase noise of the tunable ring laser was measured, whose estimated instantaneous linewidth was 283 kHz. And the ring laser showed a 0.015 dB power variance within a 600 second timeframe.

Till now, we have introduced two tunable lasers in this chapter, a reconfigurable modulator in Chapter 5, and an universally tunable optical filter in Chapter 3. In the next chapter, all these components and circuits will be combined together to form a complete single-chip signal processor system for analog optical and RF signal processing.

References

- [1] Y. Han, Y. Han, H. Park, J. Bowers, K. M. Lau, and K. M. Lau, “Recent advances in light sources on silicon,” *Advances in Optics and Photonics*, Vol. 14, Issue 3, pp. 404-454, vol. 14, pp. 404–454, 9 2022.
- [2] E. Soltanian, G. Muliuk, S. Uvin, D. Wang, G. Lepage, P. Verheyen, J. Van Campenhout, S. Ertl, J. Rimböck, N. Vaissiere, D. Néel, J. Ramirez, J. Decobert, B. Kuyken, J. Zhang, and G. Roelkens, “Micro-transfer-printed narrow-linewidth III-V-on-Si double laser structure with a combined 110 nm tuning range,” *Optics Express*, vol. 30, no. 22, 2022.
- [3] G. Roelkens, J. Zhang, L. Bogaert, M. Billet, D. Wang, B. Pan, C. J. Kruckel, E. Soltanian, D. Maes, T. Vanackere, T. Vandekerckhove, S. Cuyvers, J. De Witte, I. L. Lufungula, X. Guo, H. Li, S. Qin, G. Muliuk, S. Uvin, B. Haq, C. Op De Beeck, J. Goyvaerts, G. Lepage, P. Verheyen, J. Van Campenhout, G. Morthier, B. Kuyken, D. Van Thourhout, and R. Baets, “Micro-Transfer Printing for Heterogeneous Si Photonic Integrated Circuits,” *IEEE Journal of Selected Topics in Quantum Electronics*, vol. 29, 5 2023.
- [4] B. Haq, S. Kumari, K. Van Gasse, J. Zhang, A. Gocalinska, E. Pelucchi, B. Corbett, and G. Roelkens, “Micro-Transfer-Printed III-V-on-Silicon C-Band Semiconductor Optical Amplifiers,” *Laser & Photonics Reviews*, vol. 14, p. 1900364, 7 2020.
- [5] H. Deng, E. Soltanian, J. Zhang, G. Roelkens, and W. Bogaerts, “Wavelength Converter using Micro Transfer-Printed Optical Amplifiers on a Full SiPh Platform,” *IEEE International Conference on Group IV Photonics GFP*, vol. 2023-April, 2023.

7

Single-chip fully integrated signal processor

In this chapter, we will bring all the components and subsystems together to construct a fully integrated signal processor, which is capable of both generation and detection of analog electrical and optical signals, and program a user-defined filter response. The chip contains two widely tunable lasers, a reconfigurable modulator, optical switches, a fully tunable ring-loaded MZI based optical filter, and two high speed PDs. The individual components and subsystems have been mostly presented in the previous chapters. In this chapter, we will focus on the behavior and applications of the system and subsystems.

7.1 Schematic and Principle

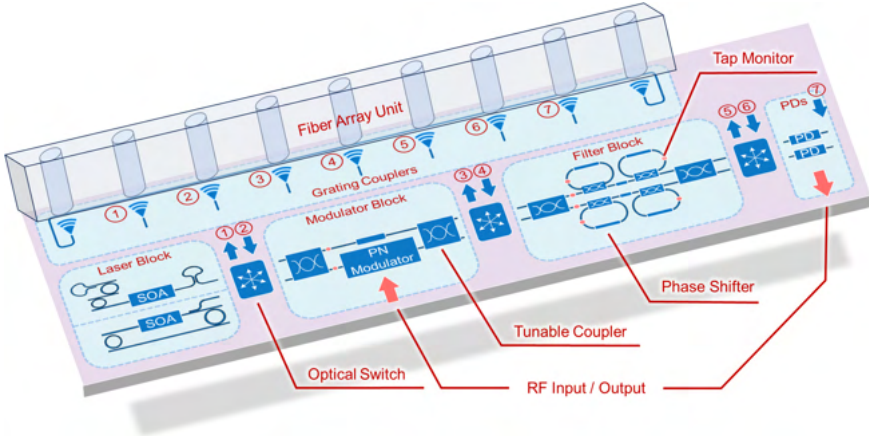


Figure 7.1: Schematic block diagram of the silicon photonic signal processor.

Our signal processor consists of four main blocks, which are

- A laser block: Two tunable lasers with transfer printed SOAs.
- A reconfigurable modulator block: A PN junction based modulator embedded in a tunable MZI structure.
- A universally tunable optical filter block: A tunable MZI structure with two tunable rings loaded on each arm.
- A high-speed PD block: Two vertical Germanium PIN detector.

The schematic is shown in Fig. 7.1.

The longest optical path starts with light generated by the laser source, which is then guided into the modulator circuit, which can be configured for either phase modulation or intensity modulation. The light, now modulated with an RF payload signal, will be fed into the optical filter block, which consists of a four-ring-loaded MZI with tunable couplers and tap monitors. After that, the filtered light signal can be converted back into the microwave domain by the high-speed PDs.

All four functional blocks are connected by optical switches, making it possible to guide the light signal in or out at each connection joint, allowing the processor configuration for both optical and RF signal processing, and even cascading of multiple processors over fiber links. The optical switches themselves are implemented as single stage MZIs or double stage MZIs, depending on the coupling ratio requirements.

7.1.1 Light generation

With the help of the micro transfer printing technology, an on-chip widely tunable laser source is built in our signal processor (details are shown in Chapter 6),

$$E_c = e^{-j\omega_c t} \quad (7.1)$$

If the light signal is coupled to output port 1 (in Fig. 7.1), the chip functions as a tunable laser source.

7.1.2 E/O conversion

Besides coupling off-chip, the light signal can also enter the modulator block (details are shown in Chapter 5). If a voltage signal $V_{in}(t) = v_{in}(t) + V_0$ is fed into the signal processor as the modulation RF drive signal, the optical output field E_{out} of the phase modulated light signal is calculated with Equation 5.3:

$$E_{out} = (1 - \kappa)\alpha E_m - \kappa e^{-j\phi_s} E_c \quad (7.2)$$

where

$$\begin{aligned} E_m &= e^{-j\frac{\pi}{V_\pi} V_{in}(t)} e^{-j\omega_c t} \\ &= (e^{-j\frac{\pi}{V_\pi} V_0} - j\frac{\pi}{V_\pi} e^{-j\frac{\pi}{V_\pi} V_0} v_{in}(t) - \frac{1}{2}(\frac{\pi}{V_\pi})^2 e^{-j\frac{\pi}{V_\pi} V_0} v_{in}^2(t) + \dots) e^{-j\omega_c t} \\ &= (1 - j\frac{\pi}{V_\pi} v_{in}(t) - \frac{1}{2}(\frac{\pi}{V_\pi})^2 v_{in}^2(t) + \dots) e^{-j(\omega_c t + \frac{\pi}{V_\pi} V_0)} \end{aligned} \quad (7.3)$$

Here we used the Taylor expansion instead of the Bessel expansion used in Chapter 5 to get the small signal linear response of the system. In this work, we just focus on the linear response of the entire system, thus higher-order sidebands are ignored for simplification.

So the output of the reconfigurable modulator is:

$$\begin{aligned} E_{out} &= (1 - \kappa)\alpha (1 - j\frac{\pi}{V_\pi} v_{in}(t) - \frac{1}{2}(\frac{\pi}{V_\pi})^2 v_{in}^2(t) + \dots) \\ &\quad e^{-j(\omega_c t + \frac{\pi}{V_\pi} V_0)} - \kappa e^{-j\phi_s} e^{-j(\omega_c t)} \end{aligned} \quad (7.4)$$

for ϕ_s is defined as the phase difference between the two arms, so it can be compensated for the static phase shift induced by V_0 . If we just focus on the first-order of sidelobes, the expression for the output field can be simplified to:

$$E_{out} \sim ((1 - \kappa)\alpha - \kappa e^{-j\phi_s}) + (1 - \kappa)\alpha (-j\frac{\pi}{V_\pi} v_{in}(t)) e^{-j(\omega_c t)} \quad (7.5)$$

Here, if we assume that the modulator's phase modulation is linear, and the input can be decomposed as:

$$\begin{aligned} v_{in}(t) &= \sum_{\omega_s} (v_s \cos(\omega_s t)) \\ &= \sum_{\omega_s} (v_s (\frac{e^{-j\omega_s t} + e^{j\omega_s t}}{2})) \end{aligned} \quad (7.6)$$

the output field becomes:

$$\begin{aligned} E_{out} &= \sum_{\omega_s} [(1 - \kappa)\alpha - \kappa e^{-j\phi_s}] e^{-j\omega_c t} \\ &\quad - j(1 - \kappa)\alpha \frac{\pi v_s}{2V_\pi} (e^{-j\omega_s t} + e^{j\omega_s t}) e^{-j\omega_c t} \\ &= \sum_{\omega_s} [A_0 e^{-j\phi_{A_0}} e^{-j\omega_c t} + jA_1 v_s (e^{-j\omega_s t} + e^{j\omega_s t}) e^{-j\omega_c t}] \end{aligned} \quad (7.7)$$

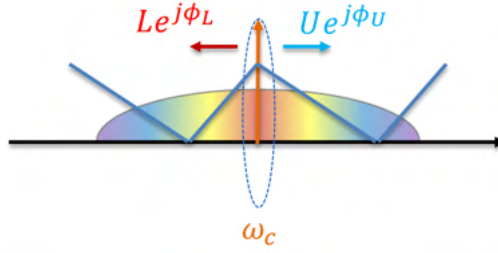


Figure 7.2: A generic optical filter.

where

$$\begin{aligned} A_0 e^{-j\phi_{A_0}} &= (1 - \kappa)\alpha - \kappa e^{-j\phi_s} \\ A_1 &= -(1 - \kappa)\alpha \frac{\pi}{2V_\pi} \end{aligned} \quad (7.8)$$

We clearly see three components of the signal: the carrier at ω_c , and the upper and lower sideband at $\omega_c + \omega_s$ and $\omega_c - \omega_s$, respectively. Now, if the modulated signal is coupled out from optical output port 3, we can get a configurable optical transmitter, which can imprint the RF signal onto an wavelength tunable optical carrier. By tuning the coupling ratio of the tunable couplers and the offset phase shifter, intensity modulation or phase modulation with optimized characteristics can be implemented, as described in Chapter 5.

7.1.3 Tunable microwave photonic filter

If this modulated signal is then fed into the filter block (*O/O conversion*), we can reshape the optical spectrum of the modulated light signal with a four-ring-loaded MZI filter. In the optical domain, the filter bank has a continuous transmission spectrum. But when we want to study the effect of the filters on the modulated microwave spectrum, it is convenient to separate the expression of the filter response into 3 parts using the laser frequency ω_s . As shown in Fig. 7.2, We can set the filtering response of the filter block as:

- Lower sideband: $L(\omega_c - \omega_s)e^{-j\phi_L(\omega_c - \omega_s)}$
- Upper sideband: $U(\omega_c + \omega_s)e^{-j\phi_U(\omega_c + \omega_s)}$
- Central frequency: $C(\omega_c)e^{-j\phi_C(\omega_c)}$

Thus the filtered optical signal can be expressed as:

$$\begin{aligned} E_{\text{filtered}} &= \sum_{\omega_s} [A_0 C e^{-j(\phi_{A_0} + \phi_c)} e^{-j\omega_c t} + \\ &\quad j A_1 v_s (U e^{-j(\omega_s t + \phi_U)} + L e^{-j(-\omega_s t + \phi_L)}) e^{-j\omega_c t}] \end{aligned} \quad (7.9)$$

and if this light signal is fed into a PD (on-chip or off-chip), the generated photocurrent will be:

$$I_{\text{PD}} = \mathcal{R} E_{\text{filtered}} E_{\text{filtered}}^* \quad (7.10)$$

where \mathcal{R} is the responsibility of the PD. Again, we just focus on the linear region and ignore the signal mixing, which results in:

$$\begin{aligned}
I_{PD} &= \mathcal{R} \left[\sum_{\omega_s} [A_0 C e^{-j(\phi_{A_0} + \phi_c)} e^{-j\omega_c t} + j A_1 v_s (U e^{-j(\omega_s t + \phi_U)} \right. \\
&\quad \left. + L e^{-j(-\omega_s t + \phi_L)}) e^{-j\omega_c t}] \right] \left[\sum_{\omega_s} [A_0 C e^{j(\phi_{A_0} + \phi_c)} e^{j\omega_c t} + \right. \\
&\quad \left. j A_1 v_s (U e^{j(\omega_s t + \phi_U)} + L e^{j(-\omega_s t + \phi_L)}) e^{j\omega_c t}] \right] \\
&= \mathcal{R} \sum_{\omega_s} [A_0 C e^{-j(\phi_{A_0} + \phi_c)} e^{-j\omega_c t} + j A_1 v_s (U e^{-j(\omega_s t + \phi_U)} \\
&\quad \left. + L e^{-j(-\omega_s t + \phi_L)}) e^{-j\omega_c t}] [A_0 C e^{j(\phi_{A_0} + \phi_c)} e^{j\omega_c t} + \right. \\
&\quad \left. j A_1 v_s (U e^{j(\omega_s t + \phi_U)} + L e^{j(-\omega_s t + \phi_L)}) e^{j\omega_c t}] \tag{7.11}
\end{aligned}$$

$$\begin{aligned}
I_{1st} &= 2\mathcal{R} \sum_{\omega_s} A_1 A_0 C v_s [U \sin(\omega_s t + \phi_U - \phi_{A_0} - \phi_C) \\
&\quad + L \sin(-\omega_s t + \phi_L - \phi_{A_0} - \phi_C)] \\
&= 2\mathcal{R} A_1 A_0 C \left[\sum_{\omega_s} (U e^{-j(\phi_U - \phi_{A_0} - \phi_C - \pi/2)} v_s \cos(\omega_s t) - \right. \\
&\quad \left. L e^{-j(\phi_L - \phi_{A_0} - \phi_C - \pi/2)} v_s \cos(\omega_s t)) \right] \\
&= 2\mathcal{R} A_1 A_0 C [U e^{-j(\phi_U - \phi_{A_0} - \phi_C - \pi/2)} - L e^{-j(\phi_L - \phi_{A_0} - \phi_C - \pi/2)}] v_{in}(t) \tag{7.12}
\end{aligned}$$

If we note that

$$\begin{aligned}
|H_{\omega_s}| &= |2\mathcal{R} A_1 A_0 C \sqrt{U^2 + L^2 - 2UL \cos(\phi_U + \phi_L - 2(\phi_{A_0} + \phi_C))}| \\
\phi_{\omega_s} &= \arctan\left(\frac{-U \cos(\phi_U - (\phi_{A_0} + \phi_C)) + L \cos(\phi_L - (\phi_{A_0} + \phi_C))}{U \sin(\phi_U - (\phi_{A_0} + \phi_C)) + L \sin(\phi_L - (\phi_{A_0} + \phi_C))}\right) \tag{7.13}
\end{aligned}$$

Then the recovered RF signal can be expressed as:

$$I_{1st} = |H_{\omega_s}| e^{-j\phi_{\omega_s}} v_{in} \tag{7.14}$$

And we can get the RF transfer function as:

$$\begin{aligned}
H &= 2\mathcal{R} A_1 A_0 C [U e^{-j(\phi_U - \phi_{A_0} - \phi_C - \pi/2)} - L e^{-j(\phi_L - \phi_{A_0} - \phi_C - \pi/2)}] \\
&= |H_{\omega_s}| e^{j\phi_{\omega_s}} \tag{7.15}
\end{aligned}$$

where A_0 and A_1 is determined by the modulator configuration (Equation. 7.8) and L , U and C are the spectral/frequency response of the filter block for the different frequencies..

Comparing Eq. 7.15 with Eq.3.19, we find that the entire photonic link can be interpreted as an interferometer for the RF signal with an extra frequency filter response, which forms a microwave photonic filter (*E/E response*). If we assume that the lower sideband region of the optical transmission spectrum (L) and the upper sideband region (U) can be configured fully independently (which is not true for continuous broadband spectrum transmissions, but is a valid assumption for microwave signals modulated on an RF carrier frequency), the microwave photonic filter design can also use allpass filters to define classical microwave band-pass filter functions, similar to the optical filter design discussed in Chapter 3.2.3.

The modulated RF signal is not following different physical paths in the circuit. Instead, we consider the upper and lower modulated sideband as two signals from the same source

that are allowed to interfere in the photodetector. The "splitter" and "combiner" in this "interferometer" are thus implemented by the modulator and the PD, which can be regarded as perfect 50:50 coupling ratio without any insertion loss, and the all-pass filter can still be implemented as ring resonators. Because the ring resonators will both act on the upper and lower sidebands, the filter design space is limited to half FSR of the ring resonators, and in the other half the response shape will be the mirror image of the first half.

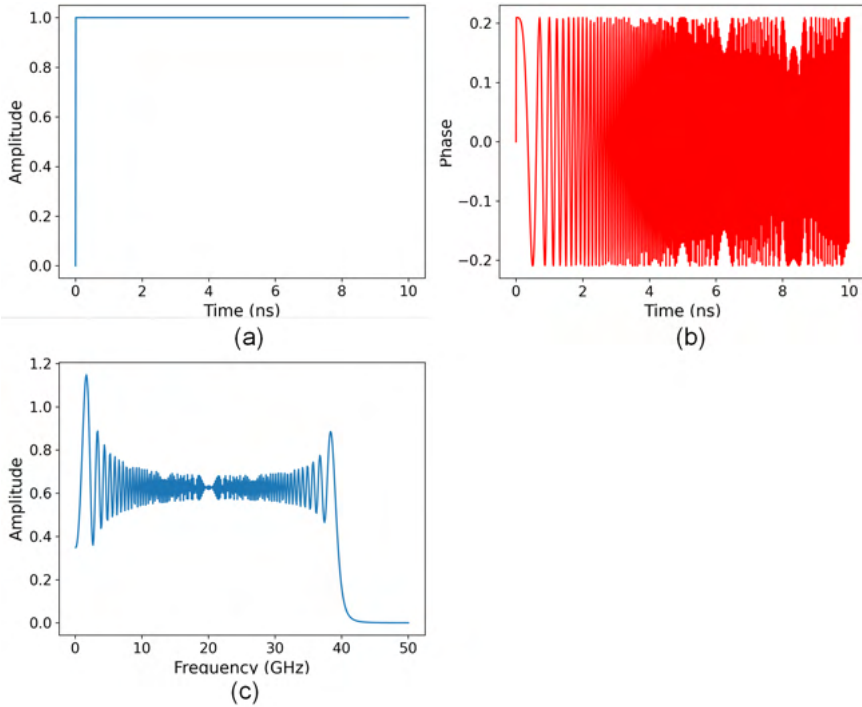


Figure 7.3: A phase modulated signal, modulated by a chirp signal. (a) Amplitude; (b) Phase; (c) Frequency.

7.2 Simulation

A simulation is done to verify this microwave filtering response. Here we use the photonic circuit simulator Caphe in Luceda IPKISS [1]. Caphe can be used for analyzing circuits both in frequency and time domain, but cannot really do an RF frequency analysis for the modulators and PDs. Thus, we use the time domain simulation tool, generate a chirped RF signal (with a broadband RF spectrum), feed the signal into the system and obtain the recovered RF signal in the time domain. By taking a Fourier transformation of the input signal and output signal, we get the simulated RF frequency responses.

We first built a phase modulator, which is based on a phase shifter model but with 0 time constant to remove the bandwidth limitation. Then, a chirped signal is applied as the modulation signal for the phase modulator. The modulated signal is shown in Fig. 7.3. Then, a double-ring optical filter model is built, and the modulated signal is fed into the filter and the output signal is shown in Fig. 7.4. Comparing the frequency spectrum of the generated signal (Fig. 7.4(c)) and the input signal (Fig. 7.3(c)), we can get the RF transfer function of this modulator with the optical filter system, as shown in the blue curve in Fig. 7.4(d). The orange curve in the Fig. is generated with Equation 7.15. As can be seen, the filtering shape of these two simulation results match very well (absolute loss is normalized).

With a reconfigurable microwave photonic filter, we can enable several applications

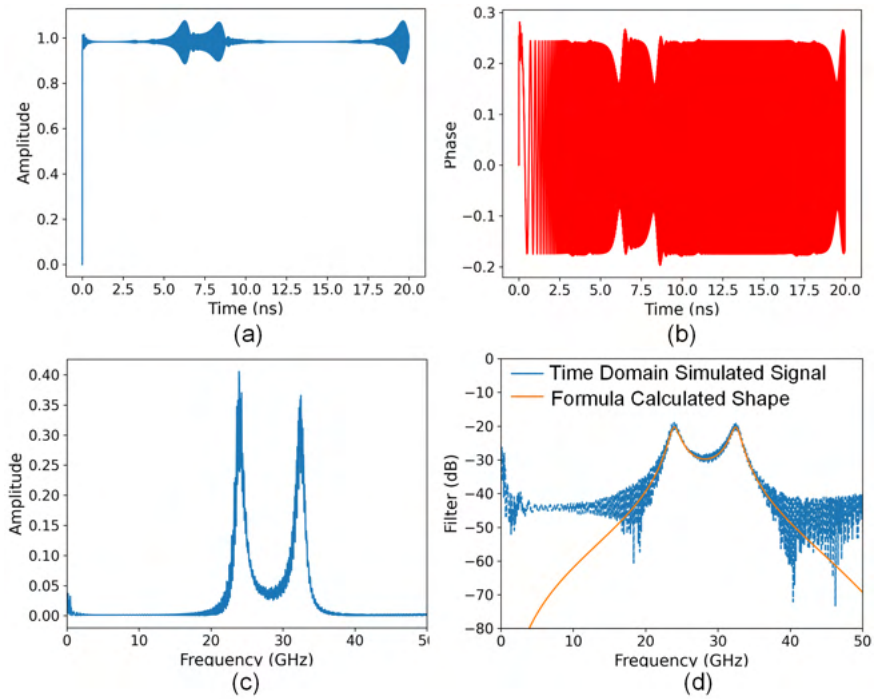


Figure 7.4: Simulated filtered signal. (a) Amplitude; (b) Phase; (c) Frequency; (d) Transfer Function.

like equalized optical transmitter or an opto-electronic oscillator (*RF Generation* in Chapter 4.3).

7.3 Sample Packaging

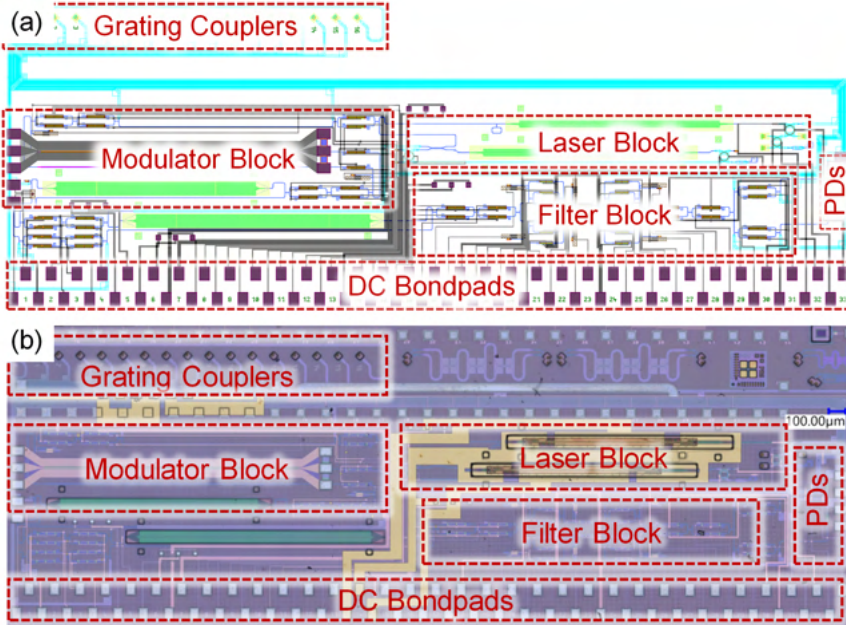


Figure 7.5: The layout of the signal processor.

The sample layouts (the design and the fabricated sample) are shown in Fig. 7.5, and a post-processed and fully packaged demonstrator is shown in Fig. 7.6. To reduce the thermal crosstalk introduced by the modulators termination (50 ohm), we wirebonded two thin-film resistors on top of the sample, which can be seen in Fig. 7.6. Experimental results show that this process did not reduce the RF bandwidth of the used modulator, which targets at 33 GHz when biased at -1 V.

The photonic integrated circuit features a total of 15 optical input/output ports, 3 RF ports (4 ports on the PCB. One is connected to a ring modulator in the system, but it is not used in this thesis work.), 52 thermal tuners, 8 monitor photodetectors, and a transfer-printed laser. As a result, a comprehensive DC, RF, and optical packaging approach is essential to ensure the stability and robustness of the system.

7.3.1 Electrical packaging

A printed circuit board (PCB) was designed for the electrical connections. The processor chip was placed face-up on the board, and the bondpads were connected using wirebonding, as shown in Fig. 7.5.

To get a lower RF propagation loss, the PCB for packaging is a 4-layer stacked PCB with high-speed materials (Megtron 6) as dielectric layers, which ensure a lower RF dissipation than normal PCB materials (eg. FR-4). The used connectors are Rosenberger solderless RF connectors, as shown in Fig. 7.5 and Fig. 7.7. A straight referencing transmission line

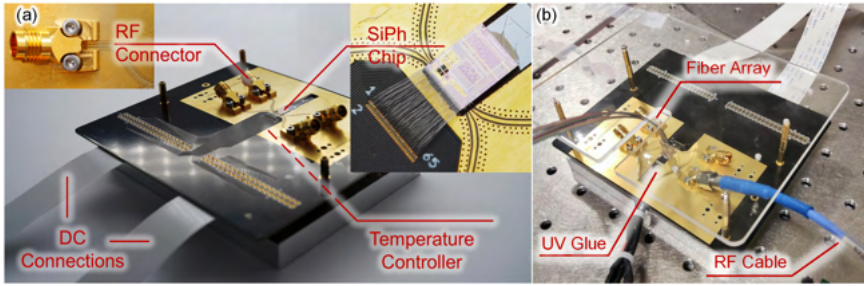


Figure 7.6: Packaged sample. (a) Before fiber array attachment; (b) With fiber array attachment.

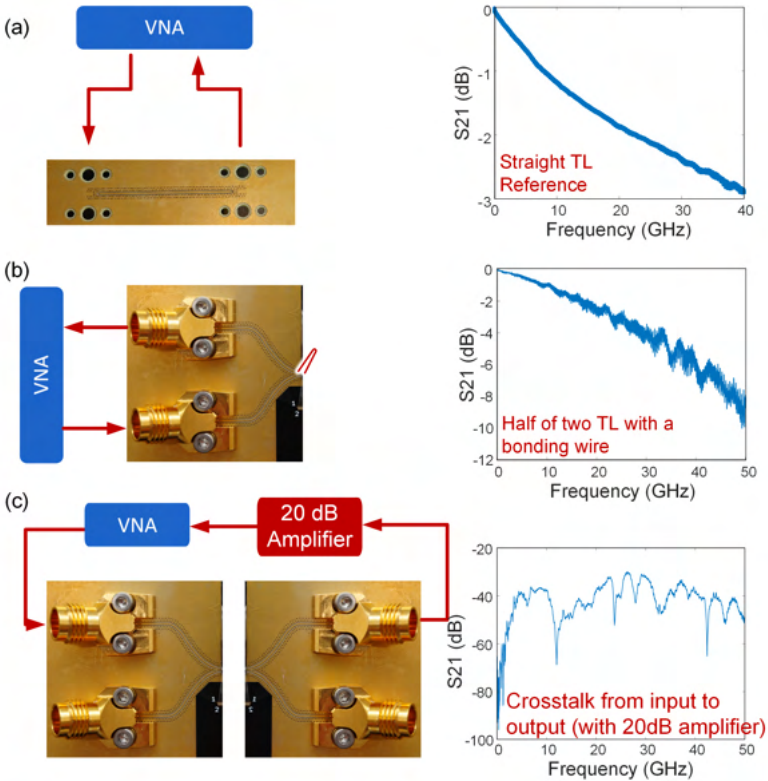


Figure 7.7: RF packaging characterization. (a) Transmission of a reference straight transmission line; (b) Half transmission of two used transmission line with a bonding wire; (c) The direct crosstalk from input RF connector to output RF connector.

(2 cm) on the sides shows a 3 dB drop over 40 GHz, which is shown in Fig. 7.7(a), but the bending loss and the wirebonding effects are not included. To evaluate the used transmis-

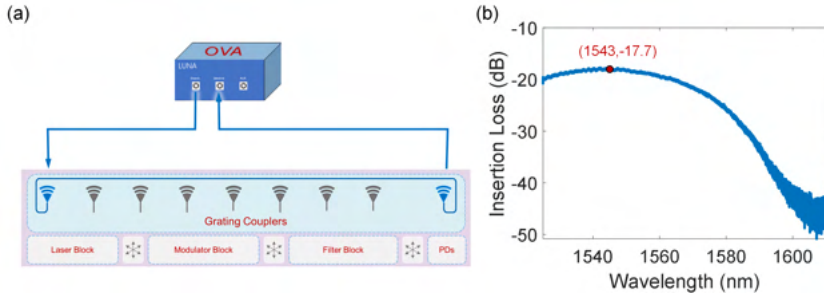


Figure 7.8: Fiber array curing characterization. (a) The measurement setup for the insertion loss of the reference waveguide. (b) The measured results.

sion lines, we wirebonded a pair of them, and got the transmission response as shown in Fig. 7.7(b). The curve in Fig. 7.7(b) is used as reference for the modulator tests. But because of the different bonding objects, the wirebonding responses for our signal processor cannot be fully calibrated. On top of this, we observed that the PCB itself introduces RF crosstalk, which couples the RF signal directly from the inputs (of the modulator) to the outputs (of the PD). This transmission response (with an 20 dB amplifier, the actual crosstalk is 20 dB lower) is shown in Fig. 7.7(c). This curve is later used in the characterization of the on-chip PDs.

7.3.2 Optical packaging

To ensure a stable and robust optical coupling, we UV-cured a vertical fiber array unit on top of the silicon photonic sample. The curing process was described in Chapter 2.3. In addition, to encapsulate the DC and RF wires, a significant amount of UV glue was added during the optical packaging process. Unfortunately, this resulted in a somewhat uneven curing process, leading to higher optical losses than normal. We used an optical vector analyzer (LUNA OVA5000) to measure the coupling loss, as shown in Fig. 7.8(a). The measurement results are shown in Fig. 7.8(b). Because the grating coupler acts as a polarizer, and the LUNA measures the average transmission for both polarizations, we observe an additional 3 dB loss incurred for the polarization averaging. Consequently, the coupling loss per pair of grating couplers was determined to be 14.7 dB, with the peak transmission at 1543.3 nm.

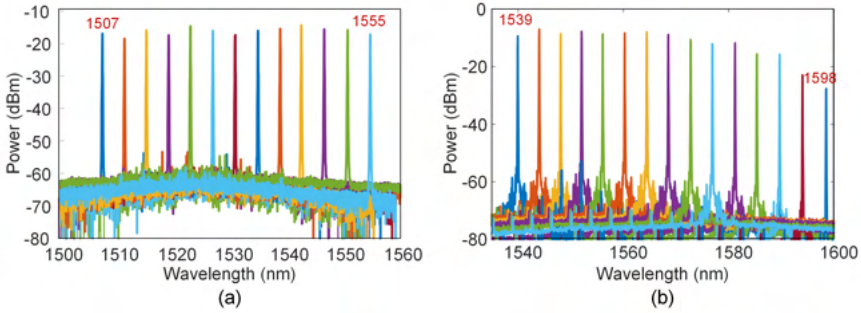


Figure 7.9: Laser block tuning results. (a) Using the Fabry–Pérot cavity laser. Results are got from another sample. (b) Using the ring cavity laser. The results are measured from grating couplers.

7.4 Characterization

7.4.1 Laser Generation

The characterization of the laser block based on the micro-transfer-printed SOA was elaborated in section 6.3. In short, the laser block can provide a widely tunable single wavelength light signal from 1507 nm to 1598 nm, as shown in Fig. 7.9 (same as Fig. 6.12).

7.4.2 Programmable Optical Filtering

The working principle and characterization of the filter block (Four-ring-loaded MZI structure) were elaborated in Chapter 3.2.3. As a classical optical filter design, this filter can be programmed to have a arbitrary filtering shape both in amplitude and phase (limited by the filter order) [2]. The configuration and tuning results are shown in Fig. 7.10

7.4.3 Analog Optical Transmitter. E/O Conversion

Firstly, we characterized the laser block and the modulator block in the system. If the on-chip laser is fed into the modulator and coupled out from optical port 3, we will get a tunable optical transmitter with a tunable optical wavelength. The system configuration is shown in Fig. 7.11(a) and the measurement setup is shown in Fig. 7.11(b). Here, we just measured the analog response of the optical transmitter, and digital signal transmission will be done in the future.

As discussed in Chapter 6, the reconfigurable modulator can work as a PN junction modulator, an intensity modulator or a optimized pure phase modulator. The configuration and experimental results are shown in Fig. 7.12. If the tunable couplers' $\kappa = 0$, the modulator block will be simplified to a PN junction based phase modulator. The DC sweep on the PN junction is shown in the middle of Fig. 7.12(b). As can be seen, the PN junction has an absorption variance of 0.23 dB with the applied voltage at its depletion mode, which will introduce spurious intensity modulation. By guiding a little bit light to the other arm of the MZI, this spurious intensity modulation can be suppressed [3], and the response is shown in Fig. 7.12(c). If the tunable couplers' κ is set to around 0.5, the modulator block would

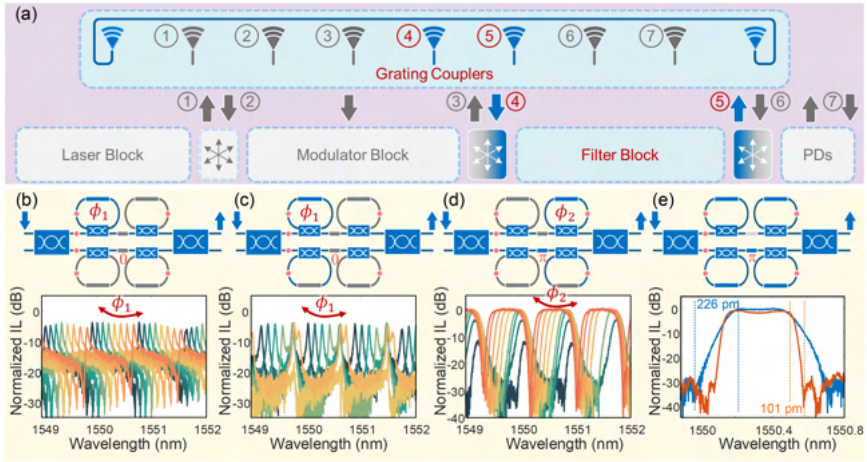


Figure 7.10: Filter block configuration and turning results. (a) The signal processor configuration for optical filtering. (b) Single bandpass filtering configuration and response; (c) Double bandpass filtering configuration and response; (d) First-order Chebyshev Type II filtering configuration and response; (e) Second-order Chebyshev Type II filtering configuration and response.



Figure 7.11: Optical transmitter characterization. (a) Sample configuration as an optical transmitter. (b) The setup for the measurement. VNA: Vector Network Analyzer; PD: Photodetector. SiPh sample: Silicon photonic sample. EDFA: Erbium-doped fiber amplifier.

work as an Mach-Zehnder Modulator for intensity modulation. The responses are shown in Fig. 7.12(a). The PN junction based phase modulator has a 20 dB lower intensity response than intensity modulation, while a tuned pure modulation configuration can be further 2 dB lower. The DC sweep in Fig. 7.12(c) is not as flat as the results shown in Fig. 5.9, which is due to the high thermal crosstalk from the RF termination (50Ω load). This RF load generates massive heat and induces drifts in surrounding photonic circuits. In this measurement, the output power of the Erbium-doped fiber amplifier (EDFA) is fixed at 7.8 dBm and the photocurrent of the PD is then at 3.2 mA, making sure that the RF power difference does not come from the optical power difference.

The modulator blocks in other samples were also measured individually with RF probes, and they showed good uniformity with a 3 dB bandwidth of 33 GHz as intensity modulators, which matched the data in IMEC's PDK handbook (33.8 GHz biased at -1 V), as shown in Fig. 7.13(a). Compared with the probed modulators, the wirebonded one shows some extra resonance in its response after the calibration, as shown in Fig. 7.12(a) and Fig. 7.13(b). The absolute RF loss difference is due to the difference in laser power and

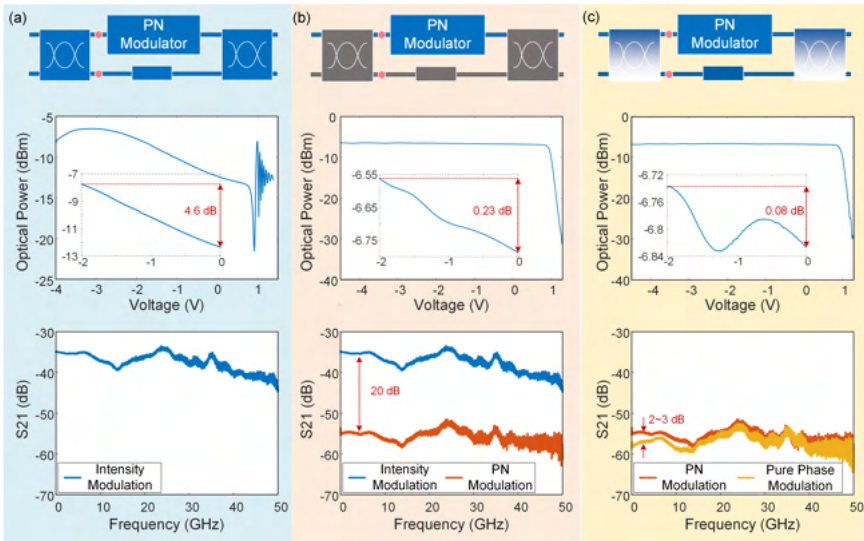


Figure 7.12: Reconfigurable optical modulator characterization. (a) The modulator block works as an intensity modulator. (b) The modulator block works as a PN junction modulator. (c) The modulator block works as a phase modulator with lower spurious intensity modulation.

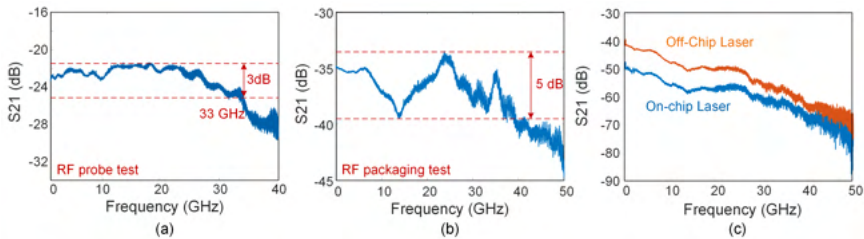


Figure 7.13: Modulator frequency response. (a) Tested with RF probes; (b) Tested with wirebonding packaging; (c) Tested with on-chip laser and off-chip laser.

different packaging. Fig. 7.13(c) compares the transmitter performance with an on-chip laser and with an off-chip laser (Santec TL550). With the off-chip chip laser, the signal transmission shows a slightly lower noise.

7.4.4 Equalized E/O conversion

With the optical filter block, the whole system can work as a microwave photonic filter, which can also be utilized as an equalizer for the optical transmitter. By carefully tuning the optical filter, we got equalized responses, as shown in Fig. 7.14. The curves in Fig. 7.14 are the raw data from VNA and not calibrated with other data, which means that all cables, bonding wires and other components' response are included. It shows that the microwave

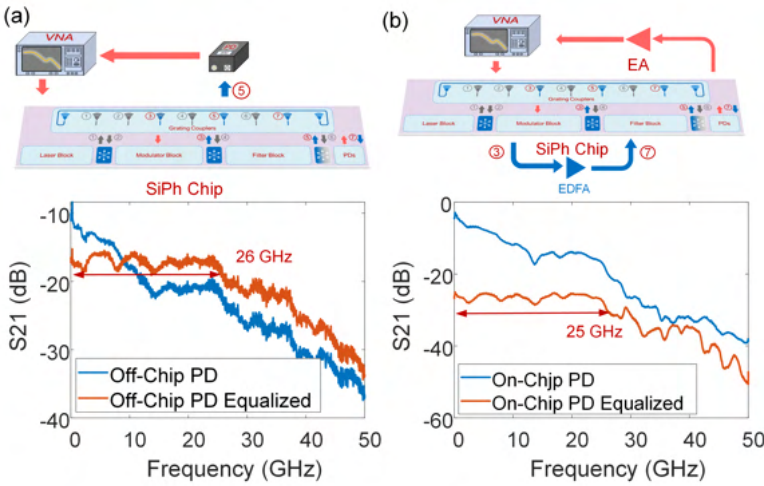


Figure 7.14: Equalized transmitter response. (a) Equalized transmission spectrum with an off-chip PD; (b) Equalized transmission spectrum with an on-chip PD

filter based equalizer can flatten the response of the whole system with an off-chip PD up to 26 GHz (Fig. 7.14(a)) and with an on-chip PD up to 25 GHz (Fig. 7.14(b)). The equalized curve in Fig. 7.14(a) is partially higher than the unequalized one is because the used EDFA provides a constant output power, and the optical sidelobes are being amplified more when the optical carrier is suppressed.

7.4.5 Microwave photonic filtering. E/E conversion

Other than equalizing the modulator's RF response, the microwave photonic filter can also work as a classical high-pass filter, a high-stop filter or a band-pass filter for RF signals. In this subsection, the PN junction is regarded as a pure phase modulator. The intensity modulation described above is weak, and only contributes a small variance in the filter response, or a small drift in the system configuration.

Here we show some demonstrations for the RF filter design. If the reconfigurable modulator is set as a phase modulator and the filter block is set as a single notch filter (a critically coupled ring resonator), we can obtain a single bandpass filter in the RF domain, as shown in Fig. 7.15(a). If two rings are used, a double bandpass filter or one-pass one-stop band filter can be realized, depending on whether the second ring is undercoupled, critically coupled or overcoupled. (shown in Fig. 7.15(b) and Fig. 7.15(c)). This modulator configuration is set for the $\kappa = 0$, thus $\phi_{A_0} = 0$ in Equation 7.8, and these RF filtering results fully match the optical filtering response when single ring or double rings used in an MZI biasing at null point.

If the ring resonators are overcoupled, they act as all-pass filters for the RF signal loaded on the light carriers. By tuning the modulator block and the cascaded rings (R1 and R2), we can get tunable high-pass filters (HPF), low-pass filters (LPF), and bandpass filters (BPF), as shown in Fig. 7.16. Fig. 7.16(a), (d), and (h) show the measured S21 responses of the tunable filters, but these responses are enveloped by the response of the original modulator

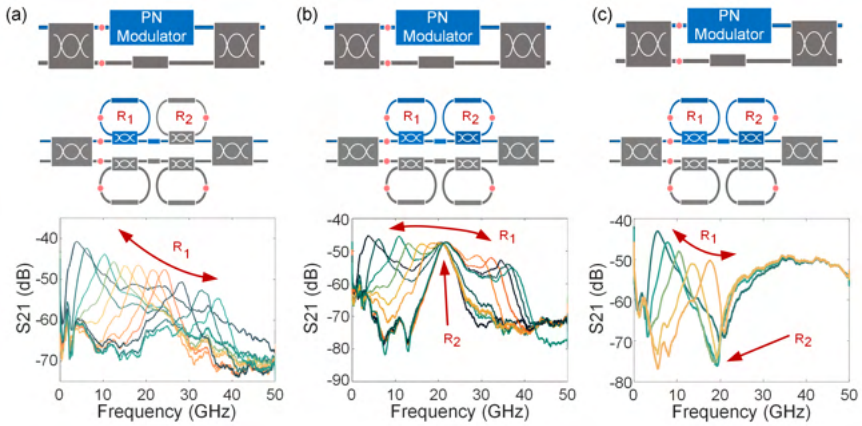


Figure 7.15: Microwave bandpass filter. (a) Microwave filter: single tunable bandpass filter; (b) Microwave filter: double tunable bandpass filter; (c) Microwave filter: tunable one-pass one-stop band filter.

and PD. Thus we constructed an "all pass" reference which combines the highest BPF and the highest LPF, as shown in Fig. 7.16(g), and all other curves are calibrated with this reference curve, which are shown in Fig. 7.16(b) and (e). These responses are more clearly show the high-pass and low-pass behaviors, The curves are further normalized by removing the insertion loss in Fig. 7.16(c) and (f). Because the responses below -70 dB are close to the noise floor at high frequency, the low-pass filter responses are not accurate at the high frequency points, thus we truncate the responses in Fig. 7.16(c) to 30 GHz, to make it more clear. Fig. 7.16(h) shows a tunable BPF response. Because of the wide roll-off of the optical ring resonator, these band-pass filters show higher losses than previous filters. The normalized BPF responses are shown in Fig. 7.16(i). The high-pass, low-pass and band-pass filters are realized with the same mechanism as the optical band-pass filters discussed in Fig. 3.13, while the RF filters are in a narrower frequency/wavelength range (30 GHz or 240 pm range at 1550 nm).

The full optical filter block can also be used to form microwave photonic filters. The final RF responses can be fully predicted with Equation 7.15, but its filter synthesis will be hard. Fig. 7.17 shows a four-pass-band filter where these four bands can be independently tuned and suppressed.

7.4.6 Opto-Electronic Oscillator. RF Generation.

As introduced in Chapter 4.3, a closed-loop microwave photonic link can oscillate and generate an RF signal if the gain in the loop is higher than the loss. Taking advantage of the low propagation loss of the optical fiber, we can build a large oscillation cavity and get a RF signal with lower phase noises. Previously we demonstrates that our signal processor can work as a tunable RF bandpass filter. Here we also build oscillators with it. We did the tests with an on-chip PD, an off-chip PD (Discovery Labuddy) and an individual on-chip PD with TIA [4]. The schematics are shown in Fig. 7.18. Here, the on-chip laser, modulator, optical filter blocks, as well as PDs formed a tunable bandpass microwave photonic filter,

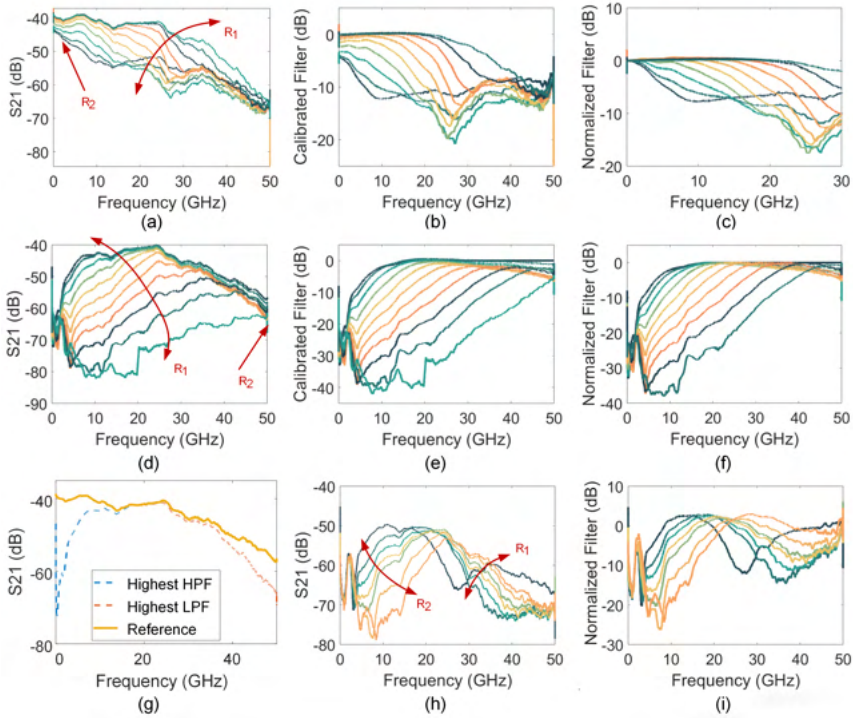


Figure 7.16: Tunable microwave photonic filter responses. (a) Measured S_{21} response of a tunable low-pass filter (LFP); (b) Using the highest one as a reference, calibrated filter response of the tunable LFP; (c) Normalized filter response of the tunable LFP; (d) Measured S_{21} response of a tunable high-pass filter (HPF); (e) Using the highest one as a reference, calibrated filter response of the tunable HPF; (f) Normalized filter response of the tunable HPF; (g) A "all pass" reference curve generated from the highest HPF and highest LFP, to calibrate the remaining filters. (h) Measured S_{21} response of a tunable band-pass filter (BPF); (i) Normalized filter response of the tunable BPF.

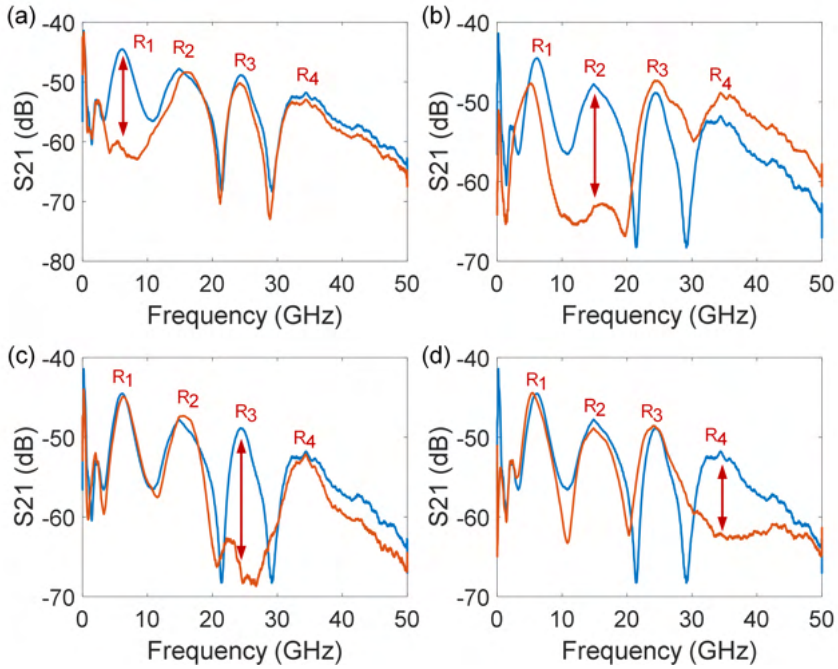


Figure 7.17: A tunable four band-pass filter and its first (a), second (b), third(c), and fourth(d) pass-band suppressed filter.

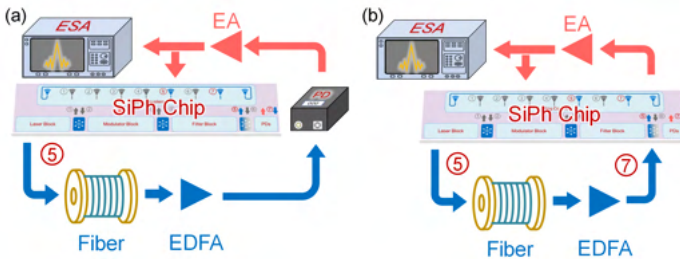


Figure 7.18: An opto-electronic oscillator demonstrator with the single chip signal processor. (a) With an on-chip PD. (b) With an off-chip PD. SiPh Chip: Silicon photonic chip. EDFA: Erbium-doped fiber amplifier. EA: Electronic amplifier. ESA: Electrical spectrum analyzer.

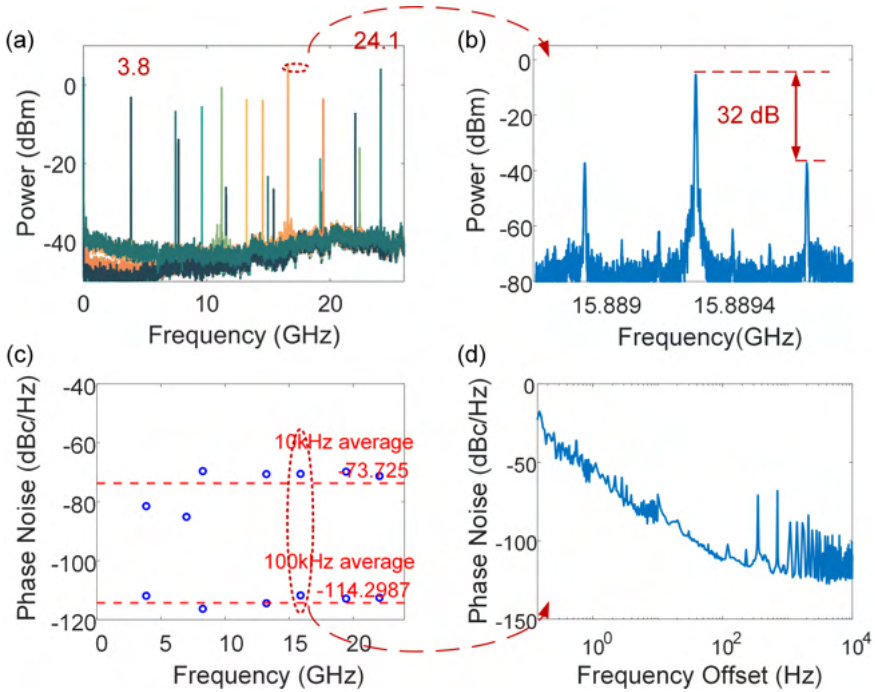


Figure 7.19: (a) Tunable RF signal generation from 3.8 GHz to 24.1 GHz with an off-chip PD, shown in Fig. 7.18(a); (b) The zoom-in spectrum of generated 15.8 GHz signal; (c) Extracted phase noises of the generated RF signals; (d) Phase noise results of the generated 15.8 GHz signal.

as shown in Fig. 7.17(a). The modulated RF signal is loaded on the optical link, filtered, amplified by an electronic amplifier and then fed back into the modulator as an RF source. The whole system thus becomes an RF loop, and it will start oscillation if the net gain is 0 dB or higher. By tuning the passband frequency of the microwave photonic filter, as discussed previously, we can tune the oscillation RF frequency and achieve a tunable RF source. Because of the mode competition, the frequency can hardly continuously tuned, and the frequency spacing in our tests almost equivalent to the 3 dB bandwidth of the microwave photonic filter. A length of extra fiber was added to the system, which extends the entire cavity to achieve a lower RF phase noise.

With an off-chip PD The RF generation results with the off-chip PD are shown in Fig. 7.19. Here, the extra fiber added is 500 m long. The spectrum of generated RF signals is shown in Fig. 7.19(a) and (b). As can be seen, the signal frequency can be tuned from 3.8 GHz to 24.1 GHz, and higher frequencies can be reachable, but limited by the used ESA (Anritsu MS2840A, 26 GHz). The zoom-in spectrum shows that the mode spacing of this oscillator is around 400 kHz and the sidelobe extinction is 32 dB. Fig. 7.19(c) and (d) show the phase noise of the generated signal. It can be noted that the strength of the phase noise is almost constant for all the generated signals.

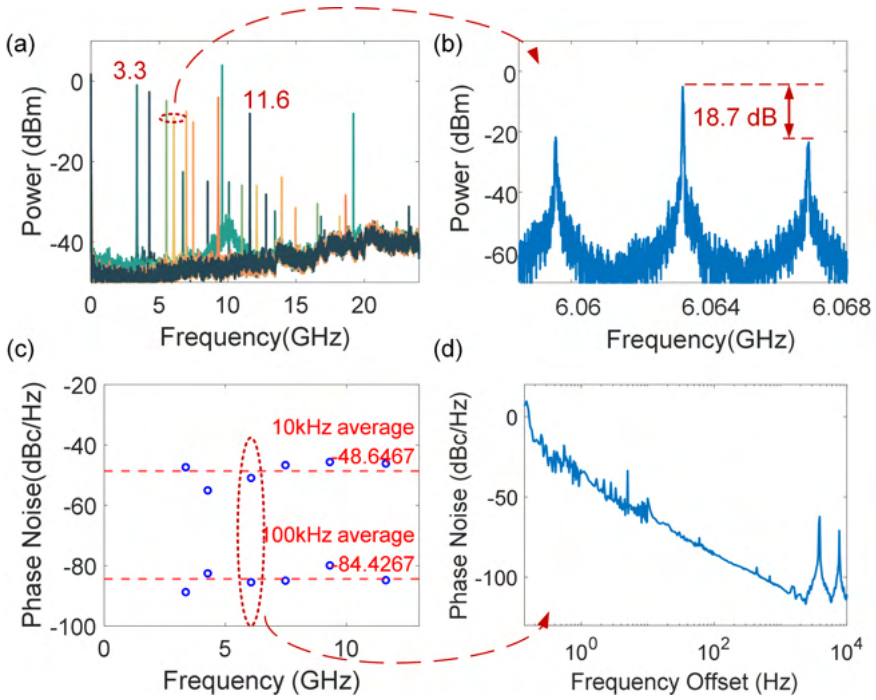


Figure 7.20: (a) Tunable RF signal generation from 3.3 GHz to 11.6 GHz with an on-chip PD, shown in Fig. 7.18(b); (b) The zoom-in spectrum of generated 6.06 GHz signal; (c) Extracted phase noises of the generated RF signals; (d) Phase noise results of the generated 6.06 GHz signal.

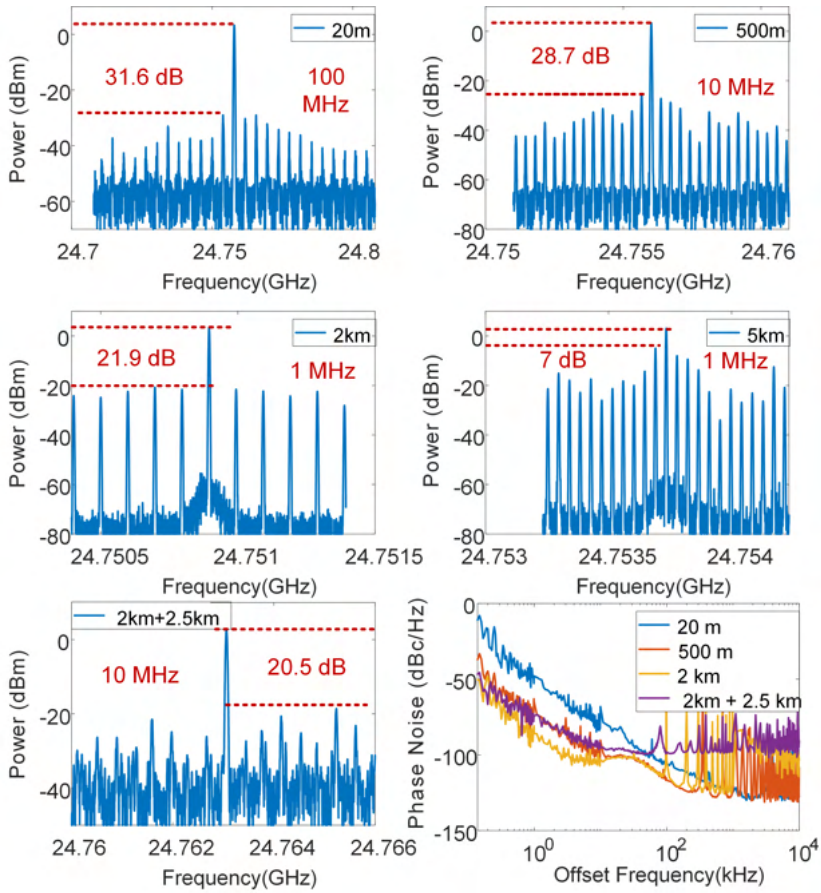


Figure 7.21: Opto-electronic oscillator demonstrator with an individual on-chip optical resonant receiver.

With an on-chip PD Demonstrators with on-chip PDs are also implemented. First we used the PD on our sample, and the results are shown in Fig. 7.20. Here, the extra fiber added is 20 m long, and the oscillator cannot keep a single mode oscillation with a longer fiber. The spectrum of the generated RF signals are shown in Fig. 7.20(a) and (b). As can be seen, the signal frequency can be tuned from 3.3 GHz to 11.6 GHz. The zoom-in spectrum shows that the mode spacing of this oscillator is around 4 MHz and the sidelobe extinction is 18.7 dB. Fig. 7.20(c) and (d) show the phase noise of the generated signal. From this we can see that with the on-chip PD, the oscillator has a higher noise than with an off-chip PD (-97 dBc/Hz at 100 kHz offset with 20 m fiber), which is due to the RF packaging crosstalk. And crosstalk also makes the oscillator unstable to work at frequencies beyond 11.6 GHz.

Phase Noise @ 100 kHz (dBc/Hz)	Labbuddy	On-chip PD	Resonant Receiver
20 m fiber	-97	-84	-105.9
500 m fiber	-114	\	-116
2 km fiber	\	\	-106.8 (on resonance)

Table 7.1: Phase noises of Opto-electronic oscillator demonstrators.

With an on-chip resonant PD We also did some tests with an on-chip photonic resonant receiver, which can only work within the frequency band from 23 GHz to 33 GHz, but with a maximum 24 dB gain compared with normal photodiodes [4]. Fig. 7.21 show the test results. As can be seen, the oscillated RF frequencies are around 24.7 GHz with different added fiber lengths. While with longer fiber, the frequency spacing of the longitudinal modes are smaller while the sidelobe ratio is also lower, but the phase noise is also lower. Thus, the maximum length of the fiber is limited if a single-frequency oscillation is required. We also build a double cavity oscillator with a 2 km fiber and a 2.5 km fiber. As can be seen, the neighboring sidelobes are fully suppressed due to the Vernier effect, but its phase noise is actually worse than with the single cavity oscillators. The "noise hills" in the phase noise measurements correspond to the sidelobes in the OEO cavities.

Signal phase noise strength with different PDs and different fiber lengths are shown in Table 7.1. As can be seen, the system with labbuddy and the resonant receiver share a lower phase noises. The high noise with the on-chip PD is most likely due to the RF crosstalk from the RF packaging (i.e. the RF input signal into the modulator is coupling directly to the output of the photodetector). A longer cavity can achieve a lower phase noise, but it is more challenging to obtain a single mode oscillation. The performance with 500m fiber are superior to the commercial products (R&S SMR, -105 dBc/Hz at 100 kHz offset frequency at 10 GHz central frequency).

7.4.7 Frequency Doubling

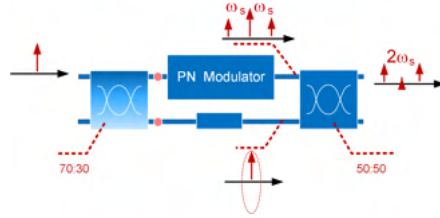


Figure 7.22: Modulator block configuration for frequency doubling, where more light is guided to the PN modulator for compensating its insertion loss.

Other than building an oscillator to generate RF signals, we can also use the on-chip optical transmitter system to obtain an RF frequency doubling. As can be seen from the Eq. 5.6, if the modulator is biased at null point, where the first-order signal is suppressed, the output RF signal will be dominated by the second-order harmonics, which will result in a frequency doubling. Here we used the modulator block to achieve frequency doubling with high original signal extinction. It is based on the carrier-suppressed double-sideband modulation scheme with the reconfigurable modulator, the configuration of which is shown in Fig. 7.22 [5]. The main advantage of the system is that the tunable splitter used in the modulator block can be tuned to compensate the extra loss of the carrier depletion modulator, and thus reach a high carrier extinction.

Demonstrations were implemented with our signal processor, as shown in Fig. 7.23. Here we used an RF source (R&S SMA40) as an RF signal generator. The generated RF signal will be modulated on the laser carrier (from on-chip laser block) by the modulator block, and then the modulated light signal will be coupled to a PD. The recovered RF signal was fed into a spectrum analyzer. The frequency-doubling results are shown in Fig. 7.24. In this part, the extinction ratio is calculated by the second harmonic signal power to the original frequency signal power. As can be seen, normal intensity modulation can keep the second harmonic signal to be 40 dB lower than the original frequency, while if the modulator is biased at null point, the second harmonic signal can be 40 dB higher than the original one. The extinction ratio's drop is mainly due to the system RF loss for higher frequencies.

We also did the same measurement with an on-chip PD (Fig. 7.23(b)), and the results are shown in Fig. 7.25. As it is shown, this frequency doubling can also work for 20 GHz, but the extinction ratio degenerates a lot at the higher frequencies. This is due to the high RF crosstalk at high frequencies, where the first-order signal is not from the optical signal but is from the direct coupling crosstalk, which can be seen in Fig. 7.25(b). One thing should be noted is that the first-order signal power is lower than the crosstalk below 10 GHz, which may be caused by the RF signal destructive interference between the optically generated RF signal with the crosstalk RF signal.

7.4.8 Optical Wavelength Meter / RF Frequency Meter

Apart from the applications discussed above, our signal processor has more possibilities. Here we show that it can work as an optical wavelength meter or RF frequency meter.

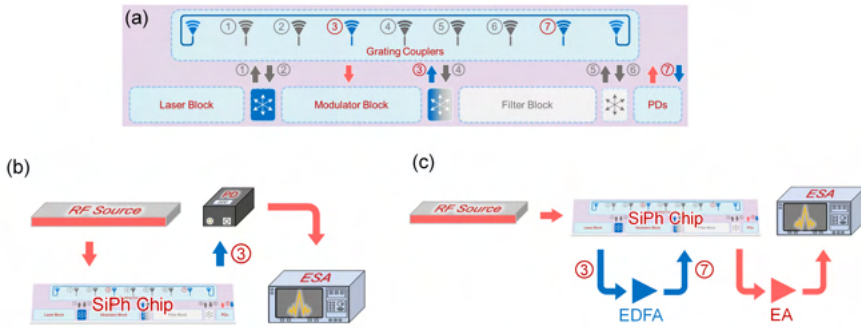


Figure 7.23: Frequency doubling tests setup. (a) Frequency doubling configuration of the sample; (b) A demonstrator with an off-chip PD; (c) A demonstrator with an on-chip PD. SiPh Chip: Silicon photonic chip. EDFA: Erbium-doped fiber amplifier. EA: Electronic amplifier. ESA: Electrical spectrum analyzer.

The optical wavelength meter or the RF frequency meter is based on the ring resonators in the filter block. The optical power in the ring can be read with the tap PD. Then if we sweep the phase shifter in the ring, we can know the power distribution along the wavelength or frequency within one FSR of the ring. The results are shown in Fig. 7.26. To avoid that the main lobe fully covers the sidelobes, the modulator block is configured to have a carrier-suppressed (not fully) modulation. From Fig. 7.26 (a) and (b) we can see that the optical carriers and modulation introduced sidelobes can be easily recognized from the PD's readout. Compared with the measurement results from an optical spectrum analyzer Fig. 7.26 (c) and (d), the overall shape are revealed in Fig. 7.26 (a) and (b). The frequency measured (a) 7.8 GHz and (b) 17.1 GHz are not accurate, but a more elaborate calibration could overcome this limitation. The spectral resolution of this optical wavelength meter or RF frequency meter is determined by the 3 dB bandwidth of the used ring resonator. A ring resonator with a higher Q factor can therefore reach a higher spectrum resolution.

7.4.9 Tunable True Time Delay

The system can also be used to implement true time delay and temporal computing for the RF signal, by using the ring resonators in the filter block. Tuning the ring resonator's Q factor and ring phase status, the group delay and the dispersion of the ring cavity can be altered. Here, a square waveform was used as the modulation signal, loaded on the light carrier, propagated through a ring resonator (other rings were turned open), coupled off-chip, received and recovered by an off-chip PD. The received results are shown in Fig. 7.27. As we can see, as the ring is turned closer to critical coupling, the signal is more delayed (here around 80 ps achieved), attenuated (signal lost in ring resonator), and distorted (getting integrated, as shown in Fig. 7.27(b)). This performance is very limited, but it shows the possible application of the signal processor.

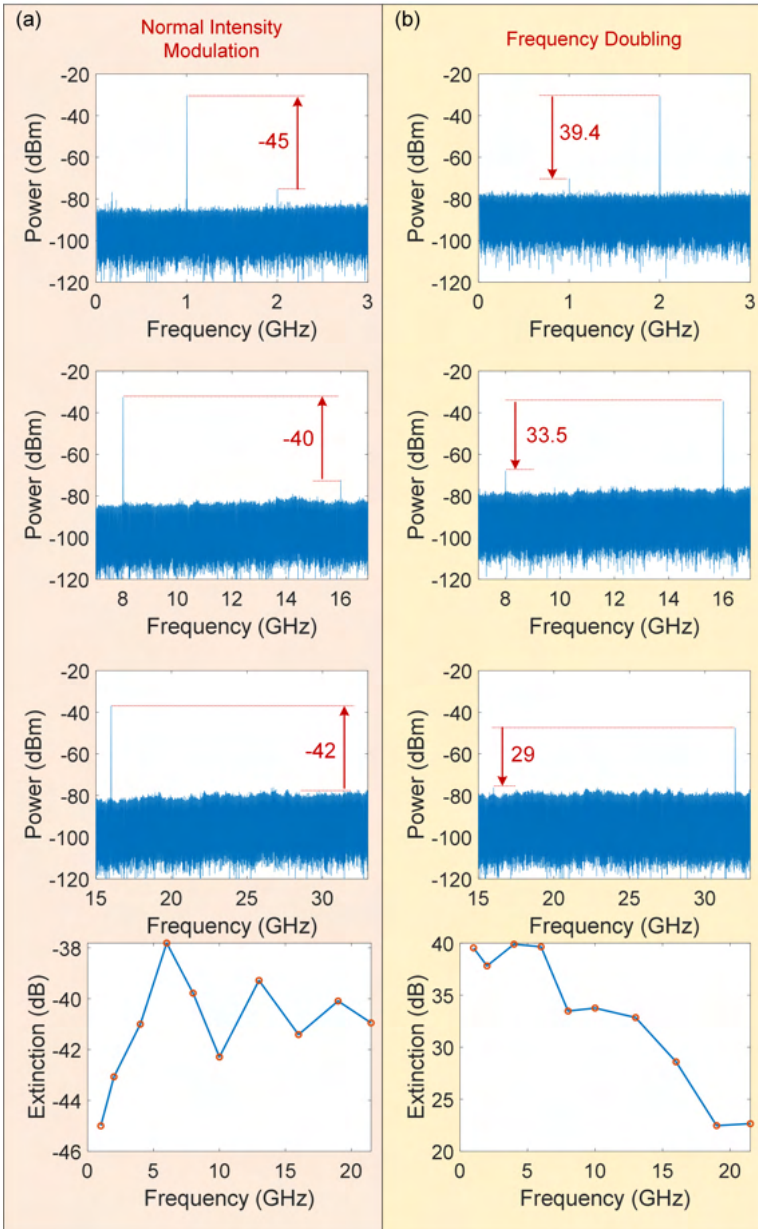


Figure 7.24: Frequency multiplying results with an off-chip PD. (a) Normal intensity modulation, first order signal is maximized; (b) Frequency doubling results, first order signal is minimized and second order signal is maximized.

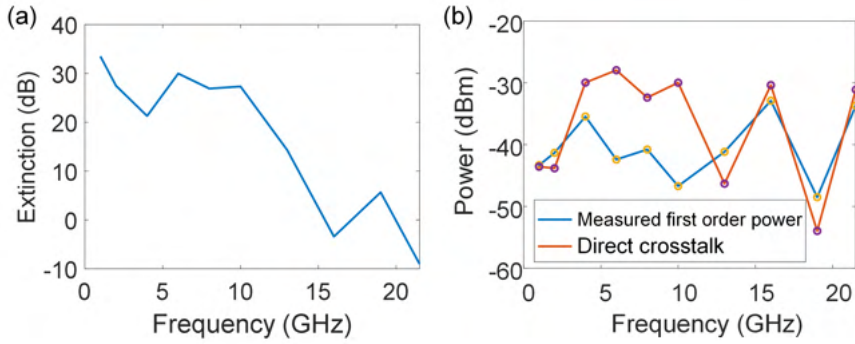


Figure 7.25: Frequency multiplying results with an on-chip PD. (a) Frequency doubling when the modulator MZI is biased at null point. (c) Measured first order signal power and directly coupled crosstalk power.

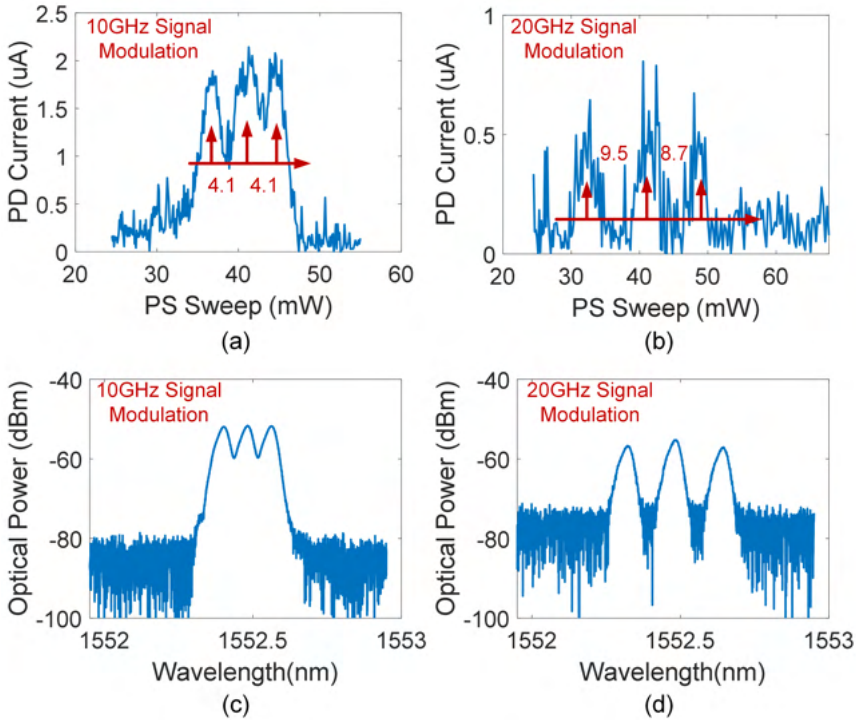


Figure 7.26: A demonstrator as an optical wavelength meter or an RF frequency meter. (a) and (c) The light carrier with 10 GHz RF signal modulated sidelobes; (b) and (d) The light carrier with 20 GHz RF signal modulated sidelobes. (a) and (b) is measured with current meter from tap PD's photocurrent. (c) and (d) is measured with an optical spectrum analyzer.

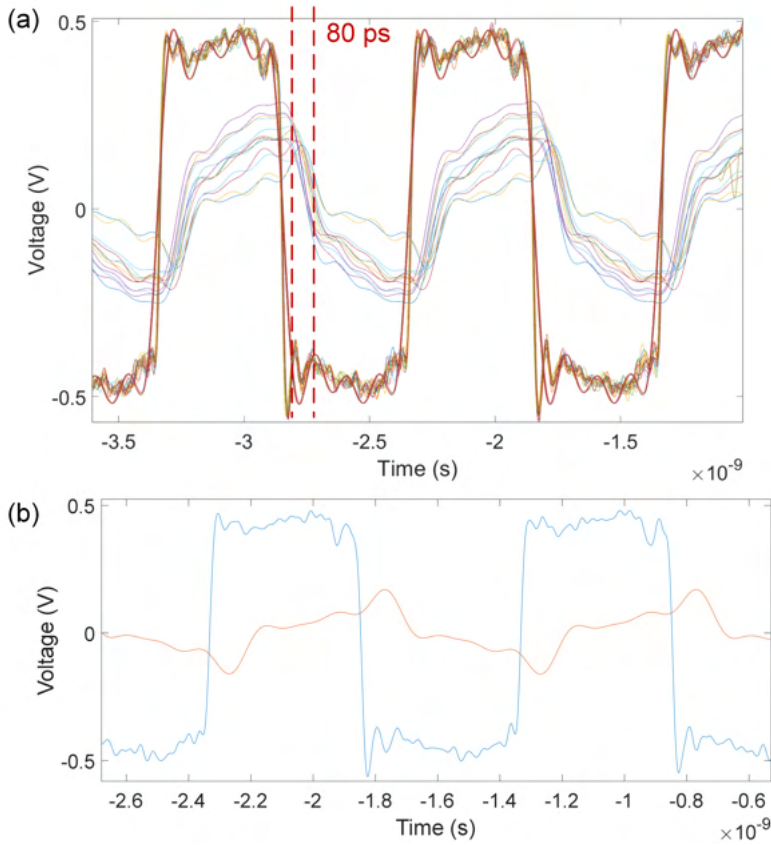


Figure 7.27: A demonstrator for signal temporal processing. (a) True time delay; (b) Signal integration.

7.4.10 Performance Evaluation

The proposed signal processor has been demonstrated several microwave photonic functionalities. In this section, we evaluate its basic figures of merit (FOM) as a microwave photonic link described in Chapter 4.1.4, including RF link gain, noise figure and SFDR. Because we lack proper TIAs, the on-chip PDs suffer from high losses, and the link gain will be very low, and therefore the noise figure will be very high. We evaluate the link with an off-chip PD for meaningful results.

RF Gain The RF gain of this system is measured when the modulator block is set as an intensity modulator. As shown in 7.12, when the PD current is 3.2 mA and the modulator is set as an intensity modulator, the whole link gain is around -35 dB. This RF loss is quite high, due to the low modulation depth of the PN junction, and the low responsivity of the off-chip PD, which is designed for high bandwidth.

If the modulator is tuned to a phase modulator configuration, the link gain can be turned as low as -60 dB, which means that the whole RF link can work as a tunable RF attenuator.

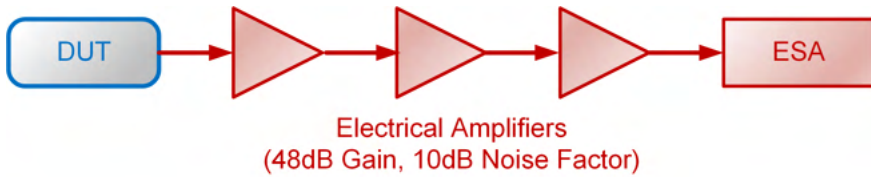


Figure 7.28: Setup for the noise floor measurements. DUT: Device under test; ESA: Electrical spectrum analyzer.

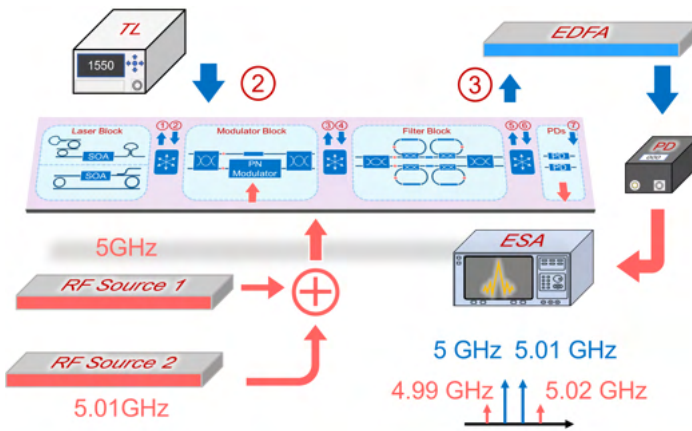


Figure 7.29: Setup for the SFDR measurement.

Noise Figure The noise figure is determined by the RF gain, and the increase of the noise floor. In order to measure the noise floor of the system, we cascaded three amplifiers, which provide 48 dB amplification in total, to pump up the noise levels, as shown in Fig. 7.28. The spectrum analyzer (Keysight N9010A) has a noise floor of -124 dBm at bandwidth of 2 Hz. With the connected amplifiers, the thermal noise at room temperature (-174 dBm/Hz) is measured around -111 dBm (a $50\ \Omega$ resistor is connected to the amplifiers as input). If the amplifiers inputs are connected to the output of the off-chip PD with a photocurrent of 5 mA (On-chip laser output -3 dBm, amplified by an EDFA), the noise floor will raise up to -92.5 dBm, indicating a 18.5 dB of noise power increase. Thus, the noise figure of this signal processor is around 53.5 dB.

SFDR We also characterize the SFDR of this signal processor. The measurement setup is shown in Fig. 7.29. As can be seen, two RF sources are used to generate a two-tone signal (5 GHz and 5.01 GHz). This two-tone signal is modulated on an optical carrier, which is generated by an off-chip tunable laser source (to reduce the crosstalk from onchip laser). The modulated signal is guided off chip, amplified by an EDFA, and then received by a PD. Because of the nonlinear response of the modulator and the PD, the generated RF signal will contain IM3 products, which in this case 4.99 GHz and 5.02 GHz. By sweeping the input signal power from the RF sources, and recording the power of the generated fundamental and IM3 signal, we can get the SFDR of this RF transmission system as 107 dB for a noise floor of -164.5 dBm/Hz [6]. The result is shown in Fig 7.30.

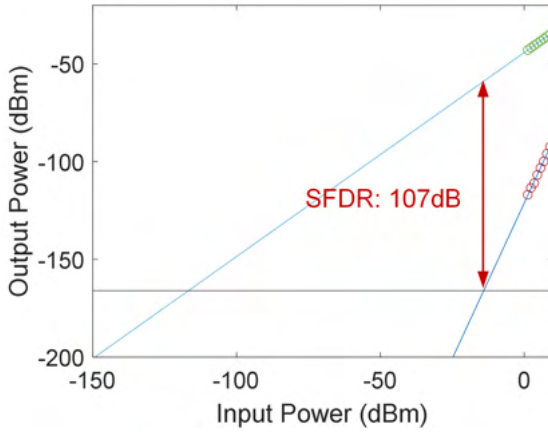


Figure 7.30: Measured SFDR of this microwave processor.

In the future work, we can integrate proper TIAs with our on-chip PDs, then the performance of the entire system could be measured and evaluated.

7.5 Discussion

The single-chip signal processor can provide a fully programmable filtering response (both for optical and RF signals) as well as generation and detection of electrical and optical signals. As a demonstrator, the performance of this processor is limited by its system scale, and the packaging and crosstalk management leave a lot of room for improvement.

Self-sufficient, fully programmable system. All tunable couplers in the proposed signal processor are followed by tap monitors. By tuning the electrical power added on the optical phase shifters in the tunable couplers, we can tune the power splitting ratio to desired values, and tune the responses of each functional block. The configuration methods of tunable couplers, the modulator block, and the optical filter block are shown in Section 3.2.1, Section 5.3, and Section 3.2.3, respectively. With the transfer printed laser sources, the system can be calibrated without any additional optical devices. When the processor is used for microwave photonic applications, it can function standalone. But when it works for optical signal processing, it needs an extra optical wavelength meter to identify the wavelength information, due to the limited FSR of the ring resonators used in the filter block.

Microwave photonic filtering based on double sideband modulation. The E/E response of the proposed signal processor is based on a double sideband modulation scheme. Compared with SSB modulation schemes [7, 8], the reported algorithms show a simpler filter design and a lower intrinsic RF loss. This algorithm makes the use of the reconfigurable modulator, which can generate RF sidebands with tunable phase difference, while the tunable couplers ensure the minimum optical loss in all scenarios. In this case, the optical filters used to filter the modulation induced sidebands can just be as simple as a bank of tunable ring resonators on the same bus waveguide.

Filtering performance and scale-up analysis. The optical and electrical filters are both based on the same optical filter block in our signal processor scheme. As a tunable filter, the minimum 3 dB bandwidth for pass bands and stop bands depends on the quality (Q) factor of the optical filter. The measured Q factors of ring resonators at critical coupling are around 50000, and the tap PDs introduce extra loss in the ring cavities, which will limit the Q factor of the rings. The PDs help to monitor the ring status, but they are not strictly necessary if the sample is fully calibrated and isolated.

The optical and electrical filtering performance is also limited by the filter order, which corresponds to the ring filters in the filter block. To reach a higher order programmable electrical filter, we only need to cascade additional ring filters to increase the order, which makes this implementation very scalable, both in optical losses and in ease of tuning. On the optical filtering side, a higher order optical filter means that we need to add ring pairs on the upper and lower arm of the MZI. So the filter design can be easily altered to match the application requirements.

Equalized E/O conversion with widely tunable optical carriers. The two on-chip laser sources both show 50 nm tuning ranges in a different wavelength region, and a total 90 nm tuning range (from 1508 nm to 1598 nm). With the on-chip modulators, an E/O conversion with widely tunable optical carriers can be reached. The programmable electrical filter can be used as an equalizer for the E/O conversion. The directly measured

modulator response and the equalized one are shown in Fig. 7.16. It shows that a 3 dB bandwidth of a 4.5 GHz modulator is equalized to 26 GHz, where the extra uneven loss of the PCB and bonding wires are equalized by the on-chip microwave photonic filter.

On the other side, the on-chip laser together with two PDs can also be configured as a coherent receiver with tunable local oscillator (LO). But due to the high RF crosstalk (discussed in the crosstalk section), we did not perform further experiments in that direction.

RF signal generation. Here we reported two demonstrations for the RF signal generation. The first one is frequency doubling. With the help of the tunable couplers in the modulator block, the extinction ratio of the doubled frequency to original one can reach 40 dB with an off-chip PD. The other demonstration is a tunable OE oscillator. With an external fiber and amplifier, the RF generation varies from 4 GHz to 24 GHz with an almost constant phase noise of -114 dBc/Hz at 100 kHz using an off-chip PD, which is superior to commercial products (R&S SMR, -105 dBc/Hz at 100 kHz offset frequency at 10 GHz central frequency). The frequency generation of the OEO system is not limited to 24 GHz with our signal processor, but its phase noise measurement is limited by the used spectrum analyzer (26 GHz).

Thermal and optical crosstalk. The whole system contains 52 thermal tuners to enable configurability. Thus the entire system is quite sensitive to the thermal environment. In addition, the transfer-printed amplifier (300 mW power consumption) and the modulator termination (80 mW power consumption at -2 V) also heat up the sample, making the thermal control much more challenging. The sample is mounted on a temperature control unit, but it still drifts with the ambient temperature. On the other hand, because of the lack of an integrated optical isolator, the laser cavities are sensitive to all optical reflections along the optical path. As reflections are not fully avoidable, especially in silicon photonics, all phase tuning elements will also change the phase of the reflected light, and introduce small perturbations to the laser cavity. Fortunately, the whole system shows a high stability and repeatability, which means that the different crosstalk contributions can be compensated with the tuners.

RF crosstalk On the other hand, the RF PCB on which the chip is mounted shows a high RF crosstalk, where the RF signal is directly coupled from the input ports to the output ports. Due to the lack of proper transimpedance amplifiers (TIAs), the signal generated from the on-chip PDs with on-chip lasers is drowned in the direct RF crosstalk and cannot be retrieved. Thus, in the previous results, we always used an off-chip EDFA to boost the modulated optical signal and then fed it back into the chip. With a proper TIA and better RF isolation, the extra EDFA would not be necessary.

References

- [1] M. Fiers, T. Van Vaerenbergh, K. Caluwaerts, D. Vande Ginste, B. Schrauwen, J. Dambre, and P. Bienstman, “Time-domain and frequency-domain modeling of non-linear optical components at the circuit-level using a node-based approach,” *Journal of The Optical Society of America B-optical Physics*, vol. 29, p. 896, 5 2012.
- [2] C. K. Madsen and J. H. Zhao, “Optical filter design and analysis : a signal processing approach,” p. 408, 1999.
- [3] H. Deng and W. Bogaerts, “Pure phase modulation based on a silicon plasma dispersion modulator,” *Optics Express*, vol. 27, p. 27191, 9 2019.
- [4] L. Bogaert, L. Bogaert, H. Li, K. Van Gasse, J. Van Kerrebrouck, J. Bauwelinck, G. Roelkens, and G. Torfs, “36 Gb/s Narrowband Photoreceiver for mmWave Analog Radio-Over-Fiber,” *Journal of Lightwave Technology*, vol. 38, pp. 3289–3295, 6 2020.
- [5] H. Deng and W. Bogaerts, “Configurable Modulator based Optical Carrier Frequency Suppressed Intensity Modulation,” *2022 IEEE Photonics Society Summer Topicals Meeting Series, SUM 2022 - Proceedings, 2022*.
- [6] O. Daulay, G. Liu, K. Ye, R. Botter, Y. Klaver, Q. Tan, H. Yu, M. Hoekman, E. Klein, C. Roeloffzen, Y. Liu, and D. Marpaung, “Ultrahigh dynamic range and low noise figure programmable integrated microwave photonic filter,” *Nature Communications 2022 13:1*, vol. 13, pp. 1–8, 12 2022.
- [7] X. Guo, Y. Liu, T. Yin, B. Morrison, M. Pagani, O. Daulay, W. Bogaerts, B. J. Eggleton, A. Casas-Bedoya, and D. Marpaung, “Versatile silicon microwave photonic spectral shaper,” *APL Photonics*, vol. 6, p. 36106, 3 2021.
- [8] J. S. Fandiño, P. Muñoz, D. Doménech, and J. Capmany, “A monolithic integrated photonic microwave filter,” *Nature Photonics 2016 11:2*, vol. 11, pp. 124–129, 12 2016.

8

Conclusion and Future work

8.1 Conclusion

Silicon photonic circuits have emerged as a widely deployed solution for managing optical signal transmission. In this thesis, we introduced the entail workflow from circuits design to sample packaging, gave introduction of photonic integrated components, circuits, and microwave photonic technologies, and then proposed and demonstrated a single chip signal processor.

The presented signal processor can be programmed as a reconfigurable filter for optical signals and RF signals. The optical filter is implemented with an MZI, loaded with two independent tunable ring resonators on both arms. The optical filter can be regarded as a universally tunable optical filter, limited by the Q-factor of the ring and the number of loaded rings. If this optical filter is used to shape an optical carrier, which imprinted an RF signal using the reconfigurable modulator, the recovered RF signal will also be filtered. In this link, cascaded optical ring filters can obtain a widely tunable RF filter, while this response is also limited by the Q-factor of the ring and the number of cascaded rings.

The processor is built with transfer-printed SOAs, which form two on-chip laser sources. There are two ring resonators, which formed a Vernier filter, used in the laser cavities to select the oscillated modes. By tuning the phase tuners in the ring resonators, we can tune the wavelength of the laser. A similar concept for RF signal generation is an OEO, realized by feeding the output of the PD into the input of the modulator in the optical link. With enough optical and RF gain, the OEO cavity will also oscillate. With a proper configuration of the signal processor, a bandpass microwave photonic filter can be used to select RF modes in the OEO cavity, and tuning the central frequency of the microwave photonic filter will result in a frequency tuning of the output RF signal from the OEO.

In addition, the reconfigurable modulator in the processor can be configured as an intensity modulator or a phase modulator, or a combining of these two. Together with the on-chip laser source, the processor can act as a configurable optical transmitter, for various modulation schemes. Furthermore, the reconfigurable modulator can implement a carrier-suppressed modulation with a high extinction ratio, which makes it suitable for frequency doubling of an RF signal.

In general, this presented signal processor suggests a promising and comprehensive approach for the generation, distribution, and processing of optical and RF signals. Compared with fiber-based system, photonic integrated circuits enable this system to have a compact footprint and high configurability. And single-chip integration with laser sources further reduces the complexity and cost of the packaging. It can be widely used in data centers, wireless and satellite communication, and other optical and microwave applications. If this signal processor is set for microwave photonic applications, no additional optical devices, as well as the fiber array, are needed, at least when a proper TIA is added to the photodetectors.

8.2 Future work

In this thesis work, we proposed a single chip signal processor, which can be programmed as a reconfigurable filter for optical signals and RF signals, and provide E/O and O/E conversions. And the processor can also be used for RF signal generation and RF frequency doubling. However, this demonstrator has more capabilities and is still not perfect from many aspects.

8.2.1 More configuration possibilities

In the original circuit design, a ring modulator is added in the light path, but we did not do any characterization on it, because the ring modulator is hard to be stabilize, especially in an environment with many heaters and a hot SOA (300 mW). We can do further work to make use of the ring modulator, and then we can implement a two-tone microwave photonic links, independent or coupled, or we can use it to generate optical combs by using a phase modulation and an intensity modulation scheme.

Additionally, the signal processor can be fully separated into two configurable microwave photonic links, which makes it possible to implement an opto-electronic oscillator with PT symmetric loops. By breaking the symmetry, the system in principle can select the longitudinal modes efficiently, which makes it possible to add longer fibers and get a RF signal with much lower phase noises.

In this thesis we show the processor for analog signal processing, while it can also be used for digital signal transmission and receiving. The reconfigurable modulator design can offer a pure phase modulation, or a low chirp intensity modulation, as well as we demonstrated an equalizer with our sample. These promise an optimized optical transmitter design.

Furthermore, this system has the potential of signals' temporal processing. In the thesis we showed a basic demonstration of true time delay and signal integration, while it should be able to do much more temporal analog computing operations.

8.2.2 Performance improvement

As shown in Chapter 7.4.10, the general performance of the proposed signal processor is limited.

The most important factor is the RF link gain. Compared to other fiber-based microwave photonic systems, the optical power of the on-chip laser source is low, and there is no optical gain available on-chip to compensate the optical losses. There are circuits for SOA boosters designed in this signal processor, but they are not populated. In the future work, we can also transfer print SOA coupons with a high saturation power, to boost the on-chip laser and get a higher optical power, which can eventually lead to a higher RF gain and lower noise figure.

The other key component in this system is the modulator design. Because the designed PN junction is not that long (1.5 mm), and we did not make use of a push-pull scheme, the modulation efficiency of the modulator is also low, leading to a high RF loss. On the other hand, the reconfigurable modulator can in principle achieve a higher SFDR than normal Mach-Zehnder modulators. In a followed fabricated run (LEAP01), we designed a reconfigurable modulator with a longer PN junction 2.5 mm with an optimized layout. Further tests need to implemented to prove the advance of this modulator block.

8.2.3 Scale-up

The signal processor for optical filtering and RF filtering results are limited by the filter's orders, which is the number of ring resonators used. A better performance can be reached if more ring resonators are used. In LEAP01 run, we designed six ring resonators in a row for implementing a higher order RF filter. The sample is packaged, and we need to test it.

The reconfigurable modulator works very well in our signal processor, but with only one modulator we cannot do complex modulation schemes. In the LEAP01 run, we designed dual-parallel reconfigurable modulator designs and quad-parallel designs, with PN junction modulator and EAM modulators, to reach high-speed, high-performance universal modulation format modulator blocks.

8.2.4 Co-packaging with RF devices

We did optical, electrical and thermal packaging on the sample, but the packaging is not perfect. In the thesis, we showed that there shows a high crosstalk between the RF inputs and outputs. And because of the lack of TIAs, the RF signals obtained from the on-chip PDs are fully immersed in the crosstalk if the optical inputs are low. A better RF PCB design and co-packaging with properly designed TIA can solve this problem, then the signal processor can work stand-alone without any optical in/outs to reach an E/E conversion.

